PRIME MINISTER'S SERVICES
SCIENCE POLICY OFFICE

Wetensschapsstraat 8 rue de la Science
1040 Brussels

D/1989/1191/10

ANTARCTICA

BELGIAN SCIENTIFIC
RESEARCH PROGRAMME
ON ANTARCTICA

SCIENTIFIC RESULTS OF PHASE ONE (OCT 85 - JAN 89)

edited by
S. CASCHETTO

VOLUME II

Part A · MARINE GEOCHEMISTRY
Part B · MARINE GEOPHYSICS

This volume presents the scientific results of researches in Marine Geochemistry and in Marine Geophysics that were carried out from January 1986 to December 1988 in the framework of **Phase One** of the **Belgian Scientific Research Programme on Antarctica.**

Studies conducted in other fields addressed by the Programme form the subject of two additional volumes issued by the Science Policy Office (Vol. I: Plankton Ecology and Vol. III: Glaciology-Climatology).

The Programme was implemented through the decision of the Council of Ministers of 29 July 1985 with the aim at contributing to the betterment of the knowledge of the functioning of the Antarctic's marine ecosystems and of the role played by Antarctica and the Southern Ocean in global changes.

The studies are being carried on within **Phase Two** of the Programme that will ensure the pursuing and the development until December 1991 of the Belgian research effort.

TABLE OF CONTENTS

SCIENCE POLICY OFFICE
Research contract
nr ANTAR/08

THE BIOGEOCHEMISTRY OF BARIUM IN THE SOUTHERN OCEAN

F. Dehairs and L. Goeyens

LABORATORIUM VOOR ANALYTISCHE SCHEIKUNDE
VRIJE UNIVERSITEIT BRUSSEL
PLEINLAAN, 2
B-1050 BRUSSEL (BELGIUM)

BELGIAN SCIENTIFIC RESEARCH PROGRAMME ON ANTARCTICA
SCIENTIFIC RESULTS OF PHASE ONE
(OCT 85 - JAN 89)
VOLUME II, PART A:
MARINE GEOCHEMISTRY

ABSTRACT

In this work some aspects of the barium biogeochemistry in the Southern Ocean were studied and the usefulness of dissolved barium as a tracer of new bottom and deep water formation and of particulate barium-barite as a tracer of passed biological activity was investigated.
The data presented were obatined as a result of our participation to the INDIGO 3 campaign in the Indian Ocean sector (January and February, 1987).

Dissolved barium was measured directly on seawater using ICP-OES techniques tested for reproducibility and accuracy. Occasional decreased barium concentrations in deep and bottom water of the Prydz Bay area, indicate new bottom and deep water formation to occur. New bottom water was detectable on the shelf and slope for stations within Wild Canyon. In addition, an intermediate layer with slightly decreased dissolved barium content was observed to extend below the salinity maximum associated with the North Atlantic Deep Water core, indicating that during formation of new bottom water on the shelf, part of this water spreads out from the slope at intermediate depths. This intermediate layer occurs over most of the area south of the Polar Front. The presence of this intermediate layer, although well marked on the barium - salinity plots, is not always identified on the Tpot - salinity and the silicate - salinity diagrams. Furthermore, between the Antarctic continental slope and the Kerguelen Plateau, evidence was found of important local stocks of "new" (i.e. with decreased barium and silicate contents) bottom water. This situation stands in contrast to the limited amount (in terms of vertical and spatial extension) of new bottom water observed on the shelf. It suggests (1) the existence of other more important sites of bottom water formation along the continent and of a specific bottom topography allowing this new bottom water to be channeled to the site where we observed it and / or (2) the process of new bottom water formation to be discontinuous.
More research is needed to clarify the complex hydrology due to bottom and deep water formation in the Prydz Bay area, but our data show the usefulness of dissolved barium as an additional tool for resolving this complex hydrology.

SEM - EMP investigations show pariculate barium to be carried mainly by discrete microcrystals of barite. This is consistent with earlier observations for other oceans. Total particulate barium was also measured by ICP-OES following a metaborate fusion and pellet redissolution in nitric acid medium. The main feature of the vertical particulate barium profiles is the coincidence of a maximum with the oxygen minimum. In the oxygen minimum region the oxygen decrease appears to be significantly anticorrelated with barite. This observation could be interpreted by considering the oxygen minimum layer to develop originally by advection to, and upwelling at the Divergence of deep oxygen poor water and subsequent spreading of this water to the North and North - East, following the general flow of the Antarctic Circumpolar Current. Sedimentation and decay of biogenic particles and oxidation of organic matter produced in local surface waters sustains an input of discrete barite crystals in the oxygen minimum layer and induces a local consumption of oxygen. Downstream, within the oxygen minimum layer these processes result in the increase of barite content and the decrease of oxygen content. Evidence is thus given for (1) the oxygen minimum layer to be the result, both of advection and local processes of production - consumption and (2) water in the oxygen minimum to flow in North and North - Eastdirection.

The involvement of biological activity in barite production is clear. Evidence was found that this involvement is expressed through (1) a passive production mechanism, whereby heterotrophic oxidation of organic detritus creates local (i.e. within microenvironments) conditions of $BaSO_4$ precipitation. and / or (2) an active production mechanism, whereby phytoplankton secretes intravacuolar barite. Passive production of barite is sustained by the observation in the euphotic layer of a positive relationship between the barite content and the remineralization rate of ammonium by heterotrophs. Active production of barite is sustained by the concurrence in the euphotic layer ofoccasional extreme barite contents with increased Chlorophyll a and decreased nitrate contents.

The barite produced in the euphotic layer is carried downwards within larger particles (i.e. biogenic aggregates, fecal pellets). The largest fraction of these carriers breaks open a few hundred meter deeper, thereby releasing smaller particles whose transport is now mainly controlled by advection. The released discrete barite crystals tend to accumulate as a result of their conservative character relative to organic matter that is oxidized.

Instantaneous rates of measured ammonium remineralization were observed to depend on oxygen content of the water. In the oxygen minimum layer and below remineralization rates therefore are inversely correlated with barite content. In the euphotic layer, however, barite appears to be positively correlated with instantaneous heterotrophic activity and also with phytoplankton biomass. It can thus be stated that in the euphotic layer barite occurrence is closely in phase with biological activity, while in the oxygen minimum water it is not but rather reflects and integrates former biological activity.

TABLE OF CONTENTS

CHAPTER 1 : STATE OF THE ART.

Elements or compounds can be identified as useful tracers if the variability of their concentrations in the oceans reflects former biogeochemical, physico-chemical, hydrodynamical or anthropogenic processes, characteristic of the formation site of the watermass in which they were measured. Since biological activity in the ocean is region specific, nutrient-type elements can be useful tracers. Barium is such an element.

Over large sections of the ocean the overall picture of the dissolved barium profile shows low residual concentrations in the surface water and increasing concentrations with depth (Chan et al., 1977; Ostlund et al., 1987; Rhein et al., 1987). This is due to the involvement of barium in biological processes which result in the production of barite microcrystals (Dehairs et al., 1980). This involvement may be both active uptake of barium and production of barite by the phytoplankton (Dehairs et al., 1987, and references therein) and passive precipitation of barite in supersaturated biogenic microenvironments (Bishop, 1988, and references therein). The kinetics of barite settling and dissolution through the watercolumn were observed to be consistent with observed enrichments of dissolved barium in the deep watercolumn (Dehairs 1979; Dehairs et al., 1980).

The usefulness of the Ba - ^{226}Ra couple as a watermass tracer was recognized during the GEOSECS program and has been outlined by Broecker and Peng (1982). During the GEOSECS program several dissolved barium profiles were obtained for different areas of the Southern Ocean (Chan et al., 1977; Ostlund et al., 1987). Some of the INDIGO 3 stations we discuss in this work were choosen such as to duplicate former GEOSECS stations. This was done for intercomparison of the physico-chemical parameters, including dissolved barium.
To our knowledge it is only in the paper by Chan et al., concerning the Atlantic Ocean with its Antarctic sector, that barium profiles have been extensively discussed with regard to watermass circulation. An overview of the discussion in Chan et al., with regard to the Southern Ocean, is given below.
Circumpolar Current water (CPC or also ACC: Antarctic Circumpolar Current) enters the Atlantic sector through Drake passage and appears to have lost most of the traces of Ross Sea Bottom Water characterized by low concentrations of the nutrient-type elements. In the Atlantic sector CPC is strongly influenced by mixing with the northern limb of the cyclonic Weddell Sea Gyre. The interaction zone between both watermasses starts at 60 °W and is identified as the Weddell Sea Confluence. For the stations in the Weddell Sea Confluence area this interaction results in extensive vertical mixing of the CPC deep water core with surface waters and Weddell Sea Bottom Water. As a result, bottom waters show again depletion of nutrient-type elements as observed for mixing between CPC and Ross Sea Bottom Water. The nutrient depleted waters occur below the salinity maximum associated with North Atlantic Deep Water entering from the Argentine Basin. These nutrient depleted Weddell Sea Bottom Water is identified as newly formed bottom water. To the east, CPC continues its course to the Indian Ocean sector, where it is entrained in the southward flowing limb of the Weddell Sea Gyre.

The mixing of Weddell Sea Bottom Water with CPC water produces a modified Circumpolar Deep Water (CPDW) which is the real precursor of Antarctic Bottom Water which flows northwards into the Argentine basin, rather than the original Weddell Sea Bottom Water.

However, Ba content is not always the result of watermass mixing alone. Evidence for in-situ production, from the dissolution of a particulate Ba phase, was found as well. Indeed, deep water sections in the southern Weddell Sea have revealed that, although Tpot - salinity plots are consistent with simple end member mixing between freezing, high salinity water of the western shelf and slope of the basin and a deep water component, resulting itself from the mixing between CPDW and Winter Water, the high silicium and barium concentrations are not consistent with this scheme. For barium the concentrations are the highest observed (106 nmol/Kg) for the Atlantic. Both for silicium and barium large scale in situ production is required to explain the observed enrichments.

For surface waters in CPC, the southern ocean profiles discussed in Chan et al. (1977) show a less marked removal of barium relative to other nutrients than at lower latitudes, highlighting the differential behaviour of plankton towards incorporation of silicium and barium. This can be understood from the following facts: (1) that it is established now that inclusion of barium into diatom skeletons is not the major process of biological barium uptake; (2) that biological activity translocates dissolved barium essentially to barite and (3) that diatoms are the dominant component of Southern Ocean phytoplankton.

While the distribution of dissolved barium in the Southern Ocean has been documented to an important extent, this is not the case for particulate barium. To our knowledge particulate barium data for only one Southern ocean profile have been published (Dehairs, 1979; Dehairs et al., 1980).

From the above it follows that a more extensive documentation of the distribution of dissolved and particulate barium in the Southern Ocean is highly needed, both as a tool for understanding the complex hydrology of the Southern Ocean and for unraveling the details of the oceanic cycle of barium itself. The work we carried out in the Indian Ocean sector of Antarctica contributes to this.

CHAPTER 2 : AIM OF THE RESEARCH

The general framework of the research presented here is the study of the combined biological, physico-chemical and hydrodynamical impact on the redistribution of biolimiting and biointermediate elements in the watercolumn and vice-versa, the usefulness of some of these elements as tracers of the biogeochemical and hydrodynamical processes at stake. While these processes occur everywhere in the World Ocean, their study in the Southern Ocean is of particular importance in view: (1) of the important contribution of this ocean as a site of deep water formation and of water exchange between the major oceanic basins, and (2) of the yet unresolved problem concerning the contradiction between low primary production and abundancy of nutrients and of the peculiar situation of phytoplankton composition, dominated by diatoms.

In this study we focused our attention on the better understanding of the barium biogeochemistry in the Southern Ocean, with the implication that barium has the recognized potential of a useful tracer for the hydrologist and for the geochemist interested in the processes controlling element transport and redistribution through the oceanic watercolumn. Full details of the biological control upon the biogeochemical cycle of barium and particularities of this biogeochemical cycle, proper to the Southern Ocean, remain to be resolved to optimize the usefulness of this tracer in the World Ocean in general and in the Southern Ocean in particular.Therefore, both the dissolved and particulate phases were analysed for barium. For dissolved barium the data were compared with information obtained from the profiles for Tpot, salinity and silicate. For particulate barium, the data were compared with other parameters indicative of biomass and with measurements of biological activity, specifically the mineralisation rates of organic matter by heterotrophs.

The data presented here were obtained as a result of our participation to the INDIGO 3 campaign (January - February 1987) in the Indian Ocean sector of Antarctica, with A. Poisson (LPCM; Univ. Pierre et Marie Curie, Paris) as Scientific Officer. Prime objectives for INDIGO 3 are the evaluation of the air - sea exchange of CO_2 and of the net transfer of CO_2 from the Atlantic to the Indian Ocean (Poisson et al., 1985). Thus, identification of deep water formation along this sector of Antarctica and evaluation of its relative importance represent some of the major tasks for INDIGO 3.

CHAPTER 3 : EXPERIMENTAL TECHNIQUES

3.1 Determination of the barium concentration (see also Dehairs et al., 1989).

3.1.1 The sampling at sea

The dissolved phase

50 ml seawater samples were collected from the 12 l Niskin bottles mounted on the CTD-rosette In prerinsed polyethylene bottles. The samples were subsequently acidified to pH 1.5 with concentrated HCl (Suprapur, Merck) and stored at ambient temperature.

The suspended phase

Seawater was sampled using 30 l Niskin bottles (General Oceanics). For each sampling operation ten bottles were mounted on a stainless steel wire with a diameter of 8 mm. The bottles were closed using brass messengers. Depths of sampling were calculated from the protected and un-protected reversed thermometer readings.

On board the ship the Niskin bottles were mounted in a frame and on-line filter holders (Millipore) were connected with silicone tubing to nipples in the bottom lids. In this configuration (design by A. Poisson) no danger exsists for loosing the fast sinking particles by sedimentation on the bottom of the Niskin bottle during filtration, as will occur when using the original outlet fitted in the lower part of the bottle flank. The Niskin bottles, with lids tightly secured, were pressurized at 0.1 bar using compressed and filtered air (0.45 µm).

The used membrane filters (Millipore AAWP; 47 mm diameter; 0.8 µm porosity) were pretreated on board by immersion in demineralized water at pH 4 during a few hours, and subsequent rinsing in Milli-Q water.
After filtration the membranes were rinsed for residual sea salt elimination with 20 ml Milli-Q water. They were then dried at 50°C and stored in sealed petri-dishes till analysis.

Determination of dissolved and particulate Ba, and of particulate Sr, Ca, Al was carried out at the department of Dr. H. Neybergh, at the Belgian Geological Survey using ICP-OES techniques.

3.1.2 Determination of dissolved barium

Introduction

Dissolved barium in seawater is currently measured by isotope dilution mass spectrometry (IDMS) techniques (Chan et al., 1977; Rhein et al., 1987). Considerable effort has been invested in elaborating other spectrometric techniques using equipment that is more accessible. Direct determination methods for barium in environmental aqueous samples

including seawater, by electrothermal atomic absorption spectrometry (Conley et al., 1979; Froelich et al., 1984; Hoenig et al., 1986), electrothermal atomic emission spectrometry (Epstein and Zander, 1979; Suzuki et al., 1981; Hui-Ming and Yao-Han, 1984), and direct-current plasma emission spectrometry (Bankston, 1981) are described in the literature. These different analytical techniques provide adequate detection limits, but are generally not suitable for routine analysis of barium in seawater due to a lack of sufficient precision. An indirect analytical technique, combining column separation of barium from major sea salt components and electrothermal atomic absorption spectrometry (Dehairs et al., 1987) seemed more promising for routine determination of barium in seawater.

In this study we demonstrate that inductively coupled plasma optical emission spectrometry, shown by others to represent a successful technique for analysis of trace amounts of barium in blood and urine (Mauras et Allain, 1979), comes up to the requirements of sensitivity and reproducibility for the routine determination of dissolved barium in seawater.

Apparatus

A Jobin-Yvon JY-38 (1983 model) sequential spectrometer with Czerny-Turner 1 m - monochromator (blazed holographic grating, 3600 lines/mm; dispersion 0.28 nm/mm; resolution 0.0054 nm) is used. A demountable torch (Durr / Jobin-Yvon) is used with six turns on the load coil. The high frequency generator (56 MHz; 5 KW operating power) is free running. The sample is introduced using a concentric pneumatic quartz nebuliser (Meinhard type C). The nebuliser argon flow is previously wetted by a humidifier filled with demineralized water to avoid clogging of the nebuliser by sea salt crystallisation. The spectrometer is interfaced (two parallel DRV11 input-output interfaces; 16 bytes) with a Digital-PDP 11/03-L computer.

Operating conditions and data acquisition

The 455.40 nm line of barium was selected. Operating power was generally 1.8 Kw. The argon flow was set as follows: coolant 19 $l.min^{-1}$; sample 0.58 l. min^{-1} with nebulizer pressure set at 2.8 $Kg.cm^{-2}$. The auxiliary flow was set at 0.25 $l.min^{-1}$. These conditions were optimised each day in order to obtain a peak to background ratio of at least 5 for a 2.5 $\mu g.l^{-1}$ barium solution.
In the profiling mode the monochromator was set at minimal wavelength increment (0.0013 nm). Signal was integrated during 200 ms with maximal amplification.

Each determination of barium is done as follows:
(1) Scanning of the 455.4 nm region (generally between 455.35 and 455.45 nm) in profiling mode for exact location of peak maximum and background intensity measurement. This is necessary to account for possible small drifts of the monochromator.
(2) Peak mode counting at a fixed wavelength coinciding with the maximum of the Ba signal obtained in profiling mode.
(3) Interpolation of the background signal at suitable distances, symmetrically about the Ba peak, for obtaining the background signal at the basis of the Ba peak.

(4) Substraction of the interpolated background signal from the Ba peak to obtain the net Ba signal.
In general the peak counting mode, after identification of the exact wavelenght position of the emission signal maximum, yields the most reliable data.
Repeated fifteen consecutive signal acquisitions, by integration over 200 ms at the wavelength corresponding with the barium maximum, yields on average 1% RSD.

Chemicals used

Barium standards were prepared from commercially available standard solutions (Titrisol, Merck). Nitric acid, used for acidification of samples and standards was of suprapur quality (Merck). Water used for dilution of samples and standards was purified on a Milli-Q grade Water System (Millipore).
Pure NaCl solutions (300 $g.l^{-1}$) were prepared free of trace amounts barium by passing them over a DIAION type CR-10 resin (Mitsubishi) with the iminodiacetic groups converted to the Na^+ form.

Effect of increasing salt content

The elaboration of a barium-free matrix, similar to natural seawater, for matrix-effect studies is a rather impossible task due to the presence of trace amounts barium in most chemicals required (Epstein and Zander, 1979; Bankston,1981). In this study we only checked the possible effect of the NaCl concentration on the background emission in the region of the 455.40 nm line.

Solutions with different NaCl content (25, 32, 33, 34, 35 and 40 $g.l^{-1}$) were obtained after appropriately diluting a 300 $g.l^{-1}$ stock solution prepared free of barium by ion-exchange. Figure 3.1 shows the obtained emission spectra in the wavelength range between 455.35 and 455.45 nm for solutions of 0, 25, 35 and 40 $g.l^{-1}$ NaCl content. In Figure 3.2, the emission spectrum for 5 $\mu g.l^{-1}$ barium in 34 $g.l^{-1}$ NaCl solution is compared with those for 0 and 40 $g.l^{-1}$ NaCl solution without barium added. From these two figures it appears that the variability of sub-peak background intensity is rather small and that the presence of barium has no effect on the background intensity. For the samples without barium addition the maximum deviation from the average background count is 11% when considering the different NaCl solutions and demineralized water together. It thus appears that there is no systematic evolution of background emission with NaCl content.

From these results it could be tentatively concluded that the NaCl matrix and possibly the sea salt matrix do not affect the Ba signal, and, therefore, that the direct calibration method using standards prepared in NaCl medium could be applied. This is checked further below.

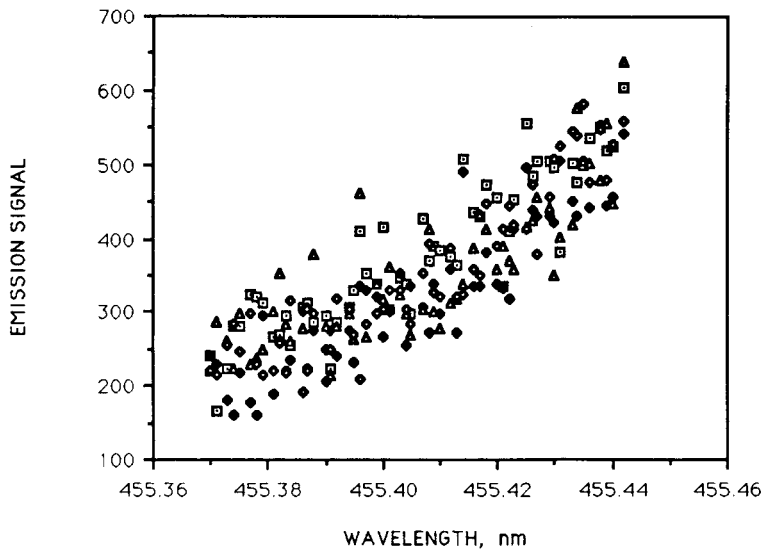

Fig. 3.1.: Background emission signals (arbitrary units; a.u.) between 455.37 and 455.445 nm for barium-free 25 $g.l^{-1}$ (□); 35 $g.l^{-1}$ (◆); 40 $g.l^{-1}$ (△) NaCl solutions and demineralized water (◇).

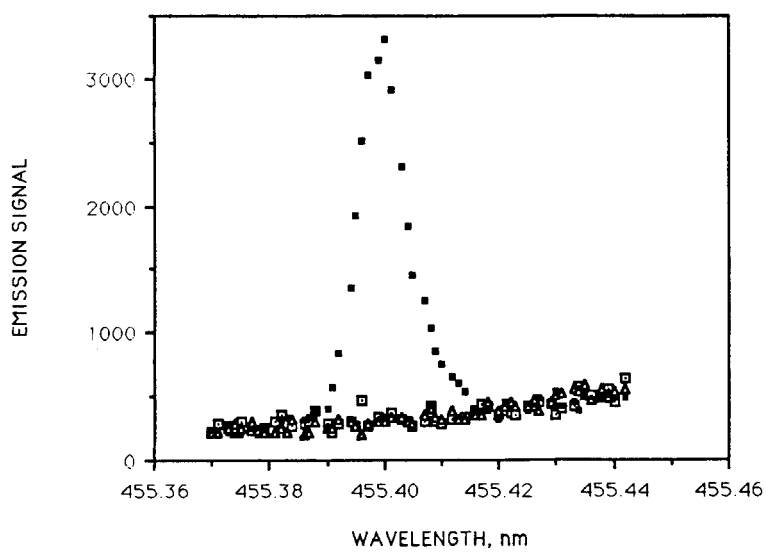

Fig. 3.2.: Emission signals (a.u.) between 455.37 nm and 455.445 nm for a barium-free 40 $g.l^{-1}$ NaCl solution (□); a34 $g.l^{-1}$ NaCl solution with 5 $\mu g.l^{-1}$ barium added (■) and demineralized water (△).

Comparison between the direct calibration and the standard addition methods

From Figure 3.3, comparing the emission spectra of natural seawater (containing barium) with the 0 and 35 $g.l^{-1}$ NaCl solutions (without barium), a difference in background intensity between natural seawater and pure NaCl solution is evident. For this natural seawater sample the interpolated background value below the barium maximum is 1.23 times the average value obtained for the different NaCl solutions and demineralized water.

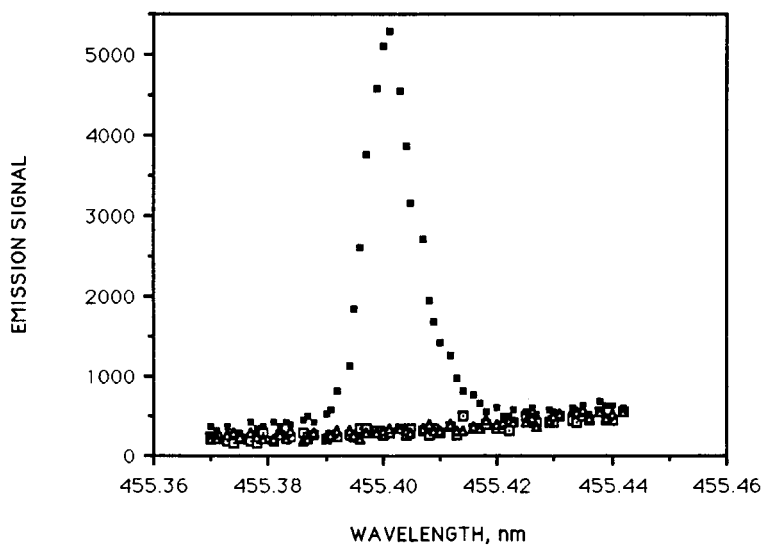

Fig. 3.3: Emission signals (a.u.) between 455.37 and 455.445 nm for a barium-free 35 g.l-1 NaCl solution (▫); demineralized water (△) and natural Mediterranean Sea water (▪)

It is now checked whether such a matrix effect has an impact on the sensitivity of the method, that is on the slope of the emission signal versus concentration regression.
Barium standards of 5,10,15, and 20 $\mu g.l^{-1}$ were prepared in demineralized water and 34 $g.l^{-1}$ NaCl solution. The pure water and 34 $g.l^{-1}$ NaCl solution without barium added were taken as the zero. To three 5 ml fractions of a Mediterranean Sea sample, we added: (1) 1ml demineralized water without barium; (2) 50 ng barium in 1 ml demineralized water; (3) 100 ng barium in 1 ml demineralized water. This gives additions respectively of 0, 8.33 and 16.66 µg.l-1 (Figure 3.4).

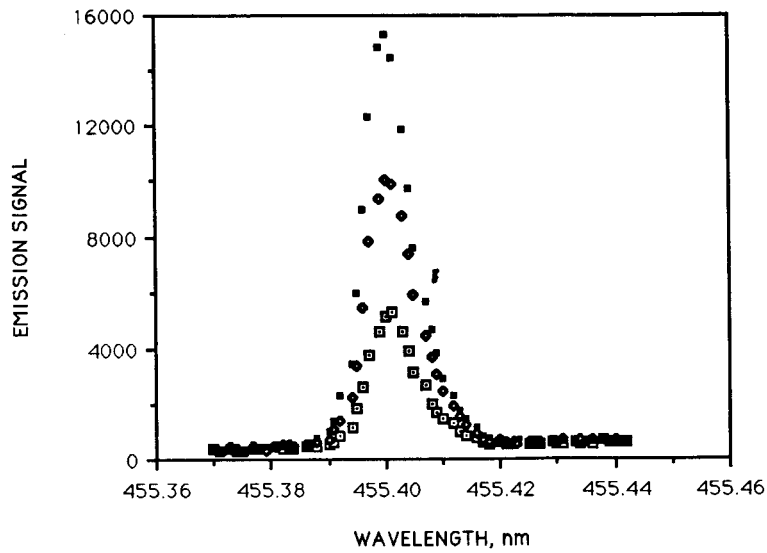

Fig. 3.4: Emission signals (a.u.) between 455.37 and 455.445 nm for a standard addition calibration on natural Mediterranean Sea water. Barium additions are: + 0 (□); + 8.33 (◇); + 16.66 µg.l^{-1} (■).

In Table 3.1 we compare the slopes of the barium calibration in demineralized water and in pure NaCl solution (34 g.l^{-1}) with the slope of the barium calibration in natural seawater.

Table 3.1: Comparison of calibration curve slopes for barium in demineralized water, 34 g.l^{-1} NaCL solution and natural seawater. Values expressed relative to the value for demineralized water (= 100 %).

Sample type	Slope value, %
Demineralized water	100
34 g.l^{-1} NaCl solution	99.4
Natural seawater	89.4*±0.04

* Mean value ± 1 σ for five standard addition series prepared from one single sample.

While slopes for demineralized water and NaCl solutions are similar, we obtain a slope ratio for natural seawater over NaCl solution of 0.9, indicating clearly a matrix effect to operate for natural seawater. Hypothesis testing (Till, 1974) indicates the mean value of the slopes for the calibration in natural seawater to be significantly different (at the 95 % confidence interval) from the mean value of the pooled slopes for the calibration in

demineralized water and 34 $g.l^{-1}$ NaCl solution. This observation precludes the use of the faster direct calibration method and renders utilisation of the standard addition method imperative.

Reproducibility and detection limit

To test the reproducibility of the technique we prepared five series of samples from the same original seawater solution, using the standard addition scheme given above. This was done for two different Mediterranean Sea samples with different barium content. The results are presented in Table 3.2. It appears that the described method allows to obtain a precision of 1.5 %, what is about half the precision obtained with the I.D.M.S. technique (0.7 %; Chan et al. 1979) but is significantly better than the precision obtained by others using different atomic absorption and emission spectrometric techniques (Epstein and Zander, 1979; Bankston, 1981 and Dehairs et al., 1987).

Table3.2: Reproducibility of five repeated barium determinations on two different Mediterranean Sea water samples.

Med. Sea 1	Ba ($\mu g.l^{-1}$)	Med. Sea 2	Ba ($\mu g.l^{-1}$)
1-1	9.56	2-1	7.78
1-2	9.87	2-2	7.64
1-3	9.78	2-3	7.60
1-4	9.46	2-4	7.76
1-5	9.64	2-5	7.59
AV. $\pm 1\sigma$ =	9.66 $\pm$ 0.165	AV. $\pm 1\sigma$ =	7.67 $\pm$ 0.09
	RSD = 1.7 %		RSD = 1.2 %

For determining the detection limit, ten below peak background values for natural seawater samples were calculated by interpolation of the emission signal at symmetrical distances about the Ba peak. The barium concentration corresponding with the 2 sigma value of these background measurements was deduced from the standard addition regression on the same seawater sample. In these conditions a detection limit of 0.05 $\mu g.l^{-1}$ is obtained .

Accuracy of the method (see also section 5.1.1)

It is difficult to test the accuracy of the technique used here, since no reference seawater with certified barium content is commercially available at present. Therefore, we can only compare our barium results with those obtained by others for the same general area. In Fig. 3.5 we compare barium-salinity plots for three vertical profiles south of the polar Front (station 92: 50°92'S-29°11'E, sea floor at 6435 m; station 93: 50°41'S-29°01'E, sea floor at 4770 m; station 94: 50°35'S-27°03'E, sea floor at 4508 m) with the one for GEOSECS station G429 (47°40'S-57°51'E, sea floor at 4600 m; Ostlund et al., 1987).

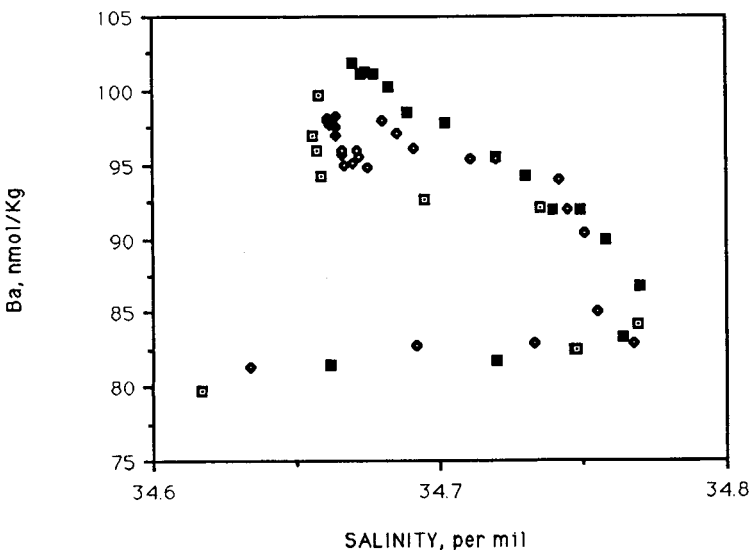

Fig. 3.5: Comparison of barium-salinity plots between INDIGO 3 stations 92 (◆), 93 (⧈), 94 (◇) and GEOSECS station G429 (■).

In Fig. 3.6 the barium-salinity plot for station 98 (38°00'S-23°21'E, sea floor at 5325 m) is compared with the one for GEOSECS station G93 (41°46'S-18°27'E, sea floor at 4953 m; Chan et al., 1977). To resolve the details for the mid and deep watercolumn the plots in Figs. 3.5 and 3.6 are restricted to salinities larger than 34.6‰, representing the watercolumn from 600 to 1000 m depth down to the sea floor, depending on the station. Both data sets are closely similar in the barium range between 75 and 94 nmol.Kg^{-1}, a region that includes the salinity maximum of the Antarctic Circumpolar Current. With increasing depth and decreasing salinities our data indicate slightly lower barium values. This feature is also apparant on the silicium-salinity plots, suggesting the lower barium values in the bottom waters at INDIGO 3 to be genuine.

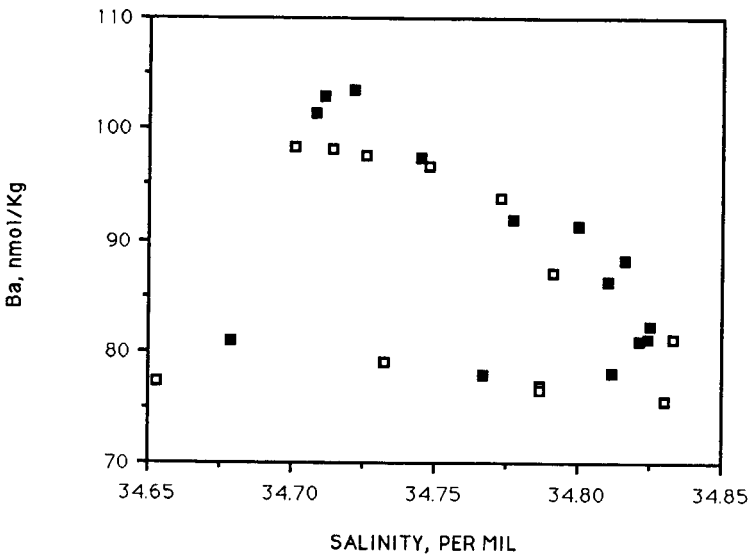

Fig. 3.6: Comparison of barium-salinity plots between INDIGO 3 station 98 (□)and GEOSECS station G93 (■).

3.1.3. Total analysis of the suspended matter (see also Stroobants, 1988).

Introduction

For the analysis of the particulate matter a digestion-mineralisation technique had to be elaborated. While strong acid digestion (e.g. HNO_3 / HCl / HF) is known to be suitable for the adequate determination of Al and certainly Ca, Sr, Si, the expected presence of barium as the mineral barite ($BaSO_4$) made this technique less attractive due to possible incomplete dissolution of the barite. Nevertheless, at least partial dissolution of suspended marine barite in dilute acid medium (0.1 N HNO_3) has been observed (Bishop, 1988). Researchers analysing for sedimentary barium-barite by atomic-emission or atomic-absorption, prefer the use of alkaline fusion techniques for the complete dissolution of this mineral (Burman et al., 1978).We have slightly adapted this latter technique for application with samples of suspended matter collected on an organic membrane (e.g. cellulose acetate + cellulose nitrate).The determination is done using ICP-OES.

Mineralization protocol

The dry membrane filters are folded and introduced into platinum crucibles. In order to precombust the organic matter from filter matrix and sampled plankton, 1 ml of HNO_3 (65%, Merck, Suprapur) is added to the crucibles which are left at 50 °C till dissolution of the filter membrane (generally after 10 min.). Crucibles are withdrawn from the heating plate and 2 ml of H_2O_2 (30 %, Merck, Suprapur) are added; the oxidation reaction is allowed to proceed for at least 30 min. at 50 °C. One additional ml H_2O_2 is added and the samples left

at 50°C till complete evaporation of the solution. The samples are brought to a temperature of approx. 700 °C, to allow for maximal combustion of the remaining refractory carbon.
When cooled-down, 50 mg of $LiBO_2$ (Johnson & Matthey; Specpure) are weighed into the crucibles. Adding either less (25 mg) or more (75 mg) $LiBO_2$ did not affect the final result, as tested on Millipore HAWP membranes doped with barium. The 50 mg addition was choosen, since this is about the minimum amount required for obtaining a more or less uniform spreading of the $LiBO_2$ in the bottom of the crucibles. After addition of the $LiBO_2$ the crucibles are left for 60 min. in a muffel furnace at 1100 °C.
The crucibles are rapidly cooled-down and the formed glassy pearl is cracked by immersion of the crucible-bottom in a cold water bath. To dissolve the glassy pearl 0.4 ml HNO_3 (65%) and 2 ml H_2O (Millipore Mflli-Q grade) are added and the samples are stirred for 60 min. at 100 °C.
Solutions are quantitatively transferred to 10 ml volumetric flasks and brought to volume. Samples are finally transferred into polypropylene tubes and stored at 4°C. Their matrix is 0.5% $LiBO_2$ and 4% HNO_3.

ICP determination of barium, strontium, calcium and aluminium

The same Jobin-Yvon-Durr torch configuration, as described above for dissolved barium, is used in this case. Torch height was set for optimal barium respons on the Jobin-Yvon 48 simultaneous spectrometer. Nebulizer type and gas flow settings are generally the same as for use with the sequential spectrometer (see above), but with the auxiliary flow now set at 0.15 $l.min^{-1}$.
Position of the primary slit is always set for optimal barium signal.
Calibration is against external standards (Titrisol; Merck) prepared in a similar $LiBO_2$ / HNO_3 matrix as the samples. After each set of five samples the series of standards are measured again.
For barium the reproducibility for 5 determinations of the same solution is found to be between 1 and 5% for final concentrations between 10 and 50 $\mu g.l^{-1}$, and <1.5% for concentrations larger than 50 $\mu g.l^{-1}$.

Recovery due to the mineralization technique and overall reproducibility

In our case recovery could impossibly be checked on natural samples due the absence of duplicates. But even in case duplicate or triplicate samples would be available, the recovery is difficult to check as particle distributions are heterogenous as well on the filter as in a given seawater environment. Therefore we prepared six Millipore HAWP membranes by allowing a microdrop, carrying 2 µg of barium, to dry on each filter. The filters were then processed as described above. Results gave a recovery of 100 % and a precision of 3.4%.

Colorimetric determination of silicium using the Technicon auto-analysis chain

A modified version of the molybdene-blue technique (Strickland and Parsons, 1968) is used here. At pH 1.2 ammonium molybdate reacts with silicate and phosphate. By adding oxalic acid the molybdo-phosphoric acid complex is broken down leaving the molybdo-

silicic acid complex unaffected. The absorption of this complex is measured at 725 nm. Concentrations were measured in the range 0 to 10 ppm. If required samples were diluted with a 0.5% $LiBO_2$ + 4% HNO_3 solution to fit within this concentration range.

Blanks

On board the ship several blank filters were treated the same way as those intended for sampling, with exception of the filtration step. For 5 blank filters the following average procedural blank values were obtained :

Ba: 33.4 ± 15.4 ng / filter (RSD = 46.2 %)
Ca: 2.98 ± 0.55 µg / filter (RSD = 18.6 %)
Sr: 51.8 ± 25.3 ng / filter (RSD = 48.9 %)
Si: 2.26 ± 0.65 µg / filter (RSD = 29.0 %)
Al: 1.39 ± 0.24 µg / filter (RSD = 17.5 %)

The above blank values were substracted from the sample values.

3.1.4. SEM-EMP analyses

A few samples of suspended matter collected on nuclepore membranes (polycarbonate matrix) were inspected for barite microcrystal presence, using a scanning electron microscope and electron microprobe equipment. These analyses were performed by P. Bernard at the Department of Analytical Chemistry (Prof. R. Van Grieken), Universitaire Instelling Antwerpen (UIA). A JEOL JXA 733 Superprobe, equipped with a TRACOR-NORTHERN energy dispersive X-ray detector (Si(Li) semi-conductor) were used.
Samples were coated with a carbon layer, ± 50 nm thick. Automatic detection of the dense barite particles was carried out using the Particle Recognition and Characterisation (PRC) programme elaborated at the UIA (description given in Van Put, 1987). The SEM is operated in the reflected-electron mode for obtaining the composition image, and is set to scan a preset number of fields (between 132 and 153 in this study) at a constant magnification (3000x). While the electron beam proceeds with successive line-scans through the selected field, particle localisation is based on the intensity of the composition image. Contour-pixels with intensity greater than a preset treshold will define the particle. From the pojected surface area of the particle a shapefactor is deduced, given by:

$$\frac{(\text{circumference})^2}{4\,\pi\,.(\text{surface area})}$$

For a sphere this shapefactor is = 1. Aggregated particles will be recorded as single large particles. This is corrected for as explained in section 5.2.1 .The selected particle is subsequently analysed for elemental ($Z \geq 11$) composition. For a barite particle this results in recording of the barium L alfa1,2 lines (resp. 4466 and 4451 ev) and the sulfur K alfa1,2 lines (resp. 2308 and 2307 ev).

3.2 The automated determination of nutrients

3.2.1 General principles

The nutrient analyses are performed by means of Technicon Autoanalyzer systems. The main property of such a system is its modular construction. By means of an automatic sampler sea water (the samples) and rince water is alternatively introduced into the system in order to separate between two consecutive samples. A peristaltic pump, which is the heart of the system, maintains a continuous and constant flow rate of reagents and sample in the manifold; flow rates and residence times, determined by the diameters of the tubes, as well as the lenghts of the mixing and delay coils, are properly choosen for an optimal reaction.
All the nutrient determinations are based on the formation of a coloured compound. Its absorption, measured by a colorimeter equipped with a flow-through-cell, is directly proportional to the concentration of the nutrient in the sea water sample.

3.2.2 The determination of nitrate (and nitrite)

The most widely accepted method for the determination of nitrate is based on the reduction of nitrate to nitrite, the diazotation of sulfanilamide by nitrite and the subsequent coupling of the diazo compound with N-(1-naphtyl)-ethylene diamine (Bendschneider and Robinson, 1952). The reaction product is a pink coloured compound, whose absorption, measured at 550 nm, is proportional to the nitrite concentration. This procedure was fully adapted to automatic analysis (Armstrong et al. , 1967; Grasshoff, 1969; Tréguer and Le Corre, 1975). Nitrate is reduced to nitrite on the manifold by passage over a cadmium-copper column (Wood et al. ,1967). This offers the advantage of passing every sample through the same column, what precludes column-to-column standardization problems. Moreover, reproducibility increases greatly as compared to the gravity feed columns used in manual analyses (D'Elia, 1983).

During the INDIGO 3 expedition a Technicon Autoanalyzer AA II, equipped with a Hewlett Packard 85 computer for data treatment and steering of the autoanalyzer system, was used.
As nitrate concentrations in the Southern Ocean mostly exceed 20 $\mu mol.l^{-1}$, a calibration with three standards - 10, 20 and 40 $\mu mol.l^{-1}$, respectively - was repeated before each run. For the stations situated north from the Antarctic Convergence, in subtropical regions, a supplementary run was inserted for the mixed layer samples with standards of 2, 4 and 8 $\mu mol.l^{-1}$. The analyses were performed at the normal speed of 40 measurements per hour.

For nitrite the same setup, with exclusion of the Cd column was used. Nitrite concentrations were obtained in function of three standards (1,2 and 4 $mol.l^{-1}$, respectively). Analyses of nitrite, however, were not performed at every station.

3.2.3 The determination of ammonium

Fundamental for this analysis is the so-called Berthelot reaction. At high pH (>11.5)

ammonium reacts with hypochlorite to form monochloramine. This compound gives formation to an indophenol blue complex in the presence of phenol and an excess of hypochlorite. Its absorption is measured at 630 nm.

Application of this method to sea water samples is made possible by complexation of the Ca and Mg ions with sodium tricitrate in order to eliminate the formation of hydroxide precipitates at high pH. As the development of the coloured reaction product happens quite slowly at ambient temperature, even with the use of nitroprusside as a catalyst, the reaction temperature is mostly raised up to 70° C.

The automation of the method is described by many different autors. Slawyk (1971) as well as Grasshoff and Johannsen (1972) used the Tehnicon Autoanalyzer 1, Tréguer and Le Corre (1975) described the technique for the Autoanalyzer 2.

A second Technicon Autoanalyzer AA II served for the ammonium analyses during INDIGO 3. The complete set up was mounted on one lab table and analyses of ammonium and nitrite were carried out in one run. The Hewlett Packard 85 computer steered both types of analyses and treated the complete measurements for reporting of the nutrient concentrations.

In this analysis also three different standards (1, 2 and 4 $\mu mol.l^{-1)}$ were used. The analyses were performed at a rate of 40 samples per hour.

3.3 The N-15 methodology

3.3.1 General principles

The introduction and use of the stable isotope N-15 was very significant for our present knowledge about the utilization and recycling of nitrogen compounds (Dugdale and Goering, 1967). The general experimental design consists of : (1) the confinement of the sea water sample, (2) the inoculation with the labeled nutrient, (3) an incubation, (4) the collection of the particulate organic material by fitration and (5) the measurement of the incorporated label. For regeneration studies an additional step is added : (6) the isolation of ammonium from its sea water matrix in order to determine its isotopic dilution (Harrison, 1983).

The analytical procedure to determine N-15 abundances requires in first instance the conversion of bound nitrogen to dinitrogen gas. Afterwards, the isotope detection is carried out by emission spectrometry.

3.3.2 Extraction of ammonium from its sea water matrix

It is necessary to strip the ammonium before subjecting it to the isotope analysis. This excludes the interference of the many other nitrogen compounds present in the sea water and mostly it signifies a concentration of ammonium into a very small sample.

Several different ways have been described for the isolation of ammonium. Initially, direct distillation (Harrison, 1978 and Caperon et al., 1979) or distillation in combination with evaporation (Glibert et al., 1982) or microdiffusion (Paasche and Kristiansen, 1982) have been used. These methods are rather time consuming and, due to extensive handling, they are prone to contamination too. More recently, extraction of ammonium by precipitation as a mercury compound (Fisher and Morrissey, 1985) and by complexation (Dudek et al. , 1986, and Selmer and Sorensson, 1986) was proposed.

Diffusion techniques as used in experiments with ammonium rich sediments (Blackburn, 1979) as well as in experiments with mixed alga-rotifer cultures and with natural marine plankton samples (Kristiansen and Paasche, personnal communication) are more common now.

In our work a similar diffusion method was set up : the ammonium was liberated from the sea water as ammonia gas, after addition of an excess of hydroxide, and trapped in a small amount of acid. Two different experimental designs were used. Primarily, to a 150 ml sea water sample 0.5 ml KOH (50%) was added, and the liberated NH_3 was transferred to the acid by a carrier gas (clean air). To reduce the manipulation steps and possible contamination during the absorption, NH_3 was immediatly trapped in the discharge tubes (see section 3.3.3) on small glass beads coated with boric acid. As it was pointed out later, fractionation of the isotopes (N-14 and N-15) can happen during the diffusion proces. With a quantification of this phenomenon it remains possible to determine correctly the N-15 abundance of the samples.

For practical reasons use was also made of a second methodological set up : serum vials equipped with a small absorption unit at the rubber stoppers of the vials. This absorption unit consists mainly of a small tin cup containing Al_2O_3 impregnated with diluted sulphuric acid. To liberate the NH_3 gas an excess of hydroxide was added too. The diffusion time for this set-up is rather long but it was pointed out that a prolongation of the diffusion for two days (or more) results in a high extraction efficiency with negligable influence of the discrimination effect.

In both methods the support (the boric acid coated beads or the tin cups), carrying the ammonium, was afterwards submitted to the conversion of bound nitrogen (see section 3.3.3) prior to the isotope analysis.

3.3.3 The conversion of bound nitrogen to nitrogen gas

Although specific conversion techniques have been described for different classes of nitrogen compounds (Faust, 1976), mainly three techniques, originally developped for the conversion of particulate material, are in use (Fiedler and Proksch, 1975 and Harisson, 1983). The Kjeldahl-Rittenberg method combines a Kjeldahl digestion, to transform the particulate nitrogen into ammonium, and a subsequent oxidation of ammonium to dinitrogen by sodium hypobromite. Less laborious is the Dumas combustion method, where an oxidation of the particulate nitrogen compound is carried out with CuO in presence of an absorptive reagent (such as CaO or molecular sieve) for interfering gases.

As it was suggested that incomplete combustion can sometimes happen a combination of both methods is nowadays very common. In the so called modified Dumas method the nitrogen compound is transformed to ammonium by the classical Kjeldahl technique and afterwards the ammonium is oxidized to molecular nitrogen by the Dumas combustion.

Both, the extracted ammonium and the particulate nitrogen are converted by means of an oxidation with CuO into dinitrogen for the isotope analysis. The conversion is carried out at a temperature of 750° C in small quartz tubes (the discharge tubes). Previously they were evacuated by means of a vacuum system, with an oil rotation pump and an oil diffusion pump, to pressures < 10^{-3} Torr . Interfering gases as CO_2, H_2O and others are absorbed on CaO brickets in the tubes.

3.3.4 The optical measurement of N-15

The determination of the N-15 concentration (%) by emission spectrometry (Kumazawa, 1973; Fiedler and Proksch, 1975) is based on an isotope shift : the mass of the molecules affects the wavelenght of light emission.

The dinitrogen molecules present in a discharge tube are excited by an external energy source (the high frequency generator). The emitted radiation, caused by the return of molecules from a high-energy state to a low-energy state, is resolved by a monochromator and the intensity of light emission at the corresponding wavelenghts is proportional to the relative concentration of these molecules.

Practically, it means that for the same transition $^{14}N^{14}N$, $^{14}N^{15}N$ and $^{15}N^{15}N$ molecules are characterised by light emission at different wavelenghts due to their mass differences. The different intensities of emission at the specific wavelenght for each molecule, recorded as different peackheights, can be translated to the percentage of each isotope present in the gas.

The percentage of N-15 present is deduced from the emission intensities at two of the three wavelenghts by means of formulas common in mass spectrometric analysis and these emission spectrometric readings are corrected to real N-15 percentages by standardization (Goeyens et al. , 1985).

Two different definitions are commonly used in N-15 studies. The N-15 abundance, or the N-15 atom percent equals the amount of N-15 isotopes present in 100 nitrogen atoms. Secondly, the definition of N-15 atom percent excess, was introduced to indicate the enrichment in N-15 as compared to its natural abundance.

The natural N-15 abundance, or the concentration of N-15 in the naturally occuring nitrogen compounds, equals 0.365%.

3.4 The chemiluminescent determination of total particulate nitrogen

In a first step the sample is oxidized at high temperature (1000 - 1100 °C) in order to

In a first step the sample is oxidized at high temperature (1000 - 1100 °C) in order to convert all the bound nitrogen into nitric oxide (NO).

$$\text{N – compound} \xrightarrow{1000\ °C} \text{NO + combustion products}$$

The NO is then mixed with ozone in the detector to form an excited nitrogen dioxide. As this excited molecule decays, light is emitted and sensed by a photomultiplier tube. This resultant light emission is specific for nitric oxide.

$$NO + O_3 \rightarrow NO_2^* + O_2 \rightarrow NO_2 + O_2 + h\nu$$

It is measured in the 650 - 900 nm range, which provides an interference-free determination of the total nitrogen amount.

These analyses were carried out with an ANTEK chemiluminescent nitrogen detector, model 720 C, in the analytical laboratory of Mobil Polymers, Brussels.

3.5 Calculation of the remineralization and assimilation rate

All the different nitrogen transformations in marine environments have been studied using nitrogen-15; however, the majority of the studies have concentrated on assimilation of nitrogen compounds by planktonic organisms as well as on recycling of nitrogen.

3.5.1 Models of NH_4 uptake and remineralization

By the work of Nees et al (1962) the use of nitrogen-15 was introduced for the study of uptake of nitrogenous nutrients by phytoplankton. Dugdale and Goering (1967) did apply it to marine systems. Of great interest in their paper is the derivation of the the formula for the calculation of uptake rates (U) :

$$U = \frac{A_{p,f} \cdot P_{p,f}}{A_{d,i} \cdot T} \quad (5, 1)\text{, with}$$

$A_{p,f}$: the nitrogen-15 atom % excess of the particulate matter at the end of the incubation,

$A_{d,i}$: the nitrogen-15 atom % excess of the nutrient (dissolved phase) at the beginning of the incubation,

$P_{p,f}$: the concentration of particulate nitrogen at the end of the incubation, and

T : the incubation time.

The dimension of U is mass of N per volume of sample and per time unit. Major assumptions of this model are that A_d remains constant throughout the incubation, and that U remains constant as well. This first hypothesis, however, is invalid as the isotope is diluted by unlabeled ammonium, produced by organic matter remineralization.

According to Hevesy 's isotope dilution principle Harrison (1978) calculated remineralization rates (R) by the formula :

$$R = \frac{P_s \cdot A_s (A_{d,i} - A_{d,f})}{A_{d,i} \cdot A_{d,f}} \quad (5, 2) \text{ , with}$$

P_s : the amount of spike added,

A_s : its nitrogen-15 atom % excess, and

$A_{d,i}$ and $A_{d,f}$: respectively the nitrogen-15 atom % excess of NH_4 (dissolved phase) at the beginning and at the end of the incubation experiment.

The fundamental models for the simultaneous calculation of uptake and remineralization have been described by Caperon et al (1979) and by Blackburn (1979). Essentially, they state that the regeneration of unlabeled NH_4 will result in an exponential decrease of A_d (nitrogen-15 atom % excess of NH_4). The mass balance equations for the ambient NH_4 pool on the one hand and for the nitrogen-15 isotope on the other hand give both the uptake rate and the remineralization rate

$$P_{d,f} = P_{d,i} + (R - U) \cdot T \quad (5, 3) \text{ , and}$$

$$\ln A_{d,f} = \ln A_{d,i} - \frac{R}{R - U} \ln \frac{P_{d,f}}{P_{d,i}} \quad (5, 4)$$

with $P_{d,f}$ and $P_{d,i}$: the final and initial NH_4 pool (dissolved phase) respectively.

In case the ambient NH_4 pool is low, and near the detection limit, or in case there is no statistically significant difference between the final and initial NH_4 pool a modified isotope dilution model is proposed (Glibert et al, 1982). The correction is accomplished by substituting A_d with an exponential average between $A_{d,i}$ and $A_{d,f}$:

$$\bar{A} = \frac{1}{T} A_{d,i} \int_0^T [\exp(-kT)]dt \quad (5, 5) \text{ , with}$$

$$k = \frac{1}{T} \ln \left(\frac{A_{d,i}}{A_{d,f}} \right) \quad (5, 6) \text{ .}$$

3.5.2 Practical set up of the incubation experiments.

1 l incubation bottles were filled with water from different depths : - 10 m (the euphotic zone), the oxygen mimimum layer and a deep water sample taken 200 m below the oxygen minimum.

From every sample a subsample was taken for original nutrient and total particulate nitrogen analysis. To the different bottles a spike with labeled ammonium was added and the incubations were carried out during minimally two days at the temperature of the surface water. After the incubation three subsamples were taken : 50 ml for nutrient analysis, 250 ml for the determination of the atompercent abundance of the ammonium and the remaining 800 ml for total particulate nitrogen analysis.

The nutrientanalyses were carried out on board with the Technicon autoanalyzers; for the total nitrogen analyses a well defined volume was filtered on GF/C filters from Whatman. The membranes were stored in deepfreezer during the expedition and later analysed in the laboratory after lyophilisation.

Each of the experiments was carried out in duplicate: one bottle was exposed to natural light and the second experiment was carried out in the dark.

CHAPTER 4 : EXPERIMENTAL DATA

The cruise track with position of the stations sampled is shown in Figure 4.1 .

4.1 Nitrate, nitrite, ammonia and barium in solution.

On board the ship, salinity, oxygen concentration and potential temperature were determined by the group of A. Poisson, LPCM, Université Pierre et Marie Curie, Paris; phosphate and silicate concentrations by C. Jeandel and M. Boulahdit of LPCH, La Mouette, CNES, Toulouse; chlorophyll a concentrations by J.H. Hecq and A. Goffart (Département d'Océanographie, Institut de Physique, Université de Liège) and nitrate, nitrite and ammonium concentrations by our group. The parameters are represented as follows : the depth (DEPTH) in meters; the potential temperature (T POT) in degrees Celcius; the density as sigma theta (SIG TA); the salinity (SAL) in per mil; the oxygen concentration (O2) in µmol/l; the nitrate concentration (NO3), the nitrite concentration (NO2), the ammonium concentration (NH4) and the silicate concentration (Si), all in µmol/l; the chlorophyll a concentration (Chl a) in µg/l. Phosphate data were not reproduced in the tables below.
Analyses of dissolved Ba were performed by our group in the shore-based laboratory. The dissolved barium concentration (Ba) is expressed in nmol/kg.
The data are presented in Tables 4.1 to 4.28 (---- indicates no data).

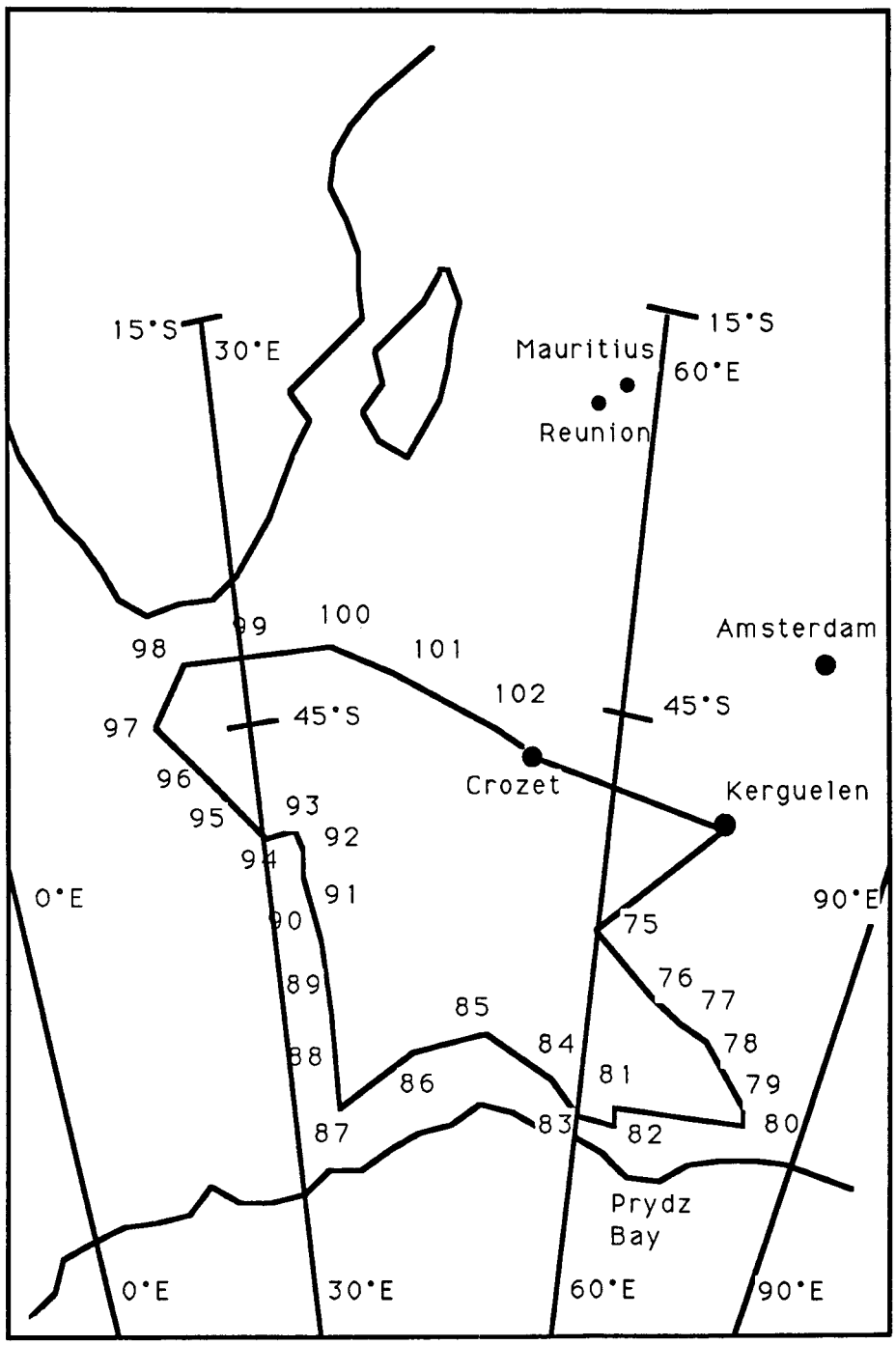

Fig 4.1: INDIGO 3 cruise track.

Table 4.1 : Chemical and physical parameters for profile **I 75** (56°29'S-63°10'E, -4800 m).

DEPTH	T POT	SIG TA	SAL	O2	NO3	Si	Ba	Chl a
-2								0.21
-12	2.326	27.084	33.922	330.1	27.3	30.7	72.8	0.21
-24	2.316	27.084	33.922	330.3	26.4	30.6	73.0	0.16
-33	2.319	27.084	33.922	330.2	27.1	30.5	75.9	0.19
-43	2.310	27.090	33.928	331.7	25.5	30.5	75.9	0.14
-51	2.311	27.086	33.924	330.9	24.6	30.5	-----	0.20
-76	1.678	27.143	33.934	334.3	26.9	30.6	76.0	0.29
-100	0.945	27.212	33.958	335.6	28.1	30.5	77.4	0.19
-126	0.641	27.243	33.974	331.3	28.3	37.2	75.6	-------
-150	0.369	27.266	33.984	332.0	27.7	37.9	73.4	0.08
-199	0.860	27.335	34.105	289.0	28.8	47.0	74.9	0.00
-250	1.492	27.443	34.291	229.5	29.4	61.1	76.02	
-308	1.910	27.528	34.436	189.8	34.2	73.3	-----	
-404	2.020	27.603	34.540	176.2	34.7	80.3	76.5	
-503	2.066	27.651	34.604	174.6	33.2	84.8	76.8	
-605	2.078	27.689	34.653	176.6	33.4	85.1	78.1	
-701	2.051	27.714	34.681	179.8	31.8	86.5	-----	
-797	1.976	27.736	34.702	183.0	32.3	89.4	80.3	
-894	1.901	27.752	34.714	185.7	32.3	91.8	82.5	
-991	1.832	27.767	34.726	189.0	31.4	93.3	83.1	
-1082	1.790	27.779	34.737	192.8	31.5	92.8	82.5	
-1199	1.703	27.791	34.744	195.5	31.3	94.2	84.2	
-1293	1.633	27.800	34.749	198.1	31.0	95.5	87.2	
-1399	1.541	27.806	34.748	200.2	30.7	98.1	87.7	
-1490	1.533	27.817	------	-----	----	----	88.4	
-1638	1.398	27.820	34.752	204.6	----	99.6	----	
-1779	1.265	27.827	34.749	204.4	30.9	103.1	90.0	
-1927	1.123	27.827	34.737	205.6	31.0	107.3	91.0	
-2085	0.966	27.831	34.729	206.0	30.0	112.2	92.9	
-2294	0.777	27.836	34.720	207.3	31.6	117.7	100.2	
-2490	0.608	27.838	34.710	208.6	32.1	123.0	99.6	
-2685	0.430	27.840	34.699	210.0	32.3	126.7	102.4	
-2891	0.297	27.840	34.690	210.9	32.2	130.4	103.1	
-3096	0.187	27.844	34.687	213.4	32.1	133.6	98.9	
-3297	0.073	27.847	34.683	216.9	31.8	136.3	96.9	
-3493	-0.048	27.848	34.677	219.8	32.5	140.3	99.0	
-3700	-0.163	27.858	------	-----	----	-----	----	
-3900	-0.267	27.853	34.669	226.7	31.5	141.5	100.0	
-4146	-0.407	27.858	34.668	232.1	31.5	141.6	100.7	

-4395	-0.494	27.859	34.664	235.3	31.9	145.8	100.7
-4638	-0.547	27.858	34.660	237.4	31.8	153.3	103.4
-4732	-0.583	27.859	34.659	238.7	32.4	154.7	107.4

Table 4.2 : chemical and physical parameters for profile **I 76** (59°28'S-69°55'E, -4440 m).

DEPTH	T POT	SIG TA	SAL	O2	NO3	Si	Ba	Chl a
-3	1.343	26.959	33.676	342.4	25.6	21.8	73.5	0.38
-12	1.344	26.955	33.671	341.8	25.3	21.8	81.0	0.4
-23	1.334	26.956	33.672	342	25.2	21.4	71.3	0.25
-32	1.324	26.956	33.671	341.2	25.1	21.2	71.5	0.33
-43	1.188	26.965	33.671	343.4	24.9	20.6	72.7	0.19
-53	0.949	26.989	33.681	345.6	26	20.6	79.5	0.36
-76	-0.696	27.106	33.723	350.6	27.6	28.5	81.6	0.28
-101	-1.642	27.192	33.792	348.9	28.9	31.1	77.3	0.18
-125	-1.337	27.258	33.883	341.7	29.3	38.6	75.3	----
-151	-0.712	27.289	------	-----	----	----	----	-----
-200	0.587	27.413	34.181	261.1	32.9	54.4	74.8	0.02
-252	1.57	27.512	34.384	207.1	33.5	68.4	75.0	
-306	1.788	27.564	34.469	187.2	33.3	76.2	77.2	
-405	1.926	27.707	34.66	176.9	33	80.8	80.7	
-505	1.988	27.662	34.61	174.6	31.8	83.2	80.6	
-606	2.003	27.701	34.66	176.9	31.7	84.1	81.6	
-706	1.993	27.721	34.685	181.2	30.9	84.6	81.9	
-805	1.964	27.746	34.713	185.4	29.9	84.1	81.9	
-904	1.916	27.76	34.726	189.1	29.6	85.1	82.3	
-1002	1.858	27.772	34.735	192.6	29.1	88.3	82.9	
-1103	1.774	27.785	34.743	195.5	28.4	88.8	85.6	
-1200	1.709	27.791	34.745	197.6	28.7	89.7	85.5	
-1302	1.603	27.801	34.747	201.9	28.7	91.1	89.1	
-1405	1.489	27.808	34.746	202.3	28.6	94.4	87.7	
-1513	1.416	27.813	34.745	202.6	28.6	96.2	90.3	
-1657	1.268	27.819	34.740	203.6	29.1	100.2	87.2	
-1803	1.114	27.822	34.730	205.0	29	104.8	91.5	
-1956	0.953	27.826	34.722	206.0	28.7	109.6	92.7	
-2102	0.828	27.828	34.715	206.4	30	114.4	94.6	
-2253	0.691	27.833	34.710	207.1	30.1	118	94.6	
-2410	0.587	27.836	34.706	208.3	30.4	120.7	95.6	
-2551	0.469	27.835	34.696	209.4	30.5	124	95.5	
-2700	0.377	27.84	34.696	209.8	30.8	127.6	94.9	
-2846	0.295	27.838	34.688	211.2	31.0	129.6	93.7	
-2991	0.204	27.84	34.684	213.8	31.1	132.7	93.9	
-3248	0.055	27.847	34.682	216.7	30.3	135.6	94.9	

-3414	-0.008	27.847	34.678	218.8	32.3	137	96.7
-3616	-0.114	27.848	34.673	221.6	35.7	139.6	95.8
-3799	-0.216	27.849	34.668	225.8	35	138.4	97.9
-4026	-0.302	27.85	34.664	229.0	36.1	137	----
-4145	-0.354	27.852	34.663	230.5	36.3	138.5	99.1
-4349	-0.506	27.859	34.663	235.8	37	148.1	98.4

Table 4.3 : chemical and physical parameters for profile **I 78** (61°45'S-76°16'E, -3990 m).

DEPTH	T POT	SIG TA	SAL	O2	NO3	NO2	NH4	Si	Ba	Chl a
-4	1.451	26.963	33.690	349.3	21.3	0.7	0.7	20.3	72.4	1.29
-13	1.445	26.963	33.690	348.6	21.2	0.6	0.8	20.2	72.2	1.11
-23	1.441	26.961	33.687	-----	21.3	0.6	0.8	20.0	71.0	0.86
-34	1.389	26.970	33.693	348.5	21.2	0.6	0.7	20.0	72.2	0.97
-42	0.935	27.085	33.800	348.8	23.3	0.6	0.7	27.6	71.4	1.18
-54	-0.483	27.205	33.857	331.3	26.7	0.6	1.5	39.9	----	1.48
-77	-1.542	27.381	34.027	307.4	30.9	---	1.2	55.1	77.1	0.21
-100	-0.213	27.496	34.231	251.1	33.2	---	0.8	65.1	75.1	0.10
-126	1.230	27.585	34.445	198.4	34.9	----	0.6	75.8	76.9	----
-152	1.511	27.615	34.507	185.8	35.2	0.3	0.7	80.5	78.1	0.04
-201	1.770	27.646	34.570	178.0	34.4	0.2	1.1	82.7	79.4	0.03
-252	1.843	27.673	34.610	174.9	34.8	0.2	0.8	82.7	79.6	----
-306	1.882	27.699	34.646	174.0	33.7		0.5	86.3	81.3	
-405	1.885	27.726	34.680	177.2	33.3		0.5	87.5	82.3	
-503	1.861	27.743	34.699	181.3	32.8		0.5	88.0	84.2	
-600	1.816	27.758	34.714	184.7	32.3		0.5	88.7	86.4	
-698	1.735	27.773	34.725	191.9	32.0		0.5	90.1	86.9	
-795	1.681	27.785	34.734	192.1	31.7		0.5	89.9	86.9	
-894	1.574	27.795	34.737	195.0	31.8		---	92.3	86.8	
-992	1.498	27.803	34.740	197.5	31.4		0.6	96.6	87.3	
-1094	1.398	27.809	34.739	199.5	31.5		0.6	97.7	87.9	
-1193	1.288	27.815	34.736	200.8	31.6		0.6	99.2	89.0	
-1289	1.213	27.819	34.735	203.0	-------		0.6	101.2	91.5	
-1390	1.118	27.822	34.731	202.9	31.9		0.7	104.4	94.5	
-1502	1.040	27.830	34.734	203.6	32.0		0.7	107.8	94.6	
-1655	0.885	27.830	34.721	204.9	32.3		0.6	111.7	97.0	
-1804	0.761	27.838	34.722	205.6	32.5		0.5	114.7	99.0	
-1953	0.635	27.829	34.701	206.0	33.1		0.6	118.7	97.8	
-2101	0.530	27.836	34.702	206.4	33.2		0.6	120.6	95.6	
-2241	0.455	27.837	34.697	207.2	33.2		0.9	122.2	98.5	
-2482	0.304	27.840	34.690	209.7	33.5		0.9	126.6	94.8	
-2725	0.167	27.844	34.686	212.6	33.3		1.0	130.3	97.1	

-2980	0.032	27.846	34.679	216.8	33.2	1.0	136.3	97.9	
-3287	-0.116	27.850	34.675	221.7	33.1	1.3	136.4	99.4	
-3587	-0.242	27.857	34.676	227.2	33.0	0.9	135.5	100.3	
-3891	-0.385	27.847	34.655	230.9	33.5	0.9	137.7	101.3	

Table 4.4 : chemical and physical parameters for profile **I 79** (64°09'S-84°03'E, -3675 m).

DEPTH	T POT	SIG TA	SAL	O2	NO3	NO2	NH4	Si	Ba	Chla
-2	0.969	27.036	33.741	347.4	23.5	0.0	0.5	28.7	71.6	1.11
-7	0.974	27.057	33.768	346.5	23.5	0.0	0.7	28.5	70.9	1.03
-18	0.991	27.043	33.752	345.9	23.6	0.0	0.6	27.6	71.6	1.28
-28	1.083	27.054	33.773	343.7	23.8	0.0	0.5	26.8	65.2	0.99
-37	1.060	27.080	33.803	343.4	24.3	0.1	0.5	28.0	75.9	1.07
-48	-1.071	27.378	34.042	329.1	27.2	0.1	0.7	49.6	76.2	1.52
-72	-1.679	27.556	34.238	297.3	30.8	0.1	0.9	69.8	76.2	0.35
-97	-1.565	27.609	34.307	294.1	30.3	0.2	0.7	71.6	80.8	0.12
-120	-1.559	27.640	34.345	296.4	30.9	0.2	0.7	72.5	79.4	----
-146	-1.417	27.649	34.362	297.5	30.9	0.2	0.6	73.0	80.8	0.03
-192	-1.387	27.663	34.380	-----	30.0	0.2	0.7	71.8	80.8	0.01
-249	-0.297	27.711	34.492	253.4	31.1	0.2	0.7	79.9	82.9	
-291	1.203	27.740	34.636	198.5	32.2	0.0	0.5	89.9	86.4	
-446	1.319	27.779	34.695	199.3	31.6	0.0	0.6	93.3	88.6	
-601	1.166	27.800	34.707	202.8	31.3	0.0	0.5	93.4	88.0	
-752	1.089	27.815	34.720	203.7	31.3	0.0	0.6	101.9	88.7	
-902	0.908	27.818	34.709	206.7	31.4	0.0	0.5	104.7	92.1	
-1047	0.817	27.824	34.709	206.4	31.2	0.0	0.6	108.4	94.2	
-1190	0.703	27.829	34.706	207.2	31.4	0.0	0.5	112.8	-----	
-1341	0.594	27.832	34.701	207.5	32.0	0.1	0.8	115.3	100.2	
-1487	0.472	27.836	34.697	208.5	32.1	0.0	0.5	117.9	100.0	
-1636	0.360	27.836	34.690	210.0	32.2	0.0	0.6	121.5	100.3	
-1783	0.277	27.839	34.687	211.7	32.3	0.0	0.5	122.4	101.7	
-1987	0.160	27.842	34.683	214.3	31.7	0.0	0.5	127.1	100.7	
-2185	0.097	27.842	34.679	214.8	32.4	0.0	0.5	131.0	----	
-2383	-0.008	27.845	34.676	218.2	32.4	0.0	0.6	129.1	99.2	
-2582	-0.088	27.847	34.673	221.7	32.2	0.0	0.5	128.5	99.9	
-2779	-0.167	27.852	34.674	222.4	31.4	0.0	0.5	126.8	99.0	
-2978	-0.245	27.855	34.673	227.9	31.8	0.1	0.5	126.9	99.2	
-3077	-0.280	27.856	34.672	229.4	32.1	0.0	0.5	126.6	96.3	
-3174	-0.317	27.857	34.671	231.0	31.9	0.1	0.6	125.5	94.9	
-3276	-0.349	27.861	34.675	232.9	31.9	0.0	0.5	122.1	96.3	
-3372	-0.379	27.860	34.672	234.7	31.7	0.0	0.5	121.0	97.1	
-3470	-0.404	27.861	34.672	235.1	31.0	0.0		119.9	99.9	
-3522	-0.419	27.861	34.670	237.4	31.9	0.0		120.4	94.4	

-3593	-0.434	27.864	34.673	235.4	31.2	0.0		120.8	95.6

Table 4.5 : chemical and physical parameters for profile **I 80** (65°10'S-84°00'E, -3255 m).

DEPTH	T POT	SIG TA	SAL	O2	NO3	NO2	NH4	Si	Ba	Chla
-2	-0.290	26.450	32.933	362.0	20.6	0.2	0.1	42.8	76.6	1.14
-14	-0.300	26.454	32.938	362.1	20.6	0.2	0.1	42.6	67.4	1.12
-24	-0.550	27.700	34.465	343.5	23.1	0.1	0.1	51.8	75.8	0.77
-45	-1.732	27.562	34.244	305.8	29.6	0.1	0.1	69.9	74.4	0.78
-78	-1.686	27.633	34.332	298.9	30.3	0.1	0.0	73.2	79.4	0.18
-102	-1.729	27.638	34.337	302.4	29.8	0.0	0.0	73.4	75.8	0.19
-153	-1.617	27.650	34.356	301.0	29.6	0.0	0.0	73.6	76.5	0.03
-204	-1.644	27.663	34.371	305.5	29.7	0.0	0.0	73.2	80.8	0.01
-352	1.015	27.760	34.645	206.8	31.2	0.0	0.0	90.3	80.1	
-500	1.208	27.798	34.709	202.6	----	0.0	0.0	96.9	84.3	
-697	0.967	27.818	34.713	206.4	30.8	0.0	0.0	104.4	87.8	
-898	0.689	27.825	34.700	208.1	30.8	0.0	0.0	113.9	----	
-1092	0.501	27.832	34.695	209.1	31.8	0.0		118.2	94.2	
-1292	0.295	27.837	34.686	212.7	32.0	0.0		123.8	90.0	
-1481	0.184	27.842	34.685	213.5	32.1	0.0		127.0	88.5	
-1664	0.066	27.845	34.681	216.1	32.5	0.0		129.7	87.8	
-1878	-0.055	27.854	34.684	221.6	31.8	0.0		127.4	89.3	
-2074	-0.143	27.857	34.682	225.2	32.0	0.0		126.7	85.7	
-2267	-0.220	27.855	34.675	228.4	32.0	0.0		126.8	87.1	
-2454	-0.288	27.858	34.674	232.0	31.9	0.0		125.1	87.8	
-2651	-0.337	27.862	34.676	233.5	31.4	0.0		123.4	88.5	
-2854	-0.384	27.863	34.675	235.9	31.2	0.0		122.5	92.1	
-3057	-0.417	27.862	34.672	236.9	31.3	0.0		122.7	91.4	
-3181	-0.445	27.874	34.685	237.7	31.4	0.0		124.0	92.8	

Table 4.6 : chemical and physical parameters for profile **I 81** (65°59'S-67°17'E, -3150 m).

DEPTH	T POT	SIG TA	SAL	O2	NO3	Si	Ba	Chla
-4	0.293	27.381	34.121	341.2	27.1	59.2	78.7	0.36
-11	0.295	27.382	34.122	340.3	27.0	59.4	80.1	0.21
-20	0.293	27.381	34.121	340.5	27.1	59.1	78.7	0.27
-32	0.228	27.393	34.132	339.9	27.3	58.9	77.7	0.32
-41	-0.224	27.459	34.185	334.6	27.9	61.0	81.6	0.33
-52	-1.442	27.618	34.322	313.3	29.7	64.4	79.6	0.32
-75	-1.633	27.701	34.418	292.5	31.3	66.4	75.7	0.19
-101	-1.646	27.715	34.434	290.2	31.4	66.8	80.9	0.12

-124	-1.599	27.721	34.444	287.3	31.5	67.8	81.3	----
-149	-1.332	27.726	34.460	281.4	31.7	71.5	81.1	0.05
-199	-0.983	27.745	34.498	271.6	32.0	75.5	82.8	0.03
-250	-0.620	27.761	34.536	259.6	32.2	78.5	82.5	
-304	0.227	27.787	34.620	231.7	31.9	84.6	85.5	
-403	0.763	27.802	34.677	214.5	32.0	92.3	----	
-502	0.715	27.822	34.698	214.5	32.2	97.4	87.8	
-607	0.758	27.819	34.698	211.0	32.3	103.3	89.8	
-698	0.660	27.819	34.691	212.5	32.3	107.0	90.9	
-792	0.669	27.826	34.700	210.3	32.7	111.4	90.5	
-894	0.619	27.822	34.691	209.0	32.6	115.3	92.2	
-1001	0.550	27.827	34.692	209.0	32.9	119.8	95.1	
-1102	0.483	27.831	34.692	209.3	33.2	124.3	95.6	
-1198	0.409	27.835	34.692	209.9	32.6	126.1	94.4	
-1302	0.363	27.841	34.696	210.0	33.4	128.4	94.8	
-1400	0.300	27.845	34.697	211.7	33.4	128.9	----	
-1486	0.229	27.845	34.692	212.5	33.4	128.7	94.6	
-1633	0.145	27.842	34.682	214.3	33.5	129.3	93.6	
-1784	0.075	27.844	34.680	216.3	33.1	131.6	94.7	
-1923	0.014	27.846	34.678	217.1	33.2	133.2	92.5	
-2074	-0.048	27.847	34.676	221.0	33.5	132.8	92.8	
-2221	-0.116	27.850	34.675	223.5	33.4	131.6	91.2	
-2368	-0.182	27.853	34.675	224.1	32.9	136.3	94.1	
-2570	-0.277	27.854	34.670	229.0	33.7	134.4	95.6	
-2772	-0.340	27.858	34.672	232.7	----	131.6	97.7	
-2872	-0.372	27.858	34.670	233.9	33.4	130.6	96.6	
-2972	-0.417	27.860	34.670	235.4	33.5	134.4	----	
-3081	-0.437	27.864	34.673	236.1	33.5	131.6	96.4	

Table 4.7 : chemical and physical parameters for profile **I 82** (67°00'S-68°04'E,.- 1350 m)

DEPTH	T POT	SIG TA	SAL	O2	NO3	Si	Ba	Chla
0							-----	0.35
-25	-0.597	27.068	33.681	345.1	26.2	56.3	74.4	0.41
-55	-1.136	27.375	34.036	324.3	28.0	60.3	76.5	0.20
-104	-1.582	27.684	34.399	298.8	30.9	66.3	78.6	0.14
-203	-1.272	27.750	34.492	288.3	31.7	73.5	82.2	0.02
-401	-0.088	27.798	34.612	238.6	32.3	90.8	85.0	
-599	0.263	27.819	34.662	221.1	32.3	104.9	86.4	
-799	0.081	27.842	34.678	223.5	30.1	111.1	89.3	
-896	0.093	27.847	34.685	220.5	32.9	117.4	92.1	
-994	-0.011	27.840	34.669	223.8	31.9	118.4	91.0	

-1092	-0.310	27.834	34.644	239.6	32.1	108.0	90.0
-1188	-0.415	27.838	34.642	243.6	32.3	105.6	88.5
-1283	-0.678	27.833	34.622	257.8	32.3	98.9	86.4

Table 4.8 : chemical and physical parameters for profile **I 83** (66°35'S-61°46'E, -1275 m).

DEPTH	T POT	SIG TA	SAL	O2	NO3	Si	Ba	Chl a
-6	0.482	27.114	33.803	350.2	25.7	53.7	74.4	----
-20	0.075	27.157	33.829	347.1	26.0	53.7	73.7	0.70
-45	-1.031	27.341	33.998	336.3	27.2	62.5	77.3	0.65
-69	-1.677	27.572	34.258	318.3	29.7	64.4	79.4	0.08
-94	-1.642	27.637	34.339	312.9	29.9	66.7	80.1	0.08
-194	-1.612	27.705	34.423	305.1	29.5	68.8	86.4	0.00
-314	-1.093	27.759	34.510	283.9	31.0	76.8	87.8	
-490	-0.645	27.803	34.587	263.0	31.3	90.5	90.7	
-711	-0.272	27.824	34.634	237.9	32.3	109.3	90.7	
-938	-0.263	27.833	34.645	235.9	32.3	114.7	94.2	
-1085	-0.245	27.841	34.656	233.4	32.5	121.9	96.3	
-1194	-0.409	27.837	34.641	243.0	32.1	114.4	96.3	

Table 4.9 : chemical and physical parameters for profile **I 84** (64°28'S-58°01'E, -4275 m).

DEPTH	T POT	SIG TA	SAL	O2	NO3	Si	Ba
-2	0.878	27.179	33.912	340.6	27.8	51.9	78.0
-15	0.869	27.176	33.908	340.4	26.3	51.7	79.4
-25	0.726	27.184	33.907	339.6	28.0	51.9	73.7
-35	0.716	27.188	33.911	341.3	28.3	51.7	75.1
-44	0.693	27.205	33.930	340.5	28.8	51.7	73.0
-53	0.318	27.235	33.942	339.2	28.7	52.3	78.0
-73	-0.691	27.426	34.119	316.7	29.9	55.2	80.8
-98	0.484	27.657	34.477	224.4	33.4	78.0	79.3
-123	1.313	27.702	34.598	190.0	34.4	88.7	78.6
-149	1.521	27.714	34.631	183.8	34.2	91.1	82.2
-201	1.561	27.732	34.658	185.2	33.6	92.6	82.2
-252	1.516	27.749	34.674	186.5	33.4	93.3	82.9
-304	1.511	27.755	34.682	186.7	32.6	94.9	84.3
-400	1.504	27.772	34.702	189.2	32.5	96.1	82.2
-495	1.461	27.784	34.713	192.0	32.0	96.4	86.4
-701	1.270	27.805	34.722	197.9	31.2	101.6	86.4
-802	1.041	27.810	34.709	203.9	31.6	102.5	87.8
-902	0.991	27.815	34.711	206.0	31.5	104.3	86.4

-1051	0.842	27.820	34.706	206.7	31.2	107.4	89.3
-1201	0.676	27.823	34.697	209.4	31.7	110.2	89.6
-1349	0.637	27.829	34.701	208.7	32.1	116.0	91.4
-1496	0.516	27.831	34.695	208.7	32.2	117.3	90.7
-1790	0.287	27.833	34.681	212.3	32.5	120.4	91.4
-1993	0.128	27.832	34.668	218.2	32.9	119.1	91.7
-2248	0.007	27.836	34.666	221.4	32.7	122.6	92.1
-2500	-0.083	27.841	34.666	222.9	32.9	126.1	94.9
-2745	-0.249	27.841	34.656	231.3	32.7	122.1	96.3
-3003	-0.327	27.848	34.660	233.2	32.8	125.2	96.3
-3250	-0.423	27.851	34.658	237.8	32.4	124.5	97.4
-3503	-0.507	27.851	34.653	241.7	32.5	123.4	92.4
-3701	-0.580	27.849	34.647	245.0	32.6	121.6	87.8
-3901	-0.660	27.850	34.644	250.3	31.7	118.0	90.7
-4054	-0.739	27.849	34.638	256.9	31.5	109.1	88.5
-4265	-0.820	27.849	34.634	262.1	31.3	102.8	87.8

Table 4.10 : chemical and physical parameters for profile **I 85** (62°20'S-50°00'E, -5070 m).

DEPTH	T POT	SIG TA	SAL	O2	Si	Ba	Chl a
-4	0.988	27.044	33.753	339.0	42.9	74.8	----
-13	0.966	27.043	33.750	338.9	42.8	70.2	0.08
-24	0.945	27.045	33.751	339.1	42.8	68.1	0.12
-34	0.944	27.045	33.751	338.3	42.8	----	0.18
-44	0.935	27.049	33.755	339.3	43.6	71.6	0.06
-54	0.926	27.052	33.758	339.7	43.6	74.4	0.09
-75	-1.533	27.301	33.929	349.0	45.6	74.4	0.17
-102	-1.582	27.356	33.995	335.9	46.6	74.4	0.15
-125	-0.833	27.447	34.138	297.6	57.4	74.4	---
-151	0.646	27.553	34.359	232.7	71.8	73.7	0.03
-198	1.533	27.641	34.541	189.0	83.2	79.7	0.00
-246	1.654	27.676	34.596	185.4	85.8	79.4	
-304	1.701	27.696	34.625	179.3	89.1	79.4	
-403	1.739	27.732	34.674	181.4	89.7	80.1	
-502	1.649	27.756	34.695	185.6	92.1	80.7	
-602	1.576	27.780	34.718	190.1	93.5	82.2	
-702	1.529	27.789	34.726	193.5	95.0	83.6	
-800	1.419	27.799	34.728	196.5	96.8	82.9	
-899	1.348	27.808	34.733	199.2	98.4	85.0	
-997	1.216	27.815	34.730	201.1	102.5	87.1	
-1098	1.126	27.819	34.728	202.5	103.9	87.1	
-1197	1.027	27.823	34.724	203.9	107.4	87.1	
-1297	0.919	27.829	34.723	205.6	110.8	90.0	

-1397	0.810	27.829	34.715	206.4	112.2	89.3
-1499	0.714	27.832	34.710	206.2	117.5	91.4
-1649	0.598	27.834	34.704	208.0	120.3	92.4
-1796	0.476	27.837	34.699	210.2	124.7	94.9
-1945	0.369	27.837	34.692	208.7	127.5	94.9
-2093	0.272	27.839	34.687	209.7	128.6	94.2
-2294	0.160	27.842	34.683	212.0	130.4	94.2
-2492	0.056	27.844	34.679	215.5	133.5	95.6
-2690	-0.028	27.845	34.675	218.6	135.0	96.3
-2889	-0.113	27.850	34.675	218.4	134.8	94.9
-3087	-0.195	27.849	34.669	224.5	135.4	97.1
-3286	-0.261	27.849	34.665	227.3	135.9	96.3
-3485	-0.334	27.853	34.665	230.1	137.7	97.8
-3750	-0.422	27.857	34.666	233.8	136.9	95.6
-3989	-0.489	27.856	34.660	236.7	135.3	94.2
-4254	-0.552	27.856	34.657	239.3	133.5	94.9
-4505	-0.605	27.859	34.658	241.3	134.2	97.1
-4756	-0.644	27.862	34.659	242.4	135.7	97.1
-5000	-0.685	27.863	34.659	243.5	143.3	96.3

Table 4.11 : chemical and physical parameters for profile **I 86** (63°45'S-42°00'E, -4725 m).

DEPTH	T POT	SIG TA	SAL	O2	NO3	Si	Ba
-3	0.828	27.137	33.856	339.4	26.6	41.5	78.0
-14	0.817	27.136	33.854	339	27.1	41.5	74.4
-24	0.810	27.137	33.855	338.8	25	41.2	75.1
-34	0.740	27.147	33.862	338.1	25	41.6	73.7
-44	0.635	27.206	33.928	337	24.6	42.4	75.8
-54	-1.497	27.435	34.095	328.4	27.5	43.6	77.2
-127	0.985	27.669	34.529	202.1	33.2	65	79.4
-152	1.330	27.695	34.591	189.0	32.1	72.3	78.6
-200	1.441	27.727	34.640	186.2	30.4	74	79.4
-251	1.467	27.744	34.664	185.6	31.2	74.8	79.4
-305	1.421	27.764	34.685	189.4	31.5	89.6	81.5
-403	1.401	27.785	34.709	193.3	30.7	90.6	85.0
-503	1.300	27.798	34.716	195.8	30.1	93	85.7
-601	1.195	27.799	34.709	198.0	30.4	93.9	85.7
-750	1.016	27.817	34.716	201.7	30.3	98	85.7
-899	0.846	27.822	34.709	204.3	29.3	101.6	87.8
-1102	0.658	27.829	34.703	206.2	30.1	105.5	89.3
-1303	0.480	27.833	34.694	208.4	31.2	109.3	88.6
-1508	0.344	27.836	34.688	208.8	29.6	112.2	88.2

-1698	0.250	27.838	34.684	209.7	31.7	115.4	----
-1900	0.153	27.841	34.681	212.4	31.5	117.3	90.0
-2109	0.054	27.847	34.682	218.1	32.1	118.9	----
-2295	-0.029	27.845	34.674	218.1	31.7	118.2	91.0
-2501	-0.112	27.847	34.671	221.5	31.9	117.5	91.4
-2701	-0.194	27.851	34.671	224.9	31.3	118.2	92.4
-3103	-0.339	27.854	34.666	230.8	31.2	117.6	92.8
-3304	-0.395	27.853	34.662	233.1	31.4	117.8	94.2
-3502	-0.445	27.854	34.660	235.4	31.8	117.9	94.9
-3703	-0.500	27.856	34.660	238.4	31.1	117.8	94.9
-4004	-0.577	27.855	34.654	242.2	31.1	117.2	95.6
-4302	-0.638	27.856	34.652	243.8	32.1	119.5	95.6
-4489	-0.658	27.858	34.654	243.6	31.7	123.7	97.1
-4659	-0.694	27.857	34.651	245.3	32.1	128.6	98.5

Table 4.12 : chemical and physical parameters for profile **I 87** (65°11'S-32°02'E, -4620 m).

DEPTH	T POT	SIG TA	SAL	O2	NO3	Si	Ba	Chl a
-3	1.055	27.123	33.856	340.0	26.4	48.7	71.6	0.12
-12	1.057	27.123	33.857	339.8	26.0	48.6	70.9	0.12
-23	0.941	27.135	33.863	340.4	26.8	49.1	70.2	0.29
-33	0.760	27.213	33.946	338.5	27.0	50.7	75.2	----
-42	-1.448	27.487	34.161	340.8	28.3	55.3	72.3	0.27
-53	-1.525	27.553	34.239	322.7	28.9	59.1	71.5	0.51
-76	-1.397	27.610	34.314	306.8	30.3	64.3	74.0	0.73
-102	-0.678	27.662	34.411	265.0	31.9	73.4	75.8	0.20
-126	0.805	27.699	34.553	209.9	33.2	85.3	79.3	----
-151	1.211	27.723	34.616	194.2	33.4	85.3	79.3	0.02
-199	1.366	27.747	34.659	189.8	33.0	92.2	79.3	0.01
-250	1.330	27.761	34.673	192.8	32.2	93.0	78.6	
-353	1.205	27.787	34.694	198.3	31.8	93.8	81.5	
-502	1.125	27.798	34.701	201.3	31.4	98.8	84.3	
-601	1.035	27.813	34.713	201.1	31.8	102.1	84.6	
-747	0.847	27.826	34.714	203.7	32.1	106.2	87.8	
-893	0.678	27.826	34.701	205.6	31.9	111.5	89.2	
-1091	0.505	27.832	34.695	207.7	32.1	114.5	90.0	
-1287	0.347	27.836	34.688	208.7	32.6	117.1	90.7	
-1485	0.224	27.835	34.679	212.0	32.5	117.5	91.4	
-1683	0.129	27.840	34.678	213.7	32.8	121.8	90.7	
-1880	0.028	27.843	34.675	217.0	32.5	122.8	90.0	
-2082	-0.063	27.844	34.671	221.2	32.3	122.8	87.8	
-2082	-0.063	27.845	34.672	221.0	32.8	124.1	87.8	
-2303	-0.161	27.845	34.666	225.4	32.7	119.1	88.5	

-2511	-0.238	27.848	34.665	228.9	31.8	118.9	93.7
-2702	-0.298	27.850	34.664	231.2	32.1	119.6	96.7
-2903	-0.361	27.851	34.661	234.6	31.8	117.2	95.6
-3108	-0.415	27.852	34.660	236.9	32.6	116.8	92.1
-3299	-0.464	27.852	34.657	239.7	32.7	115.2	90.7
-3506	-0.506	27.849	34.651	240.7	32.5	115.2	90.0
-3712	-0.539	27.853	34.654	243.2	32.4	115.2	90.0
-4015	-0.575	27.853	34.652	244.0	32.0	116.5	94.9
-4187	-0.591	27.856	34.655	246.2	32.2	115.7	95.2
-4414	-0.618	27.853	34.650	245.2	32.1	117.4	95.3
-4551	-0.648	27.855	34.651	245.7	32.6	120.4	97.0

Table 4.13 : chemical and physical parameters for profile **I 88.** (61°01'S-32°18'E, -5212 m)

DEPTH	T POT	SIG TA	SAL	O2	NO3	NO2	NH4	Si	Chl a
-14	1.288	27.051	33.786	342.1	24.6	0.3	0.5	29.0	----
-24	1.246	27.055	33.787	342.1	24.2	0.3	0.5	29.2	0.57
-33	1.216	27.056	33.786	342.5	24.1	0.3	0.5	29.2	0.49
-45	1.049	27.069	33.789	341.7	24.2	0.3	0.5	29.2	0.35
-54	-0.083	27.171	33.837	343.8	24.9	0.2	0.7	34.0	0.06
-77	-1.462	27.384	------	339.7	28.4	0.2	0.8	47.0	0.29
-103	-1.387	27.416	34.076	335.8	28.9	0.3	0.6	48.7	0.04
-128	-0.846	27.500	34.202	295.4	30.9	0.1	0.1	55.9	----
-151	0.314	27.585	------	243.5	33.1	0.0	0.1	65.2	-----
-200	1.293	27.677	34.565	196.0	34.2	0.0	0.1	75.0	0.01
-251	1.431	27.717	34.627	188.9	33.8	0.0	0.2	83.2	0.00
-251	1.431	27.717	34.627	188.8	33.5	0.0	0.3	85.5	
-313	1.453	27.739	34.656	187.4	32.8			86.6	
-412	1.421	27.764	34.685	190.4	32.2			90.0	
-506	1.371	27.785	34.706	193.0	32.1			91.5	
-607	1.281	27.796	34.712	196.6	31.8			94.2	
-758	1.098	27.812	34.716	200.7	31.7			98.3	
-908	0.911	27.820	34.711	202.9	31.9			102.7	
-1107	0.676	27.828	34.703	205.9	32.1			108.0	
-1305	0.494	27.833	34.695	207.8	32.8			111.7	
-1504	0.334	27.836	34.688	208.8	33.0			113.8	
-1700	0.224	27.838	34.682	210.7	32.1			115.7	
-1902	0.133	27.839	34.678	213.8	32.9			116.7	
-2129	0.022	27.848	----------	216.8	32.9			116.5	
-2328	-0.068	27.856	34.685	219.4	32.1			117.6	
-2577	-0.163	27.847	34.668	223.2	32.5			118.2	
-2879	-0.268	27.852	----------	227.9	32.4			117.9	

-3183	-0.357	27.854	----------	231.0	32.7	118.4
-3480	-0.437	27.856	34.663	234.6	32.0	118.1
-3777	-0.506	27.858	34.662	237.5	------	118.9
-4069	-0.564	27.857	34.658	240.3	31.4	118.6
-4360	-0.617	27.857	34.655	241.2	31.5	119.6
-4653	-0.663	27.860	34.656	243.6	-------	120.4
-4847	-0.696	27.862	34.657	244.6	31.9	121.4
-4945	-0.714	27.861	34.655	246.0	31.0	121.1
-5109	-0.738	27.862	34.654	245.9	31.0	120.9

Table 4.14 : chemical and physical parameters for profile **I 89** (57°00'S-31°47'E, -5437 m).

DEPTH	T POT	SIG TA	SAL	O2	NO3	NO2	NH4	Si	Ba	Chl a
-3	2.907	27.047	33.938	326.2	25.0	0.3	0.1	28.4	72.0	0.09
-13	2.821	27.058	33.942	326.3	25.3	0.3	0.1	28.3	72.6	0.19
-23	2.250	27.111	33.948	333.5	25.4	0.2	0.0	22.9	72.0	0.24
-32	1.908	27.142	33.954	332.6	25.4	0.2	0.1	24.9	74.1	0.25
-42	1.911	27.151	33.965	334.6	27.2	0.2	0.1	26.9	74.3	0.14
-52	1.867	27.156	33.967	334.5	27.5	0.2	0.1	27.8	73.5	0.32
-76	1.411	27.205	33.988	332.1	28.2	0.2	0.3	34.0	71.7	0.15
-101	-0.015	27.328	34.035	331.8	30.4	0.2	0.3	46.3	-------	0.06
-125	0.268	27.359	34.092	315.7	31.7	0.2	0.1	50.0	73.4	-------
-151	0.404	27.396	34.147	299.1	31.8	0.2	0.0	53.5	73.4	0.02
-199	1.136	27.483	34.311	240.7	35.5	0.1	0.0	60.9	73.6	0.01
-250	1.549	27.556	34.437	200.9	36.8	0.1	0.0	68.2	73.8	
-296	1.882	27.617	34.544	180.1	36.8			74.7	73.7	
-404	1.763	27.681	34.612	180.3	36.2			76.2	79.8	
-502	1.718	27.720	34.657	181.4	36.0			83.8	-------	
-598	1.689	27.748	----------	185.4	35.3			85.1	84.6	
-752	1.608	27.775	34.715	191.4	34.5			87.4	84.6	
-902	1.399	27.796	34.722	196.0	33.8			92.1	88.0	
-1100	1.196	27.811	34.724	200.2	34.1			96.0	92.2	
-1306	0.975	27.823	34.720	203.5	34.3			100.5	93.2	
-1504	0.729	27.827	34.706	206.2	34.6			105.7	93.5	
-1699	0.533	27.831	34.696	207.8	34.7			109.6	94.3	
-1906	0.388	27.834	34.689	209.8	35.2			112.3	94.4	
-2099	0.256	27.842	34.690	211.1	35.5			114.6	94.8	
-2353	0.128	27.840	34.679	213.5	35.2			114.5	93.9	
-2898	-0.141	27.846	34.668	222.4	35.3			115.7	94.7	
-3199	-0.260	27.848	34.664	227.0	35.0			118.0	-------	
-3499	-0.344	27.851	34.662	231.0	35.2			119.7	94.2	
-3799	-0.430	27.852	34.659	234.1	35.2			119.3	93.8	
-4099	-0.500	27.855	34.658	237.0	-------			118.1	94.0	

-4393	-0.555	27.856	34.657	239.3	34.9	120.0	94.5
-4704	-0.609	27.856	34.654	241.2	34.6	121.1	93.6
-4874	-0.634	27.858	34.655	242.2	34.8	121.1	95.2
-5147	-0.668	27.859	34.654	243.8	34.7	119.4	95.8
-5397	-0.708	27.859	34.652	244.7	34.7	120.9	106.0

Table 4.15 : chemical and physical parameters for profile **I 90** (53°01'S-31°12'E, -5180 m).

DEPTH	T POT	SIG TA	SAL	O2	NO3	Si	Chl a
-3	3.959	26.953	33.945	322.2	24.8	24.2	0.37
-14	3.854	26.966	33.948	323.4	24.8	24.4	0.27
-24	3.771	26.974	33.947	324.3	25.1	24.8	0.26
-33	3.645	26.991	33.953	326.2	24.9	24.9	0.12
-43	3.108	27.049	33.963	331.6	25.5	25.6	0.27
-52	2.046	27.16	33.989	329.0	26.6	31.3	0.38
-76	1.422	27.24	34.032	325.4	27.7	38.2	0.09
-100	1.219	27.264	34.045	321.8	28.3	41.3	0.06
-126	1.036	27.308	34.085	321.9	28.6	43.5	--------
-151	0.933	27.34	34.117	325.7	28.1	45.9	0.02
-198	1.061	27.429	34.237	257.0	32.7	56.9	0.01
-249	1.598	27.506	34.379	207.3	34.6	65.7	
-306	1.882	27.571	34.487	179.4	34.5	72.9	
-403	1.683	27.623	34.533	181.6	34.9	77.6	
-499	1.898	27.674	34.617	173.4	34.4	81.7	
-600	1.764	27.703	34.640	176.4	34.2	84.2	
-749	1.804	27.739	34.689	179.3	33.1	84.7	
-894	1.773	27.768	34.722	188.3	32	84.3	
-1093	1.626	27.792	34.738	194.4	31.5	86.0	
-1293	1.431	27.806	34.738	198.2	31.6	86.9	
-1493	1.217	27.823	---- ------	--- -----	-- ---	92.6	
-1693	0.955	27.823	34.719	204.0	-----	98.9	
-1890	0.796	27.83	34.715	206.9	32.2	101.6	
-2086	0.577	27.833	34.702	208.6	32.6	107.7	
-2349	0.374	27.833	34.687	210.5	33.3	113.4	
-2602	0.177	27.838	34.679	214.1	33.3	116.7	
-2913	0.020	27.842	34.674	218.2	33.6	119	
-3204	-0.131	27.846	34.669	222.9	33.8	119.8	
-3509	-0.24	27.848	34.665	227.7	33.2	118.4	
-3780	-0.34	27.85	34.662	231.4	33.3	120.2	
-4099	-0.444	27.854	34.66	235.1	33.1	120.3	
-4368	-0.519	27.855	34.658	237.7	33	119.6	
-4562	-0.558	27.856	34.657	239.3	33	121.1	
-4805	-0.59	27.857	34.656	240.8	32.8	121.5	

-5004	-0.602	27.857	34.656	241.3	32.9	121.7

Table 4.16 : chemical and physical parameters for profile **I 91** (51°21'S-28°31'E, -4530 m).

DEPTH	T POT	SIG TA	SAL	O2	NO3	Si	Ba
-24	3.747	26.941	33.903	327.6	22.6	18.3	73.7
-196	1.649	27.269	34.088	281.6	29.9	36.9	68.1
-498	2.133	27.553	34.489	177.8	34.8	68.6	74.0
-1002	2.098	27.736	34.714	184.9	30.3	77.1	77.4
-1506	1.739	27.800	34.759	200.4	30.0	82.3	84.2
-1997	1.249	27.829	34.750	206.4	30.6	91.7	86.3
-2508	0.744	27.837	34.719	209.8	31.6	103.8	94.3
-3469	0.083	27.841	34.677	219.4	32.2	119.3	95.2
-3740	-0.195	27.851	34.672	227.5	32.7	---------	95.4
-3946	-0.440	27.855	34.662	235.8	32.6	120.0	95.2
-4126	-0.466	27.855	34.660	236.0	31.9	121.8	94.6
-4472	-0.487	27.858	34.663	240.5	31.6	121.3	94.8

TABLE 4.17: chemical and physical parameters for profile **I 92** (50°92'S-29°11'E, -6435 m)

DEPTH	SAL	O2	NO3	PO4	SI	Ba
-4250	34.666	234.5	31.3	2.26	120.5	95.6
-4502	34.664	236	31.1	2.26	120.8	-------
-4751	34.664	236.9	30.6	2.27	121.5	97
-5001	34.664	237.3	31	2.26	122.1	97.5
-5250	34.664	237.9	30.5	2.28	122.3	98.2
-5499	34.662	238.2	30.6	2.26	123.3	97.8
-5751	34.662	238.1	30	2.27	123.1	97.6
-6002	34.662	238.2	29.6	2.27	123.3	97.8
-6253	34.661	238.1	28.6	2.26	123.3	98
-6500	34.677	238.9	28	2.25	124.7	98.2

Table 4.18 : chemical and physical parameters for profile **I 93** (50°41'S-29°01'E, -4770 m).

DEPTH	T POT	SIG TA	SAL	O2	NO3	Si	Ba
-24	5.437	26.738	33.879	308.6	21.7	7.9	62.1
-190	2.647	27.122	34.003	302.3	26.7	20.8	60.9
-495	2.381	27.394	34.315	211.2	32.3	48.8	68.2

-997	2.248	27.646	34.617	175.2	31.9	72.2	79.8
-1497	2.058	27.767	34.748	194.0	28.6	75.4	82.5
-1996	1.701	27.811	34.769	204.8	27.7	81.1	84.2
-2495	1.123	27.825	34.735	204.5	29.0	98.2	92.1
-3492	0.351	27.841	34.695	213.3	29.1	115.4	92.7
-4247	-0.499	27.855	34.659	236.9	29.4	123.0	94.3
-4439	-0.510	27.854	34.657	237.8	28.1	122.7	96.0
-4600	-0.519	27.855	34.658	237.6	27.9	122.7	99.7
-4753	-0.527	27.854	34.656	237.4	27.6	122.7	96.9

Table 4.19 : chemical and physical parameters for profile **I 94** (50°35'S-27°03'E, -4508 m).

DEPTH	T POT	SIG TH	SAL	O2	NO3	Si	Ba	Chl a
-3	3.712	26.971	33.937	325.4	24.6	25.9	72.3	0.62
-13	3.665	26.981	33.943	325.5	24.8	26.7	72.0	0.08
-23	3.152	27.076	34.001	327.3	25.4	31.5	73.1	0.13
-33	2.837	27.113	34.012	329.5	25.7	33.8	73.1	0.31
-44	2.538	27.157	34.036	330.7	26.0	35.1	75.1	0.30
-53	2.473	27.176	34.052	330.8	26.2	36.5	-------	0.34
-77	2.248	27.218	34.082	330.4	26.5	40.4	74.7	0.46
-101	1.782	27.248	----------	331.2	26.5	40.1	75.5	0.10
-125	1.341	27.293	34.092	330.8	26.4	43.2	75.6	-------
-150	1.114	27.330	34.119	327.4	27.7	47.9	72.9	0.03
-198	0.726	27.380	34.151	307.0	29.7	52.6	73.9	0.01
-248	0.861	27.475	34.279	259.6	33.0	63.4	74.3	
-304	0.783	27.524	34.333	240.9	33.8	68.1	73.9	
-403	1.689	27.615	34.524	181.1	35.5	78.8	79.4	
-504	1.839	27.661	34.595	173.8	35.1	82.8	80.6	
-602	1.818	27.694	34.634	174.7	34.6	84.8	81.3	
-752	1.942	27.731	34.692	179.9	33.3	84.7	82.8	
-900	1.935	27.764	34.733	188.8	31.9	82.6	82.9	
-1100	1.902	27.795	34.768	199.2	30.5	--- --	83.0	
-1298	1.572	27.810	34.755	200.3	31.1	88.5	85.0	
-1497	1.379	27.820	34.751	201.7	31.3	91.9	90.3	
-1692	1.178	27.829	34.745	205.0	31.6	95.7	91.9	
-1891	1.020	27.838	34.742	207.7	31.7	98.5	94.0	
-2089	0.827	27.839	34.728	208.3	32.1	103.4	-------	
-2296	0.580	27.836	34.706	210.0	32.6	108.4	96.0	
-2496	0.512	27.844	34.711	210.6	32.7	109.4	95.4	
-2696	0.307	27.840	34.691	212.9	33.3	113.2	96.1	
-2896	0.137	27.845	34.685	216.4	33.3	115.5	97.1	
-3097	0.055	27.845	34.680	219.1	33.5	116.0	97.9	
-3296	-0.064	27.847	34.675	221.5	33.7	118.1	94.9	

-3493	-0.152	27.849	34.672	224.0	33.6	120.0	95.6
-3697	-0.190	27.850	34.670	224.6	33.6	120.1	95.1
-3995	-0.227	27.851	34.669	226.4	33.7	121.1	-------
-4196	-0.241	27.853	34.671	227.3	33.7	121.3	95.9
-4397	-0.275	27.851	34.666	228.4	33.5	120.1	96.0
-4487	-0.282	27.852	34.667	228.4	33.8	121.1	95.0

Table 4.20 : chemical and physical parameters for profile **I 95** (47°08'S-23°34'E, -5560 m).

DEPTH	T POT	SIG TA	SAL	O2	NO3	Si
3	6.890	26.548	33.872	297.4	20.8	8.1
16	6.849	26.554	33.873	297.6	20.7	7.4
24	6.810	26.561	33.875	297.9	20.7	8.0
35	6.735	26.576	33.882	298.0	20.6	8.3
45	6.620	26.594	33.885	299.9	20.7	7.3
55	6.432	26.622	33.889	300.5	21.0	8.1
79	6.154	26.665	33.898	300.9	21.1	9.2
103	5.216	26.821	33.951	302.8	21.7	11.8
128	4.805	26.896	33.986	302.4	22.7	12.4
151	4.581	26.929	33.997	300.7	23.4	13.0
197	4.346	27.032	34.095	285.7	25.3	15.6
246	4.166	27.124	34.187	270.5	27.4	19.0
303	3.737	27.167	34.186	267.4	28.7	20.7
403	3.220	27.215	34.183	260.3	30.3	25.8
504	2.847	27.266	34.205	246.7	31.9	31.8
604	2.632	27.332	34.264	226.2	33.3	41.2
753	2.602	27.419	34.370	200.2	34.5	52.5
904	2.503	27.500	34.460	185.4	35.2	61.3
1100	2.429	27.595	34.571	178.5	34.3	69.3
1301	2.417	27.666	34.659	180.5	33.3	71.1
1496	2.358	27.713	34.712	186.5	32.1	71.6
1693	2.268	27.759	34.760	195.2	30.8	71.8
1893	2.075	27.790	34.779	201.9	30.1	73.9
2085	1.921	27.812	34.791	206.0	29.7	77.2
2294	1.820	27.819	34.790	208.8	29.8	--- ----
2494	1.668	27.829	34.788	210.8	29.8	80.9
2789	1.327	27.834	34.763	208.5	31.2	94.0
3088	1.044	27.838	34.744	208.8	31.6	100.8
3387	0.729	27.842	34.724	209.5	32.4	109.8
3683	0.430	27.841	34.701	210.7	33.4	118.9
3979	0.195	27.846	34.691	214.6	33.5	124.0
4279	0.040	27.850	34.685	218.5	33.4	127.6
4575	-0.039	27.850	34.680	220.0	33.5	129.4

4886	-0.103	27.850	34.676	221.8	33.7	129.4
5172	-0.136	27.851	34.675	223.3	33.7	128.8
5369	-0.151	27.852	34.675	223.4	33.7	127.9

Table 4.21 : chemical and physical parameters for profile **I 96** (44°21'S-20°52'E, -4290 m).

DEPTH	T POT	SIG TA	SAL	O2	NO3	NO2	Si	Ba
-6	8.743	26.372	33.992	285.5	16.7	0.2	4.5	-------
-14	8.749	26.373	33.995	285.6	16.6	0.3	4.8	54.9
-23	8.750	26.373	33.995	283.0	16.6	0.2	4.5	54.4
-33	8.752	26.373	33.995	285.6	16.7	0.2	4.0	52.9
-43	8.750	26.376	----------	---------	--------	-----	-----	-------
-53	8.743	26.376	33.997	285.9	16.5	0.3	4.1	54.8
-75	7.669	26.546	34.008	291.1	17.3	0.4	4.4	52.4
-101	6.680	26.750	34.093	288.5	18.8	0.8	7.7	49.9
-122	6.312	26.842	34.148	287.5	20.0	0.3	8.4	49.4
-149	6.119	26.885	34.171	287.0	20.7	0.2	8.2	49.4
-199	5.958	26.954	34.233	277.1	22.1	0.2	9.1	50.1
-252	5.855	27.022	34.302	252.0	24.5	0.1	12.1	-------
-304	5.102	27.074	34.253	253.1	26.6		14.3	53.3
-401	4.547	27.131	34.246	247.3	28.0		18.9	-------
-505	3.802	27.169	34.196	254.5	29.1		22.2	57.6
-601	3.353	27.218	34.203	248.1	30.2		25.9	61.6
-753	2.897	27.313	34.269	224.7	32.2		37.5	64.7
-900	2.669	27.392	34.343	205.6	33.6		47.2	68.7
-1107	2.689	27.497	34.477	183.4	34.5		58.2	72.4
-1304	2.504	27.579	34.560	179.4	33.8		63.8	72.9
-1508	2.503	27.662	34.663	182.3	32.3		66.2	74.0
-1706	2.467	27.718	34.729	190.8	29.5		64.7	73.9
-1903	2.406	27.757	34.771	200.3	29.5		62.5	74.9
-2104	2.310	27.783	34.794	206.5	28.0		62.8	75.6
-2296	2.202	27.802	34.806	210.5	28.1		63.9	76.8
-2402	2.154	27.809	34.810	213.1	27.9		63.4	77.6
-2494	2.077	27.813	34.808	213.1	28.0		65.5	79.0
-2699	1.941	27.826	34.810	215.2	28.1		68.2	78.8
-2900	1.828	27.838	----------	---------	-------		-------	-------
-3100	1.583	27.837	34.790	213.7	29.0		78.6	87.6
-3299	1.361	27.835	34.768	211.3	30.1		86.6	87.6
-3497	1.220	27.891	34.825	214.9	30.1		89.3	88.2
-3694	1.038	27.849	34.758	215.9	30.3		93.8	90.1
-3898	0.861	27.850	34.744	216.2	31.0		100.2	92.3
-4095	0.611	27.849	34.724	216.0	31.9		108.2	92.8

-4242	0.381	27.848	34.706	216.6	32.7		113.4	94.4

Table 4.22 : chemical and physical parameters for profile **I 97** (41°48'S-18°27'E, -4875 m).

DEPTH	T POT	SIG TA	SAL	O2	NO3	Si
-15	19.871	25.247	35.588	221.1	0.0	7.9
-26	19.870	25.248	35.588	221.2	0.0	6.9
-79	18.457	25.659	35.650	223.6	0.2	6.3
-105	18.359	25.684	35.651	223.9	0.4	6.2
-130	18.195	25.720	35.645	221.3	1.0	6.3
-152	17.718	25.807	35.605	206.1	3.5	7.7
-176	16.814	25.984	35.551	197.8	5.5	8.0
-201	16.137	26.116	35.517	203.1	5.9	7.9
-444	12.013	26.684	35.123	209.8	11.3	10.7
-594	9.324	26.864	34.739	207.0	19.5	13.4
-793	5.430	27.102	34.338	226.2	29.3	18.9
-886	4.865	27.215	34.397	205.3	28.1	30.8
-1037	3.503	27.284	34.304	218.7	29.3	34.8
-1347	2.797	27.512	34.507	179.8	31.0	58.8
-1502	2.737	27.590	34.599	176.4	30.8	62.7
-1884	2.536	27.729	34.750	196.5	26.1	58.9
-2085	2.514	27.773	34.803	208.1	25.1	53.8
-2294	2.421	27.808	34.837	214.5	24.8	53.7
-2494	2.327	27.811	34.831	218.6	24.3	53.7
-2697	2.205	27.826	34.837	221.7	23.7	54.5
-2998	2.069	27.839	34.839	224.1	23.5	57.2
-3296	1.923	27.847	34.835	224.7	24.2	60.3
-3596	1.571	27.850	34.805	221.7	24.5	72.3
-3897	1.135	27.852	34.770	218.6	26.7	84.4
-4696	0.288	27.849	34.700	218.6	32.4	108.3
-4866	0.163	27.851	34.694	219.8	32.5	111.2

Table 4.23 : chemical and physical parameters for profile **I 98** (38°00'S-23°21'E, -5325 m).

DEPTH	T POT	SIG TA	SAL	O2	NO3	NO2	NH4	Si	Ba	Chl a
-9	23.056	24.291	35.487	213.4	0.0	9.0	9.0	8.5	34.5	-------
-17	22.663	24.408	35.493	214.7	0.0	0.1	0.5	7.3	36.5	0.26
-26	22.228	24.537	35.499	216.0	0.0	0.1	-----	6.7	36.6	0.24
-36	22.176	24.555	35.504	214.1	0.0	0.1	0.5	7.1	36.7	0.23
-46	21.836	24.671	35.531	212.4	0.2	0.2	0.5	7.1	37.5	0.21
-54	21.780	24.698	35.546	212.2	0.2	0.2	0.6	7.2	35.8	0.28

-80	21.131	24.896	35.571	207.8	0.8	0.2	0.6	7.6	37.7	0.41
-92	21.156	24.903	----------	201.5	1.9	0.1	0.7	7.9	38.9	0.28
-114	18.927	25.454	35.538	185.4	-----	0.1	0.8	9.3	37.9	-------
-142	18.396	25.637	35.602	202.0	3.1	0.1	0.7	8.0	38.0	0.08
-194	17.576	25.845	35.609	213.3	3.2	0.1	0.3	7.4	37.1	0.01
-253	16.916	25.979	35.577	207.8	4.3	0.2	0.4	7.8	38.7	
-298	15.557	26.212	35.469	198.8	5.3		0.2	9.8	38.7	
-399	14.058	26.431	35.328	208.5	7.6		0.3	8.8	40.1	
-500	12.929	26.561	35.196	207.9	9.9		0.2	9.4	39.9	
-600	11.683	26.670	35.024	213.8	11.1		0.3	9.5	42.1	
-752	9.829	26.836	34.811	208.0	17.9		0.3	12.6	45.6	
-900	7.570	27.031	34.607	196.3	24.8		0.2	22.9	57.1	
-1098	5.425	27.190	34.448	197.6	29.8		0.2	34.3	52.5	
-1299	3.917	27.342	34.428	190.0	32.4		0.2	50.2	67.6	
-1496	3.418	27.483	34.543	169.1	34.3		0.2	68.0	72.9	
-1697	2.773	27.573	34.581	175.8	34.3		0.3	71.8	76.5	
-1901	2.586	27.647	34.653	181.2	32.7		0.2	73.4	77.3	
-2085	2.567	27.712	34.732	190.6	30.7		0.2	70.3	79.0	
-2343	2.510	27.761	34.787	203.5	28.5			66.7	76.8	
-2343	2.510	27.761	34.787	203.9	28.4			-------	76.5	
-2895	2.237	27.818	34.830	219.1	28.1		0.4	65.2	75.5	
-3191	2.067	27.834	34.833	222.9	26.9		0.4	67.9	81.2	
-3487	1.885	27.844	34.828	222.1	26.5		0.4	72.2	77.9	
-3790	1.560	27.839	34.791	220.3	28.8		0.3	85.9	82.3	
-4088	1.230	27.848	34.773	218.5	30.1		0.4	97.1	93.8	
-4393	0.885	27.851	34.748	213.7	31.4		0.3	109.1	92.4	
-4694	0.612	27.851	34.726	217.4	32.1		0.4	118.6	97.6	
-4985	0.435	27.851	34.714	218.2	32.7		0.4	124.3	98.1	
-5191	0.295	27.849	34.701	219.1	33.0		0.4	127.8	98.3	
-5328	0.237	27.849	34.697	219.1	33.2		0.4	129.3	-------	

Table 4.24 : chemical and physical parameters for profile **I 99** (37°59'S-30°02'E, -4118 m).

DEPTH	T POT	SIG TA	SAL	O2	NO3	NO2	NH4	Si	ChL a
13	21.711	24.821	35.682	219.2	.0	.1	9.9	8.9	-------
23	21.714	24.823	35.686	219.3	.0	.1	.5	8.7	0.26
34	21.714	24.819	35.680	219.6	.0	.1	----	8.7	0.24
41	21.710	24.820	35.680	219.0	.1	.1	.5	8.5	0.23
52	21.704	24.822	35.681	220.2	.1	.2	.5	8.5	0.21
77	19.894	25.255	35.605	216.5	.2	.2	.6	8.5	0.28
97	18.914	25.516	35.615	208.6	1.8	.2	.6	8.5	0.41
123	18.248	25.684	35.614	213.7	2.0	.1	.7	8.3	0.28

147	17.820	25.803	35.631	216.1	2.2	.1	.8	7.8	--------
173	17.357	25.905	35.618	216.5	3.0	.1	.7	8.3	0.08
198	16.996	25.993	35.620	223.6	3.1	.1	.3	8.5	0.01
246	16.913	26.016	35.624	225.5	3.1	.2	.4	8.2	
294	16.835	26.028	35.615	225.9	3.1		.2	9.0	
400	15.100	26.274	35.418	205.5	4.7		.3	9.4	
503	13.521	26.470	35.234	215.8	5.4		.2	9.6	
642	12.005	26.641	35.065	213.3	7.1		.3	9.9	
803	10.042	26.810	34.824	211.1	16.0		.3	12.4	
1008	7.492	27.038	34.602	193.3	24.8		.2	25.6	
1103	6.371	27.113	34.501	197.7	26.4		.2	29.0	
1200	5.139	27.198	34.415	205.7	29.1		.2	33.7	
1303	4.247	27.273	34.385	202.8	30.2		.2	42.2	
1451	3.757	27.395	34.474	179.3	33.0		.3	58.9	
1751	2.964	27.565	34.592	171.4	33.8		.2	74.7	
2080	2.593	27.697	34.717	185.0	31.2		.2	75.8	
2300	2.468	27.750	34.769	194.5	29.1		----	72.3	
2398	2.426	27.765	34.784	201.8	27.9		----	68.8	
2498	2.385	27.777	34.794	205.4	27.7		.4	68.7	
2592	2.325	27.792	34.807	209.9	27.4		.4	66.7	
2701	2.264	27.802	34.813	213.3	27.4		.4	66.6	
2898	2.120	27.818	34.818	217.4	26.8		.3	68.2	
3090	1.976	27.829	34.817	218.6	26.9		.4	71.6	
3297	1.796	27.834	34.806	220.0	26.7		.3	76.1	
3496	1.546	27.841	34.792	218.2	28.2		.4	85.1	
3694	1.256	27.844	34.770	217.5	29.2		.4	94.9	
3889	0.942	27.848	34.748	217.8	30.1		.4	104.0	
4107	0.773	27.850	34.737	218.5	-------		.4	109.6	

Table 4.25 : chemical and physical parameters for profile **I 100** (37°58'S-36°03'E, -5520 m).

DEPTH	T POT	SIG TA	SAL	O2	NO3	NO2	NH4	Si	Chl a
2	20.88	24.966	35.573	223.5	0.0	0.1	0.9	8.8	------
10	20.878	24.968	35.574	222.9	0.0	0.1	0.5	8.5	0.26
21	20.873	24.967	35.572	223.1	0.0	0.1	-----	9.0	0.24
30	20.864	24.969	35.571	222.9	0.0	0.1	0.5	8.1	0.23
40	20.859	24.968	35.568	223.4	0.1	0.2	0.5	7.8	0.21
49	19.57	25.246	35.483	224.1	0.4	0.2	0.6	8.1	0.28
74	18.894	25.508	35.598	204.1	2.2	0.2	0.6	8.1	0.41
99	18.417	25.639	35.612	210.6	2.0	0.1	0.7	7.7	0.28
123	18.066	25.726	35.611	208.8	2.9	0.1	0.8	8.0	--------
147	17.912	25.763	35.609	209.9	3.1	0.1	0.7	7.6	0.08
196	17.318	25.892	35.588	209.7	3.9	0.1	0.3	8.4	0.01

248	16.144	26.087	35.482	196.4	6.6	0.2	0.4	9.1
300	15.815	26.147	35.462	195.5	6.9		0.2	8.5
399	14.168	26.402	35.322	210.9	7.9		0.3	8.0
501	12.743	26.545	35.127	214.3	10.4		0.2	7.8
647	10.994	26.716	34.92	215.0	14.1		0.3	9.5
802	8.524	26.912	34.638	207.9	21.8		0.3	13.3
1001	5.041	27.131	34.316	231.6	29.2		0.2	20.0
1099	4.722	27.224	34.388	209.5	31.1		0.2	29.8
1196	4.206	27.29	34.401	198.9	33.0		0.2	37.6
1299	3.847	27.351	34.431	188.8	34.0		0.2	44.5
1448	3.652	27.447	34.527	167.9	35.2		0.3	57.4
1750	2.826	27.61	34.633	173.1	34.3		0.2	65.4
2102	2.526	27.746	34.771	186.5	32.1		0.2	67.6
2345	2.367	27.771	34.785	200.0	30.1		-----	63.7
2345	2.367	27.77	34.784	200.3	30.1		-----	--------
2891	2.047	27.823	34.817	216.3	28.5		0.4	62.3
3145	1.842	27.832	34.808	216.6	28.9		0.4	68.3
3489	1.441	27.842	34.783	216.4	30.1		0.4	78.3
3794	1.046	27.846	34.754	217.4	31.2		0.3	89.2
4089	0.693	27.851	34.732	218.4	32.3		0.4	98.2
4435	0.437	27.852	34.715	218.6	32.8		0.3	102.4
4785	0.307	27.85	34.703	219.9	33.3		0.4	107.6
5086	0.240	27.852	34.701	220.7	33.5		0.4	110.1
5389	0.148	27.851	34.694	221.4	33.7		0.4	112.3
5528	0.119	27.851	34.691	221.4	34.1		0.4	111.4

Table 4.26: chemical and physical parameters for profile **I 101** (40°32'S-40°39'E, -3262 m).

DEPTH	T POT	SIG TA	SAL	O2	NO3	NO2	NH4	Si	Chl a
12	18.670	25.413	35.400	235.8	0.0	0.1	0.9	1.8	-------
28	18.670	25.416	35.403	235.8	0.0	0.1	0.5	1.6	0.26
53	16.993	25.782	35.343	242.4	0.0	0.1	0.5	1.7	0.24
77	14.767	26.268	35.315	227.9	4.6	0.1	0.5	3.8	0.23
101	14.260	26.337	35.262	230.5	5.7	0.2	0.5	4.0	0.21
126	13.682	26.403	35.190	228.0	7.1	0.2	0.6	4.5	0.28
142	13.134	26.466	35.127	227.2	8.2	0.2	0.6	4.7	0.41
199	12.441	26.520	35.018	230.4	9.7	0.1	0.7	4.9	0.28
250	11.338	26.605	34.857	231.5	11.7	0.1	0.8	5.2	--------
299	10.681	26.676	34.796	229.3	12.3	0.1	0.7	5.9	0.08
394	9.971	26.782	34.773	217.2	12.6	0.1	0.3	6.4	0.01
491	8.864	26.891	34.679	209.1	12.8	0.2	0.4	11.2	
640	6.790	27.069	34.516	201.3	27.1		0.2	23.4	
792	5.063	27.183	34.385	211.1	30.5		0.3	28.7	

893	4.291	27.256	34.369	207.4	32.3	0.2	34.6
997	3.857	27.323	34.397	196.9	33.7	0.3	42.4
1198	3.362	27.460	34.507	174.7	35.3	0.3	56.6
1396	2.962	27.566	34.594	170.3	35.3	0.2	64.1
1597	2.741	27.642	34.664	176.4	34.1	0.2	66.4
1797	2.582	27.706	34.726	188.0	32.3	0.2	63.8
2201	2.351	27.783	34.798	207.5	29.6	0.2	59.8
2592	2.126	27.817	34.818	216.3	28.7	0.3	60.6
2897	1.898	27.831	34.813	218.6	28.9	0.2	65.4
3221	1.560	27.838	34.789	216.4	30.2	0.2	76.0

Table 4.27: chemical and physical parameters for profile **I 102** (44°41'S-48°33', -2978 m).

DEPTH	T POT	SIG TA	SAL	O2	NO3	NO2	NH4	Si	Chl a
13	8.151	26.279	33.759	298.1	20.4	0.1	0.9	6.6	-------
28	8.156	26.281	33.762	297.4	20.4	0.1	0.5	6.4	0.26
55	7.675	26.360	33.773	298.8	20.8	0.1	-----	6.4	0.24
75	4.821	26.781	33.843	312.6	22.6	0.1	0.5	8.3	0.23
102	3.797	26.924	33.888	314.5	23.9	0.2	0.5	11.7	0.21
127	3.332	26.987	33.911	310.7	25.5	0.2	0.6	15.6	0.28
151	3.073	27.037	33.944	305.2	27.3	0.2	0.6	17.7	0.41
198	3.104	27.126	34.058	284.3	29.0	0.1	0.7	20.9	0.28
249	3.445	27.184	34.171	257.6	30.5	0.1	0.8	24.1	--------
299	3.201	27.208	34.172	256.2	31.1	0.1	0.7	25.9	0.08
394	2.712	27.277	34.204	242.2	32.9	0.1	0.3	34.0	0.01
494	2.557	27.333	34.258	226.2	34.2	0.2	0.4	41.2	
645	2.468	27.430	34.369	199.2	35.7		0.2	50.5	
796	2.319	27.519	----------	183.9	36.6		0.3	56.2	
997	2.356	27.624	34.600	178.0	35.3		0.2	65.2	
1192	2.297	27.686	----------	181.1	32.8		0.3	67.8	
1394	2.235	27.734	34.725	189.7	32.4		0.3	68.2	
1594	2.088	27.771	34.756	195.8	31.7		0.2	69.6	
1792	1.915	27.799	34.774	203.2	31.0		0.2	71.2	
1995	1.766	27.814	34.779	207.5	30.5		0.2	72.9	
2288	1.402	27.826	34.760	207.6	31.3		0.2	82.4	
2585	1.138	27.833	34.746	211.1	32.0		0.3	89.1	
2793	0.998	27.836	34.738	208.8	32.5		0.2	93.2	
2914	0.823	27.839	34.728	208.5	33.2		0.2	101.0	

Table 4.28: chemical and physical parameters for profile **I 103** (47°47'S-58°04'E,-4200 m).

DEPTH	T POT	SIG TA	SAL	O2	NO3	Si
3492	0.347	27.848	34.704	213.6	33.5	123.0
3595	0.272	27.845	34.695	214.5	33.5	124.8
3685	0.204	27.849	34.695	216.1	33.6	127.3
3799	0.145	27.848	34.689	217.1	33.6	130.2
3897	0.078	27.848	34.685	218.6	33.8	132.2
4004	0.014	27.851	34.685	219.8	33.8	135.2

4.2 Composition of the total particulate material

This paragraph is the collection of the different results for particulate matter analyses and the interpolated values (from the tables in section 4.1) for dissolved chemical parameters and physical parameters at the corresponding depths : the salinity (SAL) in per mille, the potential temperature (T POT) in degrees Celcius, density as sigma theta (SIG TA), the disolved oxygen concentration (O2) in µmol/l, the nitrate concentration (NO3) in µmol/l, the apparant oxygen utilization (AOU) in µmol/l, the NO-value (NO = O2 + 11NO3) in µmol/l, the partciculate barium (Ba) in pmol/kg, particulate calcium (Ca) in nmol/kg, particulate strontium (Sr) in pmol/kg, particulate silicium (Si) in nmol/kg, particulate aluminium (Al) in pmol/kg and chlorophyll a concentration in µg/l. ---- indicates no data; * indicates values beow detection limit.

Table 4.29 : composition of particulate material for profile **I 76**

DEPTH	SAL	TPOT	SIG TA	O2	NO3	AOU	NO	Ba	Ca	Sr	Si	Al	Chla
-10	33.665	1.344	26.956	341.9	25.4	9.1	624	151	145	3397	1276	*	0.4
-40	33.67	1.225	26.963	342.8	25	8.2	620	408	242	3600	1099	2490	0.23
-70	34.691	-0.27	27.075	349.3	27.2	12.7	651	145	205	2512	1193	1190	0.3
-90	33.793	-1.23	27.154	349.6	28.3	19.4	664	66	33	423	381	*	0.22
-120	33.87	-1.4	27.244	343.2	29.2	26.8	667	48	29	346	49	*	0.15
-150	33.974	-0.71	27.289	314.8	30.5	50.2	653	112	31	519	10	*	0.1
-175	34.119	-0.08	27.35	288	31.7	73	640	201	29	737	191	*	0.06
-200	34.254	0.587	27.413	261.1	32.9	94.9	626	271	65	908	125	*	0.02
-250	34.39	1.57	27.512	207.1	33.5	141.9	579	408	42	721	173	*	
-300	34.454	1.788	27.564	187.2	33.3	159.8	577	407	44	692	97	*	
-400	34.561	1.926	27.707	176.9	33	170.1	543	541	23	498	274	40	
-500	34.618	1.988	27.662	174.6	31.8	171.4	528	341	22	400	152	*	
-600	34.654	2.003	27.701	176.9	31.7	169.1	529	395	30	424	229	2420	
-700	34.682	1.993	27.721	181.2	30.9	164.8	524	237	20	254	76	610	
-800	34.704	1.964	27.746	185.4	29.9	160.6	517	290	18	299	194	790	
-900	34.724	1.916	27.76	189.1	29.6	157.9	518	247	14	213	152	*	

-1000	34.735	1.858	27.772	192.6	29.1	154.4	516	219	36	438	125	540
-1150	34.742	1.743	27.788	196.5	28.5	151.5	513	175	29	292	45	510
-1300	34.748	1.603	27.801	201.9	28.7	147.1	520	169	16	149	31	*
-1500	34.737	1.425	27.812	202.6	28.6	147.4	520	305	32	352	139	*
-1700	34.745	1.223	27.82	204	29.1	147	527	133	13	146	45	220
-1900	34.732	1.012	27.825	205.6	28.8	147.4	525	139	65	602	38	2270
-2050	34.725	0.873	27.827	206.3	29.5	147.7	534	99	22	168	24	*
-2400	34.707	0.594	27.836	208.2	30.4	147.8	546	76	11	101	14	*
-2700	34.556	0.377	27.84	209.8	30.8	147.2	552	425	31	646	218	540
-3000	34.699	0.199	27.84	213.9	31.1	145.1	559	115	38	322	14	8470
-3300	34.685	0.035	27.847	217.4	30.9	142.6	560	160	18	159	45	110
-4000	34.681	-0.29	27.85	228.6	36	133.4	628	105	20	167	28	*
-4300	34.661	-0.47	27.857	234.5	36.8	128.5	643	160	17	138	194	*

Table 4.30 : composition of particulate material for profile **I 78**

DEPTH	T POT	SAL	SIG TA	O2	NO3	AOU	NO	Ba	Ca	Sr	Al	Chl a
-10	1.447	33.699	26.963	348.8	21.2	1.2	584	1471	333	5971	4660	1.17
-20	1.442	33.701	26.962	348.6	21.3	1.4	585	1250	408	4342	6140	0.94
-35	1.389	33.805	26.970	348.5	21.2	1.5	584	2240	391	6371	6820	0.97
-75	-1.542	33.039	27.381	307.4	30.9	63.6	650	149	22	4781	*	0.21
-100	-0.213	34.312	27.496	251.1	33.2	109.9	620	190	14	1594	*	0.10
-200	1.770	34.576	27.646	178.0	34.4	170.0	560	569	45	1615	220	0.03
-300	1.882	34.634	27.699	174.0	33.7	173.0	548	432	8	842	*	
-400	1.885	34.687	27.726	177.2	33.3	169.8	547	342	8	558	*	
-500	1.861	34.699	27.743	181.3	32.8	165.7	545	374	30	680	*	
-600	1.816	34.716	27.758	184.7	32.3	162.3	543	1067	42	690	330	
-700	1.735	34.728	27.773	191.9	32.0	156.1	547	278	20	817	1410	
-800	1.681	34.734	27.785	192.1	31.7	155.9	544	254	23	499	580	
-900	1.574	34.737	27.795	195.0	31.8	154.0	548	224	12	392	*	
-1100	1.398	34.739	27.809	199.5	31.5	150.5	549	201	50	572	650	
-1300	1.203	34.514	27.819	203.0	31.8	149.0	556	324	11	850	10170	
-1500	1.040	34.731	27.830	203.6	32.0	149.4	559	124	11	211	650	
-1750	0.806	34.719	27.835	205.3	32.4	148.7	565	130	12	308	*	
-2000	0.602	34.703	27.831	206.1	33.1	149.9	574	147	26	318	1260	

Table 4.31 : composition of particulate material for profile **I 79**

DEPTH	T POT	SAL	SIG TA	O2	NO3	AOU	NO	Ba	Ca	Sr	Si	Al	Chl a
-10	0.979	33.795	27.053	346.3	23.5	6.7	607	3646	369	3487	3390	3650	1.10
-40	0.479	33.868	27.161	339.5	25.1	17.5	618	8272	512	5371	2985	9780	1.19
-70	-1.679	34.204	27.556	297.3	30.8	74.7	639	189	127	1223	447	1770	0.35
-90	-1.597	34.287	27.594	295.0	30.4	76.0	632	119	38	493	263	--------	0.18

-120	-1.559	34.323	27.640	296.4	30.9	74.6	639	189	17	485	256	1370	0.08
-150	-1.414	34.356	27.650	295.8	30.8	74.2	638	130	12	314	66	1880	0.03
-175	-1.398	34.373	27.658	285.1	30.3	84.9	621	151	63	734	107	3930	0.02
-200	-1.234	34.394	27.670	274.4	30.2	94.6	610	193	28	509	118	4760	
-250	-0.297	34.476	27.711	253.4	31.1	108.6	599	176	19	304	135	2270	
-300	1.210	34.544	27.742	198.5	32.2	153.5	556	315	21	343	385	--------	
-400	1.285	34.690	27.767	199.1	31.8	151.9	552	300	8	335	253	*	
-500	1.266	34.708	27.786	200.5	31.5	150.5	550	261	31	502	194	3250	
-600	1.166	34.724	27.800	202.8	31.3	149.2	550	308	35	456	146	900	
-700	1.116	34.728	27.810	203.4	31.3	148.6	551	200	9	204	114	180	
-800	1.031	34.717	27.816	204.7	31.3	148.3	552	187	9	198	104	*	
-900	0.908	34.730	27.818	206.7	31.4	147.3	555	201	10	221	118	*	
-1000	0.846	34.714	27.822	206.5	31.3	147.5	554	181	9	177	62	3710	
-1100	0.775	34.707	27.826	206.7	31.3	148.3	554	179	9	158	142	*	
-1200	0.696	34.704	27.829	207.2	31.4	147.8	556	227	14	288	101	*	
-1300	0.624	34.701	27.831	207.4	31.8	148.6	560	157	16	200	55	870	
-1400	0.545	34.686	27.834	207.9	32.0	148.1	563	180	28	309	73	650	
-1500	0.462	34.697	27.836	208.6	32.1	148.4	565	132	10	188	59	*	
-1600	0.387	34.694	27.836	209.6	32.2	147.4	567	150	20	99	55	*	
-1700	0.324	34.699	27.837	210.7	32.2	147.3	568	163	33	359	59	830	
-1800	0.267	34.687	27.839	211.9	32.3	146.1	570	217	7	146	31	400+	
-2000	0.156	34.683	27.842	214.3	31.7	144.7	566	113	16	225	35	250	
-2400	-0.015	34.676	27.845	218.5	32.4	141.5	578	121	10	157	21	2560	
-2750	-0.155	34.673	27.851	222.3	31.5	138.7	572	118	22	228	24	1980	
-3200	-0.325	34.677	27.858	231.5	31.9	130.5	586	103	10	126	42	2740	
-3500	-0.413	34.677	27.861	236.4	31.5	126.6	586	181	10	132	173	4540	

Table 4.32 : composition of particulate material for profile **I 81**

DEPTH	T POT	SAL	SIG TA	O2	NO3	AOU	NO	Ba	Ca	Sr	Si	Al	Chl a
-10	0.295	34.143	27.382	340.3	27.0	17.7	634	114	200	1714	1133	-------	0.21
-25	0.266	34.146	27.386	340.3	27.2	17.7	642	49	105	905	593	1190	0.29
-50	-1.442	34.320	27.618	313.3	29.7	56.7	643	91	133	1178	551	1520	0.32
-75	-1.633	34.413	27.701	292.5	31.3	78.5	634	108	79	672	135	1410	0.19
-100	-1.646	34.428	27.715	290.2	31.4	81.8	639	110	72	662	38	-------	0.12
-200	-0.983	34.503	27.745	271.6	32.0	95.4	627	109	67	661	21	470	0.12
-300	0.227	34.620	27.787	231.7	31.9	126.3	586	248	60	747	101	1620	0.03
-400	0.763	34.670	27.802	214.5	32.0	140.5	570	283	75	741	111	2780	
-500	0.715	34.678	27.822	214.5	32.2	140.5	572	280	81	782	91	1840	
-600	0.758	34.688	27.819	211.0	32.3	144.0	570	225	15	225	80	580	
-700	0.660	34.688	27.819	212.5	32.3	142.5	571	236	37	393	83	1080	
-800	0.669	34.699	27.826	210.3	32.7	144.7	573	214	60	565	42	1950	
-900	0.619	34.697	27.822	209.0	32.6	147.0	571	178	12	141	28	*	

-1000	0.550	34.697	27.827	209.0	32.9	147.0	574	181	10	123	42	*
-1100	0.483	34.698	27.831	209.3	33.2	147.7	578	215	15	220	73	110
-1300	0.363	34.690	27.841	210.0	33.4	147.0	581	145	14	171	45	1190
-1500	0.221	34.688	27.845	212.7	33.4	145.3	582	176	13	168	24	360
-1750	0.091	34.687	27.844	215.8	33.2	143.2	584	171	5	103	31	690
-2000	-0.018	34.687	27.847	219.1	33.4	140.9	590	135	24	252	45	580

Table 4.33 : composition of particulate material for profile **I 84**

DEPTH	T POT	SAL	SIG TA	O2	NO3	AOU	NO	Ba	Ca	Sr	Al	Chl a
-10	0.869	33.908	27.176	340.4	26.3	13.5	632	47	80	536	*	0.09
-25	0.726	33.907	27.184	339.6	28.0	15.3	650	47	73	325	2890	0.08
-35	0.716	33.911	27.188	341.3	28.3	13.7	655	89	15	36	*	0.09
-50	0.318	33.942	27.235	339.2	28.7	18.6	658	56	60	380	*	0.13
-75	-0.691	34.119	27.426	316.7	29.9	48.1	649	44	77	547	70	0.18
-100	0.484	34.477	27.657	224.4	33.4	132.2	595	96	105	813	1220	0.34
-200	1.561	34.658	27.732	185.2	33.6	163.9	558	337	63	802	920	0.02
-300	1.511	34.682	27.755	186.7	32.6	162.7	549	141	2	18	*	
-400	1.504	34.702	27.772	189.2	32.5	160.3	550	103	21	125	*	
-500	1.468	34.713	27.784	192.0	32.0	157.7	547	65	2	*	*	
-600	1.373	----------	27.801	195.1	31.9	155.3	549	212	9	73	70	
-700	1.270	34.722	27.805	197.9	31.2	153.2	544	224	6	88	*	
-800	1.041	34.709	27.810	203.9	31.6	148.8	555	127	20	114	*	
-900	0.991	34.711	27.815	206.0	31.5	147.1	556	278	14	125	400	
-1000	0.893	34.708	27.818	206.5	31.3	147.2	554	186	6	7	480	
-1100	0.788	34.703	27.821	207.8	31.4	146.7	556	87	23	103	*	
-1300	0.650	34.700	27.827	208.9	32.0	146.6	564	96	21	103	*	
-1500	0.516	34.695	27.831	208.7	32.2	147.7	566	80	6	*	3400	
-1750	0.317	34.684	27.834	211.7	32.5	146.1	572	84	6	*	*	
-2000	0.128	34.668	27.832	218.2	32.9	140.9	583	106	14	47	180	

Table 4.34: composition of particulate material for profile **I 85**

DEPTH	T POT	SAL	SIG TA	O2	AOU	Ba	Ca	Sr	Al	Chl a
-10	0.966	33.750	27.043	338.9	14.3	*	24	62	60	0.08
-40	0.935	33.755	27.049	339.3	14.2	200	105	759	1010	0.12
-70	-0.948	33.888	27.242	346.8	19.8	85	196	1365	2000	0.18
-90	-1.558	33.966	27.332	341.7	29.2	80	77	703	280	0.17
-120	-0.833	34.138	27.447	297.6	68.2	153	55	595	50	0.15
-150	0.653	34.359	27.553	232.7	122.7	280	30	336	*	0.00
-175	1.099	34.452	27.598	210.4	141.9	------	----	------	---	
-200	1.533	34.541	27.641	189.0	160.3	146	9	36	3560	
-250	1.654	34.596	27.676	185.4	163.0	372	58	495	*	

-300	1.701	34.625	27.696	179.3	168.8	------	----	------	---
-400	1.739	34.674	27.732	181.4	166.4	148	12	510	*
-500	1.649	34.695	27.756	185.6	162.9	219	56	368	650
-600	1.576	34.718	27.780	190.1	158.9	217	15	225	*
-700	1.529	34.726	27.789	193.5	155.8	174	8	144	*
-800	1.419	34.728	27.799	196.5	153.6	108	18	66	*
-900	1.348	34.733	27.808	199.2	151.4	141	11	140	*
-1000	1.216	34.730	27.815	201.1	150.4	171	8	140	*
-1150	1.074	34.726	27.821	203.2	149.3	124	9	*	*
-1300	0.919	34.723	27.829	205.6	148.0	108	6	107	*
-1500	0.714	24.710	27.832	206.2	148.8	58	5	70	*
-1700	0.556	34.702	27.835	208.8	147.3	35	26	99	670
-1900	0.401	34.694	27.837	209.2	148.0	93	63	574	*
-2150	0.240	34.686	27.840	210.4	147.9	13	21	62	*
-2400	0.104	34.681	27.843	213.9	145.4	68	5	92	*
-2700	0.136	34.675	27.845	218.6	140.4	91	9	118	*
-3000	-0.159	34.672	27.849	221.8	139.3	63	13	10	*
-3300	-0.266	34.665	27.849	227.5	134.4	25	24	77	280
-3700	-0.405	34.666	27.856	233.1	129.7	87	14	33	*
-4100	-0.212	34.660	27.856	236.7	124.8	63	60	492	370
-4500	-0.277	34.658	27.859	241.3	120.6	58	44	358	140

Table 4.34 : composition of particulate material for profile **I 86**

DEPTH	T POT	SAL	SIG TA	O2	NO3	AOU	NO	Ba	Ca	Sr	Si	Chl a
-10	0.821	33.858	27.136	339.1	26.9	14.9	638	32	82	706	1134	0.23
-25	0.810	33.854	27.137	338.8	25.0	15.2	616	113	242	2171	1439	0.24
-35	0.740	33.864	27.147	338.1	25.0	16.9	616	195	327	2750	1387	0.23
-50	0.644	33.873	27.343	331.8	26.3	23.2	624	164	182	1570	1470	0.25
-75	1.607	34.195	27.510	318.3	29.1	30.7	641	31	95	871	652	0.41
-100	0.123	34.335	27.597	253.3	31.1	105.7	599	155	27	447	776	0.28
-200	1.441	34.645	27.727	186.2	30.4	163.8	524	543	10	481	187	0.01
-300	1.421	34.684	27.764	189.4	31.5	160.6	539	207	75	677	177	
-400	1.401	34.705	27.785	193.3	30.7	156.7	534	361	22	287	87	
-500	1.300	34.714	27.798	195.8	30.1	155.2	530	341	18	259	402	
-600	1.195	34.721	27.799	198.0	30.4	154.0	535	216	65	635	350	
-700	1.076	34.723	27.811	200.5	30.3	151.5	537	186	65	644	364	
-800	0.959	34.719	27.819	202.6	30.0	150.4	536	171	58	570	------	
-900	0.846	34.713	27.822	204.3	29.3	149.7	530	292	94	735	4	
-1000	0.752	34.710	27.825	205.2	29.7	149.8	535	537	10	252	94	
-1100	0.658	34.705	27.829	206.2	30.1	148.8	540	246	85	790	35	
-1300	0.480	34.696	27.833	208.4	31.2	148.6	555	120	62	541	42	
-1500	0.344	34.693	27.836	208.8	29.6	149.2	537	100	57	510	49	
-1750	0.225	34.686	27.839	210.4	31.6	147.6	561	144	49	430	326	

-2000	0.106	34.683	27.844	215.1	31.8	143.9	568	130	69	607	------

Table 4.35 : composition of particulate material for profile **I 87**

DEPTH	T POT	SAL	SIG TA	O2	NO3	AOU	NO	Ba	Ca	Sr	Al	Chl a
-10	1.057	33.857	27.123	339.9	26.0	13.1	629	58	15	176	750	0.12
-30	0.761	33.946	27.190	339.1	27.0	15.9	639	119	67	727	3150	0.03
-50	-1.524	34.239	27.535	327.6	28.9	43.4	648	61	91	994	1720	0.51
-75	-1.396	34.314	27.610	306.8	30.3	63.2	643	62	74	802	510	0.73
-100	-0.675	34.411	27.662	265.0	31.9	100.0	619	83	14	360	2610	0.20
-200	1.376	34.659	27.747	189.8	33.0	160.2	556	367	14	378	-*	0.01
-300	1.269	34.683	27.773	195.5	32.0	155.5	551	212	6	148	250	
-400	1.180	34.696	27.790	199.2	31.6	152.8	550	156	14	196	9260	
-500	1.149	34.701	27.798	201.3	31.4	150.7	550	260	14	229	1840	
-600	1.066	34.713	27.813	201.1	31.8	151.9	554	115	21	261	*	
-700	0.908	34.714	27.822	202.9	31.9	150.1	557	191	16	234	2850	
-800	0.792	34.709	27.826	204.4	32.0	150.6	560	157	12	173	*	
-900	0.722	34.701	27.826	205.6	31.9	149.4	560	116	29	342	*	
-1000	0.585	34.698	27.829	206.7	32.0	149.3	562	147	18	232	370	
-1100	0.560	34.695	27.832	207.7	32.1	148.3	564	128	9	131	8440	
-1300	0.347	34.688	27.836	208.7	32.6	149.3	571	146	11	153	1580	
-1500	0.224	34.679	27.835	213.0	32.5	145.0	574	96	7	114	720	
-1750	0.095	34.677	27.841	214.8	32.6	144.2	577	146	48	522	1660	
-2000	-0.026	34.673	27.834	219.5	32.4	140.5	579	118	32	365	1020	

Table 4.36 : composition of particulate material for profile **I 89**

DEPTH	T POT	SAL	SIG TA	O2	NO3	AOU	NO	Ba	Ca	Sr	Si	Al	Chl a
-10	2.847	33.939	27.055	326.3	25.2	13.7	606	50	143	1156	1238	1050	0.16
-30	1.908	33.948	27.142	332.6	25.4	14.4	615	93	186	2186	1823	1700	0.25
-50	1.867	33.965	27.156	334.5	27.5	12.5	640	53	133	2255	1633	870	0.32
-75	1.411	33.983	27.205	332.1	28.2	17.9	645	135	190	2463	1608	1910	0.15
-100	-0.015	34.026	27.328	331.8	30.4	28.2	669	189	157	1955	260	760	0.06
-200	1.136	34.298	27.483	240.7	35.5	111.3	635	355	28	887	194	*	0.01
-300	1.882	34.506	27.617	180.1	36.8	166.9	589	398	48	811	301	*	
-400	1.763	34.608	27.681	180.3	36.2	167.7	582	415	34	699	274	7030	
-500	1.718	34.672	27.720	181.4	36.0	166.6	581	291	34	558	198	400	
-600	1.689	34.694	27.748	185.4	35.3	162.6	577	286	25	496	281	360	
-700	1.635	34.720	27.766	189.4	34.8	159.6	576	295	113	878	260	------	
-800	1.541	34.746	27.782	192.9	34.3	156.1	574	259	77	841	184	1840	
-900	1.399	34.730	27.796	196.0	33.8	154.0	571	194	72	714	87	330	
-1000	1.299	34.731	27.803	198.1	33.9	152.9	574	251	74	735	121	290	

-1100	1.196	34.737	27.811	200.2	34.1	151.8	579	224	80	754	128	470
-1300	0.975	34.726	27.823	203.5	34.3	149.5	584	244	80	714	135	1300
-1500	0.729	34.722	27.827	206.2	34.6	148.8	590	177	65	586	73	650
-1750	0.497	34.700	27.832	208.3	34.8	148.7	595	142	63	554	59	760
-2000	0.324	34.701	27.838	210.4	35.3	147.6	602	157	72	665	87	1150

Table 4.37 : composition of particulate material for profile **I 90**

DETH	T POT	SAL	SIG TA	O2	NO3	AOU	NO	Ba	Ca	Sr	Al	Chl a
-10	3.854	33.947	26.961	323.0	24.8	10.0	598	94	140	1455	780	0.27
-30	3.645	33.953	26.985	325.6	24.9	8.4	602	385	153	2224	1170	0.12
-50	2.046	33.989	27.135	329.6	26.6	16.4	625	220	157	2004	1750	0.38
-75	1.422	34.032	27.234	325.4	27.7	24.6	633	140	69	1163	220	0.09
-100	1.219	34.045	27.264	321.0	28.3	30.0	635	200	30	1106	*	0.06
-200	1.061	34.237	27.429	257.0	32.7	96.0	620	575	64	1217	1880	0.01
-300	1.882	34.487	27.571	179.4	34.5	167.6	562	412	19	562	*	
-400	1.683	34.533	27.623	181.6	34.9	166.4	569	291	33	575	*	
-500	1.898	34.617	27.674	173.4	34.4	173.6	555	184	16	262	1300	
-600	1.764	34.640	27.703	176.4	34.2	171.6	556	200	24	324	--------	
-700	1.784	34.673	27.725	178.2	33.7	169.8	552	223	11	195	630	
-800	1.789	34.701	27.747	182.5	32.6	177.5	544	201	5	160	*	
-900	1.773	34.722	27.768	188.3	32.0	159.7	544	122	5	119	6560	
-1000	1.700	34.731	27.779	191.5	31.7	156.5	543	202	7	179	240	
-1100	1.626	34.738	27.792	194.4	31.5	154.6	544	166	10	186	690	
-1300	1.431	34.738	27.806	198.2	31.6	151.8	549	131	8	159	1660	
-1500	1.217	----------	27.823	---------	-------	---------	------	134	4	83	*	
-1750	0.876	34.718	27.824	204.8	-------	149.2	------	137	10	133	*	
-2000	0.577	34.708	27.832	207.8	32.4	148.2	567	127	21	247	*	

Table 4.38 : composition of particulate material for profile **I 94**

DEPTH	T POT	SAL	SIG TA	O2	NO3	AOU	NO	Ba	Ca	Sr	Al	Chl a
-10	3.665	33.943	26.978	325.5	24.8	8.5	601	454	117	1454	*	0.08
-30	2.837	34.012	27.102	328.8	25.7	11.2	614	112	187	1890	1100	0.31
-50	2.473	34.052	27.170	330.8	26.2	12.2	622	158	246	2821	4660	0.34
-75	2.248	34.082	27.218	330.4	26.5	13.6	625	63	124	1226	850	0.46
-100	1.782		27.248	331.2	26.5	16.8	625	51	79	905	260	0.10
-200	0.726	34.151	27.380	307.0	29.7	48.0	637	200	41	708	900	0.01
-300	0.783	34.333	27.524	240.9	33.8	114.1	616	278	19	387	2340	
-400	1.689	34.524	27.615	181.1	35.5	166.9	575	103	3	109	*	
-500	1.839	34.595	27.661	173.8	35.1	173.2	563	261	39	633	*	
-600	1.818	34.634	27.674	174.7	34.6	172.3	559	198	26	443	890	
-700	1.830	34.663	27.718	178.1	33.9	168.9	554	153	39	477	*	

-800	1.939	34.713	27.742	182.8	32.6	163.2	545	179	42	529	950
-900	1.935	34.733	27.764	188.8	31.9	157.2	543	190	45	606	4090
-1000	1.919	34.751	27.780	194.0	31.2	153.0	540	94	95	986	650
-1100	1.902	34.768	27.795	199.2	30.5	147.8	538	------	----	------	------
-1300	1.572	34.755	27.810	200.3	31.1	148.7	546	163	43	515	650
-1500	1.379	34.751	27.820	201.7	31.3	148.3	549	49	2	47	1400
-1750	1.099	34.744	27.832	205.8	31.6	146.2	557	----	---	----	--------
-2000	0.924	34.735	27.839	208.0	31.9	146.0	562	80	45	460	*

Table 4.39 : composition of particulate material at station **I 95**

DEPTH	T POT	SAL	SIG TA	O2	NO3	AOU	NO	Ba	Ca	Sr	Al
-10	6.868	33.873	26.551	297.5	20.7	15.0	527	89	120	1289	690
-30	6.769	33.879	26.569	298.0	20.6	15.0	527	105	158	1820	910
-50	6.526	33.884	26.608	300.2	21.0	14.0	533	76	94	1278	840
-75	6.200	33.897	26.658	300.8	21.1	16.0	535	88	100	1198	770
-100	5.216	33.951	26.821	302.8	21.7	20.0	544	95	44	624	160
-200	4.346	34.095	27.032	285.7	25.3	44.3	567	176	30	486	*
-300	3.737	34.186	27.167	267.4	28.7	66.6	586	206	52	719	*
-400	3.220	34.183	27.215	260.3	30.3	76.7	597	209	38	511	-----
-500	2.847	34.205	27.266	246.7	31.9	93.3	601	279	64	809	-----
-600	2.632	34.264	27.332	226.2	33.3	115.8	596	249	59	650	870
-700	2.613	34.332	27.388	209.4	33.9	132.6	586	180	24	204	1600
-800	2.571	34.980	27.444	185.4	34.9	156.6	573	220	27	329	330
-900	2.503	34.460	27.500	185.4	35.2	156.6	576	153	17	222	930
-1000	2.466	34.516	27.547	182.0	34.8	161.0	568	139	13	152	440
-1100	2.429	34.571	27.595	178.5	34.3	164.5	559	111	20	239	*
-1300	2.417	34.659	27.666	180.5	33.3	162.5	550	167	18	167	880
-1500	2.358	34.712	27.713	186.5	32.1	156.5	543	148	17	133	690
-1750	2.213	34.765	27.768	197.1	30.5	147.9	534	123	14	143	330
-2000	1.898	34.786	27.802	204.2	29.9	142.8	536	69	14	120	*

Table 4.40 : composition of particulate material for profile **I 97**

DEPTH	T POT	SAL	SIG TA	O2	NO3	AOU	NO	Ba	Ca	Sr	Al
-10	19.871	35.588	25.247	221.1	0.0	0.0	221	127	63	523	1520
-40	19.868	35.588	25.248	221.0	0.0	0.0	221	66	138	901	3060
-80	18.457	35.650	25.659	223.6	0.2	7.4	226	82	102	623	3450
-100	18.359	35.651	25.679	223.9	0.2	7.1	226	69	112	722	1220
-150	17.718	35.605	25.807	206.1	0.1	29.9	207	229	59	592	1400
-175	16.814	35.551	25.984	197.8	5.5	44.2	259	49	10	106	*
-200	16.137	35.517	26.116	203.1	5.9	43.9	269	130	186	1534	3770
-250	15.318	35.448	26.249	207.4	6.3	45.6	277	81	28	168	1210

-250	15.318	35.448	26.249	207.4	6.3	45.6	277	81	28	168	1210
-300	14.390	35.354	26.346	207.8	7.0	51.2	285	49	68	654	•
-400	12.700	35.188	26.598	209.1	9.7	61.9	317	131	38	363	3540
-500	11.009	34.980	26.751	208.8	14.4	74.2	369	94	33	316	1420
-600	9.324	34.739	26.864	207.0	19.5	88.0	423	393	228	2226	3150
-700	7.250	34.525	26.991	217.2	24.7	91.8	491	144	30	264	10580
-800	5.430	34.338	27.102	226.2	29.3	95.8	551	168	26	201	2490
-900	4.865	34.397	27.215	205.3	28.2	120.7	518	125	20	193	2510
-1000	3.837	34.327	27.267	215.4	29.3	117.6	541	222	27	200	2610
-1150	4.030	34.523	27.406	168.8	30.5	163.2	507	109	28	257	2650
-1300	3.167	34.529	27.494	174.0	31.0	164.0	518	144	25	207	4110
-1500	2.737	34.599	27.590	176.4	30.8	164.6	518	193	61	545	1940
-1700	2.633	34.677	27.662	186.8	28.4	155.2	502	139	20	131	1760
-1900	2.536	34.750	27.729	196.5	26.1	145.5	486	180	44	487	1260
-2150	2.485	34.814	27.782	210.1	25.0	132.9	488	161	60	564	5010
-2400	2.371	34.834	27.810	216.6	24.6	126.4	490	511	39	334	3570
-2700	2.205	34.837	27.826	221.7	23.7	123.3	485	171	34	252	4350
-3000	2.069	34.839	27.839	224.1	23.5	121.9	485	137	21	147	4650
-3300	1.923	34.835	27.847	224.7	24.2	122.3	493	141	19	140	3310
-3700	1.420	34.821	27.851	220.6	25.3	129.4	501	87	52	470	3430
-4100	0.933	34.754	27.852	217.5	29.2	135.5	542	60	20	145	2150
-4500	0.654	34.728	27.850	216.3	32.4	138.7	576	423	34	186	9820

4.3 Incubation experiments

The summaries of the different incubation experiments (tables 4.41 to 4.45) show the initial and final pools of dissolved nitrogen (ammonium), Pd,i and Pd,f, both in µmol N/l, and the initial and final atom percent abundances of ammonium, Ad,i and Ad,f, as well as the initial and final pools of particulate nitrogen, Pp,i and Pp,f in µmol N/l, and the initial and final atom percent abundances of particulate nitrogen, Ap,i and Ap,f. A distinction is made between dark (D) and light (L) bottles for three different depths : euphotic zone (EZ), oxgen minimum (OM) and deep water (DW), i.e. below the oxygen minimum.

Table 4.41 : experimental data of the incubation experiment for profile I76

Incub	Pd,i	Pd,f	Pp,i	Pp,f	Ad,i	Ad,f	Ap,i	Ap,f
EZ/L	1.70	1.00	1.52	1.58	6.04	0.65	0.37	1.58
EZ/D	1.70	2.90	1.52	1.17	6.04	0.47	0.37	0.63
OM/L	1.50	1.00	1.99	0.90	6.79	0.82	0.37	0.37
OM/D	1.50	0.50	1.99	1.07	6.79	1.01	0.37	0.42
DW/L	1.60	0.01	3.77	1.34	6.39	0.49	0.37	0.37
DW/D	1.60	0.60	3.77	2.01	6.39	0.68	0.37	0.42

Table 4.42 : experimental data of the incubation experiment for profile I81

Incub	Pd,i	Pd,f	Pp,i	Pp,f	Ad,i	Ad,f	Ap,i	Ap,f
EZ/L	1.70	0.80	4.28	1.95	6.03	0.61	0.37	1.53
EZ/D	1.70	0.30	4.28	1.22	6.03	0.68	0.37	0.53
OM/L	1.50	0.50	1.93	0.41	6.79	0.52	0.37	0.38
OM/D	1.50	0.60	1.93	0.15	6.79	0.64	0.37	0.37
DW/L	1.50	0.50	2.40	0.63	6.79	0.54	0.37	0.37
DW/D	1.50	0.50	2.40	0.24	6.79	0.68	0.37	0.53

Table 4.43 : experimental data of the incubation experiment for profile I86

Incub	Pd,i	Pd,f	Pp,i	Pp,f	Ad,i	Ad,f	Ap,i	Ap,f
EZ/L	1.60	0.90	1.57	1.69	4.07	0.64	0.37	1.09
EZ/D	1.60	0.80	1.57	2.01	4.07	0.62	0.37	0.49
OM/L	1.20	0.10	0.92	0.15	4.75	0.60	0.37	0.43
OM/D	1.20	0.30	0.92	0.77	4.75	0.77	0.37	0.37
DW/L	2.20	0.01	0.88	0.57	3.38	0.88	0.37	0.37
DW/D	2.20	0.50	0.88	0.93	3.38	0.81	0.37	0.46

Table 4.44 : experimental data of the incubation experiment for profile I89

Incub	Pd,i	Pd,f	Pp,i	Pp,f	Ad,i	Ad,f	Pp,i	Pp,f
EZ/L	1.00	3.90	1.38	1.04	10.00	0.42	0.37	2.23
EZ/D	1.00	3.20	1.38	0.95	10.00	0.38	0.37	0.81
OM/L	1.10	4.50	0.77	0.32	9.12	1.30	0.37	0.62
OM/D	1.10	0.20	0.77	0.66	9.12	1.30	0.37	1.36
DW/L	1.70	0.01	1.30	1.52	6.03	0.41	0.37	2.31
DW/D	1.70	0.10	1.30	1.31	6.03	0.38	0.37	2.11

Table 4.45 : experimental data of the incubation experiment for profile I103

Incub	Pd,i	Pd,f	Pp,i	Pp,f	Ad,i	Ad,f	Ap,i	Ap,f
EZ/L	5.00	2.10	....	1.58	2.30	0.38	0.37	1.35
EZ/D	5.00	4.99	....	1.12	2.30	0.39	0.37	0.61
OM/L	1.10	1.00	....	0.60	9.12	0.61	0.37	0.48
OM/D	1.10	1.50	....	0.23	9.12	0.65	0.37	0.58
DW/L	7.10	0.10	....	0.46	1.73	0.38	0.37	0.44
DW/D	7.10	0.10	....	0.84	1.73	0.39	0.37	0.60

CHAPTER 5 : DISCUSSION

5.1. Dissolved barium

5.1.1. Comparison with GEOSECS data

Two GEOSECS stations (G 93: 41°46'S - 18°27'E and G 429: 47°40'S - 57°51'E) with Ba profiles published (Chan et al., 1977; Ostlund et al., 1987) are located in the same general area investigated during INDIGO 3. In figure 5.1 we plot the dissolved Ba concentrations versus salinity for the mid- and deep water region (salinities between 34.65 and 34.85 per mil).

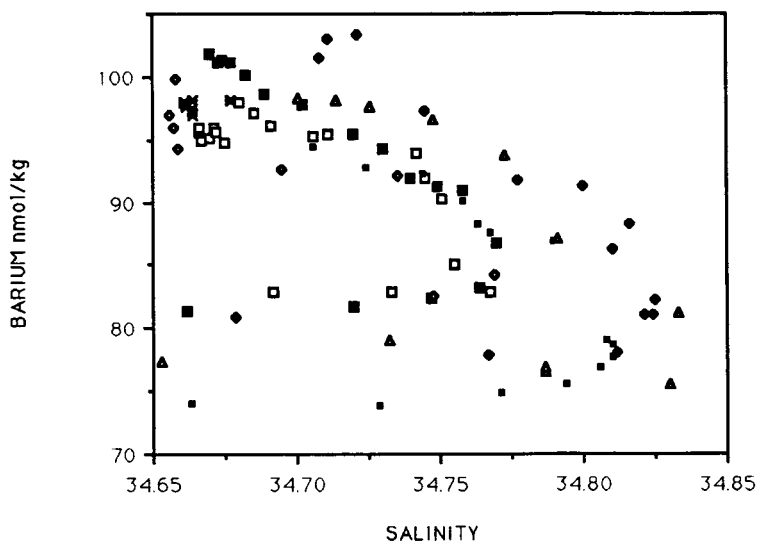

Fig 5.1 : Ba-sal. plot for GEOSECS stations G429 (■); G93 (◆) and I3 stations 92 (×); 93 (◇); 94 (□); 96 (▪); 98 (Δ).

The plots for both GEOSECS stations are compared with plots for INDIGO 3 (I 3 hereafter) stations 92; 93; 94; 96; 98 the closest by stations for which Ba data were obtained. It can be seen that I 3 stations 93, 94 closely fit the G 429 plot, with exception of the deep and bottom waters where lower barium values are observed for I 3. Stations 96 and especially 98 closely fit the G 93 plot in the salinity maximum layer, but again show less barium with decreasing salinities in deep and bottom waters. The Ba - salinity plot for I 3 stations 96 and 98 clearly show barium in deep and bottom waters to join the G 429 values.
When comparing Si - salinity plots (Figure 5.2) the same features are apparant : I 3 stations 92, 93, 94 show less silicium in deep and bottom waters relative to station G 429. Plots for I

3 stations 96 and 98 fit the G 93 one, and in deep and bottom waters plots for all these three stations join the G 429 plot, what is not the case for the Ba- salinity plot of station G 93 (Fig. 5.1).

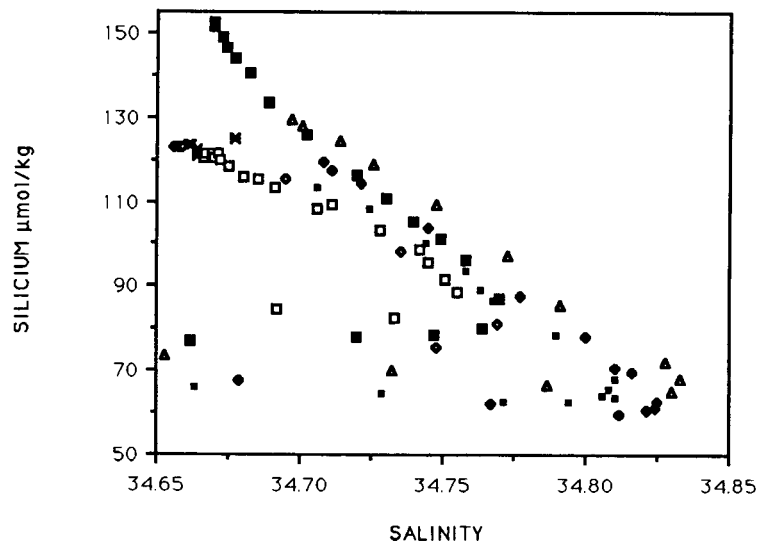

Fig 5.2 : Si-sal plots for GEOSECS stations G429 (■); G93 (◆) and I 3 stations 92 (✱); 93 (◇); 94 (□); 96 (▪); 98 (Δ).

In the latitudinal belt comprised between 50°90'S and 47°40'S (I 3 stations 92, 93, 94 and G 429) the above observations are consistent with the observed increase of barium in bottom waters from west (I 3 stations 92, 93, 94 : 27°E) to east (G 429 : 58°E) (Broecker and Peng, 1982). It can be concluded from the above that the dissolved barium data obtained here, by direct determination using ICP-OES, are consistent with those obtained by the IDMS technique, which has however a higher precision (see above section 3.1.2).

5.1.2. Surface water profile of dissolved barium.

In Table 5.1 we present the barium data for surface waters sampled between 61°57' S and 42°38' S when cruising from Antarctica to southern Africa. Concentrations decrease from 76 nmol.l^{-1} at 61°57' S to 40 nmol.l^{-1} at 42°38' S, north of the Subtropical Convergence (see also Figure 5.3.A). Maxima of dissolved barium can be clearly recognized in the vicinity of the Polar Front (sample at 50°38'S), the Subantarctic Front (sample at 47°34'S) and the Subtropical Convergence (sample at 43°47'S). The positions of these frontal systems was deduced from the surface water temperature (Fig. 5.3.B)3 and Chl-a content (Goffart and Hecq, 1987). South of the Polar Front, at 51°23'S and 53°43'S two more barium maxima can be clearly seen. No apparent correlation with physical or biological parameters is observed for these latter two maxima.

Table 5.1: Horizontal profile of dissolved Ba between Antarctica and southern Africa.

POSIT. °S	TEMP.	BA nmol/l
61.95	1.3	76.1
55.37	3.8	69.2
54.67	4.1	67.7
53.72	4.1	74.3
52.57	4.1	68.9
52.2	4.2	68.4
51.97	4.35	65.5
51.67	4.35	67.7
51.38	4.05	73.2
51	4.4	69.2
50.73	3.6	56.8
50.68	5.2	59
50.68	5.58	59.7
50.67	3.8	72.1
50.63	4.4	75.7
50.58	4	70.6
50.07	4.9	57.5
49.68	5.85	59
49.35	6.2	58.2
48.9	6.8	55.3
48.77	6.58	54.6
48.02	5.4	57.5
47.57	5.4	64.1
47.12	7.05	54.6
47.03	7.5	56.1
46.77	7.95	56.8
46.4	7.25	52.8
45.98		53.5
45.48	7.75	51.6
45.32		56.4
44.93		55.1
44.08		54.2
43.78		57.7
43.47		52.9
43.2		43.9
42.63	11.8	39.6

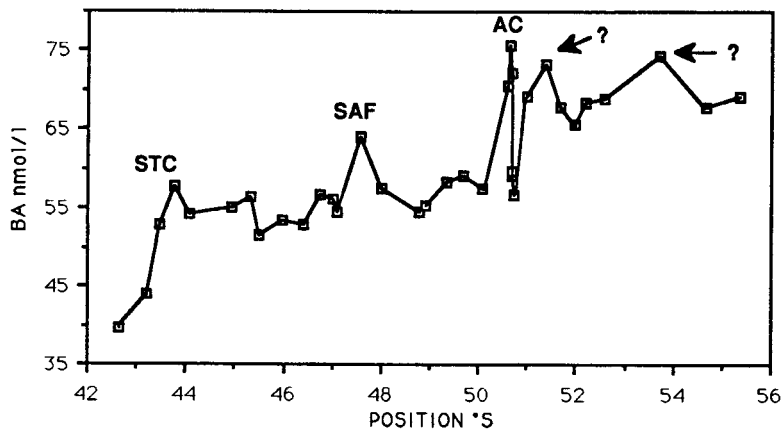

Fig 5.3.A : Barium in surface waters between 55°22'S and 42°38'S. STC = Sub-Tropical Convergence; SAF = Sub- Antarctic Front; AC = Antarctic Convergence.

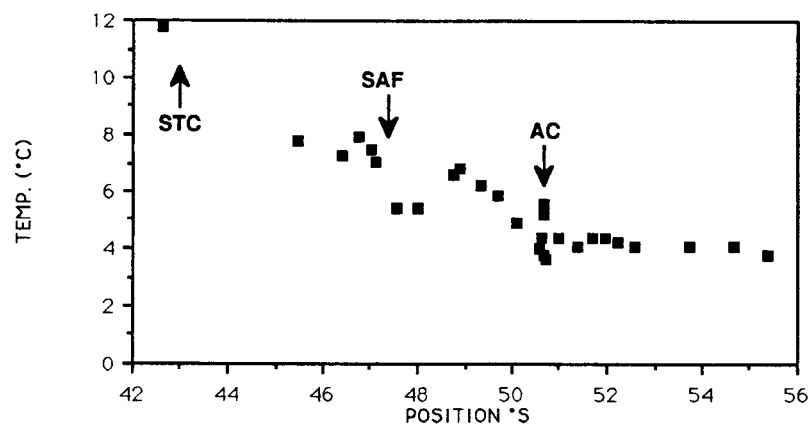

Fig. 5.3.B: Surface water temperature between 55°22'S and 43°38'S.

5.1.3. Vertical profiles of dissolved barium.

Interesting information is obtained from inspection of Ba-salinity and Tpot-salinity diagrams for the 34.65 to 34.75 per mil salinity region, encompassing the salinity maximum. Below we discuss the stations located south of the Polar Front.
Station 82, located on the continental shelf, at the head of Wild Canyon, shows a lower Ba content for the bottom samples extending below the salinity maximum (Figure 5.4). This decrease of barium goes with a decrease of silicate and has been interpreted as an indication of the presence of newly formed bottom water (Dehairs and Goeyens, 1988).

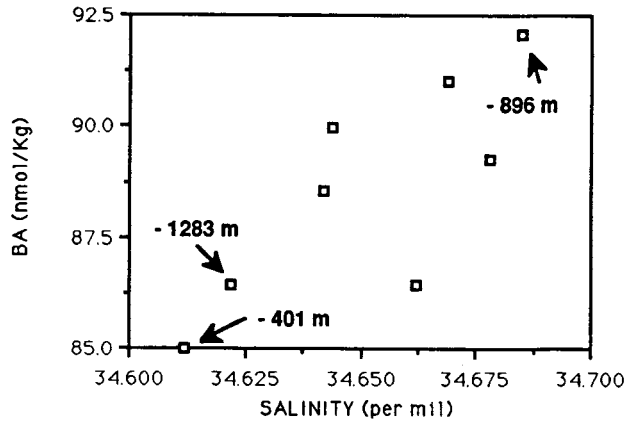

Fig 5.4A : Station 82; Ba-SAL plot.

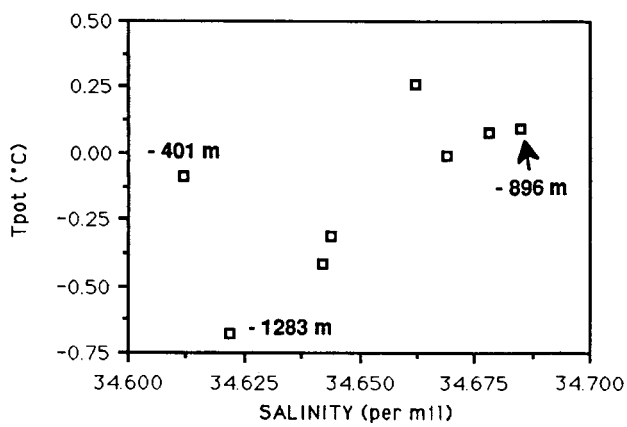

Fig 5.4B : Station 82; T pot- SAL plot.

Surface waters are always lower in barium and other nutrients than bottom waters and their transfer to the deep, during the bottom water formation process, thus introduces nutrient and Ba "poor" waters in the deep and bottom part of the watercolumn. The information concerning bottom water formation we deduce from our Ba data, generally fits to the one deduced from the freon-11 data (F. Mantisi, pers. Commun.).

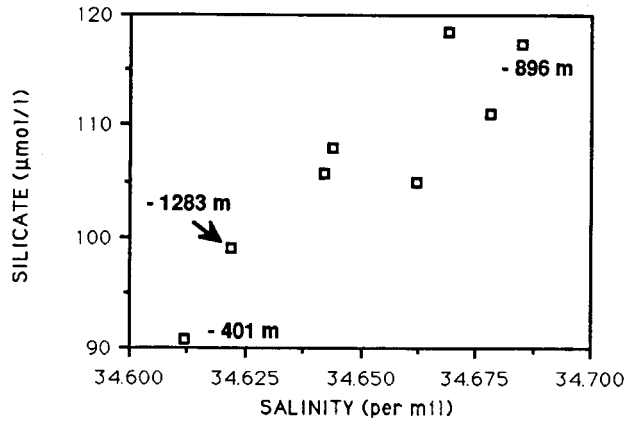

Fig. 5.4C: Station 82; Silicate - SAL plot.

Station 81, located more offshore, on the slope within Wild canyon, reveals that the deep layer with low Ba content (93 nmol/Kg) has been split by a watermass enriched in Ba (98 nmol/Kg). The Ba-Sal. plot shows two Ba minima, at 34.680 and 34.670 ‰, with the latter salinity value for the watermass just above the sea floor (Figure 5.5).

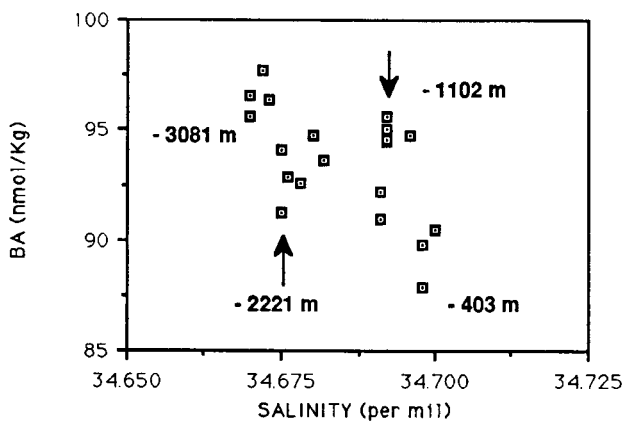

Fig 5.5A : Station 81; Ba-SAL plot.

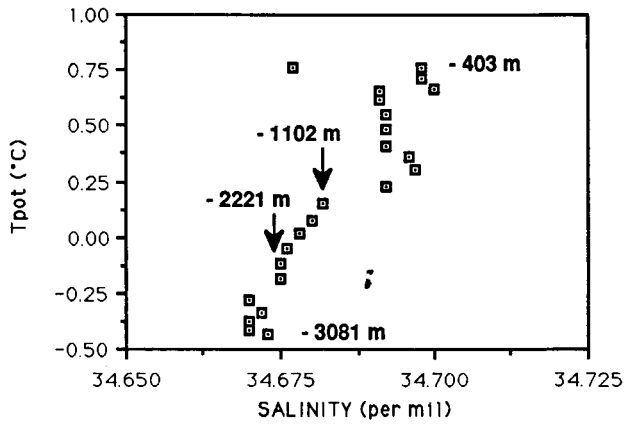

Fig 5.5B : Station 81; T pot-SAL plot.

These Ba minima coincide with inflexion points at corresponding salinity values on the Tpot-salinity diagram. The overall picture shows the Ba rich deep water, extending below the salinity maximum to have been split by the upper branch of a Ba poor water, we identify as newly formed bottom water. The bottom most branch of this newly formed bottom water underrides the Ba rich layer and spreads just over the sea floor . This branch appears to have been mostly eroded away by the Ba rich water above.

The upper branch of newly formed bottom water (or better newly formed deep water) can be identified on most Ba-salinity plots for the stations south of the Polar Front (see figures below).

Station 85 shows the same general features as station 81, but these are now strongly eroded away as indicated by the inflexion points at 34.685 ‰ and 34.660 ‰ in the Ba-salinity and Tpot-salinity diagrams (Figure 5.6).

Station 80 (Figure 5.7) clearly shows the upper branch of newly formed bottom water (inflexion point at 34.682 ‰). This layer splits the Ba rich watermass in two. At this station no lower branch of the Ba poor newly formed bottom or deep water can be seen.

This same picture can be recognized from the Ba-salinity and Tpot-salinity diagrams for stations 76, 78 and 86, although the newly formed Ba poor bottom water is strongly eroded away by Ba rich deep water (see resp. Figures 5.8; 5.9 and 5.10). At station 76 the inflexion point indicating the presence of newly formed deep water occurs at 34.688 per mil salinity. At station 78 this inflexion point occurs at 34.696 per mil and at station 86, at 34.688 per mil salinity. Station 89 (Figure 5.11) shows a slightly different picture with more or less constant Ba values between salinities of 34.724 (-1100 m) and 34.654 per mil (-4704 m), and increasing Ba values on from 4700 m. In this case no clear Ba minimum can be distinguished.

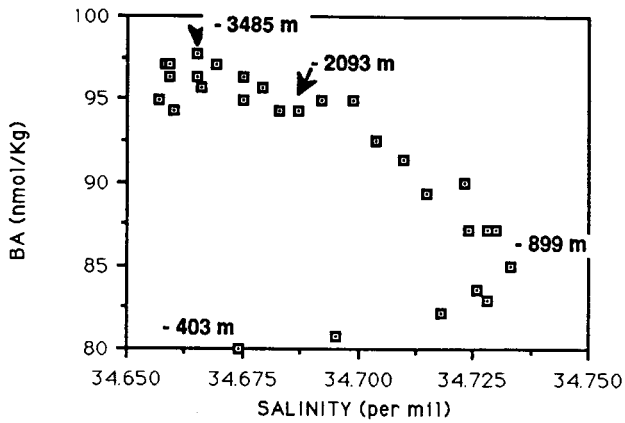

Fig. 5.6A : Station 85; Ba-SAL plot.

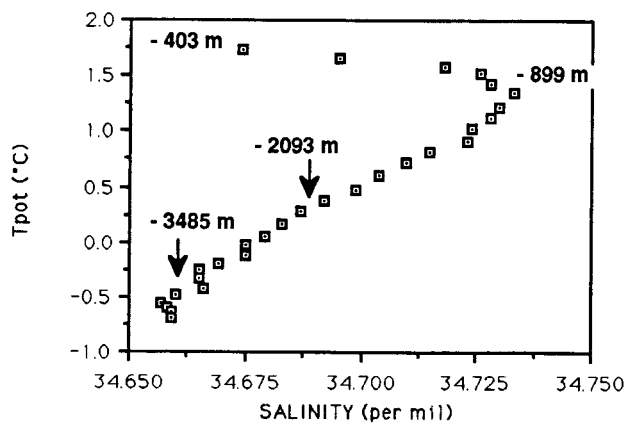

Fig 5.6B : Station 85; T pot-SAL plot.

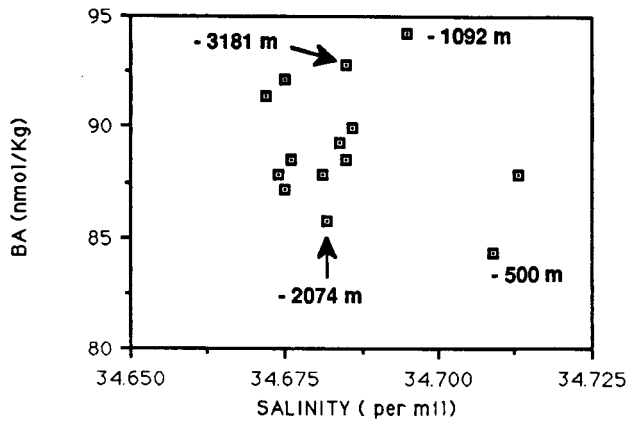

Fig 5.7A : Station 80; Ba-SAL plot.

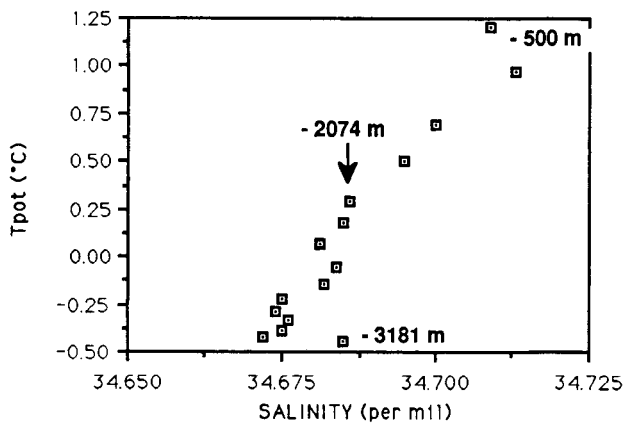

Fig 5.7B : Station 80; T pot-SAL plot.

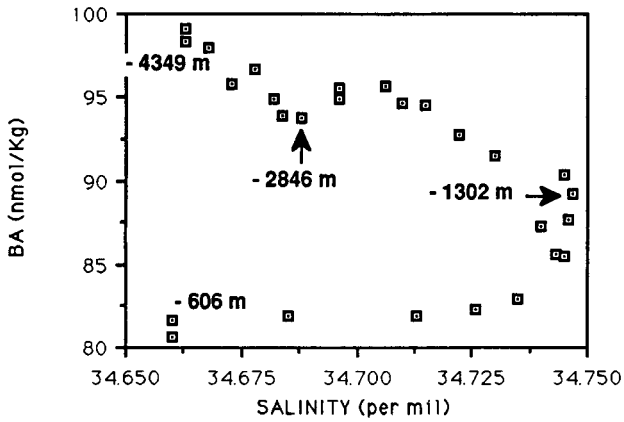

Fig. 5.8A: Station 76; Ba - SAL plot.

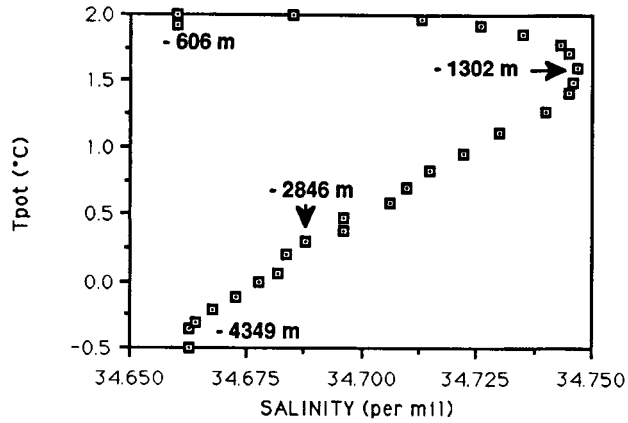

Fig. 5.8B: Station 76; Tpot - SAL plot.

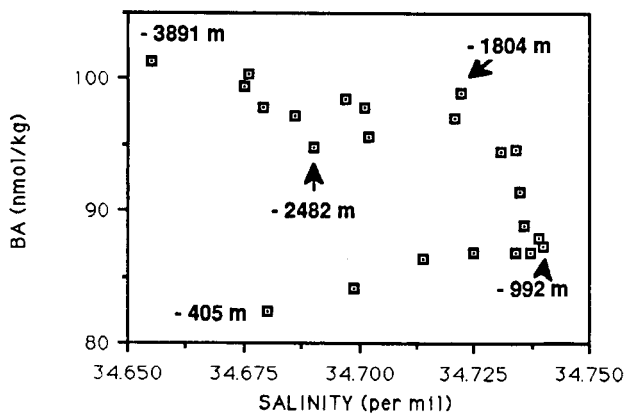

Fig 5.9A : Station 78; Ba-SAL plot.

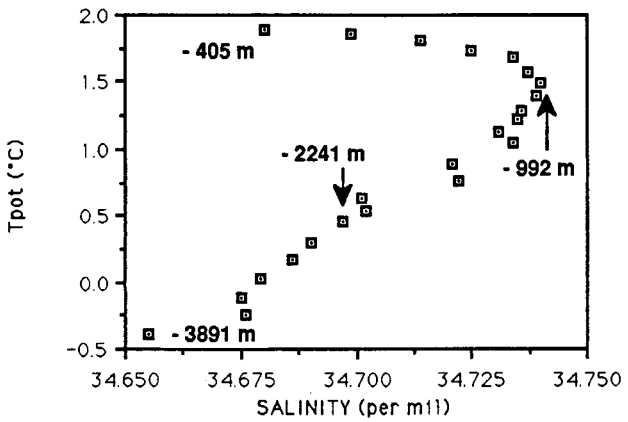

Fig 5.9B : Station 78; T pot-SAL plot.

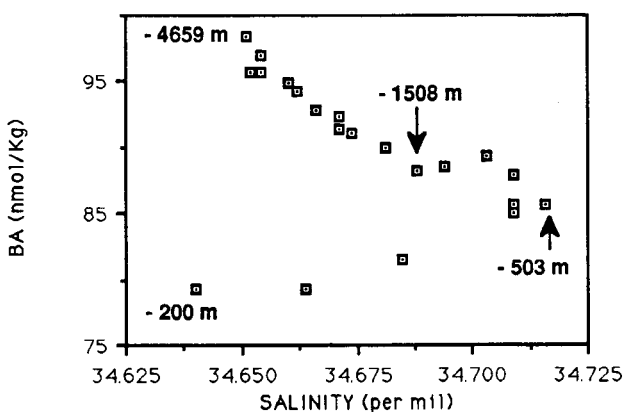

Fig. 5.10A : Station 86; Ba-SAL plot.

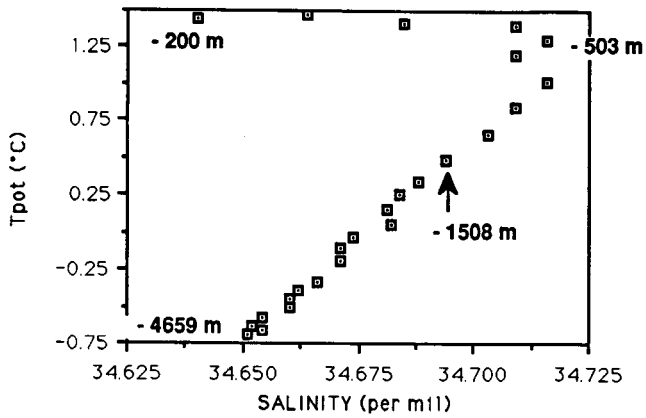

Fig. 5.10B : Station 86; T pot-SAL plot.

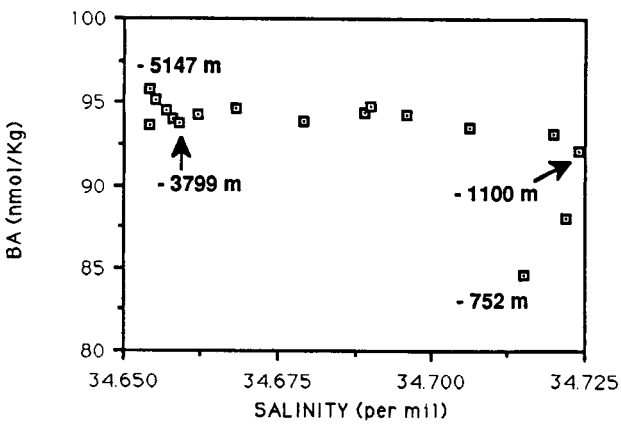

Fig. 5.11A : Station 89; Ba-SAL plot.

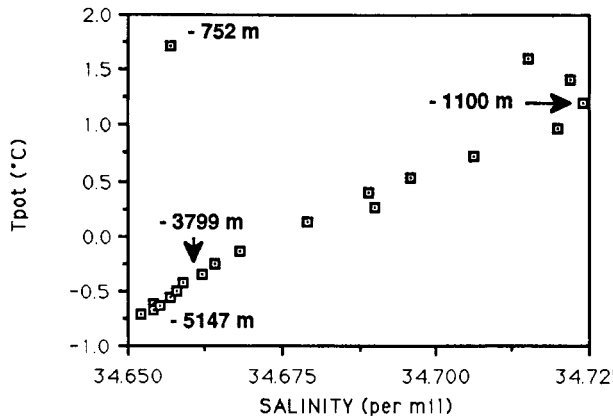

Fig. 5.11B : Station; T pot-SAL plot.

Stations 84 and 79 represent somewhat peculiar situations. Although located much more offshore than station 82 on the shelf, they show a similar pattern of the Ba-salinity and Tpot-salinity plots (Figures 5.12 and 5.13). Ba rich deep water, below the salinity maximum, is underriden by Ba poor water (newly formed bottom water ?) which appears as a very thick layer of 1400 m at station 79 and 1000 m at station 84, extending down to the sea floor in both cases. This stands in contrast to the situation at other offshore stations where newly formed bottom water spreads either separated in two branches, one just above the sea floor and one at intermediate depth (stations 80, 76,78, 86).

It thus appears as if both stations 84 and 79, between Antarctica and the Kerguelen plateau, are fed by an important flow of this newly formed bottom water from other areas on the shelf than the area investigated here (compare with stations 82, 81). The discrepancy between the stock of new bottom water observed at stations 84, 79 and the one at stations 82, 81 can be the result of : (1) seafloor morphology (presence of unknown canyons and channels) channeling new bottom water from other areas along the slope to these sites; (2) an accumulation (i.e. increased residence time) of new bottom water in the area between the slope and the Kerguelen plateau and (3) a discontinuity in the production process of new bottom water. In the latter case the low barium concentrations at stations 84, 79 should reflect a situation of bottom water formation (winter situation ?) anterior to the one actually observed at station 82, 81 on the shelf and slope.The latter possibility is backed by conclusions drawn from silicate and oxygen contents for shelf and basin waters in the same area (Princess Elisabeth Through; P. Tréguer, pers. commun.). Further comparison of our data with those obtained by the group of A. Poisson (freon-11; tritium; ...) is required to fully understand this feature.

From the above it can be concluded that dissolved barium is indeed a powerful tracer of watermasses, with a high resolution that is not always obtained in Tpot-salinity plots.

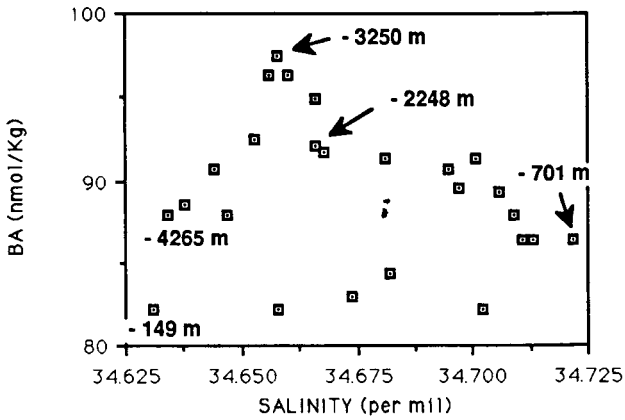

Fig. 5.12A : Station 84; Ba-SAL plot.

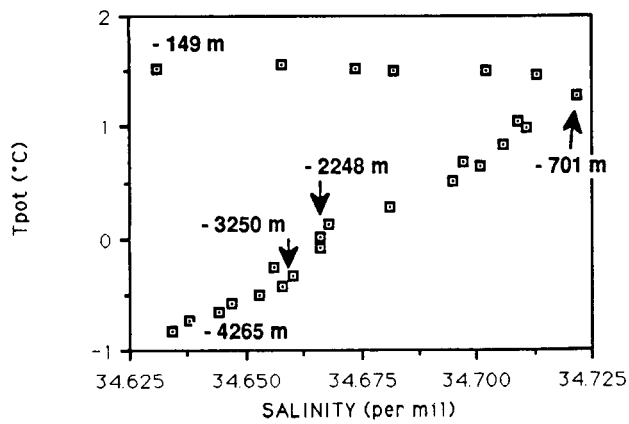

Fig. 5.12B : Station 84; T pot-SAL plot.

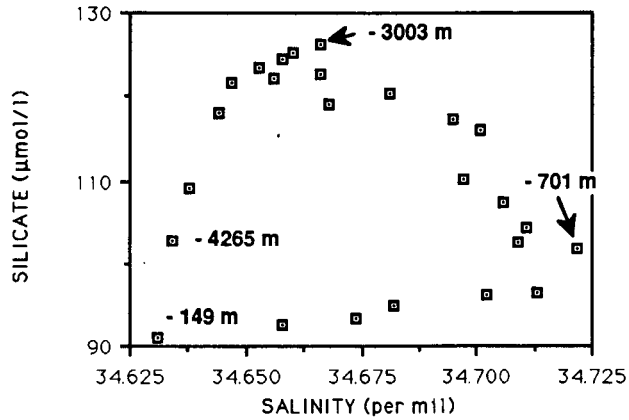

Fig.5.12C: Station 84; SIL - SAL plot.

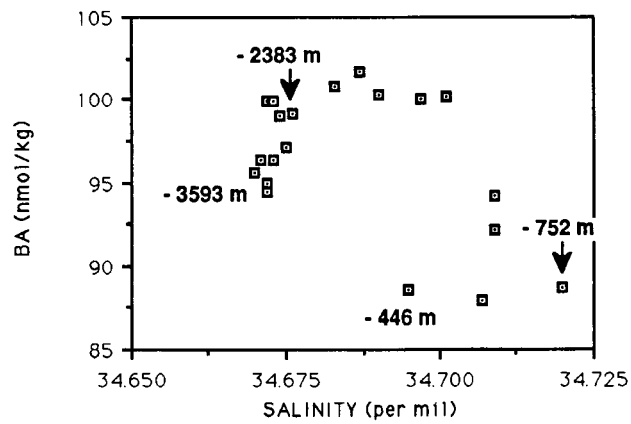

Fig. 5.13A : Station 79; Ba-SAL plot.

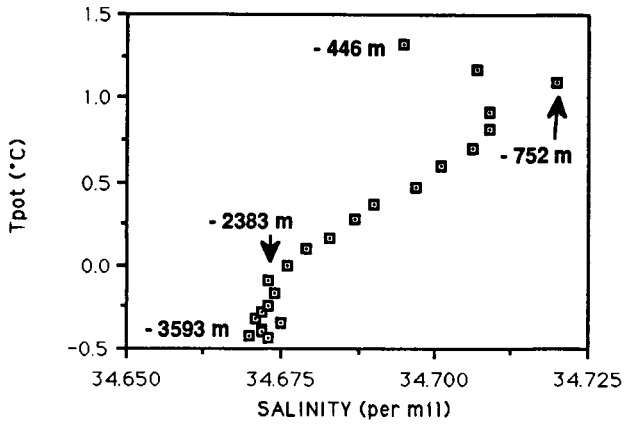

Fig. 5.13B : Station 79; T pot-SAL plot

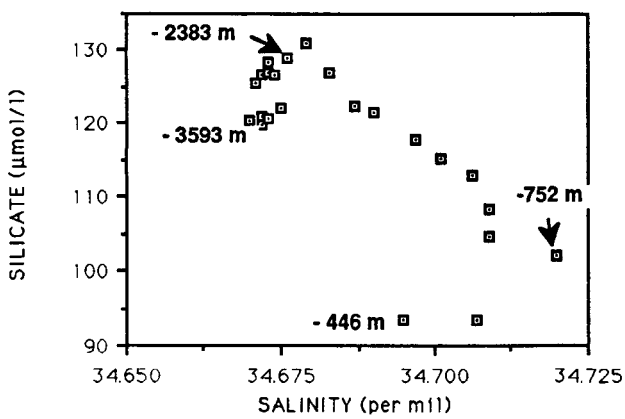

Fig. 5.13C: Station 79; SIL - SAL plot.

5.2. Particulate barium

5.2.1. Barite as the main carrier of barium in suspended matter.

It is known for other oceans that the main carrier of particulate Ba in suspended matter is barite (Dehairs et al., 1980). We have checked this for the Southern Ocean by (1) estimating the fraction of Ba in excess of the one associated with aluminosilicates and (2) searching for barite microcrystal presence using the SEM-EMP and comparing the calculated amount of barium carried by the detected crystals with total barium.
The fraction of the Ba associated with aluminosilicates in suspended matter is calculated using the Ba/Al ratio for mean crust (Al: 82,000 ppm; Ba 500 ppm; Bowen, 1979) and the Al content of the sample:

$$(Al)_{sample} \times (Ba/Al)_{crust} = (Ba)_{sample\ assoc.\ with\ aluminosilicates}$$

This excercise showed that the highest fractions of Ba in aluminosilicates are ≤ 17 %. Such values can occur in surface waters and bottom waters. Atmospheric deposition and sediment resuspension may be responsible for this observation. For the rest of the watercolumn the fraction of Ba in aluminosilicates is generally less than 10 %. This points towards another component as the main Ba carrier.
SEM-EMP analyses were carried out on samples (collected on Nuclepore membranes) from three depths of profile 76 (10, 500 and 700 m). These analyses revealed that Ba is carried by barite microcrystals of spherical shape (shape factor = $(\text{circumference})^2/4\pi^2R^2$ is in general ≤ 1.3), corroborating earlier findings (Dehairs et al., 1980). At 500 and 700 m barite crystals are well separated and occur as discrete particles homogenously distributed over the filter surface. At 10 m, on the contrary, crystals occur as heterogenously distributed barite aggregates mostly associated with large aggregates of diatom frustules and organic detritus.
For calculation of the Ba amount carried by the barite crystals, particles were assumed to be spherical and the used value for particle diameter is the one for the projected area diameter. Further a barite density of 4.5 $g.cm^{-3}$ and a molar ratio of Ba in $BaSO_4$ of 0.59 are used. The Ba content of a barite particle is thus given by:

$$(0.59 \times 4.5) \times \pi/6 \times D^3$$

Individual barite particles are mostly ≤ 1.5 µm in diameter. Therefore, particles recorded by the automatic recording using the PRC programme (see section 3.1.4), as being ≥ 1.5 µm (= aggregates of barite crystals) were arbitrarily split up in 2 or 3 smaller particles of equal diameter. Per sample the following number of fields were scanned under constant magnification (3000 X): 10 m (132 fields); 500 m (132 fields) and 700 m (153 fields). Since the total volume of seawater filtered and the surface scanned by SEM-EMP are known the Ba content carried by barite crystals can be expressed as a concentration per unit volume.
In Table 5.2, these calculated Ba concentrations are compared with the values for total Ba as obtained from the ICP analysis. The agreement between these data sets is rather good. For the samples at 500 and 700 m we calculate more than 80 % of total Ba to occur as

barite. The good agreement for the sample at 10 m may be fortuitous, since barite particles were detected in only a few of the 132 fields scanned.

Table 5.2: Comparison between Ba-barite concentrations and total Ba concentrations at station 76.

Depth	Ba-barite (A)	Number of crystals	Total Ba (B)	A / B
m	pmol / l	# / l	pmol / l	%
10	170	30360	151	112
500	294	26250	341	86
700	193	31580	237	81

Barite particle size distributions at 500 and 700 m are shown in Figure 5.14. Particles are classified using a geometric progression with size class boundaries obtained by multiplying the lower limit of the smallest size class by $(\sqrt[4]{2})^n$; with n = 1,2,3,... .
The modes of the distributions at 500 and 700 m occur resp. at 1.00 and 0.84 µm. The smallest crystals recorded at 500 m are 0.32 µm in size and 0.08 µm at 700 m. Thus, with increasing depths a shift occurs towards smaller particles, probably indicating barite dissolution.

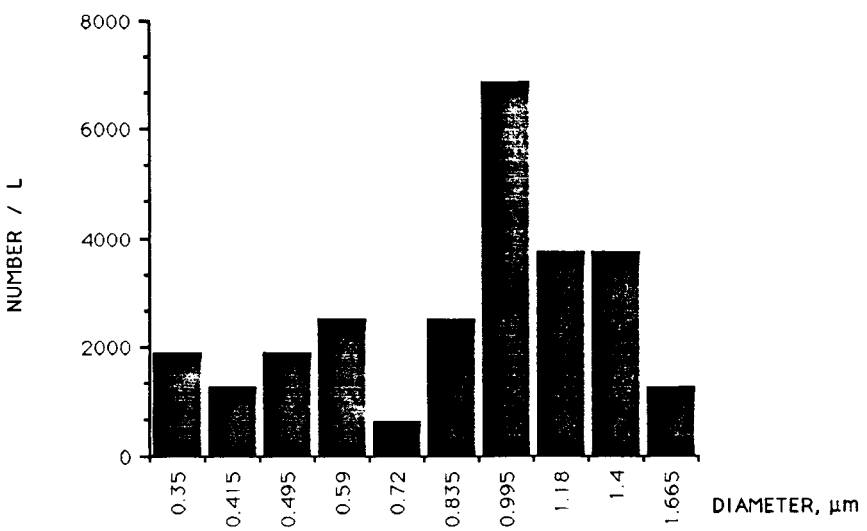

Fig. 5.14A: Station 76; size distribution (geometric progression) of barite particles at 500 m Indicated sizes correspond to class midpoints

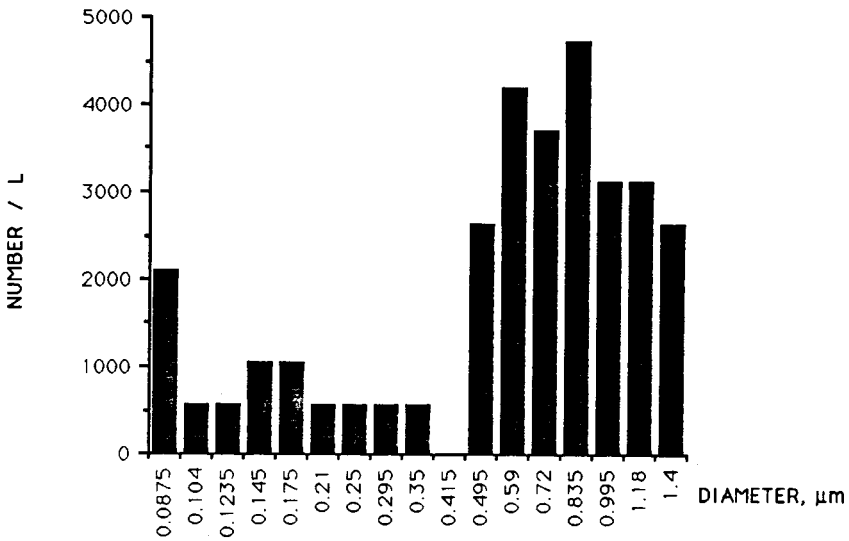

Fig 5.14B : Station 76; size distribution (geometric progression) of barite particles at 700 m. Indicated sizes correspond to class midpoints.

5.2.2. The particulate barium maximum in the oxygen minimum.

All profiles show a Ba maximum in the subsurface layer (generally somewhere between 200 and 1000 m depth). This maximum in most cases coincides with the oxygen minimum layer or occurs just above the oxygen minimum layer in the gradient leading towards the oxygen minimum. As an example the vertical profiles of particulate barium and dissolved oxygen for stations 76, 81, 84 and 90 are shown in Figure 5.15.

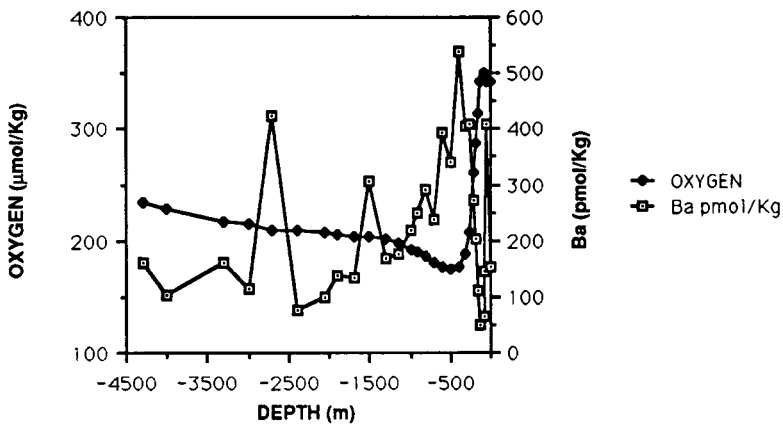

Fig. 5.15A : Station 76; vertical profiles of dissolved oxygen and particulate barium.

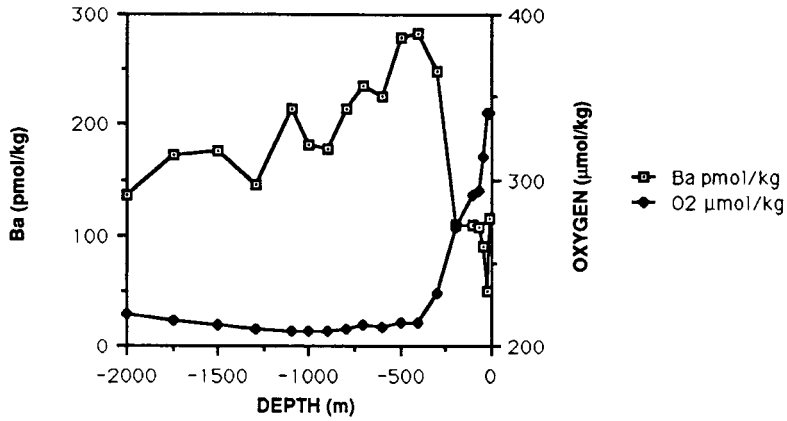

Fig. 5.15B : Station 81; vertical profiles of dissolved oxygen and particulate barium.

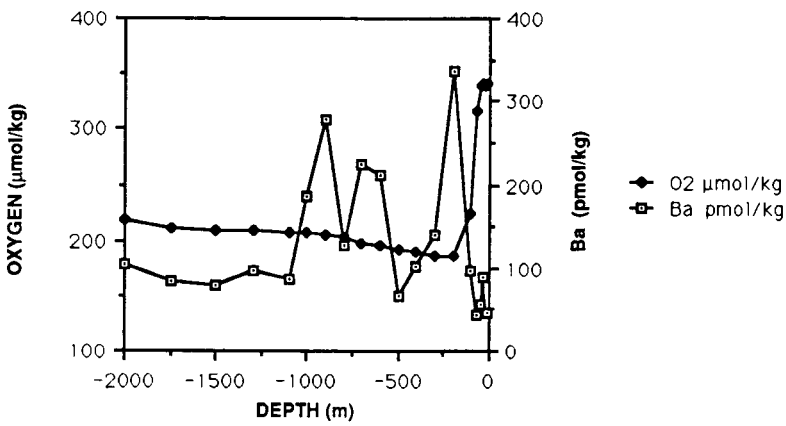

Fig. 5.15C : Station 84; vertical profiles of dissolved oxygen and particulate barium.

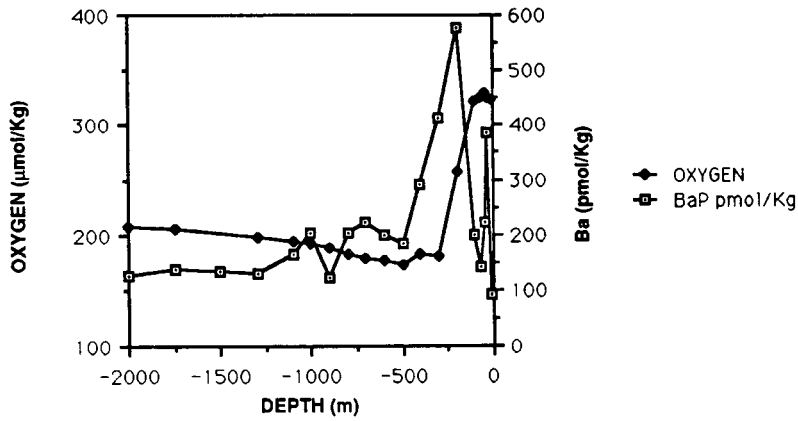

Fig. 5.15D : Station 90; vertical profiles of dissolved oxygen and particulate barium.

How can this coincidence of the Ba maximum with the oxygen minimum layer be explained? Bishop (1988) has observed that between the euphotic layer and the subsurface layer barite is transferred from a large particle fraction (> 53 m) to a small particle fraction (< 53 µm). This can be understood when considering that barite is passively formed in microenvironments such as biogenic aggregates and fecal pellets, or also if the barite formed in living plankton is originally transferred to a large particle class trough the effect of grazing and fecal pellet production (see discussion in section 5.2.3 below). In both cases, bacterial degradation of the large carrier particles will inject (or re-inject) the barite microcrystals as discrete particles in the watercolumn, explaining the shift observed by Bishop from the >53 µm to the < 53 µm size class between surface and subsurface. This process will also set free organic matter, the oxydation of which consumes oxygen. Our own SEM-EMP observations for station 76 are consistent with the above. Indeed, while barite is present as discrete micron-sized particles in the O2-minimum and below, at -10 m barite is mainly associated with aggregates of biogenic detritus (organic matter and empty diatom frustules). The association of barite and empty diatom frustules was also stressed by Bishop (1988).

If the above outlined scenario indeed reflects reality, the following facts apply. First, disintegration of carrier particles through bacterial mediation apparantly occurs mainly in the vicinity of the oxygen minimum. Second, the decreased particulate Ba concentrations we observe in the euphotic layer at most stations (with exception of stations 78 and 79, discussed in section 5.2.3, below), are an artefact induced by the type of sampler used. Indeed, it is well known (Bishop and Edmond, 1976) that large, fast settling particles (> 50 µm; such as the biogenic aggregates carrying barite) are not sampled in a statistically significant way by sampling 30 liter of seawater (i.e. the volume sampled with the Niskin bottles used here), since such particles are too small in number. The study of these large particles requires the sampling of much larger volumes (several m^3) of seawater, as is done by Bishop (1988) using a high voulme sampler with in-situ filtration.

From the data in Tables 4.29 to 4.40 and in Figure 5.15 (see case of station 76) it is also observed that occasionally isolated high Ba values do occur in deep water (i.e. below 500 m) These high Ba values often go together with higher Ca, Sr and Si values. This can be explained by assuming that a fraction of the large particles, produced in the euphotic layer, survives breakdown in the layer above and in the O2-minimum and settles to greater depths where they eventually break open and set free their content of small particles.
However, advective transport as well can induce deep maxima in the deep particulate Ba profile, as suggested by the data for station 84 (Fig. 5.15). For this station a broad maximum is situated between 500 and 1200 m and coincides with the salinity maximum layer, suggesting in this case advective transport of discrete barite crystals with the salinity maximum water.

Below we check, for the oxygen minimum zone, whether there exists a relationship between the magnitude of the oxygen depletion and the content of Ba-barite. In the following, oxygen depletion is expressed as A.O.U. (Apparant Oxygen Utilisation). For each depth AOU is calculated as the difference between the oxygen content at saturation (O2 SAT) and the measured oxygen content. The Tpot and salinity values of each depth define the corresponding O2 SAT value.
In Figure 5.16 we have plotted the Ba values for the subsurface Ba maximum depth region coinciding with the oxygen minimum layer against AOU in the oxygen minimum layer. Each Ba and AOU data generally represents the average of the values at two or more depths. A highly significant positive relationship is apparant, with a slope value $\Delta Ba / \Delta AOU \sim = 7.10^{-6}$.
Three geographical zones can be distinguished with regard to Ba and AOU values: (1) Stations 81 and 79, closest to the Antarctic Divergence show the lowest Ba and AOU values; (2) Stations 84, 85, 86, 87 located along Antarctica, but north of the Divergence, show intermediate values; (3) Stations 76, 78, 90 still more to the north of the Divergence, but south of the Polar Front, show the highest Ba and AOU values. For stations 95 and 97 north of the Polar Front, the Ba / AOU values do not fit the observed relationship. Station 94, within the area of the Polar Front does not fit the relationship either. For this latter case, however, it is possible that the low Ba value for the sample at -400 m (103 pmol/Kg in between 278 pmol/Kg at -300 m and 261 pmol/Kg at -500 m) is erroneous and thus that the real Ba maximum was missed.

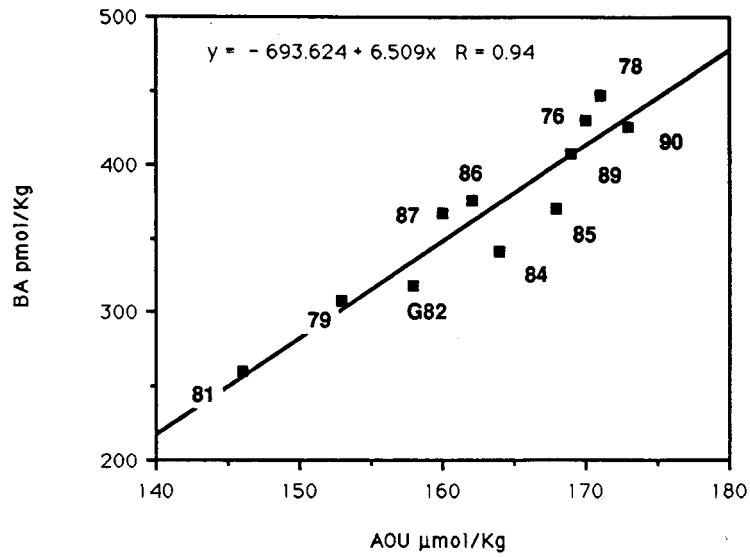

Fig. 5.16 : Part Ba-AOU plot for stations south of Polar Front.

How can this Ba / AOU relationship be interpreted? It suggests that vertical transport out of the local euphotic layer is superposed upon advective transport within the O2-minimum layer.

It must be noted that the Southern Ocean GEOSECS station G82 (56°15.7'S - 24°55.2'W) also fits the relationship (Ba data for G82 from Dehairs, 1979). However, other GEOSECS profiles from the North and South Atlantic Ocean do not fit at all the relationship, showing generally much smaller AOU values for similar Ba values as observed here (Ba data from Dehairs, 1979). Also, for these Atlantic profiles, coincidence of Ba maxima with well defined oxygen minima is less clear. These Atlantic profiles differ from the Southern Ocean profiles presented here, in that the watermasses in the oxygen minimum layer can certainly not ne considered to have a common origin, while this is most likely the case for the profiles south of the Polar Front. Thus, when comparing waters in the oxygen minimum that have different origins, the AOU values should not necessarily correspond to the value given by the relationship in Figure 5.16. But it could be that the ΔBa / ΔAOU ratio is universal, that is: at any place in the ocean the consumption of oxygen along a sequence of stations, with waters in the oxygen minimum layer having the same origin, gives rise to an increase in the Ba-barite content as predicted from the ΔBa / ΔAOU ratio observed for the Southern Ocean. The Atlantic GEOSECS stations with Ba data are too few in number and too far apart to check the possible ubiquity of this ΔBa / ΔAOU ratio.

The general picture, discussed above, of oxygen min. layer water originating at the Divergence and spreading northwards and eastwards, as entrained by the Antarctic Circumpolar Current (ACC), is sustained by the observed ΔO_2 / ΔNO_3 evolution (in the O2 -

minimum) between stations close to the Divergence and stations more to the north and to the east. The excercise outlined below consists in checking whether the consumption of oxygen in the oxygen min. layer is in agreement with the production of NO_3 from organic matter mineralisation and nitrification. It is a general feature that oxygen minima and nitrate maxima do not coincide, with the nitrate maxima situated slightly above the oxygen minima. We have compared the ΔO_2 in the oxygen minimum with ΔNO_3 in the nitrate maximum (Figure 5.17), but the observed relationship holds also when NO_3 and O_2 are taken at the same depth. If organic matter oxidation by heterotrophs is the process at stake, ΔO_2 / ΔNO_3 should be similar to the Redfield ratio (= -8.6; Redfield et al., 1963). For the deep Atlantic the $\Delta O_2/\Delta NO_3$ ratio was observed to be -6 (Broecker and Peng, 1982). More recent estimates, based on data for thermocline and deep waters from the Atlantic, Indian and Pacific Oceans, indicate the ΔO_2 / ΔNO_3 ratio to be closer to -11 (Takahashi et al., 1985; Broecker et al., 1985; Peng and Broecker, 1987).

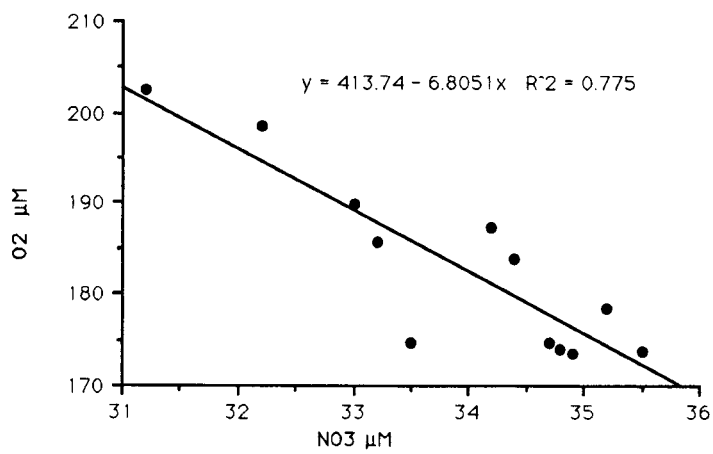

Fig. 5.17: Dissolved oxygen in the oxygen minimum versus nitrate in the nitrate maximum

In Fig. 5.17 the slope of this relationship, $\Delta O_2/\Delta NO_3$, is -8, what is close to the ratios found by others (i.e. between -6 and -11). This suggests the ageing of the water in the oxygen minimum layer to occur in a general south to north, north-east direction and therefore points towards a single origin of this water layer.

This origin is likely to be upwelling along the Divergence. At the Divergence (station 81, southernmost station) the minimum oxygen value is 209 µM at 900 to 1000 m depth with sigma theta = 27.822 - 27.827. The 204 - 209 µM oxygen value is found at the same isopycnal surface (sigma theta range between 27.82 - 27.84) at all stations south of the Polar Front (Figure 5.18). This suggests the occurrence of the 209 µM value as a minimum at station 81 to be induced through advection. For stations north of station 81 the oxygen minimum occurs at shallower depths and is not located on a single isopycnal surface. Indeed, sigma theta in the oxygen minimum is decreasing from 27.714 (station 87; 65°11´S) to 27.661 (station 94; 50°35´S).

To resume, it seems likely that a low oxygen value (i.e. the 209 µM value) is originally advected to the south and rises to shallower depths along the 27.83 isopycnal surface.

From the Divergence on the water carrying this oxygen value returns northwards. Its oxygen minimum is now affected by local processes of oxygen consumption which appear to pull the minimum diapycnally to shallower, less dense, waters.

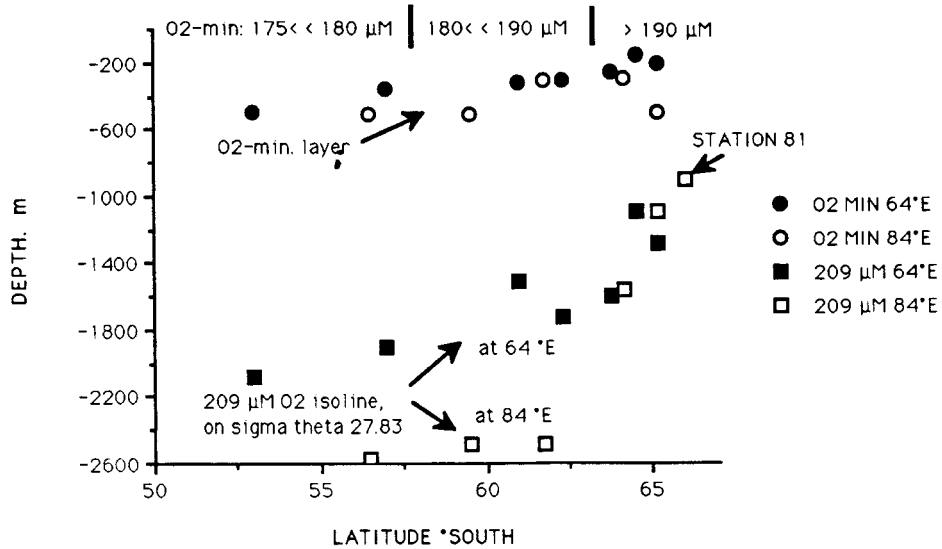

Fig. 5.18: Position of the 209 µM O2 value and of the O2-minimum between 50° and 67° latitude south.

We can now try to estimate the speed of water advection in the oxygen minimum layer. We consider water movement between stations 87 and 78, about 2500 km apart and with station 78 located north-east of 87, and thus downstream with regard to the general circumpolar water flow. During transfer between these stations some 19 µmol of oxygen have been consumed per liter seawater in the oxygen minimum layer. For an oxygen minimum layer extending over 200 m this O_2 consumption is 3800 $mmol.m^{-2}$ and is equivalent to the oxidation of 2760 mmol carbon per m^2 (i.e. 3800 x 127/175, as based on the $\Delta O2/\Delta C$ ratio in Takahashi et al., 1985 and in Peng and Broecker, 1987). Estimates of primary production values in the Southern Ocean range from 100 to 350 mg $C.m^{-2}.d^{-1}$ (e.g. Wefer et al., 1982; Le Jehan and Tréguer, 1983). We consider a value of 200 mg $C.m^{-2}.d^{-1}$ and assume it applies for four months of the year. Thus a year averaged primary production of 70 mg $C.m^{-2}.d^{-1}$ (= 6 mmol $m^{-2}.d^{-1}$) is obtained. If, as a first approximation, we assume that all this carbon is re-oxidized in the oxygen minimum layer, the observed decrease in oxygen between stations 87 and 78 is obtained in about one year (i.e. 2760 $mmol.m^{-2}$ / 6 $mmol.m^{-2}.d^{-1}$ = 460 days). In this case water would move with a speed of 5.4 $km.d^{-1}$ or 6.3 $cm.s^{-1}$. This value is similar to geostrophic speeds calculated for the Antarctic Circumpolar Current at 200 m depth, south of the Polar Front, along the prime meridian (between 2 and 15 $cm.s^{-1}$; Whitworth III and Nowlin jr., 1987). For decreasing fractions of

photosynthetically produced organic carbon remineralized in the oxygen minimum layer, this speed will decrease.
We will now check whether the estimated ageing of the water in the oxygen minimum layer is consistent with the observed accumulation of barite. Assuming Stokes sedimentation law to apply and without consideration of the dissolution effect, a 1 μm large barite crystal will need about half a year to cross a 200 m thick water layer (what is about the width of the oxygen minimumlayer); a 0.5 μm barite crystal will need about 2 years. Furthermore, barite dissolution in seawater is a slow process with a dissolution rate estimated at 0.075 $\mu m.y^{-1}$ (Dehairs, 1979; Dehairs et al., 1980), what in this case will have a negligible effect on barite residence time. Thus barite residence time in the oxygen minimum layer can be of the order of one year.
From the above discussion it thus appears that there is evidence for internal consistency between ageing of the oxygen minimum layer over a given distance as controlled by advection velocity, and accumulation of barite in the oxygen minimum layer as controlled by sedimentation and dissolution. In this case barite content reflects and integrates former biological processes.

The general picture could then be as follows. Oxygen is continuously consumed in the O2-minimum layer due to heterotrophic consumption of organic matter both, settling from the surface and advected. Heterotrophic breakdown of organic matter settling from the euphotic layer sets free micron-sized discrete barite crystals.The discrete barite crystals injected in the O2-minimum area tend to accumulate as a result of (1) a relatively small settling rate, due to their small size and (2) their small dissolution rate.

5.2.3. The origin of particulate Ba-barite.

The biological origin of suspended and sedimentary marine barite has been extensively demonstrated before (Dehairs et al., 1980, 1987; Bishop, 1988; Schmitz, 1987; Dymond, 1985). The exact mechanism of barite production in the open ocean, however, is not fully resolved. Active production of barite by planktonic and benthic organisms has been described (Fresnel et al., 1979; Gayral et Fresnel, 1979; Tendal, 1972; Gooday, 1982; Fenchel and Finlay, 1984). However, excepted for the benthic Rhizopods, no direct evidence (e.g. from SEM-EMP investigations) for intracellular barite presence in oceanic plankton exists. Our own SEM-EMP investigations for station 76 neither have revealed such an association.
Bishop (1988) has done extensive SEM-EMP work on suspended matter collected from Warm Core Rings and observed barite microcrystals to be associated, to a large extent, with empty diatom frustules. The occurrence of barite could thus be explained by a passive precipitation of $BaSO_4$ in supersaturated microenvironments provided by organic detritus and diatom frustules. Our own SEM-EMP investigations for station 76 are consistent with this explanation by Bishop: barite at -10 m occurs in association with biogenic detritus (organic matter + diatom tests). However, other observations discussed below, indirectly sustain the fact that active production of barite might occur as well.
Inspection of the particulate Ba data for stations 78 and 79 (Tables 4.30 and 4.31) reveals that very high concentrations occur in the first 40 m, exceeding the Ba maximum in the

vicinity of the oxygen minimum below. For these stations Chla contents are higher (2 to 5 times) than at other stations, while nitrate content in surface waters is lower (Figure 5.19). This indicates the presence of a higher biomass in the area of stations 78, 79. For station 80 no particulate matter was sampled, but the high Chla and the low nitrate values in the euphotic layer suggest that here also high barium concentrations are present. The fact that Si is lower at station 78 than at station 76, suggests that at 78 the increased biomass is mainly due to phytoplankton not dominated by diatoms. At station 79, however, Si is significantly higher than at station 76 idicating again diatom dominance. Without being able to discriminate between the different groups composing the phytoplankton community, it seems thus likely that for the area covering stations 78 and 79, the increased biomass of plankton actively produces barite.

However, an alternative explanation could be that increased phytoplankton biomass goes with increased bacterial biomass. In this case barite production in the euphotic layer could also be passive, through the precipitation in the detrital microenvironment explained above. This is suggested by the observed positive relationship between remineralization rate and barium presence in the euphotic layer at other stations (Figure 5.20; see also discussion in section 5.4.2 below) Since for stations 78 and 79 no mineralization rates were measured, we do not know whether the observed relationship with barium applies also for these sites with extreme barium contents in the euphotic layer. The possibility of passive barite production is not fully sustained by the data on bacterial biomass (countings on acrydin-orange stained samples) obtained during the same cruise (Dezan, 1987). Indeed, bacterial biomass at station 78 is not significantly higher (1.6 µg.l-1), relative to other stations with low Chla content, but it is at stations 79, 80 and 81 (resp. 2.5; 5.1 and 4.3 µg.l^{-1}; Dezan, 1987). For station 81 this high bacterial biomass does not coincide with a high barium content. Therefore the evidence for passive precipitation of barite, as based on bacterial biomass, is not clear. Further investigations with the SEM-EMP are required to settle the problem of the barite production mechanism.

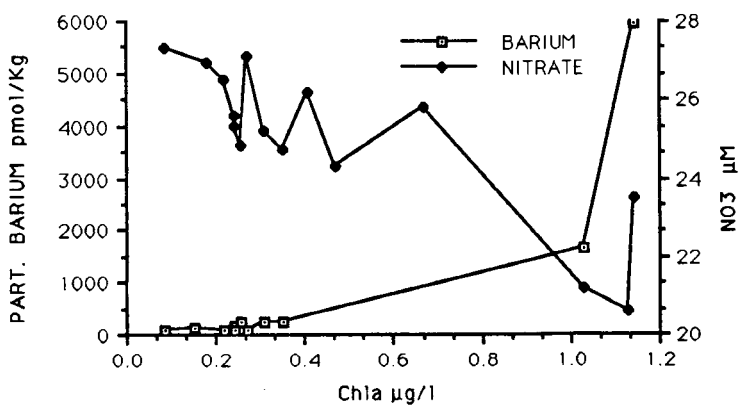

Fig. 5.19: Particulate Ba and nitrate versus Chla in the euphotic layer

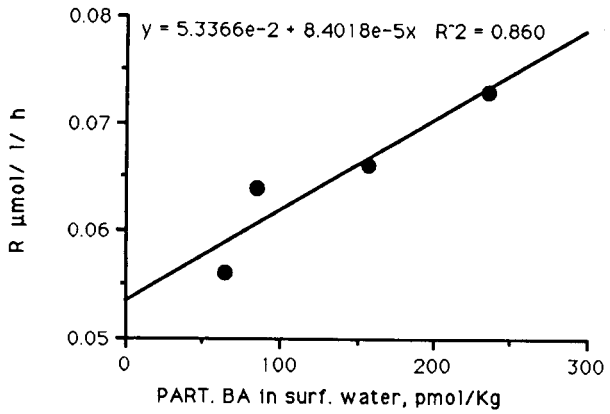

Fig. 5.20: Ammonia remineralization rates versus particulate Ba content in the euphotic layer.

5.2.4. Si, Ca and Sr.

While the highest concentrations of Ca, Sr and Si always occur in the euphotic layerClose inspection of the profiles for Ca, Sr and Si reveals that in most cases these elements as well have a (secondary) maximum in the oxygen min. layer. This is consistent with the fact, discussed above, that large heterogenously composed bioaggregates produced in surface water sediment to deeper layers where they disintegrate in the oxygen min. layer setting free their constituing components.
Below the euphotic layer, Si is occasionally observed to co-vary rather well with Ba. As an example we show the case of station 76 in Figure 5. 21 . This observation again fits those by Bishop (1988) who described barite association with empty diatom frustules.

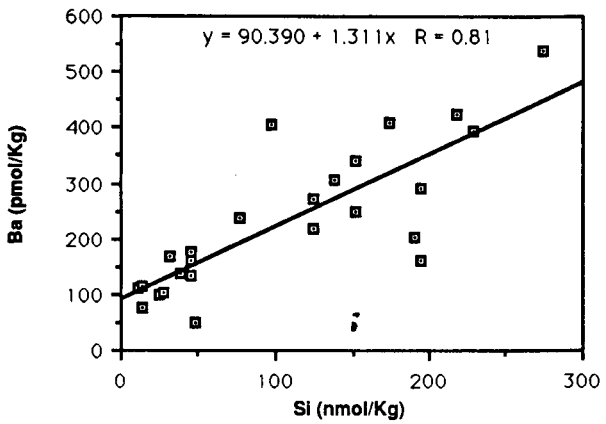

Fig. 5.17: Ba-Si plot for depths below 90 m, at station 76.

For Ca and Sr a highly significant positive correlation is observed, with the slope of the regression being generally close to 10, the molar ratio of Ca to Sr in the seawater solution. This could indicate a possible artificial origin for Ca and Sr, due to dessication of seawater droplets on the filter membranes during sample collection. This, however, is highly unlikely, since: (1) filters were systematically rinsed with deionized water, immediately after sampling and (2) vertical profiles are not erratic, but are consistent with those of Si, showing high contents in surface waters (due to the occurrence of living plankton) and decreasing contents with increasing depth, due to dissolution. At this point no explanation, except biological control, can be offered for the constant Ca / Sr molar ratio in suspended matter, similar to the ratio for the dissolved phase.

5.3 Evaluation of the nutrient profiles

It was pointed out in the preliminary report that nutrient concentrations figure as important tracers in water mass characterisation. This property was confirmed by an accuracy test showing the good agreement for the nitrate profiles of the stations 96 (44°21'S, 20°52'E) 97 (41°48S, 18°27'E) 98 (38°00'S, 23°21'E) and GEOSECS G93 (44°46'S, 18°27'E), as well as for the stations 94 (50°35'S, 27°03'E) and GEOSECS G429 (47°40'S, 57°51'E). The data for the stations are represented in Figures 5.22 and 5.23.

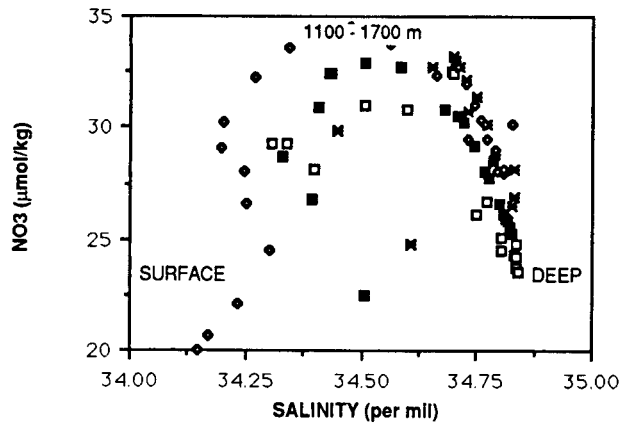

Fig. 5.22: Nitrate - SAL plot for GEOSECS station G93 ( ) and INDIGO 3 stations 96 ( ), 97 ( ), 98 ( ).

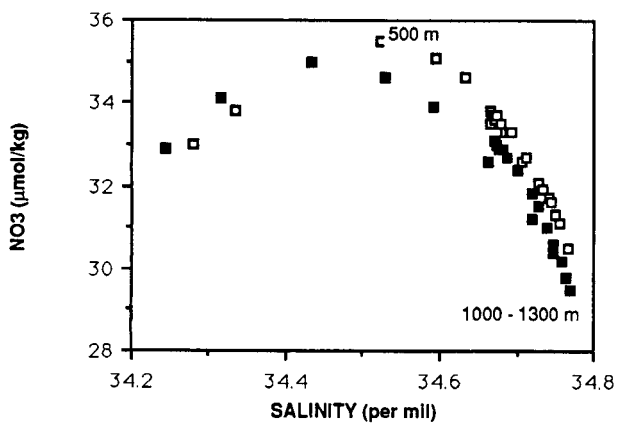

Fig. 5. 23: Nitrate - SAL plot for GEOSECS station G429 ( ) and INDIGO 3 station 94 ( ).

5.4 The remineralization rates

5.4.1 Nitrogen-15 abundances

As previously mentioned (chapter 3) the ammonium must be stripped from its sea water matrix before it can be analysed for its isotopic composition. The described diffusion process, as wel as any other extraction procedure probably, is subject to isotope fractionation. This phenomenon can alter the nitrogen-15 to nitrogen-14 ratio, simply

because the diffusion rate of the havier isotope is not as high as for the other one. Evidently, this phenomenon can induce errors into the results as the nitrogen-15 abundances are underestimated due to this discrimination between the isotopes.

A check of the extraction method with North Sea samples (Monteny, 1986) pointed out that the underestimation can amount to 15%. If the nitrogen-15 abundances of the extracted ammonium are about 15% higher then the measured value, the corresponding remineralization rates are overestimated by 8 to 17%.

A second error, that can possibly have altered the results, is the enhanced remineralization due to long incubation times (Glibert et al, 1982). They indicate difficulties in applying the isotope models when the assumption of constant uptake and constant remineralization with time does not hold, as data from oceanic systems show variable rates with time.

These reflections led us to consider the obtained remineralization rates as "maximal' rates, which can only be translated to the natural situation when taking into account these different remarks. Literature data for remineralization rates in the Southern Ocean are scarce; only Glibert (1982) describes some stations in the Scotia Sea, with for three of the stations values between 0.02 and 0.13 $\mu mol.l^{-1}.h^{-1}$, and for all the other stations values < 0.01 $\mu mol.l^{-1}.h^{-1}$. For a similar study, carried out by the same research group in the Sargasso Sea, the mean remineralization rate amounts 0.07 $\mu mol.l^{-1}.h^{-1}$.

A general property is the important daily and seasonal variability

5.4.2 Discussion of the obtained results

Comparison of the remineralization rates at the different stations

The incubation experiments were carried out at five different stations (76, 81, 86, 89 and 103) and at each of the stations three different samples were taken. A sample of the euphotic zone (EZ) at 10 m depth, one at the oxygen minimum layer (OM) and a deep water (DW) sample taken 200 m below the oxygen minimum are compared.

As for each depth data of the different experiments with light bottles as well as dark bottles are available, the average values are considered in this interpretation (Table 5.3).

Table 5.3: Remineralization rates (µmol N/l.h), AOU (µmol/l), bacterial biomass (µg C/l) and Ba_p (pmol/kg) for the incubation experiments.

INCUBATION	R	R, % OF R-EZ	AOU	BACT. BIOM.	PART Ba
76, EZ	0.073	100.00	9.1	1.49	151
76, OM	0.030	40.69	171.4	0.62	426
76, DW	0.024	33.10	164.8	0.37	307
81, EZ	0.064	100.00	17.7	3.54	114
81, OM	0.068	106.25	140.5	0.76	191
81, DW	0.063	98.44	142.5	0.74	180
86, EZ	0.066	100.00	14.9	1.55	32
86, OM	0.030	45.04	155.2	0.73	370
86, DW	0.031	46.56	151.5	0.57	248
89, EZ	0.056	100.00	13.7	1.66	50
89, OM	0.037	65.18	166.6	1.05	389
89, DW	0.013	22.32	159.6	0.89	331
103, EZ	0.253	100.00			
103, OM	0.051	20.20			
103, DW	0.094	37.23			

In the EZ the remineralization rates (R) for the stations 76, 81, 86 and 89 vary between 0.072 and 0.051 µmol $N.l^{-1}.h^{-1}$. These values are about five times smaller than the one for station 103. This important difference, however, is not confirmed by the OM data. For the OM layer all the R values are between 0.064 and 0.030. Remarkable for this layer is the very small increase of the value at station 81 as compared to the measured value in the EZ, where all the other stations show a net decrease. For the DW samples it is hard to point out a general trend. The significance of the difference between the results, obtained for the OM and for the DW, is not always clear. However, the collected results indicate a small decrease in remineralization rate from the OM layer to the DW.
The results are represented in two different graphs. The first one (Fig 5.24) compares the different R values for the five stations at their different depths. In the second graph (Fig 5.25) R is represented as the corresponding percentage of the EZ value in order to highlight on the evolution with depth at each of the different stations.

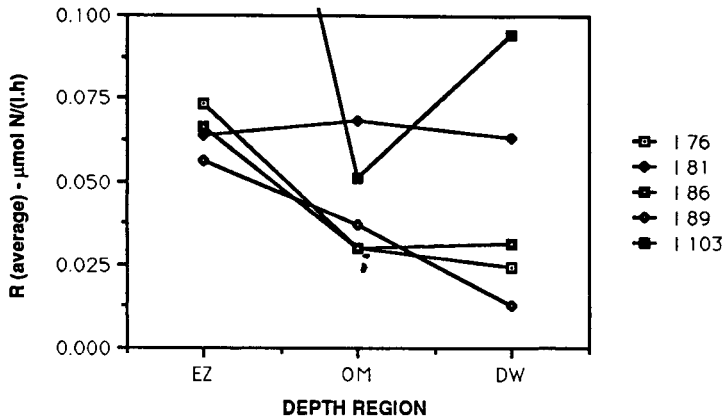

Fig.5.24 : Remineralization rate to depth relation for the five stations.

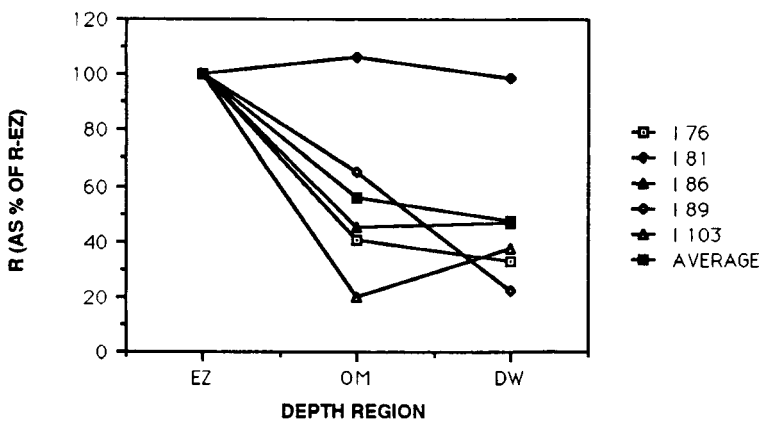

Fig. 5.25 : Proportional variation of the remineralization rate with depth.

Relation of R to other parameters of biological acitivty

The relation between apparent oxygen utilisation (AOU) and the remineralization rate is studied for four stations (76, 81, 86, and 89). Due to the bad weather conditions no complete data set for station 103 is available. As only four values can be compared, the correlation must be interpreted as a trendsetting more then a significant mathematical figure. However, at the three different depths, R decreases with increasing AOU (Fig 5.26 A, B and C). The correlation for the EZ data is rather bad, but anyhow for the three linear relations a similar slope and far more significant correlations for the OM and DW data are found, what confirms the decrease of R with increasing AOU. This behaviour must probably be explained as a cause / effect relation: larger AOU values, due to an important passed remineralization, induce smaller instantaneous remineralization rates.

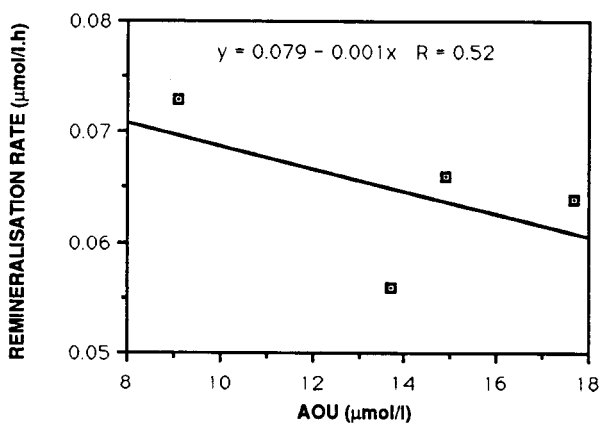

Fig. 5.26A : remineralization rate to AOU relation in the euphotic zone.

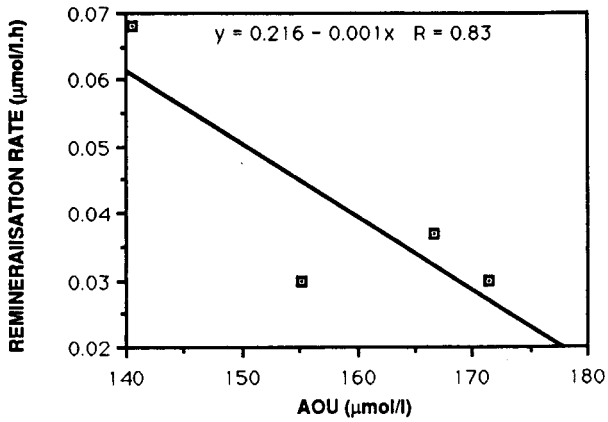

Fig. 5.26B : remineralization rate to AOU relation in the oxygen minimum layer.

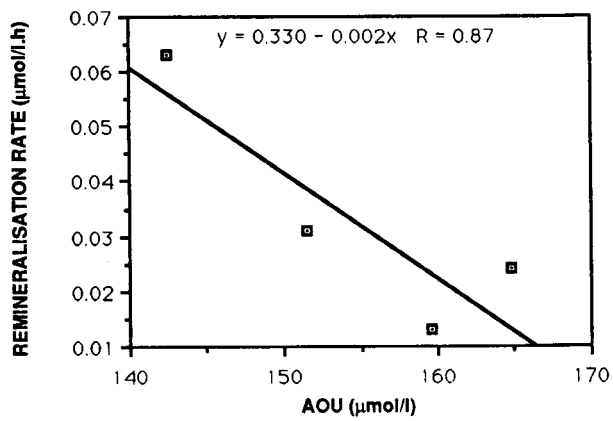

Fig. 5.26C : remineralization rate to AOU relation in the deep water.

Secondly, the relation is checked between R and the bacterial biomass, determined by Dezan (1987), for the same four stations. For none of the depth regions a significant correlation between R and the bacterial biomass is evidenced. Moreover it is impossible to deduce a relation between R and AOU for these depths.
Here must be mentioned, however, that only a few bacterial biomass data at depths below the mixed layer are available, and that the correlations are based on comparisons of R values with interpolated data for bacterial biomass.

In third instance, we deal with the relation between the particulate Ba concentration and R, also for the same four stations. The data for the EZ show a positive correlation (see above, Fig 5.20), suggesting that for surface waters mineralization activity can result in the

production of particulate barium. This trend is the inverse of what is observed for the OM and for the DW layers: R decreases with increasing part. Ba contents (Figs. 5.27A and 5.27B). In both these latter cases a highly significant correlation (correlation coefficient = 0.97) between R and the particulate Ba concentration is observed. But part. Ba and oxygen are inversely correlated (see above, sectin 5.2.2) indicating that for the OM and DW layers, however it is the local oxygen content that regulates the magnitude of R.

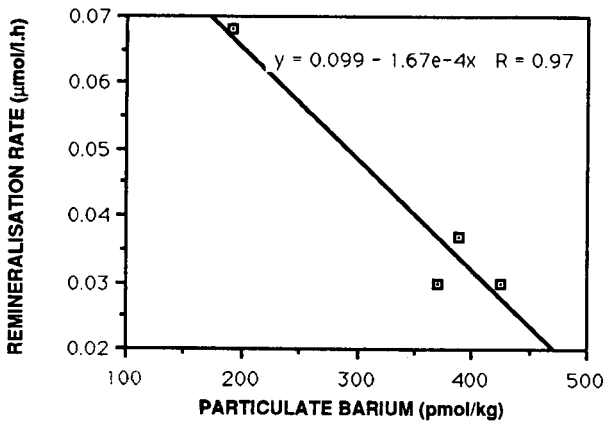

Fig. 5.27A : Remineralization rate to particulate barium relation in the oxygen minimum layer.

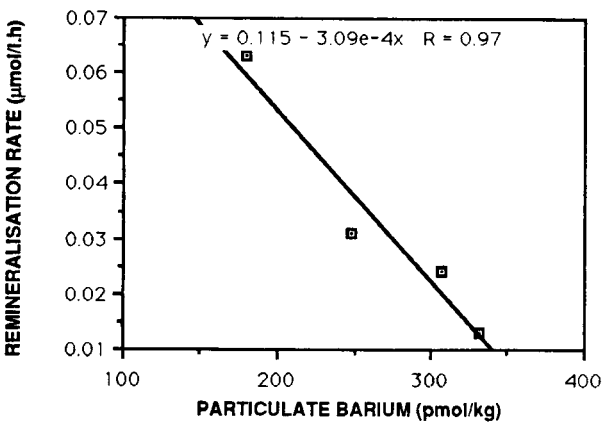

Fig. 5.27B : Remineralization rate to particulate barium relation in the deep water.

CHAPTER 6 : CONCLUSIONS

(1) Our Southern Ocean dissolved barium data, obtained by direct measurement using the ICP-OES technique, are shown to be consistent with earlier GEOSECS observations for the same area obtained by others using the IDMS technique.
Dissolved barium - salinity plots for the watercolumn section below the salinity maximum, at stations south of the Polar Front, show variabilities that reflect a barium poor bottom water intruding a barium rich deep water layer. This bottom water is newly formed bottom water, as inferred from freon-11 data. It spreads in two branches, one just over the sea floor and one at intermediate depth, below the salinity maximum.The intermediate branch with low barium can be identified at most stations south of the Polar Front.
These results indicate that barium is indeed a usefull watermass tracer. It adds to the resolving power of simple Tpot-salinity diagrams for discriminating between different watermasses present. The results also sustain the fact that deep water formation processes can occur at different places around Antarctica and not solely in the Weddell Sea and the Ross Sea.

(2) Barium in Southern Ocean suspended matter is shown to be mainly carried by barite microcrystals, confirming earlier observations for other oceans. This barium-barite shows maximum values in the vicinity of the oxygen minimum where it correlates with AOU. This relationship is consistent with the known association of barite production with biological activity taken in a broad sense (i.e. primary production and / or hetrotrophic activity). The overall scheme of barite production and redistribution at depth we can distill from our observations is as follows. In the euphotic layer barite is produced either by active plankton, or by passive precipitation in the supersaturated micro-environment composed by biogenic detritus. The visual evidence of barite association with biogenic aggregates composed of organic detritus and empty diatom frustules, and the observed positive correlation in surface water of barium-barite and rates of organic matter remineralization by heterotrophs, are in favor of the passive production mode. However, SEM-EMP investigation of a few stations with high Chla contents and high barium-barite in surface water could possibly resolve the question of whether or not active barite production occurs in the natural oceanic environment. The transport of barite downwards is most likely through large particle settling. This large particle can be the bioaggregate carrying barite precipated within it, or the fecal pellet with barite concentrated trough the process of grazing. The largest fraction of this large particles desintegrate within the first 500 m, the depth limit of the oxygen minimum south of the Polar Front, setting free the smaller constituting particles including barite. Hetrotrophic oxidation of the organic matter, thus set free, further accentuates the oxygen minimum.

This oxygen minimum layer advects while continuously receiving a flux of matter from the surface. Barite injected in this depth layer accumulates in a given proportion to oxygen consumption. Barite in the oxygen minimum thus integrates former processes, and, in contrast to surface water, is no longer comparable with remineralization rates, which reflect instantaneous processes. Indeed, barite content and remineralization rates in the oxygen minimum anticorrelate, due to dependency of remineralization on partial pressure of oxygen.

REFERENCES

Armstrong et al. , 1967, Deep Sea Res. 14, 381.

Bankston, 1981, Proc. Int. Winter Conf. on Developments in Atomic Plasma Spectrometric Analysis, 627- 634.

Bendschneider and Robinson, 1952, J. Mar. Res. 11, 87.

Bishop, 1988, Nature, 332, 431 - 343.

Bishop and Edmond, 1976, J. Mar. Res., 34, 181 - 198.

Bowen, 1979, Environmental Chemistry of the Elements, Acad. Press.

Blackburn, 1979, Appl. Environ. Microbiol. 37, 760.

Broecker and Peng, 1982, Tracers in the Sea, Eldigio Press, 690 pp.

Broecker et al., 1985, J. Geophys. res., 90, 6925 - 6939.

Burman et al., 1978, Anal. Chem., 50, 679 - 680.

Caperon et al. , 1979, Mar. Biol. 54, 33.

Chan et al., 1977, Deep Sea Res., 24, 613 - 649.

Conley et al., 1979, Instrum. Lab., 11, 1 - 5.,

Dehairs, 1979, Discrete suspended particles of barite and the barium cycle in the open ocean, Ph. D. Thesis, Vrije Universiteit Brussel, 285 pp.

Dehairs et al., 1980, Earth Planet. Sci. Letters, 49, 528 - 550.

Dehairs et al., 1987, Anal. Chim. Acta, 196, 33 - 40.

Dehairs et al., 1987, Biogeochem. 4, 119 - 139

Dehairs et al., 1989, An Chim. Acta, in press.

Dehairs and Goeyens, 1987, in: Proc. Belg. Natl. Colloq. Antarctic Res. Brussels, Oct. 20, 80 - 96.

D'Elia, 1983, in 'Nitrogen in the Marine Environment', eds Carpenter and Capone, 731.

Dezan, 1987, Bacterial Biomass and Activity in North Sea and Antarctic Waters, M. Sc Thesis, Vrije Universiteit Brussel, 111pp.

Dudek et al. , 1986, Mar. Chem. 18, 59.

Dugdale and Goering, 1967, Limnol. Oceanogr. 12, 196.

Dymond, 1985, EOS, Trans. Am. Geophys. Un., 66, 1275, abstract.

Epstein and Zander, 1979, Anal. Chem., 51, 915 - 918.

Fenchel and Finlay, 1984, J. Exp. Biol., 110, 17 -33.

Fiedler and Proksch, 1975, Anal. Chim. Acta 78, 1.

Finlay et al., 1983, Geochim. Cosmochim. Acta, 47, 1325 - 1329.

Fisher and Morrissey, 1985, Mar. Chem. 16, 11

Fresnel et al., 1979, C. R. Acad. Sci. Paris, 288 D, 823 - 825.

Froelich et al., 1984, Est. Coast. Shelf Sci., 20, 239 - 264.

Gayral et Fresnel, 1979, Protistologica, T. XV, fasc. 2, 271 -282.

Glibert, 1982, Mar. Biol. 70, 209.

Glibert, et al. , 1982, Limnol. Oceanogr. 27, 639.

Goeyens et al. , 1985, Analyst 110, 135.

Goffart and Hecq, 1987, in: Proc. Belg. Natl. Colloq. on Antarctic Research, Oct. 20, 147 - 166.

Gooday and Nott, 1982, J. Mar. Biol. Ass. U.K.,62, 595 - 665.

Grasshoff, 1969, Advances in Automated Analysis, Technicon International Symposium, Chicago, 133.

Grasshoff and Johannsen, 1972, J. Cons. Int. Exlor. Mer 34, 516.

Harisson, 1978, Limnol. Oceanogr. 23, 684.

Harrison, 1983, in: 'Nitrogen in the Marine Environment', eds Carpenter and Capone, 763.

Hoenig et al., 1986, J. Anal. At. Spectrom., 1, 449 - 452.

Hui-Ming and Yao-Han, 1984, Spectrochim. Acta, 39B, 493 - 499.

Kumazawa, 1973, Jasco Report.

Le Jehan and Tréguer, 1983, in: Antarctic Nutrient Cycles and Food Webs, eds. W.R. Siegfried et al., Springer-Verlag, Berlin, 22 - 29.

Mauras and Allain, 1979, Anal. Chim. Acta, 110, 271 - 277.

Nees et al., 1962, Limnol. Oceanogr. 7, 163.

Ostlund et al., 1987, GEOSECS Atlantic, Pacific and Indian Ocean Expeditions, Shore Based Data and Graphics, Vol. 7, National Science Foundation, Washington D.C..

Paasche and Kristiansen, 1982, Mar. Biol. 69, 55.

Poisson et al., 1985, in: Les rapports des campagnes à la mer à bord du "Marion Dufresne" MD 43/INDIGO 1, N° 85-06, 267 pp.

Peng and Broecker, 1987, Global Biogeochem. Cycles, 1, 155 - 161.

Redfield et al., 1963, in: The Sea, vol. 2, ed. M.N. Hill, Interscience, N.Y., 26 - 77.

Rhein et al., 1987, Deep-Sea Res.., 34, 1541 - 1559.

Selmer and Sörensson, 1986, Appl. Environ. Microbiol. 52, 577.

Schmitz, 1987, Paleooceanogr. 2, 63 - 77.

Slawyk, 1971, Sur l' utilisation de l' isotope ^{15}N pour la mesure de l' assimilation de l' azote nitrique par le phytoplankton marin, Ph. D. Thesis, Université d'Aix-Marseille.

Strickland and Parsons, 1968, A Practical Handbook of Seawater Analysis, Fish. Res. Board of Canada, Ottawa.

Stroobants, 1988, Biogeen bariet in de suspensiestof van de Zuidelijke Oceaan, Licentieverhandeling, Vrije Universiteit Brussel, 66 pp.

Suzuki et al., 1981, Anal. Chem., 53, 1796 - 1798.

Takahashi et al., 1985, J. Geophys. Res., 90, 6907 - 6924.

Tendal, 1972, A monograph of the Xenophyophora (Rhizopoda, Protozoa), Galathea Report, 12, 7.

Till, 1974, Statistical methods for the earth scientist, an introduction, MacMillan Press Ltd.

Tréguer and Le Corre, 1975, in 'Manuel d' analyse des sels nutritifs dans l' eau de mer', Université de Bretagne Occidentale, Brest, France.

Van Put, 1987, Gedrag van suspensiepartikels in estuaria, Werkverslag le doctoraatsjaar, Universitaire Instelling Antwerpen, 62 pp.

Wefer et al., 1982, Nature, 299, 145 - 147.

Whithworth III and Nowlin jr., 1987, J. Geophys. Res., 92, 6462 - 6475.

Wood et al. ,1967, J. Mar. Biol. Ass. U. K., 47, 23.

SCIENCE POLICY OFFICE
Research contract
nr ANTAR/09

REFLECTION SEISMIC INVESTIGATIONS IN THE WEDDELL SEA AND ALONG THE ANTARCTIC PENINSULA

J.P. Henriet(*), H. Miller(+), R. Meissner(o), A. Moons(*), D. Huws(*), W. Jokat(+), N. Kaul(+), E. Van Heuverswyn(*) and W. Versteeg(*)

(*)RENARD CENTRE OF MARINE GEOLOGY
RIJKSUNIVERSITEIT GENT
KRIJGSLAAN 281
B-9000 GENT (BELGIUM)

(+)ALFRED WEGENER INSTITUT FUR POLAR- UND MEERESFORSCHUNG
COLUMBUSSTRASSE
D-2850 BREMERHAVEN (F.R.G.)

(o)INSTITUT FUR GEOPHYSIK
CHRISTIAN ALBRECHTS UNIVERSITAT ZU KIEL
OLSHAUSENSTRASSE 40
D-2300 KIEL (F.R.G.)

BELGIAN SCIENTIFIC RESEARCH PROGRAMME ON ANTARCTICA
SCIENTIFIC RESULTS OF PHASE ONE
(OCT 85 - JAN 89)
VOLUME II, PART B:
MARINE GEOPHYSICS

Reflection seismic investigations in the Weddell Sea and along the Antarctic Peninsula

Abstract

Within the framework of the first phase of the Belgian Antarctic Research Programme (1986-1988), the Renard Centre of Marine Geology (RCMG) at the State University of Ghent has participated in two cruises organized by the Alfred-Wegener-Institut für Polar- und Meeresforschung (Bremerhaven).

Both cruises addressed different marine geological domains: the passive margin of the eastern Weddell Sea (cruise Antarktis V/4) and the active western margin of the Antarctic Peninsula (cruise Antarktis VI/2).

In the Weddell Sea some 2650 km of high-resolution reflection seismic profiles have been shot, partly in connection with the drilling operations of ODP Leg 113 off Cape Norvegia. This site has been used as a stratotype for an integrated seismic-stratigraphic reassessment of the Weddell Sea Basin, a joint venture of German, Norwegian and Belgian research teams. The study off Cape Norvegia also allowed to propose a new tectonic model for the origin of the Explora-Andenes Escarpment and the associated outer high.

Another study region in the eastern Weddell sea was the distal part of Crary Fan, off Halley Bay. The very high resolution achieved there over the fan units allowed a detailed analysis of sediment deformations and mass transport. Large unconformities, calibrated by tentative long-range correlations to ODP Site 693, might yield some clues about the paleoceanography of the Mesozoic and Cenozoic South Atlantic domain. They seem to support the hypothesis of a Late Mesozoic Transantarctic initiation of an early Antarctic Circumpolar Current. Cenozoic unconformities are well controlled by paleoclimatic factors.

The Antarctic Peninsula survey involved the recording of some 1800 km of reflection data with larger penetration, both in Bransfield Strait and along the Bellingshausen margin. The reassessment of the seafloor magnetic anomalies helped to constrain the seismic-stratigraphic analysis and also yielded some new insight in the local dynamics of spreading and subduction, e.g. suggesting phenomena like a slab pull induced spreading accelleration preceding ridge-trench collision. The seismic-stratigraphic interpretation of the oceanic sediments is in good agreement with the results found at DSDP well 325 and with those proposed by Japanese studies further to the west.

Seismic profiles across Anvers and Hero Fracture Zones illustrate different aspects of thermal plate contraction, including thermal bending and magmatic diapirism. The seismic evidence that the submarine ridge of Hero F.Z. might be a diapiric serpentinite body, similar to the situation at Vema F.Z. in the central Atlantic, has several implications for the segmentation of the western margin of the Antarctic Peninsula. One new aspect about this segmentation confirmed by the present study is the presence of a fore-arc basin on the shelf south of Hero F.Z..

Contents

Part 2 : the Antarctic Peninsula

Acknowledgements

It is a particular pleasure to acknowledge with sincere thanks the active and efficient support of the Science Policy Office throughout the different phases of this Antarctic Research Programme. We are also most grateful to the Alfred-Wegener-Institut für Polar- und Meeresforschung for the open spirit of international cooperation and for the hospitality enjoyed on two cruises on board of R.V. "Polarstern". Part of the study on the ODP Site 693 has also been supported by the Belgian National Fund for Scientific Research.

The pleasant cooperation with the Geophysical Institute of Kiel University is also gratefully acknowledged. We are further indebted to Prof. Dr. K. Hinz and Prof. Dr. Y. Kristoffersen for constructive comments.

The merits of this study are shared by many partners in this research. Possible errors in this report, a normal ingredient of any learning process, are the sole responsibility of the undersigned.

Ghent, December 1988

Jean-Pierre Henriet

Introduction

Within the framework of the first phase of the Belgian Antarctic Research Programme (1986-1988), the Seismostratigraphy Unit of the Renard Centre of Marine Geology (RCMG) at the State University of Ghent participated in two cruises organized by the Alfred-Wegener-Institut für Polar- und Meeresforschung (Bremerhaven) : the Antarktis V/4 cruise (December 1986 - March 1987) in the Weddell Sea and the Antarktis VI/2 cruise (October - December 1987) along the western margin of the Antarctic Peninsula (fig. 2). The latter study was jointly promoted by the AWI and the Geophysical Institute of the University of Kiel.

Both the data acquisition and the interpretation of the data carried out in a cooperative effort yield fresh insights in the geological evolution of the Antarctic margins in the Southern Atlantic domain. These insights have been acquired by carefully blending seismic stratigraphic interpretations with the analysis of related geophysical, sedimentological, paleoceanographic and paleoclimatic data. Preliminary results of this joint study are presented in this report.

Part 1 : the Weddell Sea

1.1 Research objectives

A basic objective of the marine geophysical research effort in the Weddell Sea within the framework of the Belgian Research Programme on Antarctica is to carry out high-resolution reflection seismic investigations, which possibly could yield a better insight in the structure and history of this important sedimentary basin. A particular attention is hereby paid to the identification of paleoceanographic and paleoclimatological signals locked in the sedimentary record of the Antarctic continental margins, both in the fine-scale stratigraphy of the depositional sequences and in the patterns of sediment erosion and deformation.

These objectives could be achieved through a collaboration of the Renard Centre of Marine Geology (RCMG) with the Alfred-Wegener-Institut für Polar- und Meeresforschung (AWI) in Bremerhaven. A joint survey was carried out on board of R.V. "Polarstern" from December 1986 to March 1987 along the eastern margin of the Weddell Sea (fig.1). This survey coincided with the drilling operations of "Joides Resolution" in the Weddell Sea in the framework of Leg 113 of the "Ocean Drilling Program" (ODP). "Polarstern" hence was the first vessel to shoot high-resolution reflection seismic profiles over boreholes 692 and 693, immediately after their completion. The

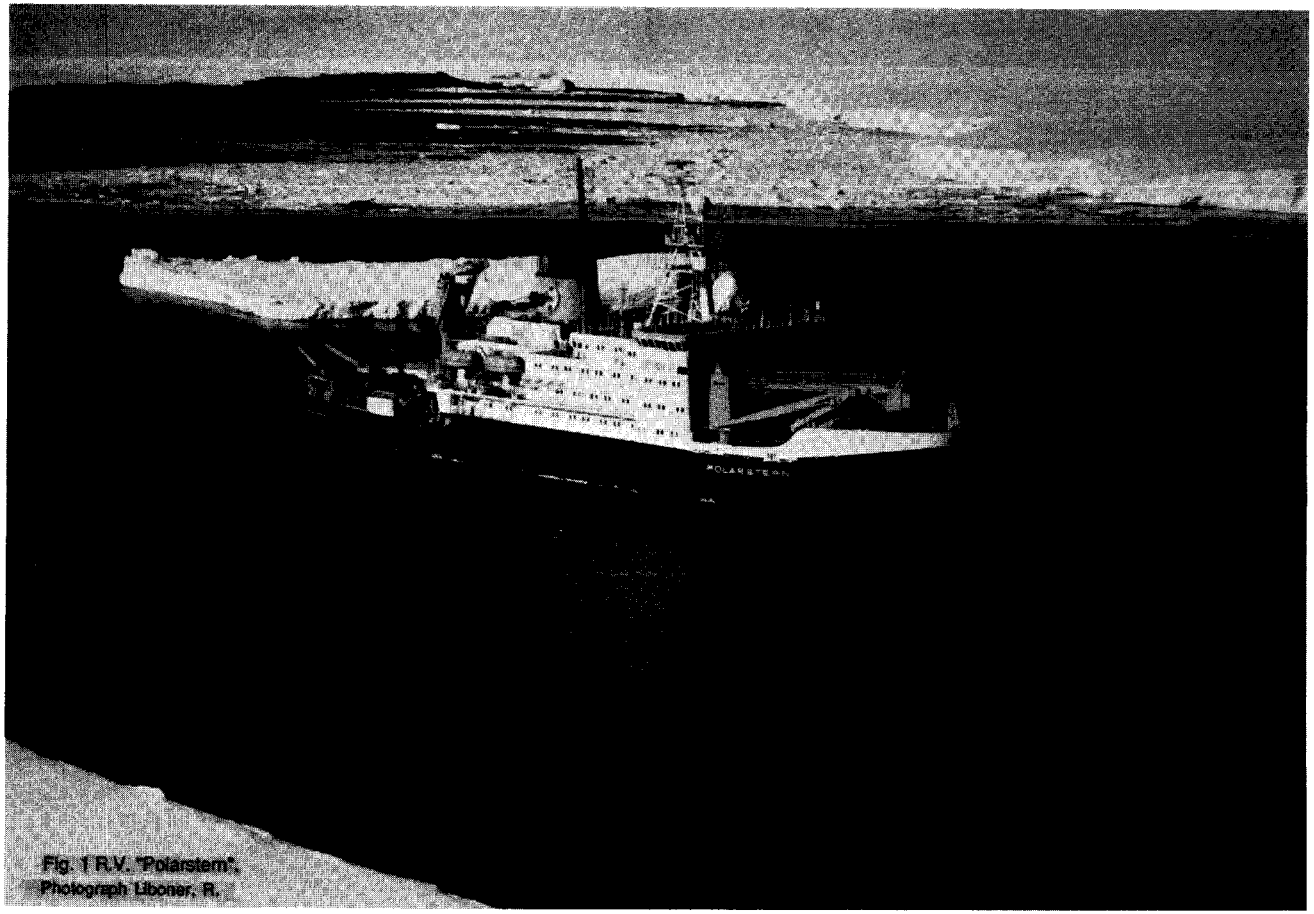

Fig. 1 R.V. "Polarstern".
Photograph Liboner, R.

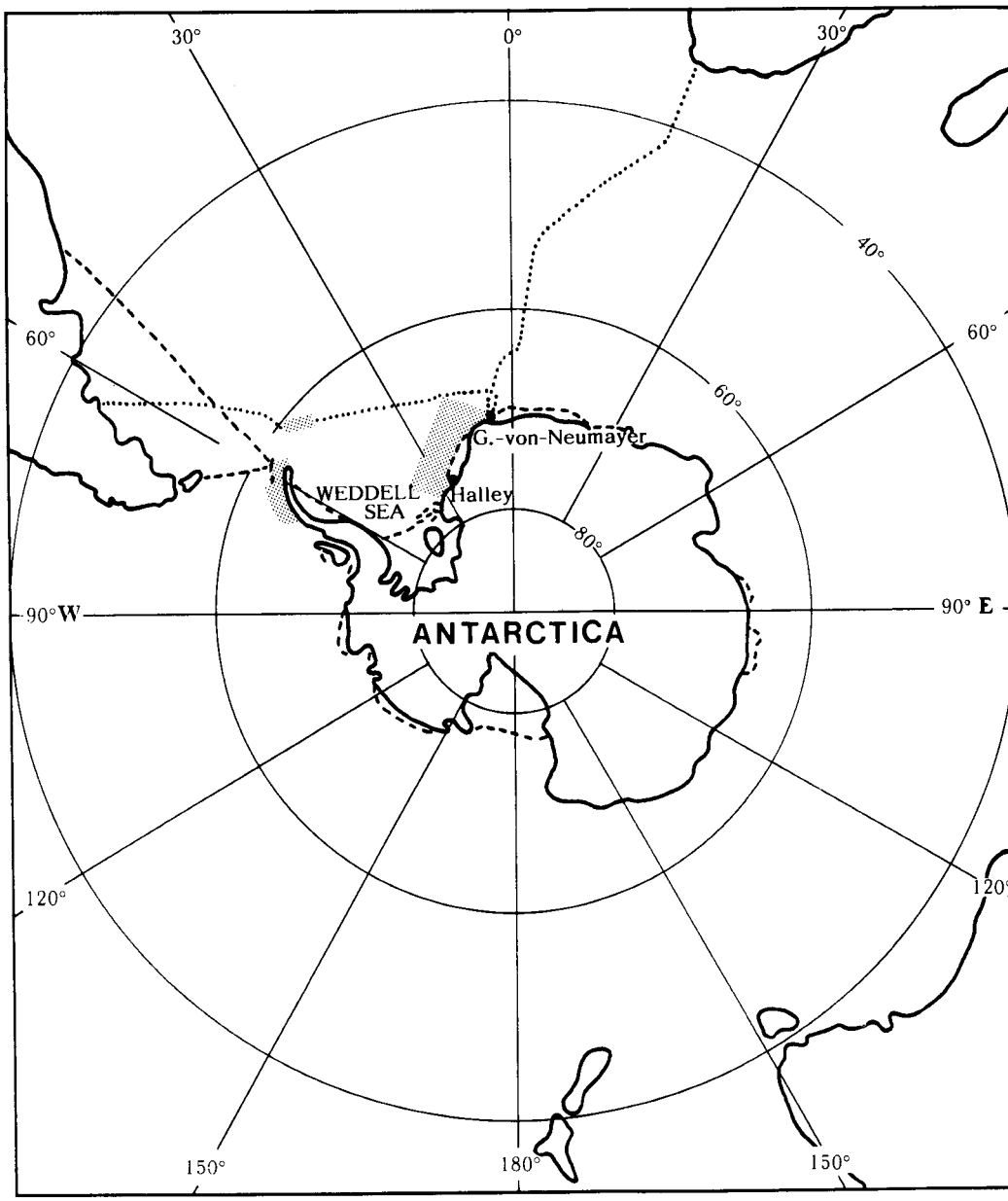

Fig. 2 Survey area during the Antarktis V/4 and VI/2 cruises

integration of the seismic and borehole data does not only prove a valuable asset for the valorization of the seismic results, but also significantly broadens the output of the ODP operations in this basin.

Some preliminary results of this joint research have been presented at the National Colloquy on the Belgian Scientific Research Programme in Antarctica in Brussels (Miller e.a. 1988) and at the NATO Advanced Research Workshop "Geologic History of the Polar Oceans : Arctic versus Antarctic" in Bremen (Miller e.a. 1989 and Henriet e.a. 1989). A number of data and figures in this report have been borrowed from the above mentioned publications.

1.2 Previous research

The geological and geophysical reconnaissance of the continental margins of the Weddell Sea has steadily progressed in the past ten years. A review of multichannel seismic investigations hitherto carried out in the Weddell Sea basin is presented in Table 1.

Year	Institution	Country	Vessel	Profile length
1977	Bergen University	Norway	Polarsirkel	1000 km
1978	Bundesanst. Geow. Rohst.	Germany	Explora	5850 km
1978	Lamont-Doherty Geol. Obs.	U.S.A.		
1979	Bergen University	Norway	Polarsirkel	1010 km
1983	Nat. Oil Corporation	Japan	Hakurei-Maru	1500 km
1985	Bergen University	Norway	Andenes	2600 km
1986	Bundesanst. Geow. Rohst.	Germany	Polarstern	6260 km
1987	Alfr. Weg. Inst., RCMG	Germany, Belgium	Polarstern	2850 km

Table 1: multichannel seismic investigations in the Weddell Sea (after Hinz e.a. 1987 and Fütterer 1988)

Only few of these surveys could penetrate into the southwestern part of the Weddell Sea, where severe ice conditions prevail throughout the seasons. Only a few isolated profiles have been recorded there by Bergen University (1977), Soviet scientists (1982) and BGR (1986), in front of the Ronne and Filchner ice shelves. In contrast, the eastern and southeastern margins of the Weddell Sea are now relatively well documented. A map of the seismic tracks recorded with German and Norwegian vessels in this region is shown on fig. 3.

A first coherent geological picture of the eastern margin of the Weddell Sea resulted from the extensive surveys of BGR, partly carried out as a reconnaissance for ODP Leg 113. The 1978 survey shed light on a remarkable wedge-like structure with seaward dipping reflectors : the "Explora Wedge". By analogy with similar wedge-like structures identified in drillholes of Leg 104 on the Voring Plateau in the Norwegian Sea, these dipping layers are considered to be of

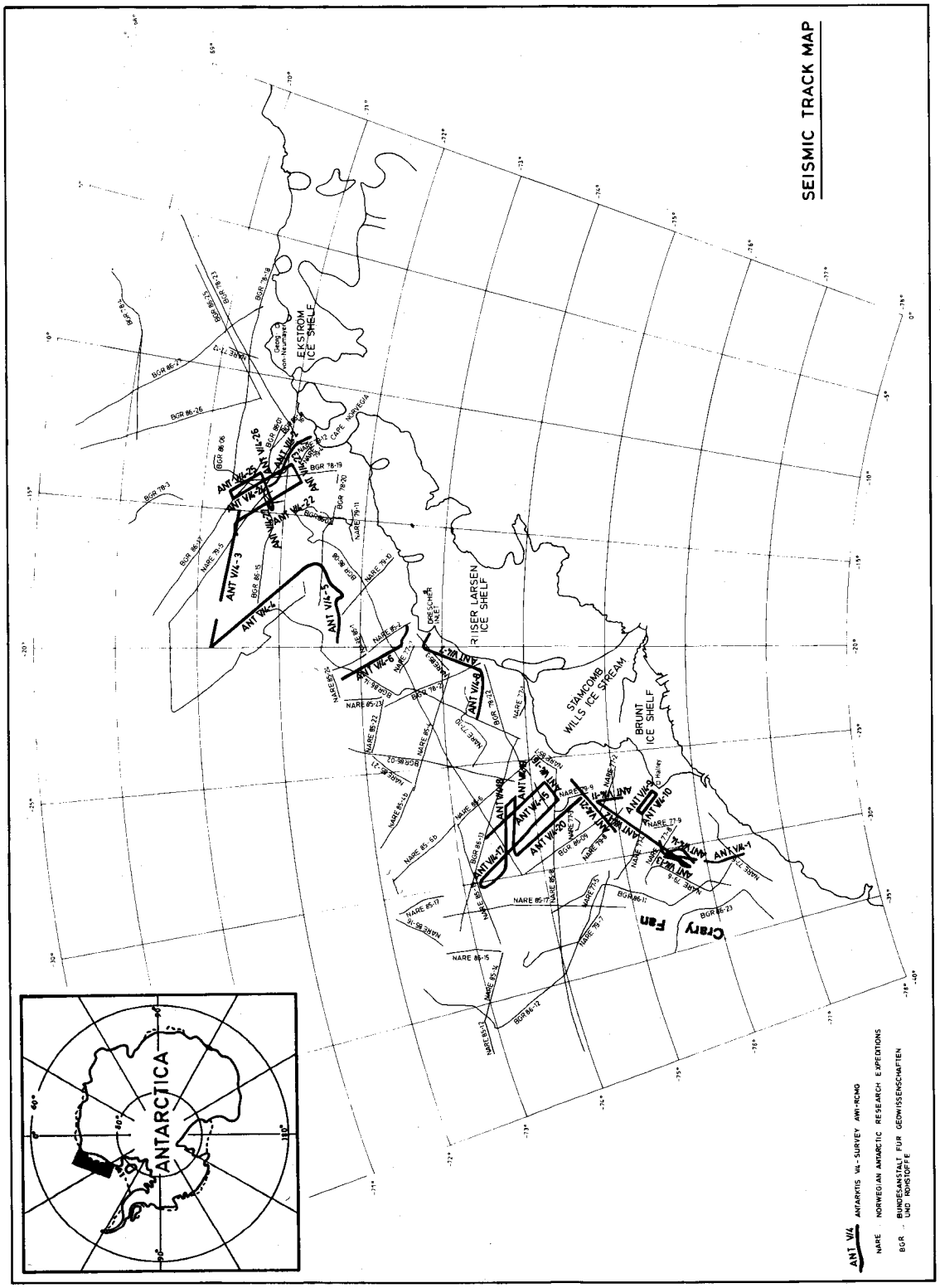

Fig. 3 Seismic track map of the Antarktis V/4 cruise and of former seismic investigations in the eastern Weddell Sea.

volcanic origin. Off the northeastern part of the Weddell Sea margin, the lower continental slope at depths of 1500 to 3000 m was found to be abruptly bounded by a steep escarpment, leading to the continental rise at depths over 4000 m. This scarp, named the "Explora Escarpment" (Hinz and Krause 1982), could later be traced further south by the Norwegian scientists in 1985 and was consequently named the "Explora-Andenes Escarpment".

The 1986 survey of BGR led to the discovery of a conjugate set of dipping reflectors further south. Both sets frame a central basin with oceanic crust, identified as a failed rift-drift basin (Hinz and Kristoffersen 1987). This basin, probably an early witness of the fragmentation of Gondwanaland, is obliquely transsected by the Explora-Andenes Escarpment, which is probably the surface morphological expression of a large transcurrent fault.

The seismic stratigraphy of the sedimentary cover in the Weddell Sea Basin was first approached by Hinz and Krause (1982), Haugland, Kristoffersen and Velde (1985) and Hinz and Kristoffersen (1987).

Hinz and Krause (1982) identified two major units, separated by the distinct "Weddell Sea continental margin unconformity" ("U9"). The upper, tectonically undisturbed unit could be subdivided into four depositional sequences. The lower unit consisted of the volcanic Explora Wedge sequence. Circum-Antarctic correlations between the Weddell Sea unconformities and some major ones identified in the Ross Sea, off Terre Adélie and in the Tasman Sea have been proposed by Hinz and Block (1984) and Hinz and Kristoffersen (1987).

Haugland, Kristoffersen and Velde (1985) mainly documented the seismic stratigraphy of the Crary Fan, a large submarine fan complex in the southeastern Weddell Sea off Filchner and Ross ice shelves, and proposed a tentative correlation with fan sequences in the Eastern Basin of Ross Sea.

All time connotations of the seismic stratigraphic interpretations in the Weddell Sea however remained highly speculative until the ODP wells of Leg 113 had provided the first ground truth.

1.3 Methods

13.1 High-resolution reflection seismic data acquisition

The seismic tracks surveyed by AWI and RCMG during the Antarktis V/4 cruise (1986-1987) are shown on fig. 3.

Out of the 27 profiles recorded in the Weddell Sea Basin, 21 have been shot with an array of PRAKLA-SEISMOS airguns with volumes of 0.5 l, 2.5 l and 5 l, totalizing a capacity generally not exceeding 10 l. The guns were powered by 6 JUNKERS type 4FK 115 compressors, delivering each 2 cubic metres per minute of air compressed at 14 MPa (140 bars). With this source

configuration, data of excellent definition have been recorded down to two thousand metres below the sea-floor.

In the shallower shelf zone off Halley Bay and on ODP Site 693, 7 profiles have been shot with high-resolution sources such as a 12-electrode sparker fired at 4.5 kJ or a SODERA S-15 watergun, with a volume of 0.25 l. On Site 693 in water depths of about 2400 m, the watergun yielded a resolution better than 5 m over the whole depth of drilling (some 500 m).

Most data have been recorded with a PRAKLA-SEISMOS streamer with an active length of 600 m and 96 hydrophone groups, clustered into a 24-channel configuration. Some shallow shelf profiles shot in difficult ice conditions have been recorded with an 8-channel TELEDYNE streamer with an active length of 100 m. The digital data acquisition system consisted of an EG&G GEOMETRICS ES 2420 seismograph with data storage on two CIPHER tape drives. Analog monitor records of excellent quality and different scale have been obtained on two EPC recorders after adequate bandpass filtering and time variant gain amplification.

13.2 Reflection data processing

Due to the limited computer capacity presently available at RCMG, the bulk of the processing of the more than thousand magnetic tapes of the Weddell Sea survey is being carried out on the CONVEX computer with DISCO seismic software at AWI in Bremerhaven. Examples of stacked sections are shown on figs. 10 and 12.

13.3 Reflection data interpretation

133.1 Profile interpretation and display

A large part of the interpretation has been carried out on the analog monitor records, in parallel with the digital data processing. This was not only a matter of time gain, but also a question of resolution, as very fine structures are usually better preserved on the single channel analog records than on stacked sections. Several examples of analog reflection records are shown on figs. 9, 15, 19, 20, 21, 22, 23 and 26.

Significant reflectors identified on the sections have been digitized and introduced into RCMG's seismic databank "NORFILE", which performs the transformation of the variable horizontal scale into a linear one in function of the true coordinates recorded on fix points, as well as the conversion of two-way reflection time into depth, in accordance with a selected velocity model. Other routines in NORFILE are used for preparing track maps in different scales and projections, posted depth maps, contoured maps (isobath and isopach maps) and three-dimensional representations.

133.2 Seismic-stratigraphic analysis

The early analysis of the seismic stratigraphy of the eastern Weddell Sea by the BGR has led to the identification of a number of major breaks in the sedimentary record, labeled U9, U7, U6, U5, U3 and U2 (Hinz e.a. 1987). This subdivision is inherent to a model of the evolution of the oceans of the Earth, where the major unconformities are interpreted in terms of geodynamic, oceanologic or climatologic events of global relevance. Such an approach proved its value in the earliest attempts to fit the emerging geological picture of the Antarctic continental margins into a global context and to orient further exploration, in particular in the framework of the Ocean Drilling Program.

However, as exploration progresses and more factual evidence about the age of local unconformities becomes available, this approach with a time-bound terminology proves inconvenient. Any reassessment of the age of an unconformity compells to change its name on profiles and maps, which may lead to confusion in literature. In order to avoid this problem, four seismic research teams[1] meeting at the Bremen Workshop in 1988 decided to strive for a common, horizon- and sequence-bound seismic-stratigraphic nomenclature for the Weddell Sea.

In this approach, profile ANT V/4-22 which passes over ODP Site 693 is used as a seismic-stratigraphic stratotype section, on which a basic series of depositional sequences are identified and named. The capital character *W* followed by a rank digit is assigned both to a major depositional sequence and to its basal unconformity identified on the stratotype section[2]. The rank of the digits increases from lower (older) units to higher (younger) units, as in standard stratigraphic practice. Further subdivisions of sequences as a consequence of the introduction of an increased resolution can be accommodated by adding more digits behind the main label, separating them from it by a decimal point (e.g. *W* 1.1, *W* 1.2, *W* 11.1, etc.).

It should be mentioned that the concept of depositional sequence is used here in its original seismic stratigraphic definition, being *any* "stratigraphic unit composed of a relatively conformable succession of genetically related strata, bounded at its top and base by unconformities or their correlative conformities" (Mitchum, Vail and Thompson III 1977). The term "unconformity" in this definition is taken in its broadest sense, encompassing both subaerial and submarine surfaces of erosion or nondeposition. In the more recent sequence stratigraphic approach (Vail e.a. 1987), the term "sequence" is used in a more restrictive sense. A sequence in this definition is bound by "unconformities" which are surfaces marked by subaerial exposure on their landward portions. A sequence is then the highest order unit, grouping all "systems tracts" associated with one major relative sea level movement. Systems tracts (sensu Brown and Fisher 1977) are linked and contemporaneous depositional systems which are also usually

---

[1] The Alfred-Wegener Institut für Polar- und Meeresforschung (Bremerhaven), the Bundesanstalt für Geowissenschaften und Rohstoffe (Hannover), the University of Bergen (Norway) and the Renard Centre of Marine Geology of the State University of Ghent (Belgium)

[2] only the sequence symbol is noted in italic characters

intergradational (for example linked fluvial, delta, shelf and slope systems). Systems tracts take a well defined position within the sequence and are characterized by the stacking pattern of "parasequence sets" and "parasequences", the fundamental building blocks of sequences.

The sequence stratigraphic approach being much more interpretative is difficult to apply at the level of basin reconnaissance, which still is the status of the Weddell Sea investigation. At the present level of analysis, the main objective is the unifying use of a common and unbiased communication tool between the cooperating teams. Once all stratigraphic units are adequately analysed both in their areal extent and their genetic context, a possible move towards a sequence stratigraphic approach can be envisaged.

Coming back to the naming procedure here adopted for sequences and bounding unconformities, it should be noted that a problem arises in using the same symbol for a sequence and its basal unconformity when it turns out that different depositional sequences lap out on the same basal surface. The approach initially proposed in the agreement between the four aforecited teams and outlined in the paper presented at the Bremen workshop (Miller e.a. 1989) was to keep unaltered the name of the basal unconformity which has been defined on the stratotype section, as this might facilitate long-range correlations along the continental margin (e.g. here with W1 and W4, which seem to be tracable over the larger part of the continental margin). However, there are some strong arguments in favour of assigning a separate symbol (differing from that of any depositional sequence) to such complex onlap surfaces. One argument is the presently emerging evidence of the presence of additional major onlap surfaces, which is the result of the ongoing joint reassessment of former interpretations (e.g. of BGR lines BGR 86-08 and BGR 86-13, courtesy K. Hinz). Such complex onlap surfaces will consequently be referred to in this paper with the symbol WO (Weddell Sea Onlap Surface), which is a higher level symbol : a complex onlap surface will catenate the basal reflectors of successive onlapping depositional sequences, as illustrated on fig. 4.

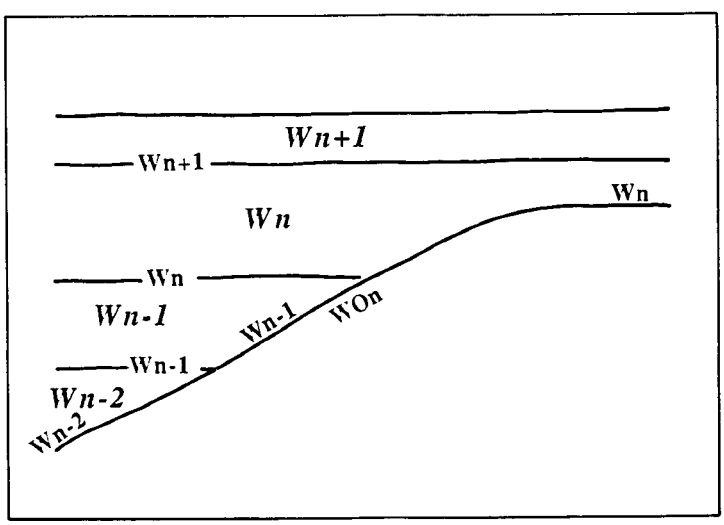

Fig. 4 Seismic stratigraphic terminology in the Weddell Sea.

In order to avoid confusion with the Bremen terminology, the complex onlap surfaces coinciding on the ODP stratotype section with W1, W4 and W5 will respectively be referred to in this paper as WO1, WO4 and WO5. It should be emphasized that this approach still has to be submitted to the Weddell Sea research partners and hence is subject to possible modifications.

Sedimentary units deposited in genetically related systems which apparently bear no direct relationship with those identified on the stratotype section (e.g. the Crary Fan deposits and associated major channel fills, basin floor fans associated with canyons, etc.) can be assigned different characters. The units identified in the Crary Fan for instance have provisionally been assigned the *WF* symbol (Weddell Sea Fan), and the associated channel fill deposits the *C* symbol. These units should in a forthcoming effort be correlated with "SWS" units defined by Haugland e.a. (1985), which might lead to a revision of their name in concert with the Norwegian authors.

Correlation of seismic stratigraphic units			Site 693
this report	Hinz e.a. 1982	Hinz e.a. 1987	TWT(s) bel.sea. fl.
W 7			
- - - - W 7 -			0.05
W 6			
- - - - W 6 -	WS-1		0.23
W 5			
- - - - W 5 -			0.33
W 4			
(WO4)- W 4 - - - - - - - - - - - - - - -		U 3 - - - -	0.48
W 3	WS-2		
- - - - W 3 -			0.82
	- - - - - - - - - - - - - -	U 5[1] - - - -	0.94
W 2	WS-3B		
- - - - W 2 - - - - - - - - - - - - - - -		U 6 - - - -	1.22
W 1	WS-3A		
(WO1)- W 1 - -	"Weddell Sea cont.- - -	U 9 - - - -	1.90
	margin unconformity"		
	WS-4	"Explora Wedge"	

Table 2 : tentative correlation between seismic-stratigraphic nomenclatures for the Weddell Sea

[1] Note

There is some discrepancy between the terminology used by the Shipboard Scientific Party in the Initial Report of the Ocean Drilling Program of Leg 113 (1988) and the original terminology proposed by K. Hinz and co-authors. The latter authors have defined U6 as boundary between units WS-3A and WS-3B and U5 as boundary between WS-3B and WS-2 (cfr. fig. 3 in Hinz e.a. 1982 and fig. 28 in Hinz e.a. 1987), while the former authors refer to U6 as the boundary between WS-3B and WS-2 (e.g. p. 316 or p. 358).

Table 2 gives an overview of the sequences and unconformities discussed in this report, their present identification and their tentative correlation with former definitions found in literature, in particular the "WS" units and the bounding "U" unconformities defined by Hinz e.a. (1982) and Hinz e.a. (1987). It should be noted that this table simply technically translates the names used for seismic marker horizons on figures in both aforementioned papers into the new marker terminology : e.g. the marker labeled U6 on fig. 28 in Hinz e.a. 1987, which also forms the boundary between the WS-3A and WS-3B units on fig. 3 in Hinz e.a. 1982, now reads as W2.

In addition to the definition of depositional sequences by the analysis of the nature of their boundaries, due attention has also been paid to the diagnostic value of the internal seismic facies of the sequences, which shows to full advantage on the high-resolution profiles. These facies characteristics do reflect both the depositional and the early compaction history of the Weddell Sea sediments. The latter evolution is vividly illustrated by spectacular aspects of sediment flowage and internal slumping, which have been put into evidence in various sequences.

13.4 Refraction seismics

Very strong multiple reflections have been observed on the shelf of the southern Weddell Sea, both during the BGR survey of 1986 and the AWI-RCMG survey. Such multiples are extremely resistant to any form of processing. They argue for the presence of a shallow, hard horizon, which could be explained by two processes :

- overconsolidation of shelf sediments by glacial loading, a phenomenon well documented in the Norwegian Sea and Barents Sea (Elverhoi e.a. 1989) ;
- submarine permafrost, as reported in the Beaufort Sea, Alaska (Rogers and Morack 1983).

Considering the importance of this problem both for geophysical and geotechnical applications in polar regions, a refraction configuration consisting of a single-electrode sparker as sound source and a 16-channel streamer has been lowered and stretched on the sea bottom on two shelf sites, one in Atka Bay (near Georg von Neumayer Station) and one in heavy pack-ice south of Halley Bay. Water depth on both sites ranged between 220 and 270 m, and the water temperature measured above the sea bed was -1.9° C.

The results of Atka Bay are shown on figs. 5 (record) and 6 (interpretation). This record clearly shows a two-layer case with a 1.9 m thick top layer with a velocity of 1460 m/s above a substratum with a velocity of 2140 m/s. The velocity of the top layer is very similar to the velocity measured in water (1420 m/s with the refraction array when pulled up, 1444 m/s calculated from CTD measurements), and thus probably corresponds with water-logged unconsolidated mud. The velocity of the bottom layer, which could be well reproduced on neighbouring sites, is high. However, it does not allow for the time being to discriminate unambiguously between non-frozen coarse sediments and frozen silty clays, which display a similar range of velocities (King and Pandit 1981). Additional information will be needed in such

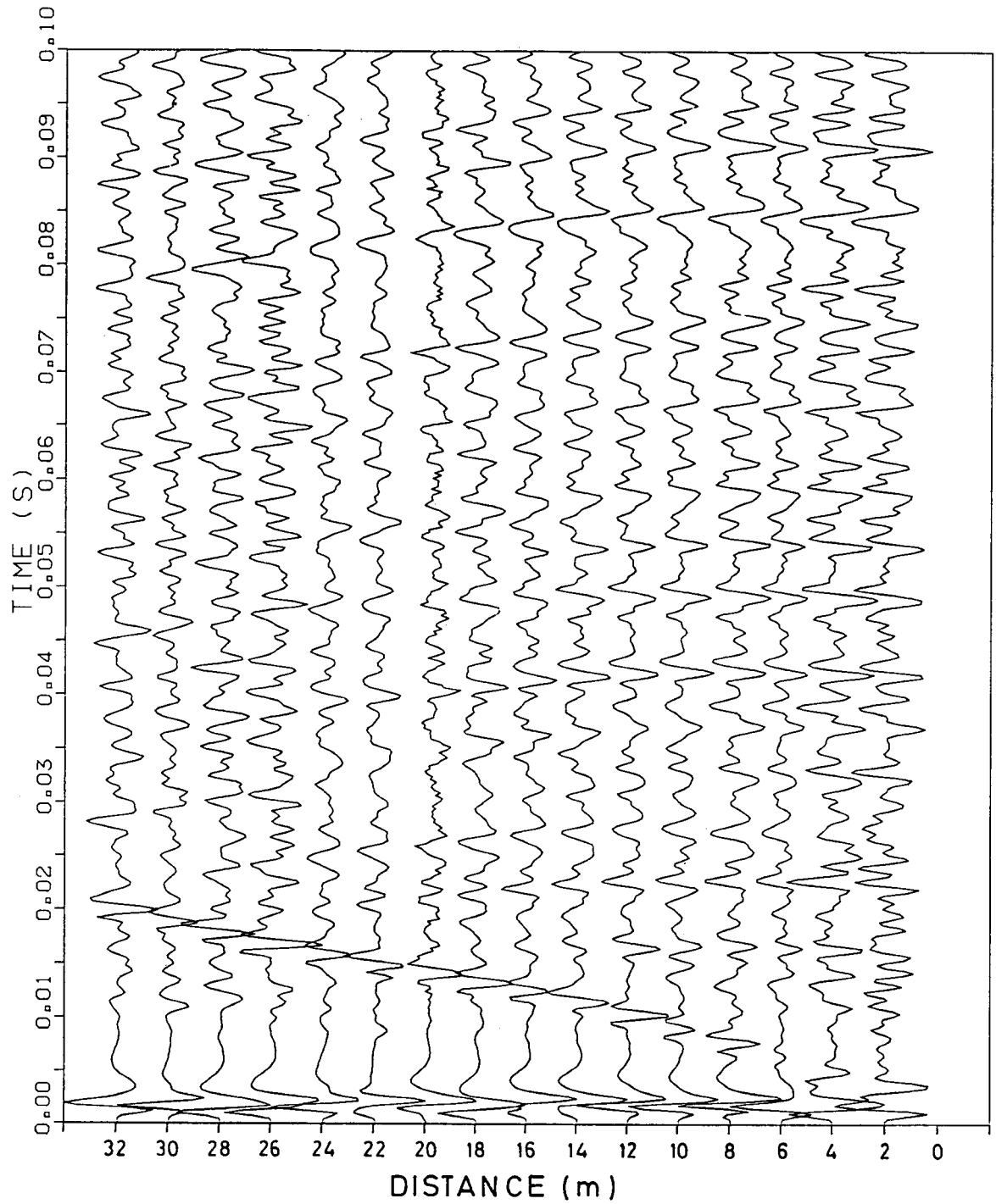

Fig. 5 Refraction record.

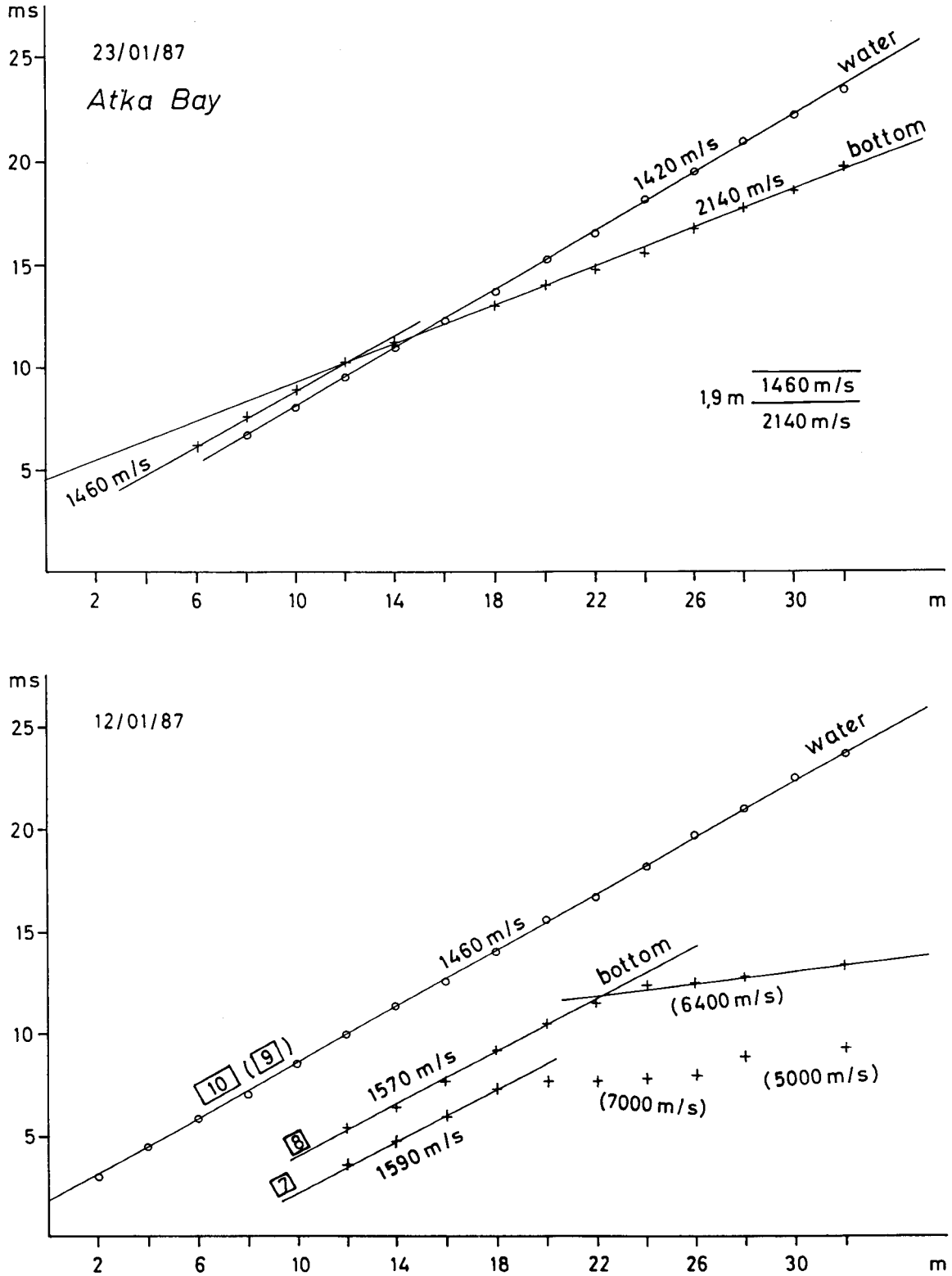

Fig. 6 Interpreted refraction profile.

an analysis. Time constraints did unfortunately not allow to multiply such experiments on a wider range of shelf sites.

1.4 Geological interpretation

Two main survey areas are discussed in this report :

a) a seismic grid shot off Cape Norvegia in the area of the ODP Sites 692 and 693, framing an important submarine canyon (Wegener Canyon) and exploring the local geological setting of the Explora Escarpment ;

b) a high-resolution seismic transect and grid covering the continental shelf, slope and rise north of Halley Bay and yielding a very fine-scale picture of the distal part of the Crary Fan deposits.

14.1 Sedimentary sequences off Cape Norvegia

141.1 Survey structure

The target area for the ODP drillholes 691 to 693 off Cape Norvegia presents a remarkable marine morphological and structural setting. The results of the seismic stratigraphic analysis and of the well control are however not less rewarding.

The survey area shows the Explora-Andenes Escarpment, bordering the lower continental slope at depths between about 2000 and 3000 m and the continental rise at a depth of more than 4000 m. This prominent structural feature is a large transcurrent fault, considered to mark the boundary between oceanic crust of not yet well defined age and subsided continental crust. It shows in the seabed morphology as a steep scarp, locally deeply incised by canyons. "Wegener Canyon", stretching between the ODP Sites 692 and 693, has been mapped in detail with "Polarstern" 's SEABEAM system (figs. 7 and 8).

A sparker line (ANT V/4-2) has been shot in the early part of the seismic survey from the shelf edge at Cape Norvegia down to the upper part of Wegener Canyon, close to the site where the "Joides Resolution" had started drilling wells 691 and 692. After all wells had been spud, "Polarstern" shot a tie line across Wegener Canyon over Sites 692 and 693 (ANT V/4-26), as well as three parallel dip lines running from the lower continental slope down to the rise, at more than 4500 m depth (ANT V/4-22, 24 and 25). The survey was completed with a short watergun profile with shallow penetration but very high resolution over Site 693 (ANT V/4-27).

An analog monitor record of profile ANT V/4-22, selected as seismic-stratigraphic stratotype section, is presented on fig. 9, while a horizontally expanded digital section is shown on fig. 10. Both figures have been annotated with the information from well 693. The results of the velocity analyses performed at BGR and AWI are also presented on fig. 10. An interpretation of line

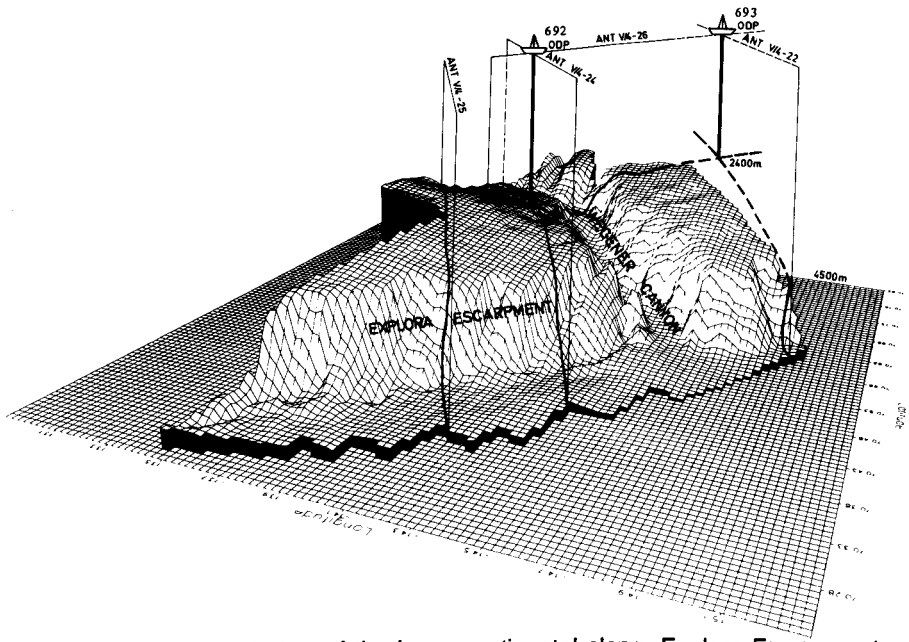

Fig. 7 Three-dimensional view of the lower continental slope, Explora Escarpment and continental rise in the region of Wegener Canyon, with localisation of the ODP sites and the seismic tying lines (SEABEAM plot, AWI).

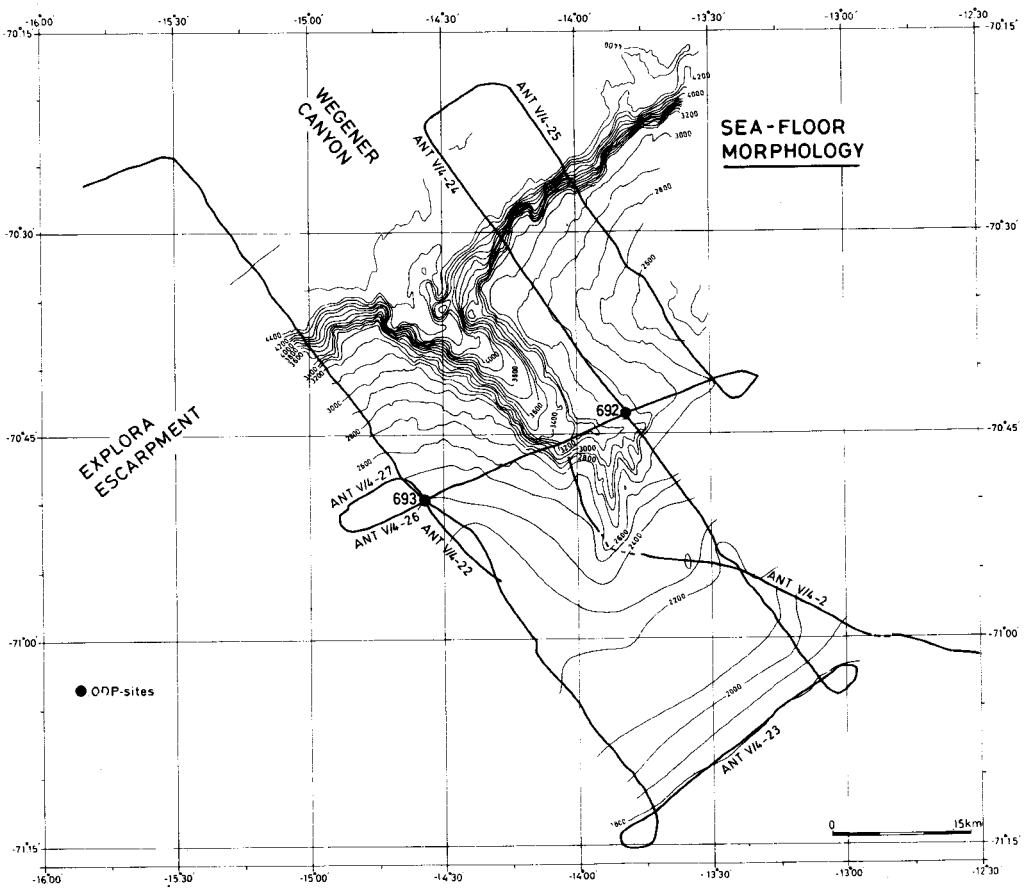

Fig. 8 Map of the seismic tracks framing Wegener Canyon.

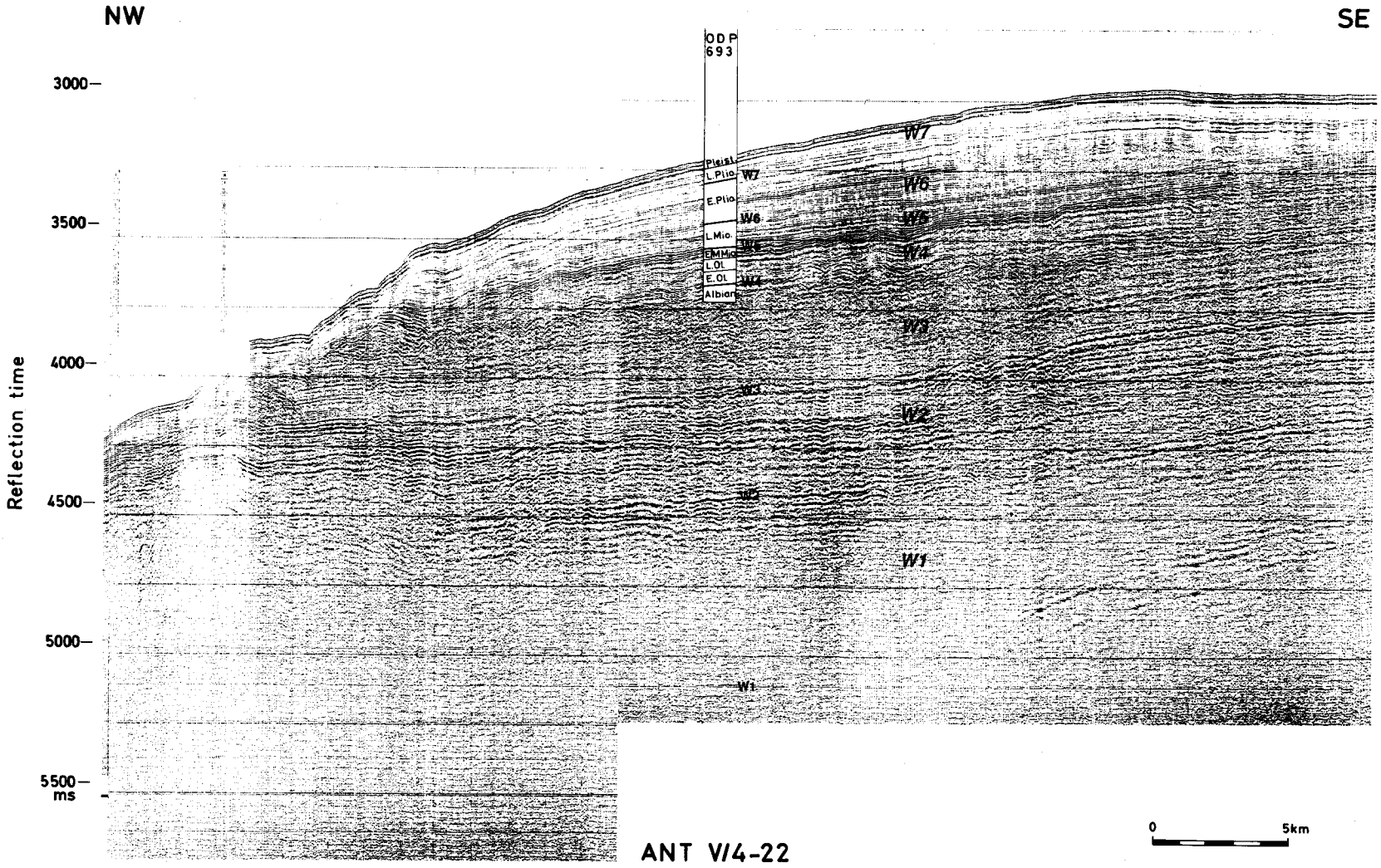

Fig. 9 Analog monitor record of the seismic stratigraphic stratotype profile (ANT V/4-22) through ODP Site 693.

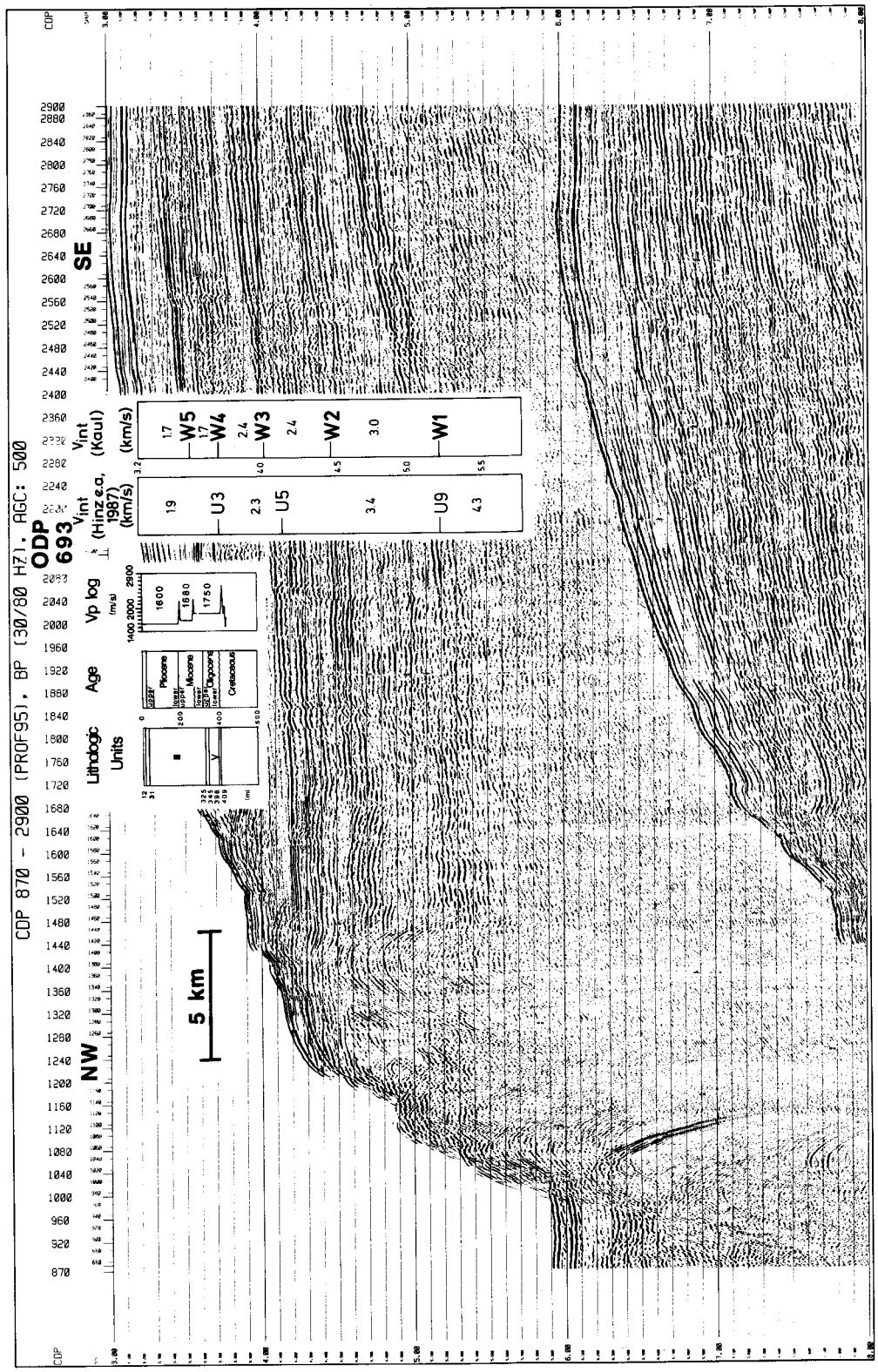

Fig.10 Processed seismic stratigraphic stratotype profile (ANT V/4-22) through ODP Site 693. Litho- and chronostratigraphic logs and velocity models.

22 with a larger vertical scale exaggeration for a better resolution of the stratigraphy of the Cenozoic cover is shown on fig. 11.

A digital profile of the tie line between both wells is shown on fig. 12. This profile bears clear evidence of a fault control of Wegener Canyon. Interpreted sections of the full set of airgun profiles in the considered area are shown on fig. 13.

141.2 Mesozoic stratotype sequences

The Mesozoic depositional sequences identified in the vicinity of Wegener Canyon are the *W1*, *W2* and *W3* sequences. The basal unconformity WO1 corresponds with the "Weddell Sea Continental Margin Unconformity" U9, postulated of Late Middle Jurassic age (Hinz and Kristoffersen 1987). WO1 is best defined on fig. 8, where the lower frequency seismic events are better preserved. The underlying diverging set of oceanward dipping reflectors of the "Explora Wedge" (unit WS-4 in Hinz and Krause 1982), of probable volcanic origin, is but faintly visible on the AWI-RCMG records, due to the limited power of the used airgun array.

Sequence *W1*, which onlaps on the basal surface WO1 in landward direction, has a thickness of about 1000 to 1200 m below Site 693 (700 ms two-way time, interval velocity 3000 to 3400 m/s). It is characterized by some low-frequency events in the basal interval ; these are less obvious on profile ANT V/4-22 but show up as a good marker horizon (W1.2) on neighbouring BGR profile 86-08. Above W1.2, there is a reflection-poor interval followed by a distinct but discontinuous reflector, which can also be traced some distance further south on BGR 86-08. Sequence *W1* can be physically correlated with sequence WS-3A defined by Hinz and Krause (1982), which was also described by those authors as a landward onlapping unit, suggesting deposition on a subsiding base (ref. : profile BGR 78-19, crossing profile ANT V/4-24).

Sequence *W2* is a stack of continuous, sub-parallel reflectors, affected by faulting in the vicinity of the "outer high", the apparently structureless wall bordering the plateau at the Explora-Andenes Escarpment. According to Hinz and Krause (1982), the boundary between WS-3A and WS-3B (here surface W2) is an erosional unconformity. Sequence *W2* is about 500 to 600 m thick below Site 693. On profiles ANT V/4-24 and 25, it wedges out in a landward diverging reflection configuration against the back of the outer high. Both the diverging pattern and the slight buckling of these layers visible on profiles 24 and 25 suggest a layer emplacement which was contemporaneous with a rotational uplift of the outer high (cfr. 142.3 and Henriet e.a. 1989). Sequence *W2* includes unit WS-3B and the basal interval of unit WS-2 (Hinz and Krause 1982), as shown on table 2.

Sequence *W3* is characterized by a sub-parallel to wavy reflection pattern with moderate coherency. As these deposits have been identified as Lower Cretaceous organic mudstones in the ODP well, shale tectonic deformations which are quite common in organic-rich shales are a possible cause of the wavy reflection pattern. The basal reflector W3 is a clearly defined erosional

Fig.11 Interpreted stratotype profile showing the detail of the Cenozoic sequences. Profile ANT V/4-22.

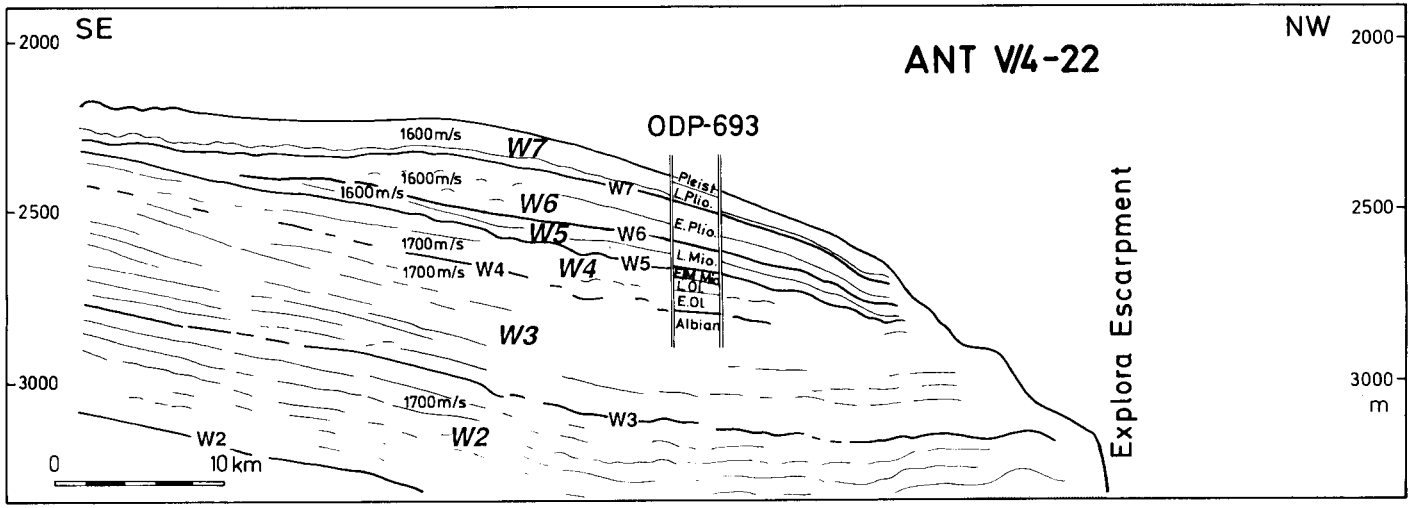

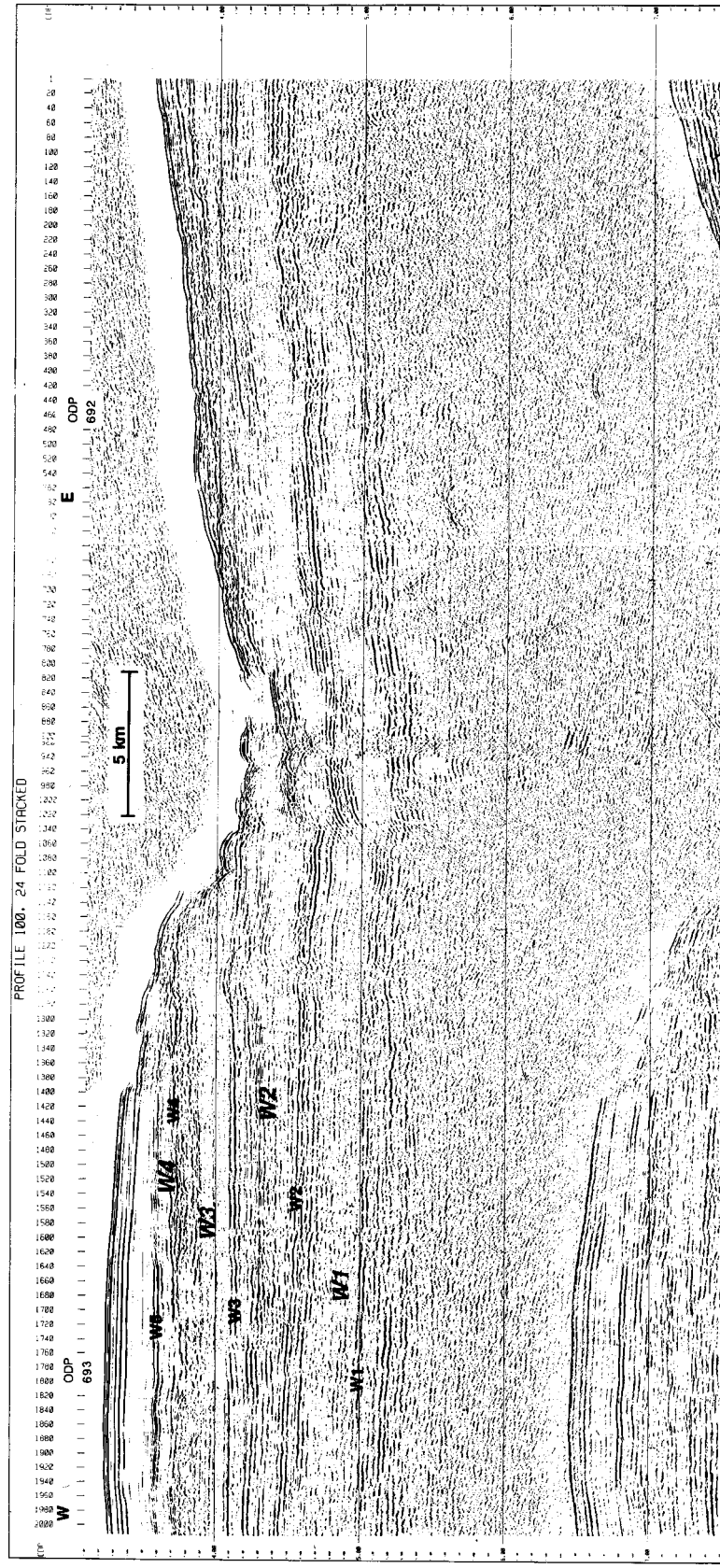

Fig. 12 Processed tying line ANT V/4-26 through ODP Sites 692 and 693.

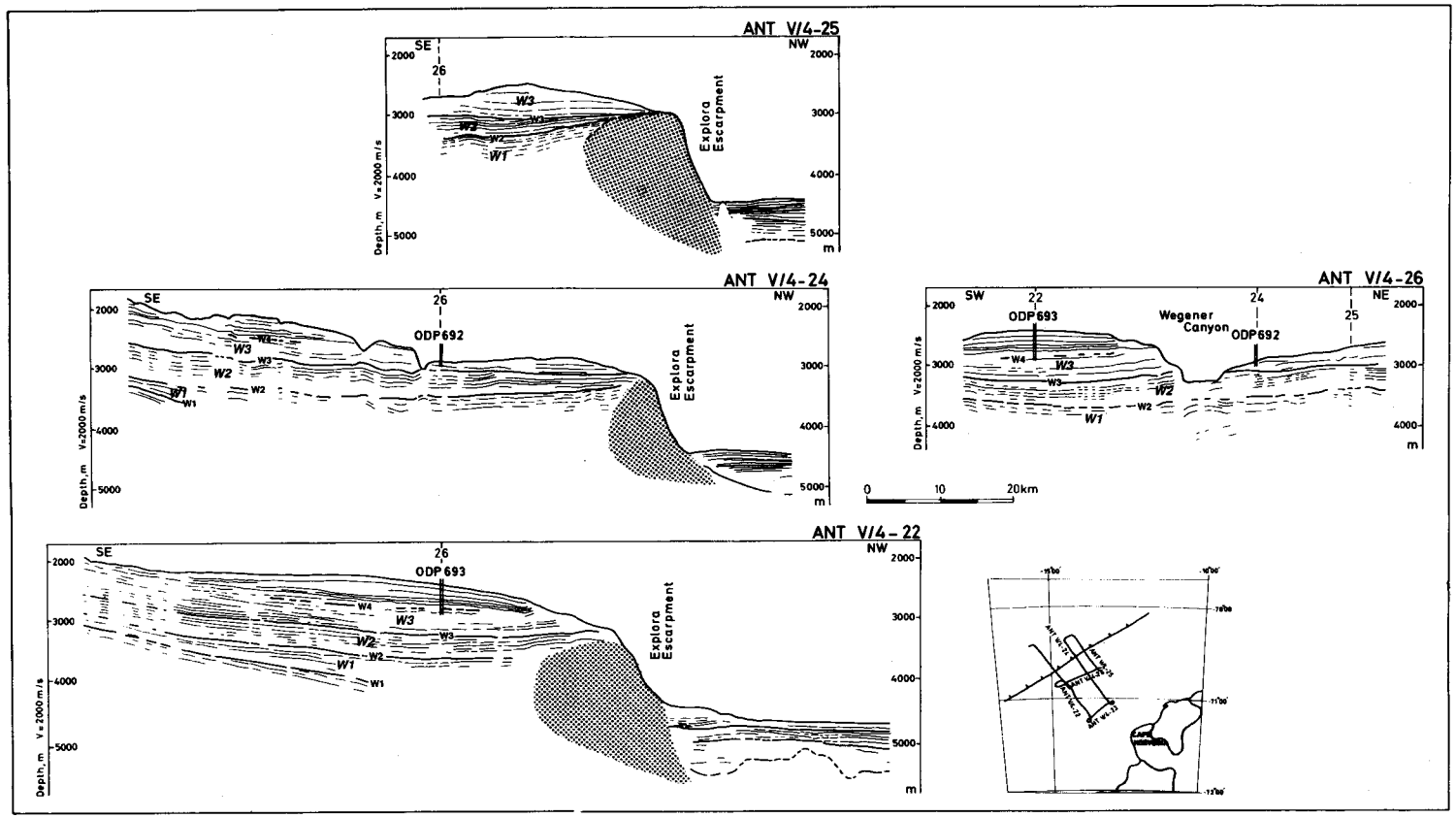

Fig. 13 Interpreted sections of the Wegener Canyon area. Profiles ANT V/4-22, 24, 25 and 26.

unconformity, truncating both the underlying *W2* sequence and the top of the outer high (profiles ANT V/4-24 and 25, fig. 8). The thickness of *W3* on Site 693 is about 400 m. It has been penetrated over a depth of 75 m in the cored section. The relative absence of continuous reflections in this sequence has also been reported by Hinz and Krause (1982), who noted only some low-amplitude sub-parallel bedding in the lower part of sequence WS-2. Sequence WS-2 should in our opinion be correlated with *W3* and the top interval of *W2*, above a prominent reflector defined as U5 by Hinz and Kristoffersen (1987) (table 2).

The top interval of *W3* was found to be of Aptian to Albian age at Site 693, while the lower interval of organic-rich claystones drilled at Site 692, about 150 m above W3, showed possible age associations ranging between upper Tithonian and late Hauterivian, depending upon the studied fossil assemblage (Shipboard Scientific Party 1988). If WO1 is indeed of late Middle Jurassic age, as proposed by Hinz and Kristoffersen (1987), this implies the presence of about 1500 to 1800 m of sediments of probably late Middle Jurassic to Upper Jurassic age below Site 693 (sequences *W2* and *W1*). Such a thickness suggests long-term average sedimentation rates of 20 to 40 m/Ma in the Jurassic and Early Cretaceous (Shipboard Scientific Party Leg 113, 1988), which are similar to the rates found for shorter intervals on the Falkland Plateau, at that time not far away. There is however evidence that larger thicknesses and additional sequences - probably also of Mesozoic age - are found in the interval between WO1 and WO4 when moving further south. Deposition apparently may have been more continuous and generous on the Weddell Sea margin than on the Falkland Plateau in Late Mesozoic times.

141.3 Cenozoic stratotype sequences

The seismic stratigraphy of the Cenozoic deposits on the stratotype section is straightforward : most stratigraphic boundaries identified in well 693 have distinct reflection responses on the high-resolution profiles.

The deposits of sequence *W4* show a characteristic draping configuration, arguing for continuing shale tectonic deformations in the underlying Lower Cretaceous after emplacement of the new sediment load. In well 693, sediments mainly consisting of nannofossil-bearing clayey mud and diatom silty to clayey mud have been assigned an Early to Late Oligocene and Early to Middle Miocene age (lithostratigraphic units IIIc, IV and V, Shipboard Scientific Party 1988). This implies that the WO4 unconformity here represents a local hiatus of about 60 Ma. The basal reflection WO4 is very weak and discontinuous, especially on the analog record (fig. 9). In fact the whole seismic facies of *W4* looks rather noisy, with many diffractions and very weakly defined subparallel discontinuous reflections. In this context it should be noted that slumping has been reported in much of the Early Oligocene sediment in hole 693B. Above a basal slumped section, some 40 m thick, there is a 5-6 Ma hiatus around the boundary between Early and Late Oligocene in the borehole log, which cannot be resolved from the basal WO4 reflection on seismic sections but

which seems possibly to correlate with a climatic signal, like the other Cenozoic unconformities (cfr. 15.3).

In contrast to the noisy facies of this sequence, the top boundary WO5 is a very strong, continuous and locally wavy reflection. This prominent reflector WO5 corresponds to another - though minor- hiatus in well 693, where most of the Middle Miocene is lacking. Directly above the hiatus is a thin nannofossil mudstone, which possibly significantly contributes to the reflection response. Horizon WO5 heralds a dramatic change in seismic facies, well visible on the high-resolution profile of fig.9. All units above WO5 display a regular and thin-bedded pattern of parallel, continuous reflections, only affected downslope by some incipient slumping phenomena. This change in seismic facies no doubt reflects the increasing role played by glacial marine sedimentation, related to the renewed cooling and major expansion of the East Antarctic ice sheet from Middle Miocene times onwards. This event is also well documented in the oxygen isotope records of benthic foraminifera in Atlantic DSDP Sites (fig. 30).

Notwithstanding the relatively homogeneous seismic facies and also lithologic composition of the deposits above WO5 (lithostratigraphic units IIIA, II and I), the very high resolution of the records allows a further seismic stratigraphic subdivision to be made : two sequences named *W5* and *W6* are truncated upslope and covered by a continuous top sequence *W7*. The boundary between *W5* and *W6* is a well defined reflector (fig. 9), possibly related to the jump in velocity observed on the P-wave velocity log at a depth of 190 m below sea floor in well 693 (from 1600 to 1680 m/s, fig. 10). Sequence *W5* would thus correlate with Late Miocene silty and clayey diatom-bearing muds, with a P-wave velocity of 1680 m/s. Sequence *W6* then corresponds with Early Pliocene deposits of similar composition, but with a velocity of 1600 m/s. Upslope the unit becomes chaotic and is truncated by W7. The passage from Early Pliocene to Late Pliocene and Pleistocene sedimentation is thus locally marked by an erosional unconformity. This observation might support the results of Ledbetter and Ciesielski (1982), who have advanced a Late Pliocene to Early Pleistocene hiatus of regional significance in the northeastern Weddell Basin. Again this unconformity clearly seems to correlate with a significant drop in the $\delta^{18}O$ record, as illustrated on fig. 30.

141.4 Continental rise deposits

The sediments at the foot of the Explora-Andenes Escarpment are characterized by cut and fill structures, as shown for instance on profile ANT V/4-4 (fig. 14). Such structures may bear witness of successive episodes of scouring and deposition of turbiditic sediments in basin floor fans, associated with the periodic activity of slope-edge canyons like Wegener Canyon. Alternatively, these structures could be explained by episodic variations in longslope currents induced by variations of bottom water flux, with an implicit climatic control.

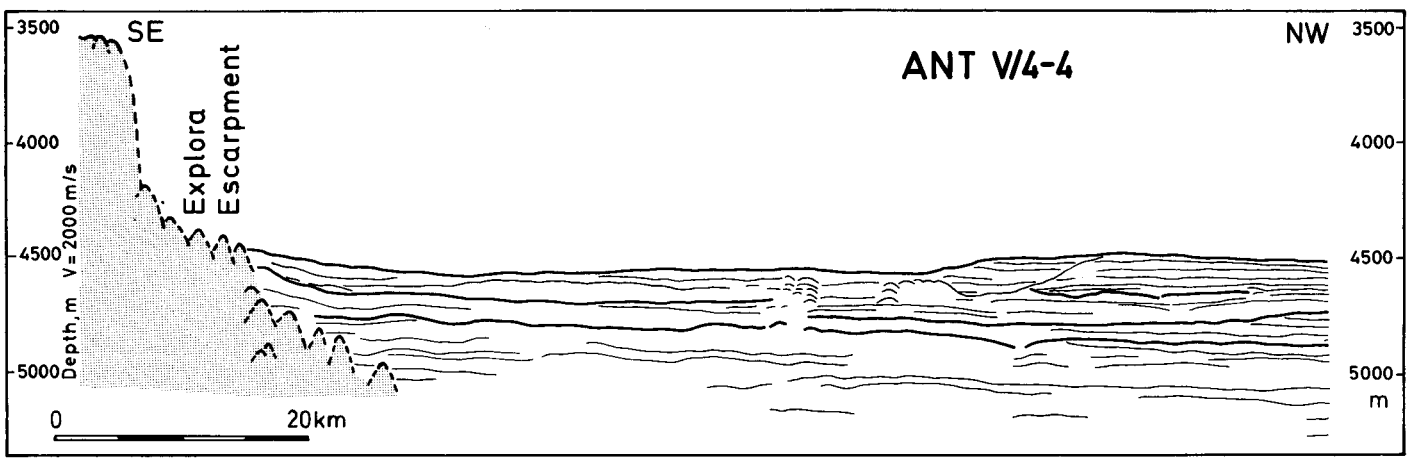

Fig. 14 Cut and fill structures at the foot of the Explora Escarpment. Profile ANT V/4-4

14.2 The nature of the Explora-Andenes Escarpment

The seismic observations made over the Explora-Andenes Escarpment during the Antarktis V/4 cruise have triggered a critical re-evaluation of existing geophysical data, which might possibly lead to some new insights in the origin of this prominent feature in the seafloor morphology of the eastern Weddell Sea.

142.1 The outer high

The apparently volcanic sequence of oceanward dipping reflectors known in the eastern Weddell Sea as the Explora Wedge abuts in oceanward direction against the so-called "outer high", a mound-like structure which is characterized on many seismic profiles by numerous diffraction hyperbolae and the virtual absence of continuous reflectors. This outer high was initially regarded as a basement high by Hinz and Krause (1982), essentially on the basis of the observation of refraction seismic velocities of 5 km/s to more than 7 km/s in their refraction profile S 22. The oceanward flank of the outer high shapes the Explora-Andenes Escarpment, which as already stated is thought of being caused by a large transcurrent fault, obliquely transecting the failed rift basin identified by K. Hinz (Hinz and Kristoffersen 1987).

The assumption of the presence of an outer high of magmatic origin which would have acted as a retaining sill for the sediments overlying the dipping reflectors of the Explora Wedge along the Dronning Maud Land margin has subsequently been taken over by the Shipboard Scientific Party of ODP Leg 113 (1988, p. 316). These authors moreover refer to such an outer high as a common feature of seaward-dipping reflector provinces (citing e.g. Roberts e.a. 1985) ; such a high would be located where oceanic basalt has erupted at shallow depth. In the model advanced by the ODP Leg 113 Scientific Party, the erosion of Wegener Canyon would have followed a two-step evolution. By the early Late Miocene or before, a gently sloping canyon floor covered by a coarse gravel lag would have developed at the level of the shoulder of ODP Site 692. Subsequently, a steep inner canyon would have formed (Site 691) and cut rapidly headward through the sediments on its landward side once the basaltic sill had been breached. This rejuvenation of the canyon probably began in the late Middle Miocene, as the East Antarctic glaciation deepened and the supply of sediment to the margin started to increase. The ODP Leg 113 Scientific Party already suggested a fault control on the location of the canyon, on basis of an offset of the oceanward scarp of the outer high. The presence of faults in the basement strata of Wegener Canyon has been confirmed by profile ANT V/4-26, tying ODP wells 692 and 693 across the canyon (fig. 12).

142.2 Some comments

A first comment to be made is that the hypothesis of a magmatic outer high bordering the Explora-Andenes scarp in the region of Wegener Canyon has not yet been supported by any fully conclusive evidence. Refraction profile S 22 refered to by Hinz and Krause (1982) and situated some 350 km south of Wegener Canyon in water depths of 3900 m proves the presence of high-velocity rocks (5.4 to 7.7 km/s), however below about 3000 m of sediments with velocities of 2.33 to 4.15 km/s (Hinz and Krause 1982, Table 2). Magnetic profiles measured over the escarpment both by BGR and during the Antarktis V/4 survey are characterized by long-wave anomalies, suggesting deep-seated causative bodies rather than a towering magmatic high.

It should further be remarked that the two phases of erosion of Wegener Canyon proposed by the ODP Leg 113 Shipboard Scientific Party might very well reflect a climatic control rather than a prolonged resistance to submarine scouring offered by a magmatic sill.

142.3 New observations

The detailed SEABEAM bathymetric mapping of Wegener Canyon, carried out during the Antarktis V/4 cruise, does not give a conclusive morphological evidence of the presence of rocks with strongly contrasting resistance in the lower canyon reaches (figs. 7 and 8). One might expect that the breach of a magmatic wall in such a canyon would have been marked by a narrowing of the valley and a steepening of the slopes, which is not the case.

A processed seismic section shot by R.V. "Polarstern" in the area of ODP Sites 691 to 693 shortly after their completion (Miller e.a., 1989) showed a first evidence of a reflector which can be followed some distance below the otherwise structureless outer high, without any noticeable velocity pull-up.

Another observation on the high-resolution seismic records is that sedimentary units leaning upon the landward flank of the outer high display a characteristic pattern of diverging and slightly buckling reflectors, which might suggest a layer emplacement which was contemporaneous with a rotational uplift of the outer high (cfr. the analog monitor records of profiles ANT V/4-24 and 25, shown on fig. 15).

Finally it should be mentioned that grab sampling carried out by "Polarstern" along the flanks of Wegener Canyon after the seismic survey yielded a range of shallow-water sandstones with glassy inclusions, but not a single basalt sample[1].

[1] Personal communication G. Kuhn, Alfred-Wegener-Institut für Polar- und Meeresforschung

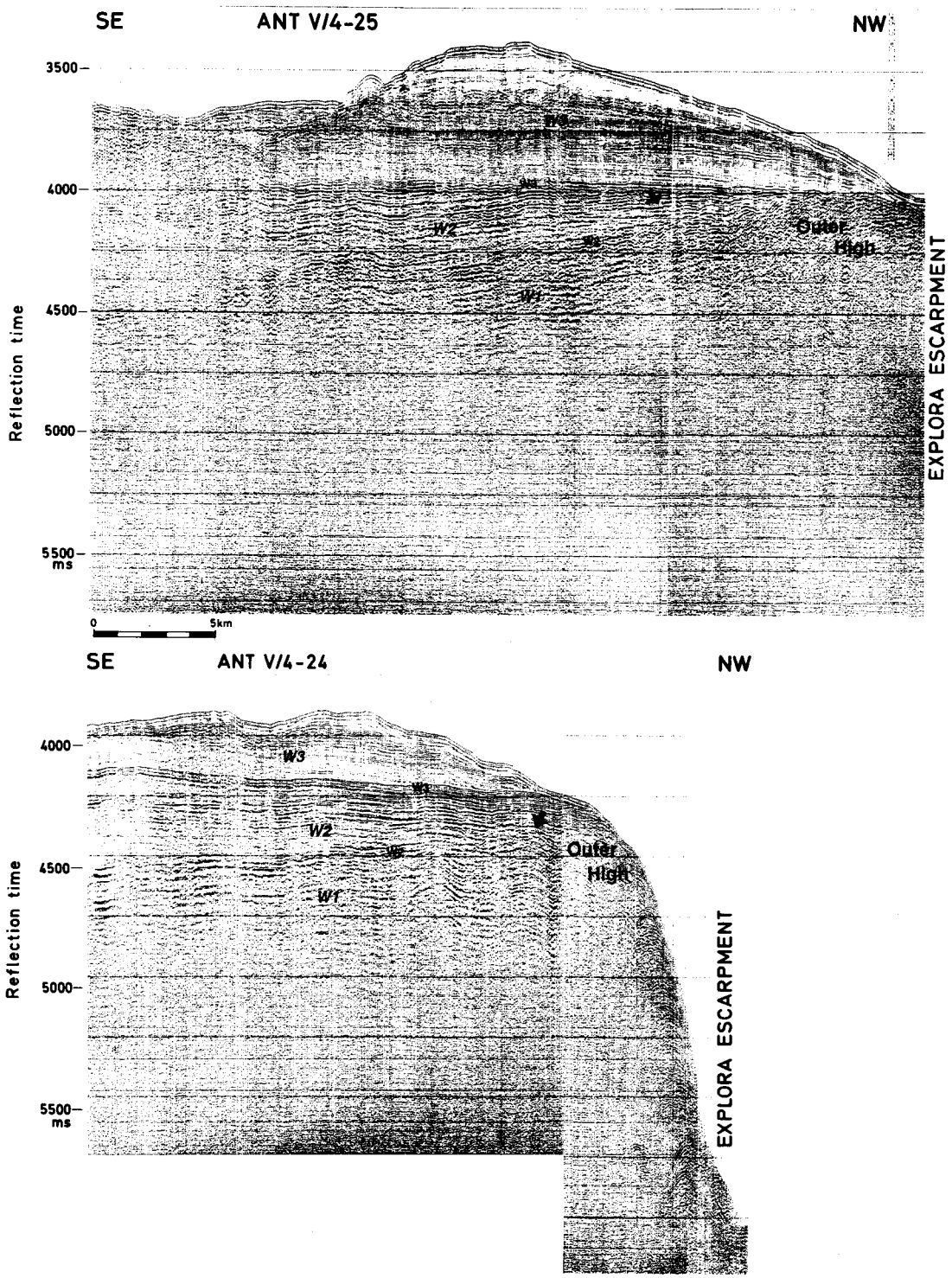

Fig. 15 Analog seismic profiles (ANT V/4-24 and 25) across the sedimentary cover on the landward flank of the "outer high", Explora Escarpment.

142.4 A new hypothesis

The scarcity of conclusive evidence about the nature and origin of the Explora-Andenes Escarpment found in literature leaves space for some conjectures, which can be nourished by the above mentioned observations.

If the transcurrent fault supposed to mark the escarpment has operated in a right-lateral sense, the regional displacement sense in the separation between Antarctica and Africa, the slightly arcuate northerly segment of the fault must have been subject to compressive stress components, in addition to the major shear component associated with the strike-slip motion (fig. 16). Such a situation is not likely to generate large leaks of magmatic material, but on the contrary might result in some underplating.

In this hypothesis, the scarp wall known as the outer high may to some extent consist of a stack of material of sedimentary nature, scraped off the early oceanic crustal plate by the overthrusting continental plate. The lithologic nature of the dredged samples is not in contradiction with this hypothesis : the course sands including volcanic glass grains could well fit into a model of shallow sea sedimentation on the early oceanic crust of Middle to Late Jurassic age. Any presence of minor inclusions of crustal or other magmatic origin amid the sediment stack is certainly not ruled out in this model.

The observation of the diverging set of slightly buckling deposits (of apparently sedimentary nature), abutting against the landward flank of the outer high, might confirm this hypothesis, arguing for a progressive build-up of the sediment stack on the overthrusting plate edge, possibly in a similar way as accretionary wedges are formed along converging margins. Similar structures are indeed known on the back of typical accretionary stacks such as that associated with the Barbados Ridge complex (Westbrook e.a. 1988).

The above hypothesis is in no way proposed as an ultimate one. It can easily be tested by further magnetic, gravity and seismic experiments, supported by meticulously planned geological sampling. Such work will probably be scheduled in the forthcoming geophysical programmes to be carried out with "Polarstern" in the Weddell Sea (season 1989-1990).

14.3 Sedimentary sequences off Halley Bay

143.1 Survey structure

The study area north of Halley Bay can be subdivided into two parts (fig. 17) : a shelf area south of 74°30'S, with water depths of 300 to 500 m, and a continental slope and rise area north of 74°30'S, in water depths ranging from 2000 to 3500 m. With exception of lines ANT V/4-1, 9 and 10, shot with the 4.5 kJ sparker or the 0.25 l watergun and of refraction line ANT V/4-21 (recorded with full available airgun power and two ocean bottom seismographs), all profiles have

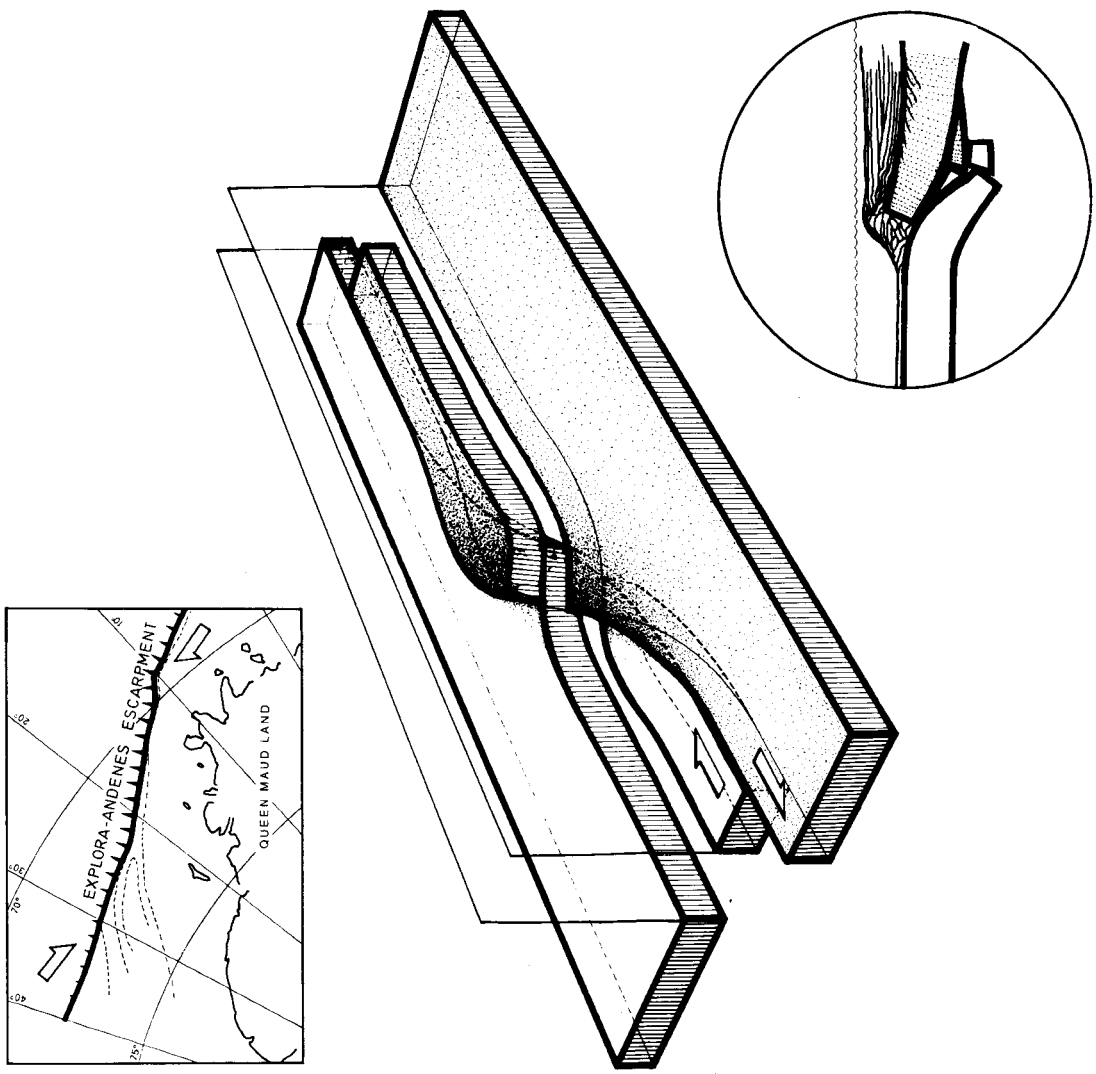

Fig. 16 Underthrusting along the Explora Escarpment as a consequence of the arcuate shape of the transcurrent fault.

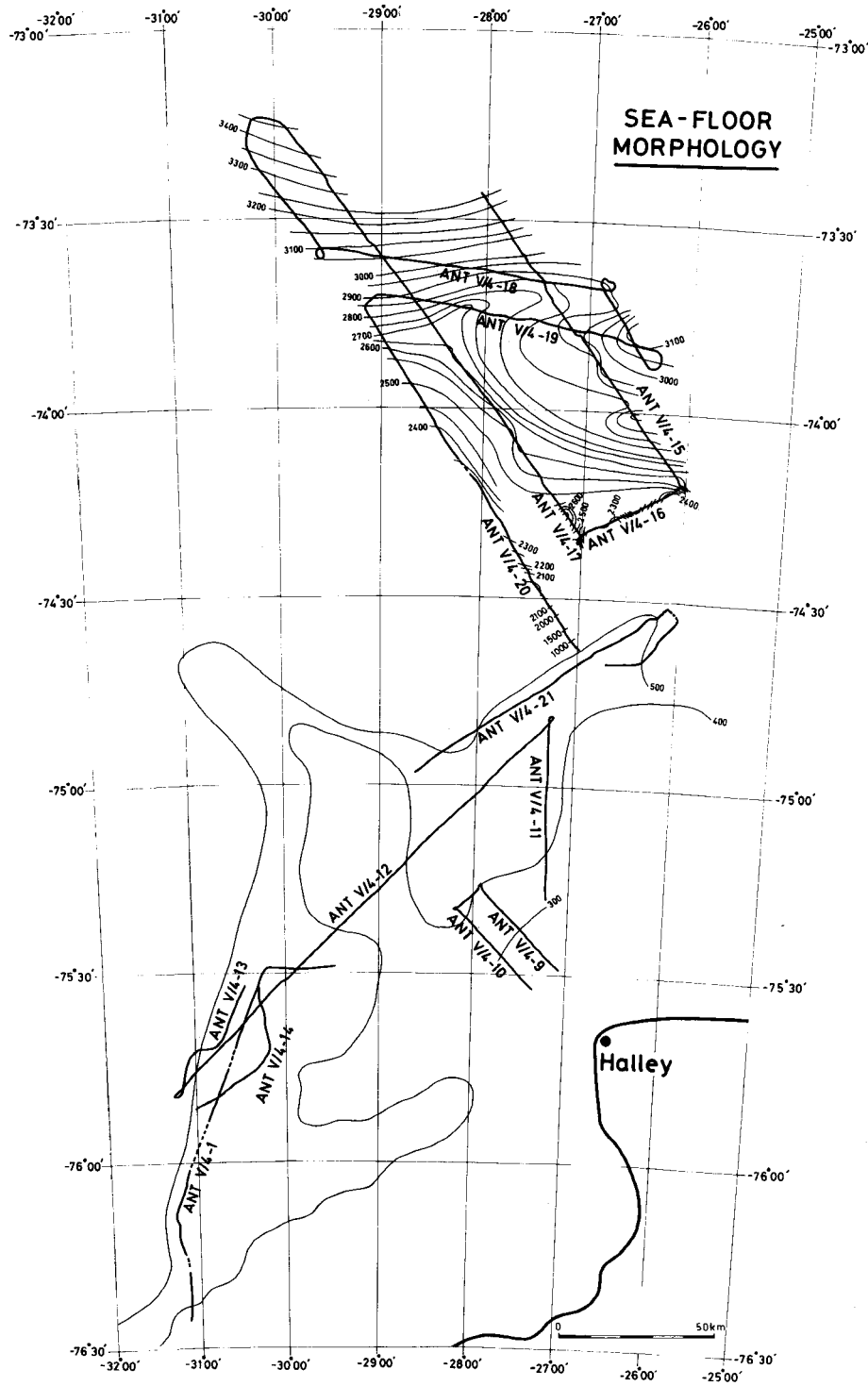

Fig.17 Sea-floor morphology and track map of the seismic survey over the continental shelf, slope and rise north of Halley (distal fan sequences, Crary Fan).

been shot with the above described airgun array (13.1), optimally trimmed for high-resolution acquisition.

143.2 Shelf sequences

The shelf profiles have been shot along the edge of the pack ice. Line ANT V/4-1, starting from a nearshore outcrop of the East Antarctic basement (fig. 18), has been extended by line ANT V/4-14 and 12 with the purpose of tying the Norwegian lines NARE 77-6, 8, 4, and 2 and NARE 79-6 and 8. These profiles show the top sequences of the obliquely prograding wedges, already described by Haugland (1982), Haugland e.a. (1985) and Hinz e.a. (1987). The deltaic progradation and associated submarine fan evolution have caused the important northward migration of the shelf edge in the southern Weddell Sea, probably in relatively recent Cenozoic times.

The sections on fig. 18 show at least five depositional sequences, which provisionally have not yet been named, as this will be done in agreement with the Norwegian partners. Most sequences show a rather complex internal bedding, with downlap and other lateral pinchout patterns and channel cut and fill structures.

The lowermost two sequences are both up-building in an onlap pattern on the cratonic basement and out-building in basinward direction. Channel erosion scars on top of the lower unit and a clear onlap of the overlying unit on the progradational front of the lower unit argue for a sea level lowering between both depositional phases. The second sequence also displays buried channels in its upper interval, visible for instance on profile ANT V/4-13 (figs. 18 and 19). Its top surface is also an erosional unconformity, which moreover truncates a third sequence at the far northeastern end of the profile. This erosional surface can possibly be regarded as the product of a prograding grounded ice sheet. The two last mentioned units are both covered by a relatively thin sequence (about 50-80 m thick) which on its turn onlaps on the basement surface. The most superficial unit (100-150 m thick) is of limited lateral extent on the considered profile.

Assigning an age to these sequences is still highly speculative. The correlation with the SWS units defined by Haugland e.a. (1985) still has to be worked out. According to these authors, the younger SWS shelf sequences (SWS-A to D) in the Weddell Embayment might correlate with strongly prograding shelf sequences of postulated Early Miocene to Pliocene age (Hinz and Krause 1984).

143.3 Slope fan sequences

Profiles ANT V/4-15, 17 and 20 and their tie lines ANT V/4-16, 18 and 19 (fig. 17) show a very high resolution picture of the distal units of Crary Fan and of a large associated buried channel, which trends in northeastern direction along the foot of the upper continental slope.

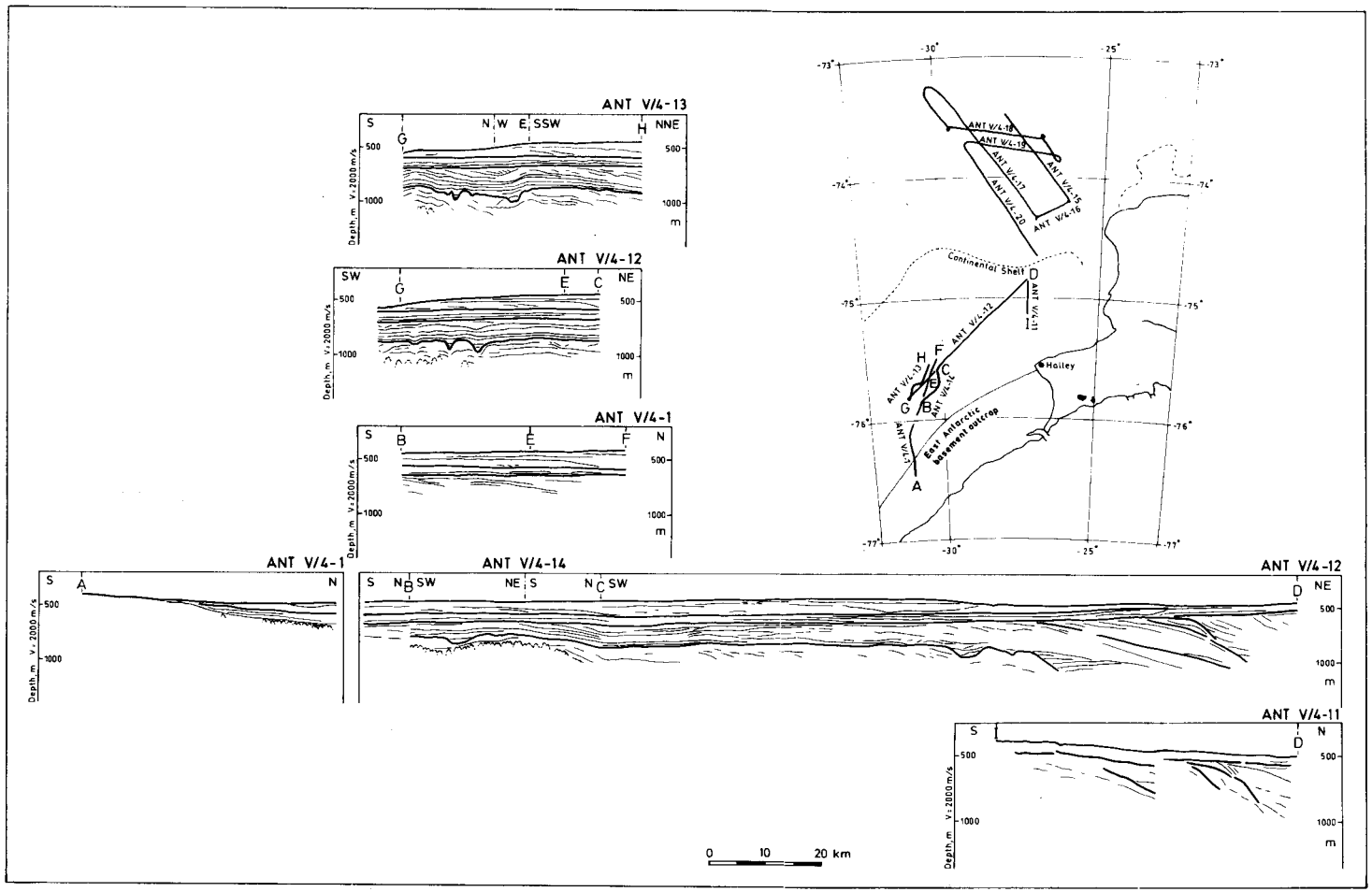

Fig. 18 Interpreted shelf profiles with prograding wedges north of Halley Bay. Profiles ANT V/4-1, 11, 12, 13 and 14.

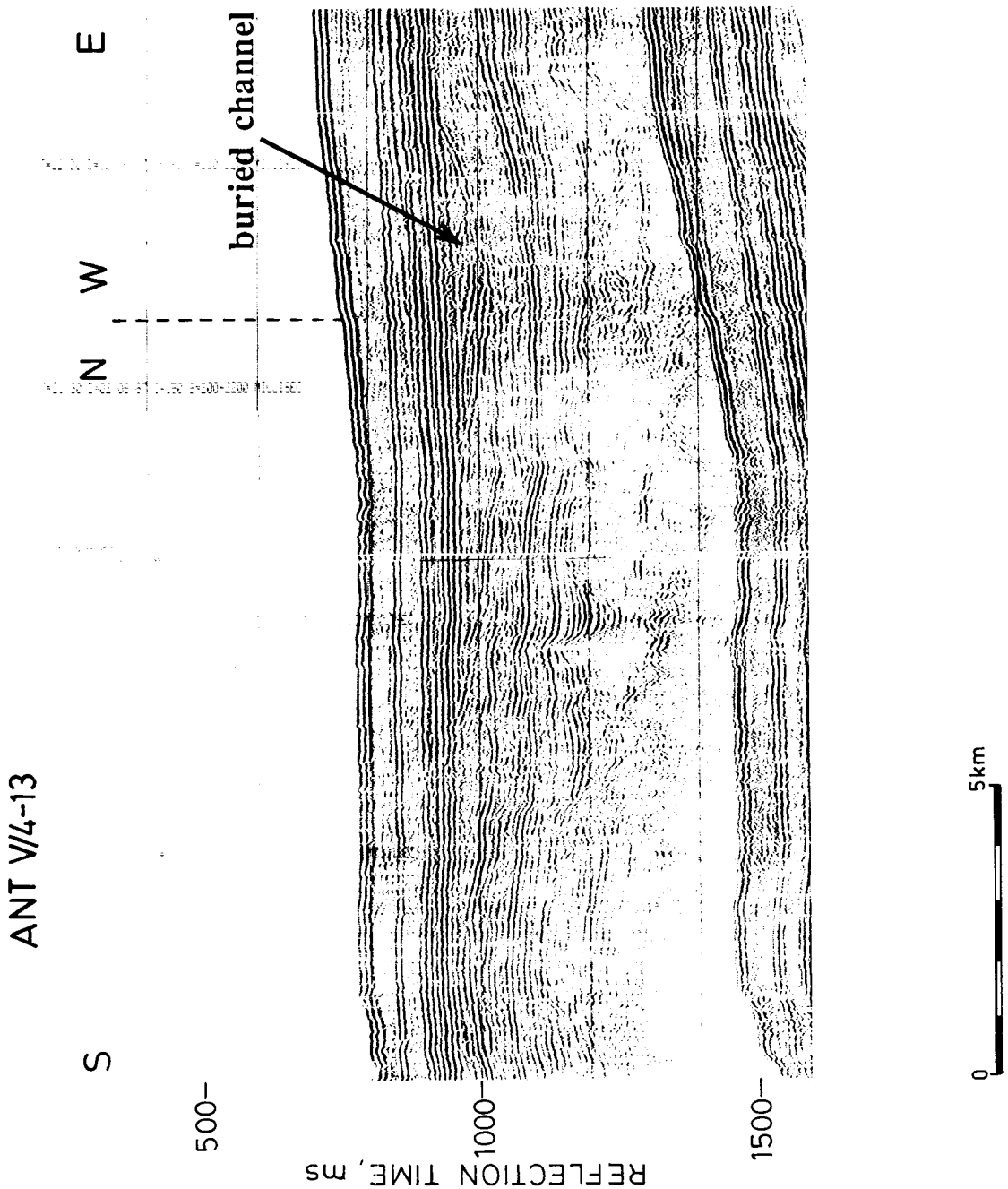

Fig. 19 Detail of the shelf wedge deposits with buried channel at the top of a depositional sequence. Profile ANT V/4-13.

Four major fan sequences can be identified, all downlapping or onlapping on a sloping erosional surface. It looks as if this erosional surface can be followed on BGR profile 86-08 over the whole length of the continental margin of the eastern Weddell Sea up to ODP Site 693, where it matches unconformity WO4 at the base of sequence *W4* . For reasons related with an observation reported below, this unconformity at the base of the fan deposits off Halley Bay will for the time being be called WO4b. This surface acts as an acoustic basement on the AWI-RCMG profiles (figs. 20, 21, 22, 23), due to the limited power of the seismic sources.

BGR lines across this area (e.g. BGR 86-08 and BGR 86-13) however confirm the presence of more than 3000 m of sediments below WO4b. In fact it appears that two practically adjacent major supersequences can be identified below the level of WO4b on profile BGR 86-13, both about 2 s thick (which corresponds with thicknesses of about 3000 m each, taking into consideration velocities between 2.8 and 3.5 km/s at that depth, Hinz e.a. 1987). Both supersequences locally rest on the unconformity WO1 and are separated by a major erosional unconformity which obliquely truncates the lower supersequence. This lower supersequence essentially rests on continental crust topped by the Explora Wedge. The upper supersequence is essentially resting on oceanic crust and onlaps on the sloping unconformity, provisionally named WO4a.

An important remark is that the WO4b unconformity merges with WO4a when followed along the intersecting line BGR 86-13 in landward direction, hence forming again one single unconformity WO4, a situation remembering that on Site 693. It is not excluded that a similar merging would occur along line BGR 86-08, but it has not yet been demonstrated in a conclusive way. We cannot exclude either the hypothesis that WO4b would correlate with WO5, which would imply a Late Miocene to Pliocene age of the onlapping fan sequences. This preliminary interpretation will be further discussed among the Weddell Sea research partners before interpretative profiles can be presented.

The submarine fan sequences observed north of Halley Bay clearly belong to a completely different systems tract than the Cenozoic stratotype sequences overlying surface WO4 at Site 693, which obviously complicates any correlation effort. Hence the fan sequences have been provisionally named *WF 1, WF 2, WF 3* and *WF 4* in this study. This terminology is subject to revision when forthcoming correlation work with Norwegian and BGR data has been completed, as mentioned above.

Sequence *WF 1* is characterized by weak, sub-parallel reflectors. It has a thickness of about 500 m in the westernmost part of the study area (profile ANT V/4-19, fig. 23) and rapidly wedges out in landward direction. The lapout pattern of sequences *WF 1* to *WF 3* shown on the map on fig. 24 is probably to be regarded as the lateral wedge-out of northeasterly prograding fan lobes.

Sequence *WF 2* , characterized by weak, discontinuous reflectors, keeps a fairly constant thickness of about 200 m until it also wedges out against WO4. Its basal unconformity WF 2 clearly truncates the underlying sequence on profiles ANT V/4-17 and 19 (figs. 21 and 22).

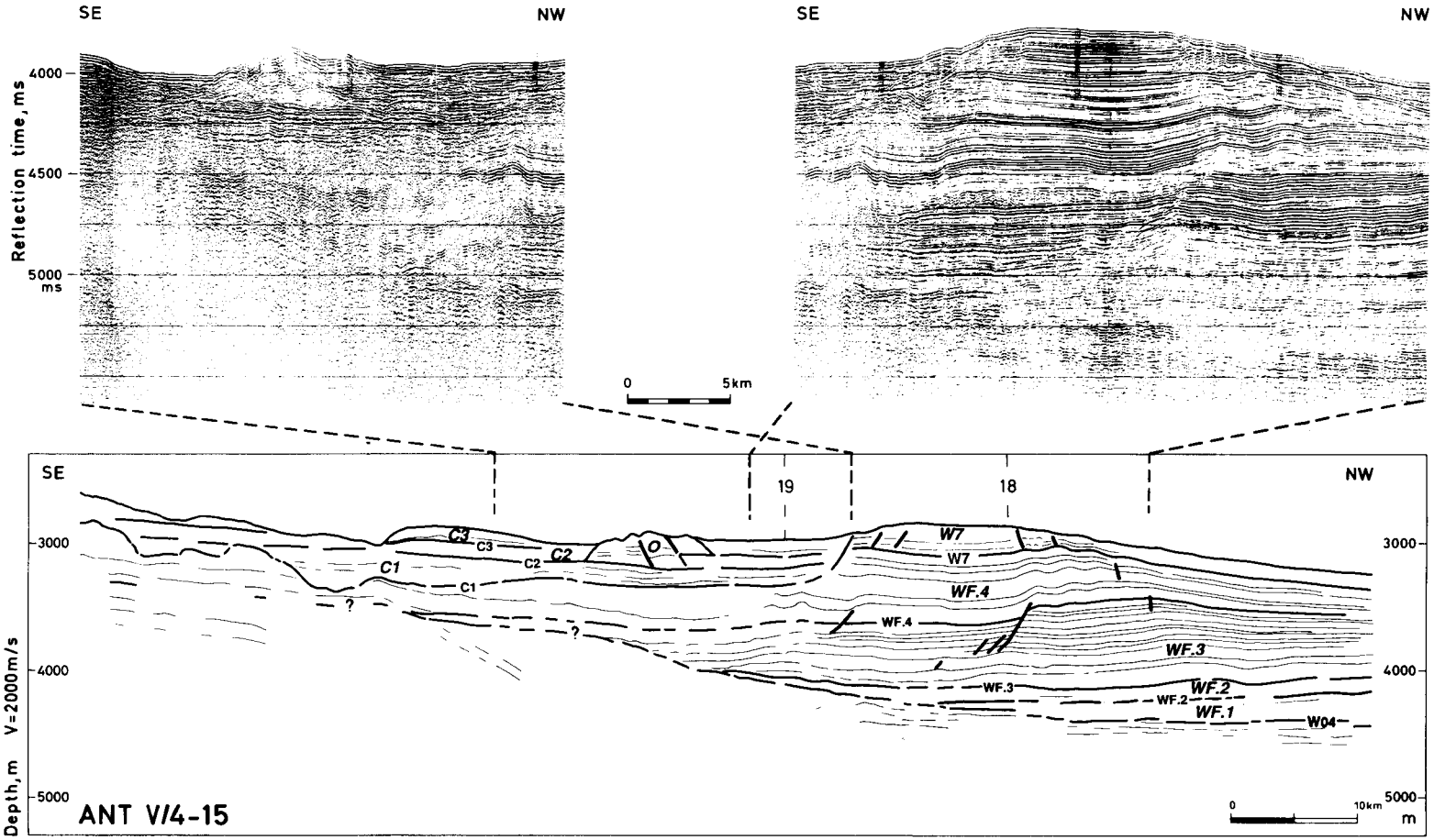

Fig. 20 Distal fan sequences onlapping on unconformity W4. Channel sequences (C) and olistoliths (O). Profile ANT V/4-15.

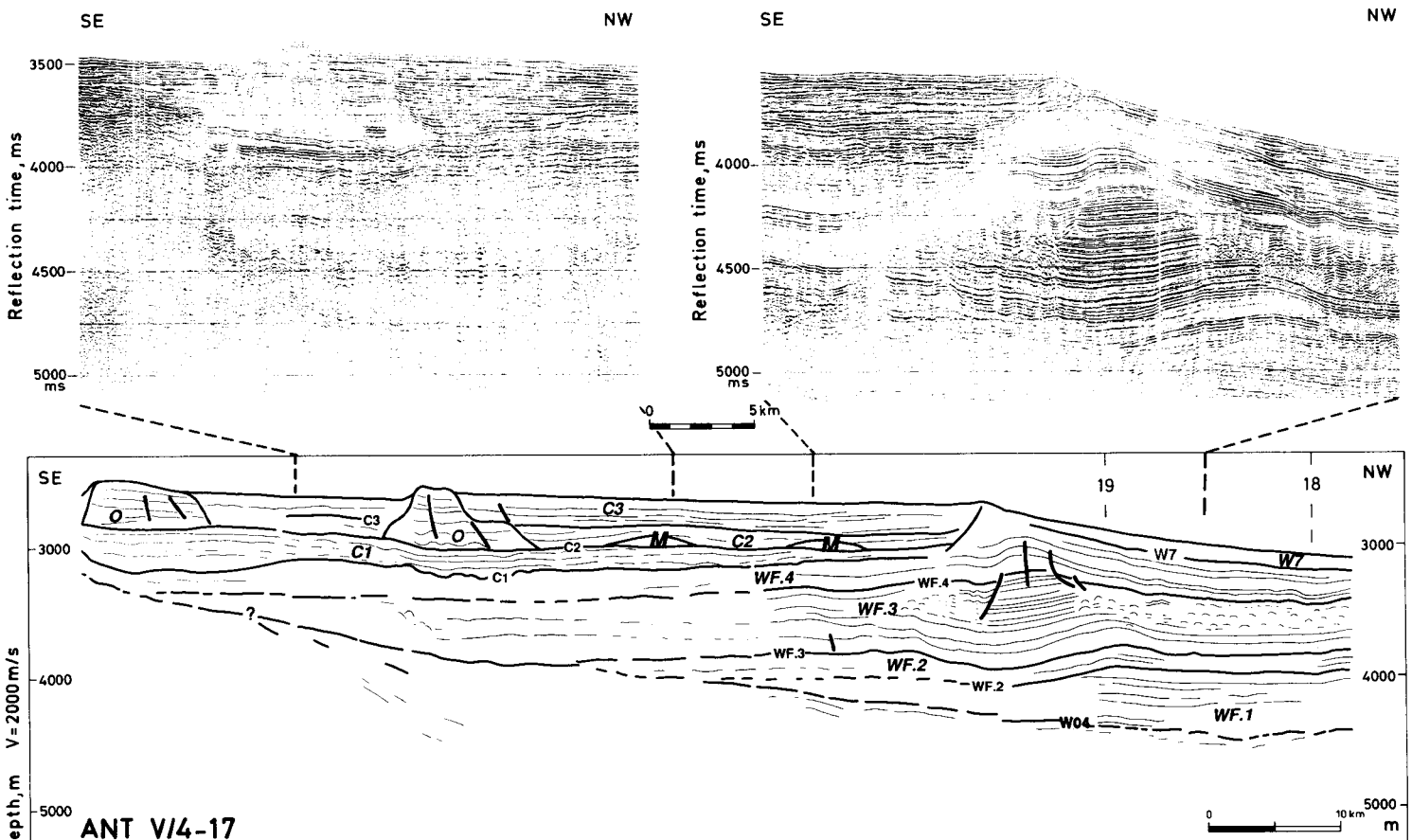

Fig. 21 Distal fan sequences onlapping on unconformity W4. Channel sequences (C) and olistoliths (O). Profile ANT V/4-17.

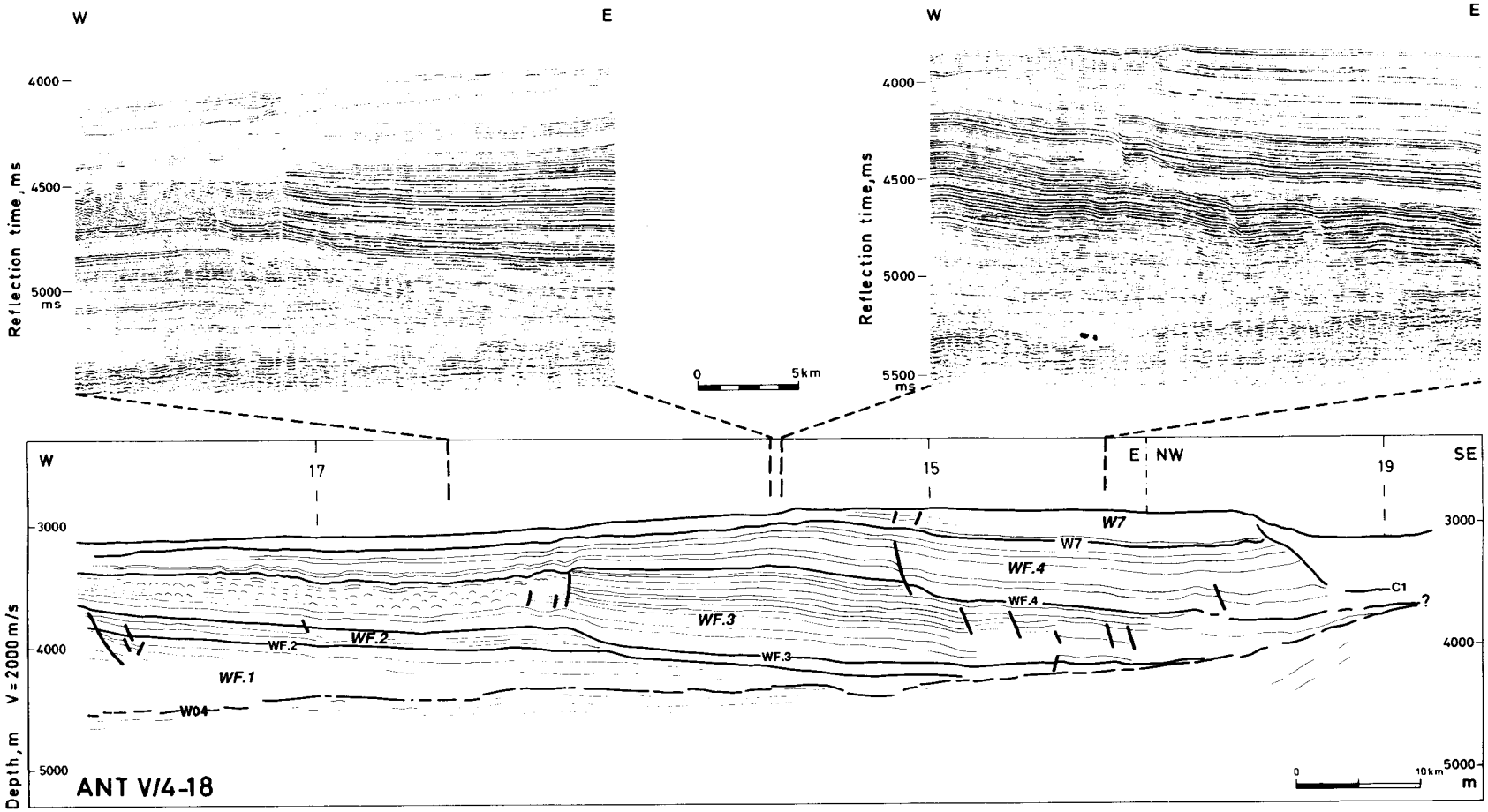

Fig. 22 Distal fan sequences downlapping on unconformity W4. Profile ANT V/4-18.

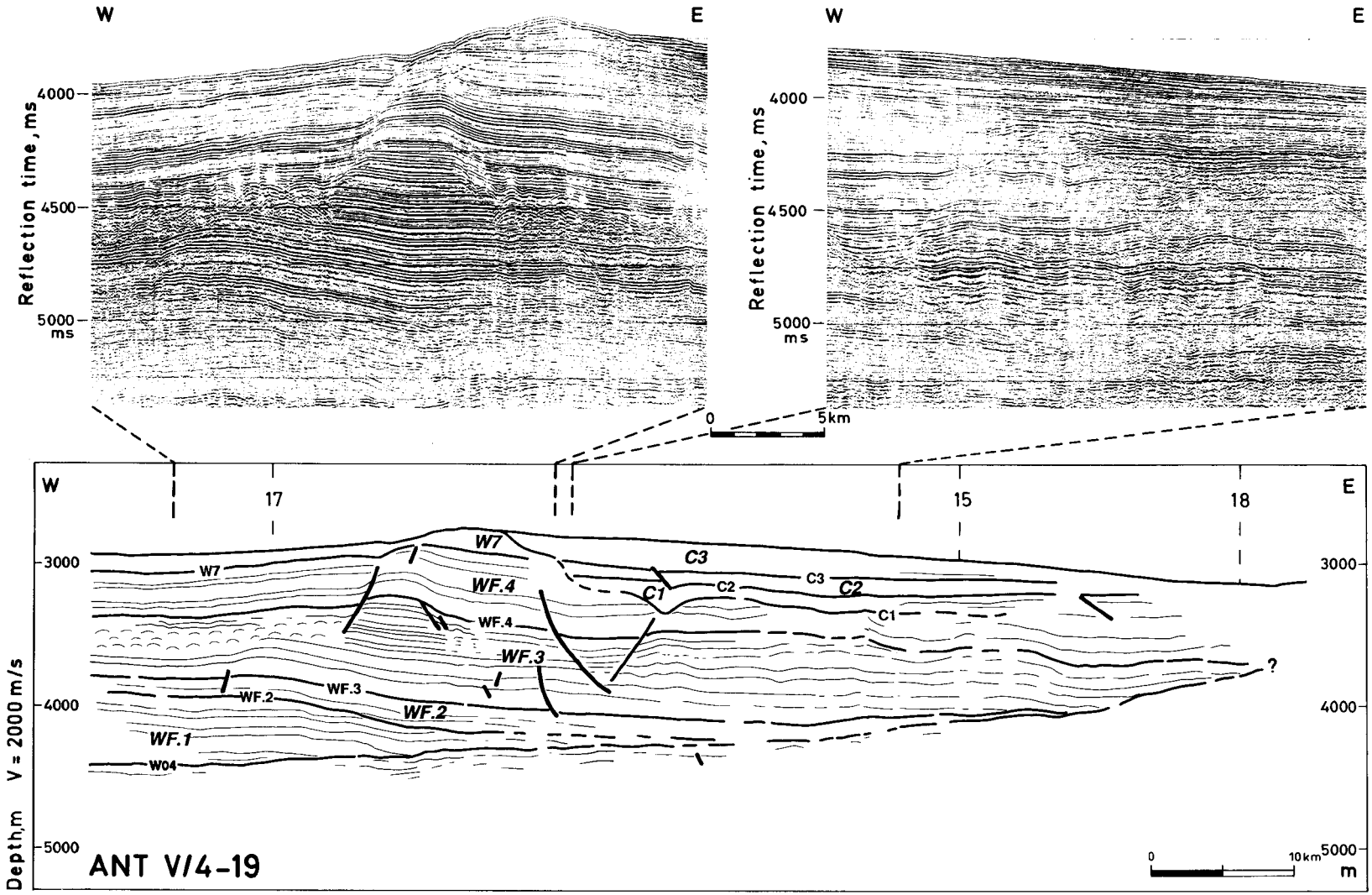

Fig. 23 Downlapping fan sequences with detail of buried erosional ridge flanked by slumped deposits. Profile ANT V/4-19.

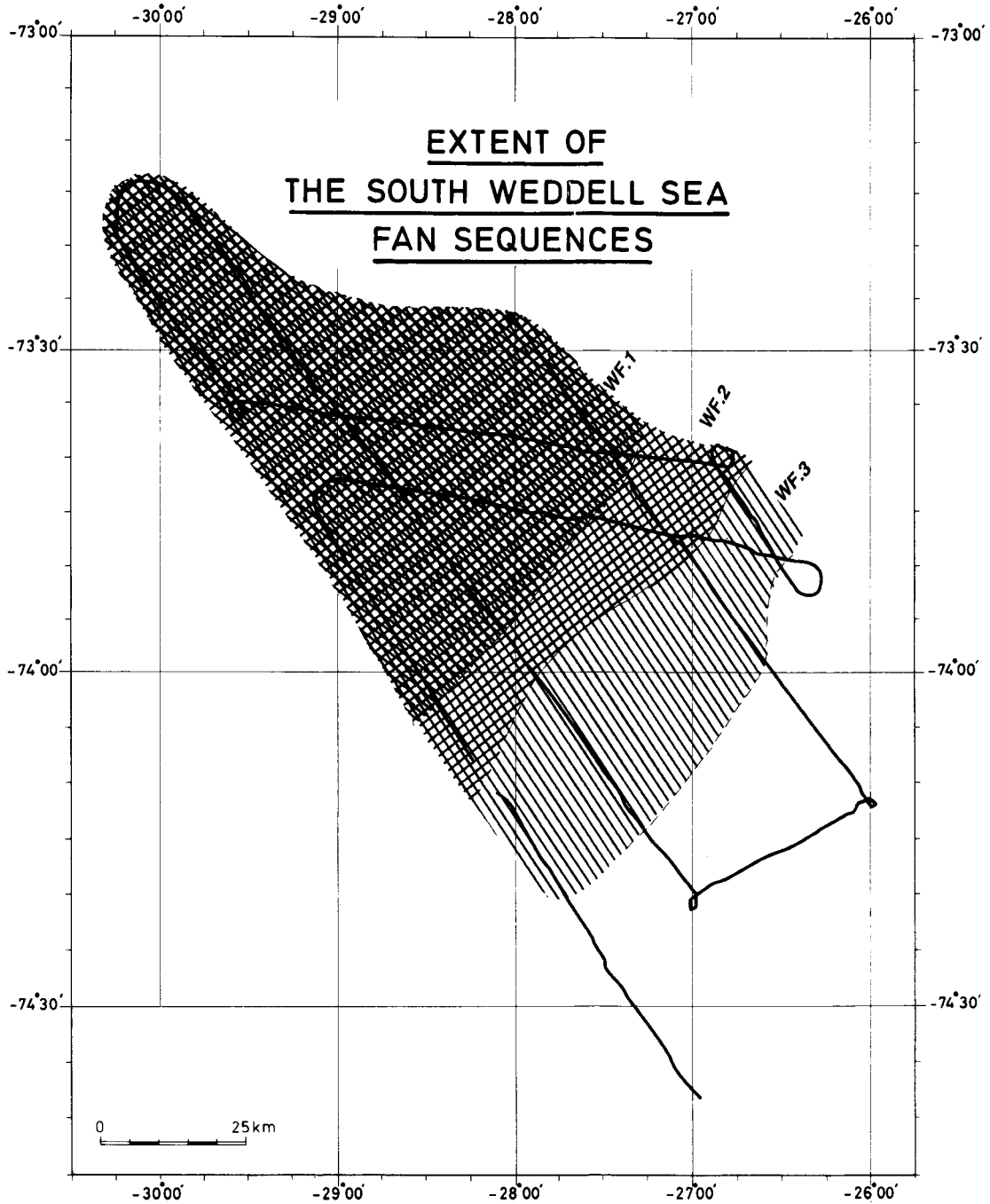

Fig. 24 Lateral onlap pattern of distal fan lobes on the W4 unconformity.

The basal unconformity of sequence *WF 3* erodes the distal part of sequence *WF 2* , as observed on profile 18 (fig. 22). Sequence *WF 3* is no doubt the most striking unit in this part of the study area. It reaches a maximal thickness of 700 m in the considered area and thins out both in southeasterly and northwesterly directions. Its facies is characterized by a series of strong, continuous and parallel reflections, locally disturbed by remarkable sediment-tectonic features. Some of the listric faults observed also affect the overlying sequence, but none of them can be traced down in the underlying unit. The origin of these deformations should consequently be sought in sequence *WF 3* itself and is most probably related to a shear strength reduction in temporarily overpressured horizons. This hypothesis seems to be corroborated by the observation of extensive sediment fluidization and slumping phenomena, affecting the footwall of some major listric faults. The slumped horizons are marked by an undulating to chaotic seismic facies, with numerous diffraction hyperbolae (figs. 21, 22, 23). The hanging wall of the considered listric faults displays a larger stratigraphic thickness, building up a prismatic paleoridge. The areal extent of faults, slumped areas and paleoridge are shown on fig. 25. The fact that some stratigraphic units disappear across the faults might argue for an early slumping activity, which would have caused the remobilization and removal of the upper part of the slumped sediment sections (shortly after deposition but before burial by the following sequence). In an alternative interpretation, such paleoridges might be seen as sedimentary drift structures formed by bottom currents (K. Hinz, 1989, pers. communication).

The paleoridge structure and the slumped areas described above are draped by sequence *WF 4* , where the deformations initiated in the underlying sequence progressively fade out. This unit is itself covered by a draping, continuous sequence with relatively constant thickness. By virtue of affinities in emplacement, seismic facies and thickness with the top sequence on ODP Site 693, this unit has been named sequence *W7.*

Close to the foot of the upper continental slope, which has a very rough topography, the fan sequences and especially sequence *WF 4* have been deeply ravinated by a broad longslope channel, which shows different sequences of sediment infill named *C1* to *C3*. The seismic facies of the valley fill sequences is very different from that of the fan deposits : quite striking are the high-amplitude, discontinuous reflections, suggesting a high-energy depositional environment, probably turbiditic.

Very large olistolith-like structures, some of them characterized an internal seismic facies displaying striking analogies with that of sequence *WF 4* , are resting on top of the lower fill sequence (fig. 21). A major argument for the identification of such sediment bodies as olistoliths is this analogy in facies with *WF 4* and the observation of remarkable basal disharmonic folds, suggesting the presence of a slip surface (fig. 26). An alternative interpretation, as advanced by some sedimentologists, is that these sediment bodies should be identified as leveed channel deposits. The facies characteristics of these sediment units however seems to contradict this hypothesis. The occurence of the olistolith-like structures has been mapped and represented on fig. 21. The

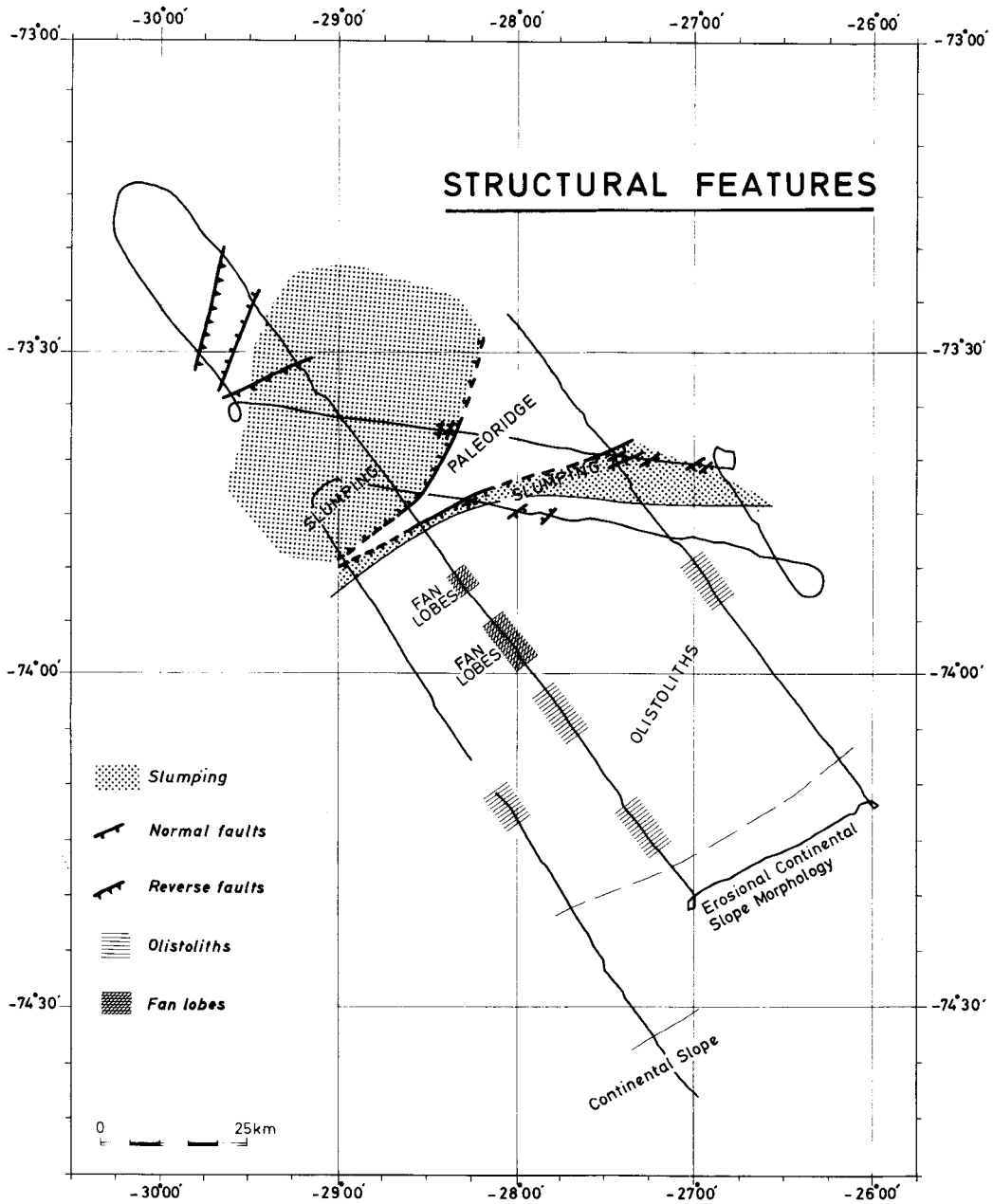

Fig. 25 Sediment-tectonic features in fan sequence *WF 3* and areal distribution of olistolith-like structures in the buried channel at the foot of the upper continental slope.

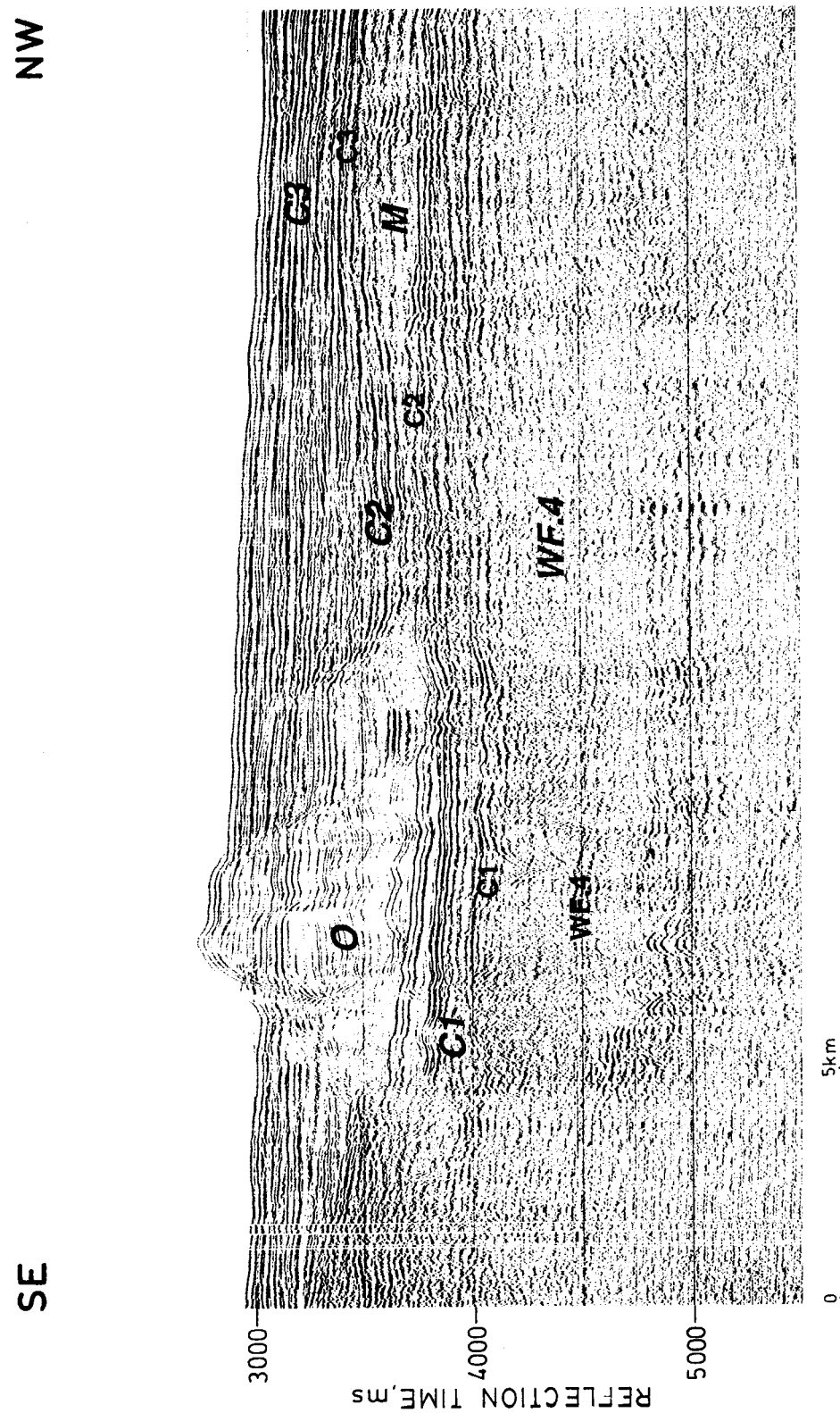

Fig. 26 Detail of an olistolith-like structure, showing the disharmonic folding above the supposed slip plane. Profile ANT V/4-17.

apparent alignement of three of these structures on parallel profiles might be used as an argument for identifying them as one single leveed channel, but this apparence of an alignement might simply be fortuitous.

The detachment and sliding of large slabs of sequence *WF 4* from flanks of the valley (here most probably from upper reaches of the valley) should not be utterly surprising, considering the emplacement of this unit on top of a sloping fan sequence itself characterized by extensive areas of sediment fluidization and slumping. Also the locally observed very steep valley flank with a height of about 750 m (on the southeastern end of profile ANT V/4-18, fig. 22) may bear witness of past large-scale sliding events, which might have fed large sediment slabs into the lower reaches of the valley. These sediment bodies have subsequently been buried beneath the apparently high-energy deposits of sequences *C2* and *C3*.

Another characteristic form of sediment deposits also mostly resting on surface C2 are the mound-shape fan lobes (*M*). Such depositional structures are quite frequent in basin floor fans (P. Vail 1989, pers. communication) and are usually built up of coarse grained sediments.

1.5 Broadening the picture

15.1 New insights in the Mesozoic South Atlantic sedimentary province

The identification of the *W 3* sequence with Lower Cretaceous black shales on ODP sites 692 and 693 sheds some new light on the importance of the Mesozoic sequences and the extent of the Cretaceous anoxic event on the southern margin of the early South Atlantic sedimentary province. The southernmost representatives of these sediments were hitherto only known from the DSDP boreholes on the Falkland Plateau (DSDP Site 511), the marginal Magallanes Basin and the Cape Basin (DSDP Site 361).

Although the true extent and stratigraphical importance of these sequences is not yet fully elucidated, there is little doubt that the southeastern Weddell Sea margin is characterized by comprehensive Late Jurassic to Early Cretaceous sequences. Whether the sequences below the WO4b unconformity in the southeastern Weddell Sea (off Halley Bay) do include Upper Cretaceous, Paleocene and/or Eocene sequences is difficult to evaluate at the present time.

The confirmation of an oxygen deficiency in the Late Jurassic to Early Cretaceous sediments of the Antarctic margin of the incipient South Atlantic Ocean is in itself not surprising. The important corollary of this observation however is that it possibly puts an additional constraint on the plausible paleocirculation models of the early Weddell Sea, a constraint which can be added to the analysis of the sequence of depositional phases and erosional events as observed on seismic sections.

There are indeed two fundamental models which address the problem of the widespread preservation of organic-rich sediments in the Cretaceous ocean, a key problem of paleoceanography (Zimmerman e.a. 1987). One is the preservational model, which implies a very low flux of dissolved oxygen to the site of deposition and consequently a very low vertical circulation. The other one is the productivity model, based on a greatly increased surface productivity which overwhelms the oxygen content of the water column ; the ocean dynamic corollary of this model is an enhanced vertical circulation (Southam e.a. 1982).

The preservational model with its restricted vertical circulation seems to apply to tectonically isolated basins such as the Black Sea or also the Late Jurassic to Lower Cretaceous South Atlantic (McCoy e.a. 1977, Natland 1978, Arthur e.a. 1979, de Graciansky e.a. 1984, Zimmerman e.a. 1987). Palinspastic reconstructions of the Late Jurassic to Cretaceous Southern Atlantic Ocean, shown on fig. 27 (after Zimmerman e.a. 1987), illustrate its confined setting.

If the preservational model holds, there are few reasons for expecting vigorous erosional events in such an environment. Such a situation most probably persisted at least up to Albian times in the Weddell Sea, considering the discovery of Albian black shales on Site 693. This reasoning thus possibly settles a lower boundary for the age of the major erosional unconformities observed on seismograms in the Weddell Sea above the WO1 unconformity.

15.2 Paleoceanographic control of Weddell Sea unconformities

Of all major unconformities identified in the Weddell Sea, only one has a purely tectonic control : the basal unconformity WO1, corresponding with the Middle Jurassic event U9 of Hinz and Kristoffersen (1987), which here along the Antarctic margin separates the sedimentary cover from the underlying magmatic crust. In a way it is unfortunate that the name "Weddell Sea Continental Margin Unconformity" has been introduced for this unconformity, considering that it certainly has the least significance in terms of paleoceanography or paleoclimatology.

Far more intriguing is the WO4 unconformity, constrained in age by the ODP drillhole data of Leg 113, as well as its possibly correlative and strongly erosive counterpart WO4a, identified off Halley (WO4b is a clear onlap surface at the base of Crary Fan deposits but it does not significantly truncate lower sequences). In view of the above considerations, it should normally fit into the interval from Late Albian to Early Oligocene.

According to Zimmerman e.a. (1987), the anoxic episode was terminated in the Southern Atlantic by a generalized erosional event in Cenomanian - Early Turonian times, associated with the establishment of the deep connection between the North and South Atlantic. This erosional event results in a generalized Cenomanian - Early Turonian hiatus, immediately following Albian times (fig. 28).

The onset of the hiatus on top of the Albian deposits on Site 693 might thus correlate with this event, although the dramatic influence of such a remote event in the Weddell Sea is

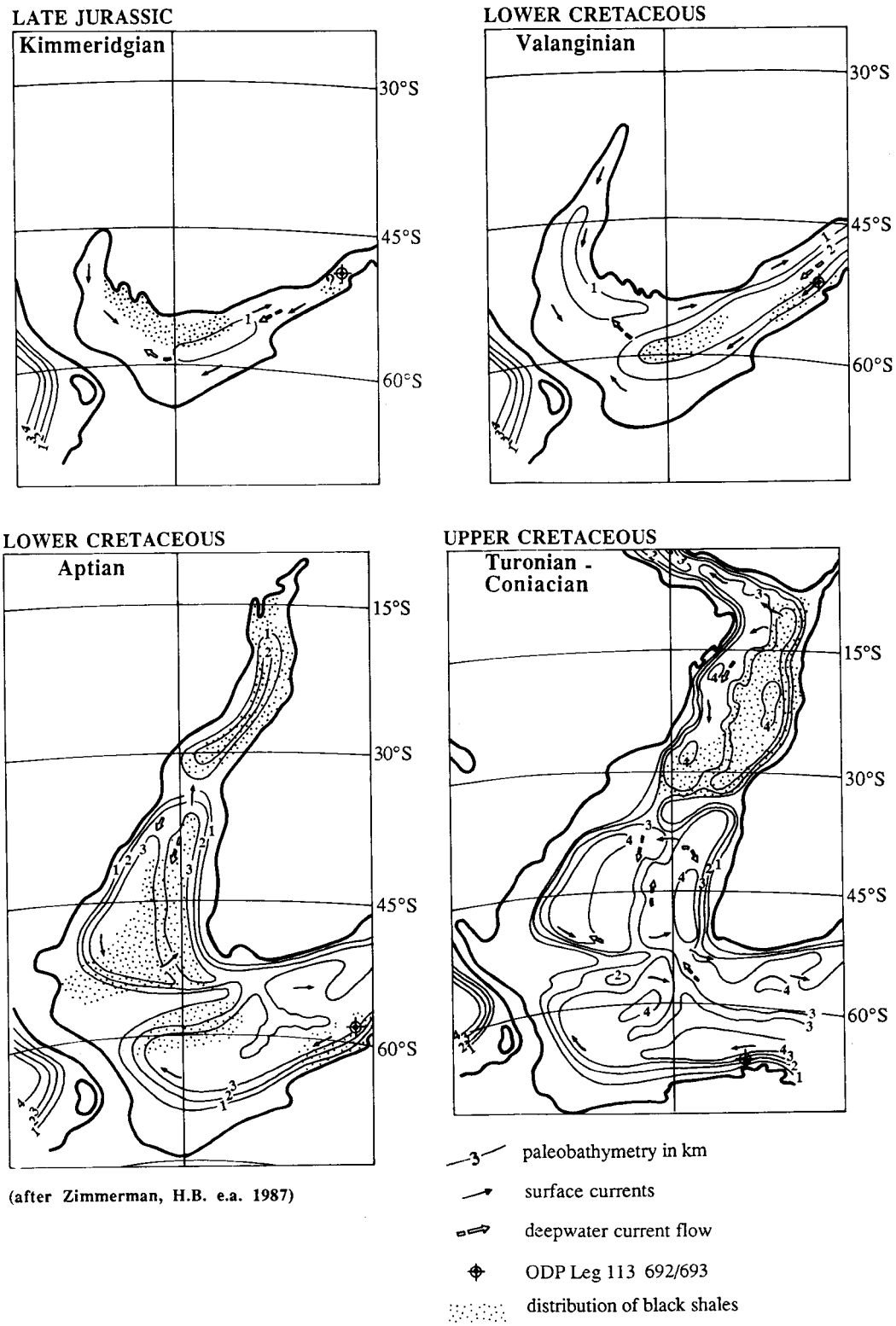

(after Zimmerman, H.B. e.a. 1987)

Fig. 27 Palinspatic reconstruction of the Late Jurassic to Cretaceous Southern Atlantic.

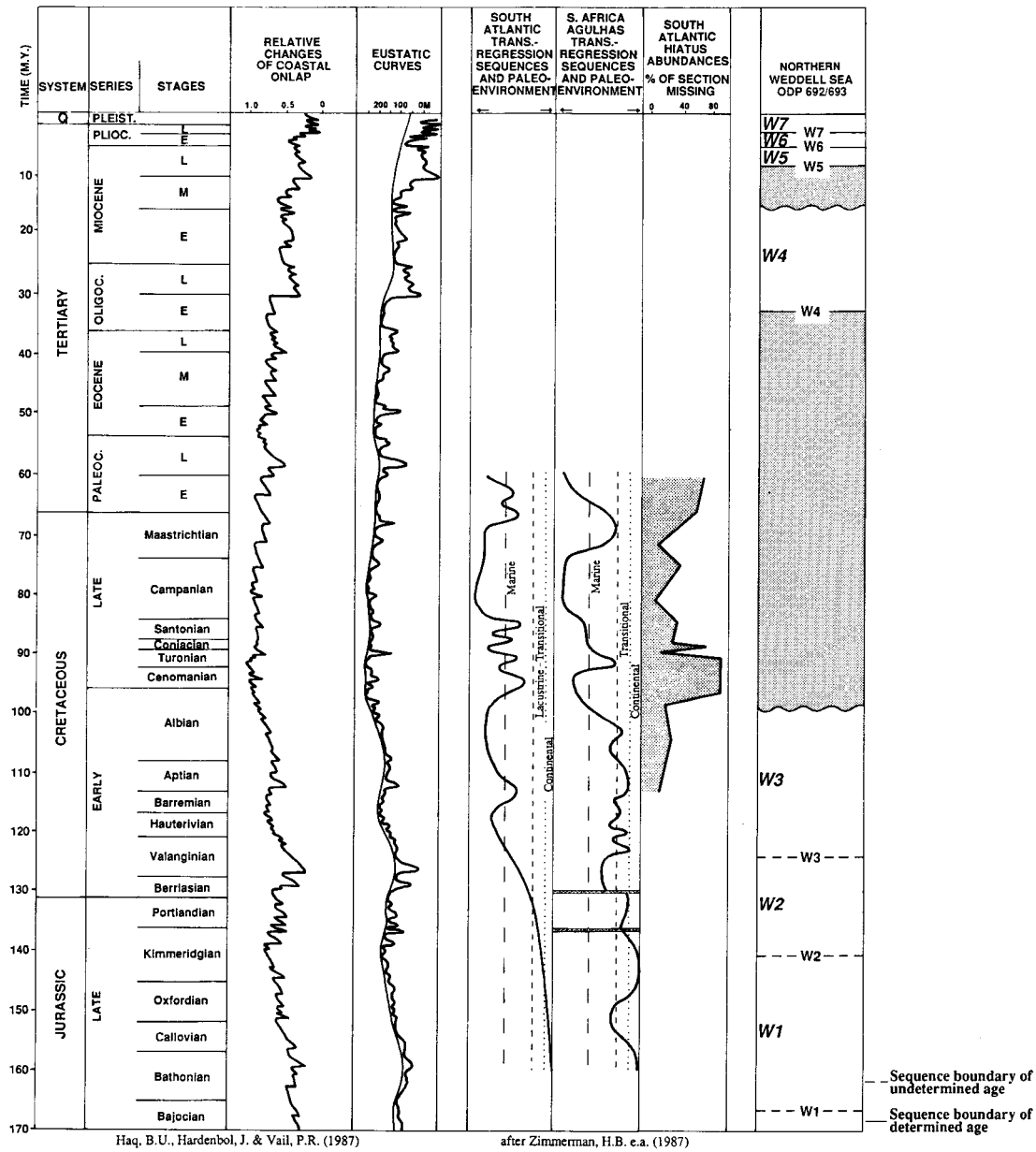

Fig. 28 Tentative correlation of the depositional sequences of the Weddell Sea with South Atlantic and global chronostratigraphy, sea level changes and hiatus occurence.

questionable. One might therefore also pay some closer attention to more proximate factors, which has led to scrutinize the fate of the Transantarctic region in those times.

A recent study of the dispersion of Upper Cretaceous planctonic and benthic foraminifera by B. Huber (1988, unpublished thesis) shows evidence of a Transantarctic marine seaway in Campanian-Maastrichtian times (fig. 29). Such a gateway might have caused vigorous bottom currents and countercurrents in the Weddell Sea Embayment, and hence erosion. One might expect a most vigorous erosion closer to the mouth of such a gateway, in the southern Weddell Sea, which could explain the strongly truncating unconformity off Halley (WO4a) and the more mildly erosional unconformity WO4 off Cape Norvegia. Further north, on Maud Rise, a full sequence of Late Campanian/Maastrichtian to Paleocene, Eocene, Oligocene and Miocene to Plio-Pleistocene sediments has been drilled in ODP boreholes 689 and 690 of Leg 113, arguing for an undisturbed sedimentation environment.

The closure of this seaway could have occurred in mid-Eocene times, after about 50 Ma ago , as a consequence of the uplift of the Transantarctic Mountains (Gleadow e.a., in press, cited by B. Huber 1988). This uplift could at the same time have created a significant source of sediment supply towards the Weddell Sea Embayment, which possibly could have contributed to the huge sediment sequence of the supersequence off Halley Bay, bracketed by the WO1 and WO4b unconformities and onlapping on WO4a.

The seismic-stratigraphic study of the Weddell Sea hence seems to provide an independent support to Huber's hypothesis of a Late Cretaceous and possibly Early Cenozoic Transantarctic seaway. Such a seaway may have initiated a current system engirdling East Antarctica and Australia (in Late Cretaceous times). Later, after the rifting between Antarctica and Australia, it might have evolved into an early circumantarctic current. According to Mutter e.a. (1985), the breakup between Antarctica and Australia may have started at 85 Ma B.P., however at a very low spreading rate. Considering that there is considerable speculation about the possible causal relationship between the progressive isolation of Antarctic landmass by a circling current and a climatic cooling effect, it will be evident that a hypothesis of an early ACC will also deserve attention in terms of a possible paleoclimatological impact. One should however bear in mind that both a Transantarctic current and any initial current between Antarctica and Australia had to circulate over shallow sills (e.g. the Tasman ridge in the latter seaway). This situation -if it occured- is consequently not to be compared with the present ACC, involving deep water circulation, stronly affecting the Southern Ocean circulation pattern.

The onset of the present Antarctic Circumpolar Current is related to the opening of another seaway, caused by the spreading of Drake Passage, between the Antarctic Peninsula and South America. There is some evidence that shallow marine channels connecting the Pacific and South Atlantic Oceans developed in the earliest rifting phase of Drake Passage, around 30 Ma ago. A major argument is the westward migration of planctonic foraminifera of the genus *Guembeletria* from the Australian province into South African waters (Bearman, ed., 1989). Coherent sea-floor

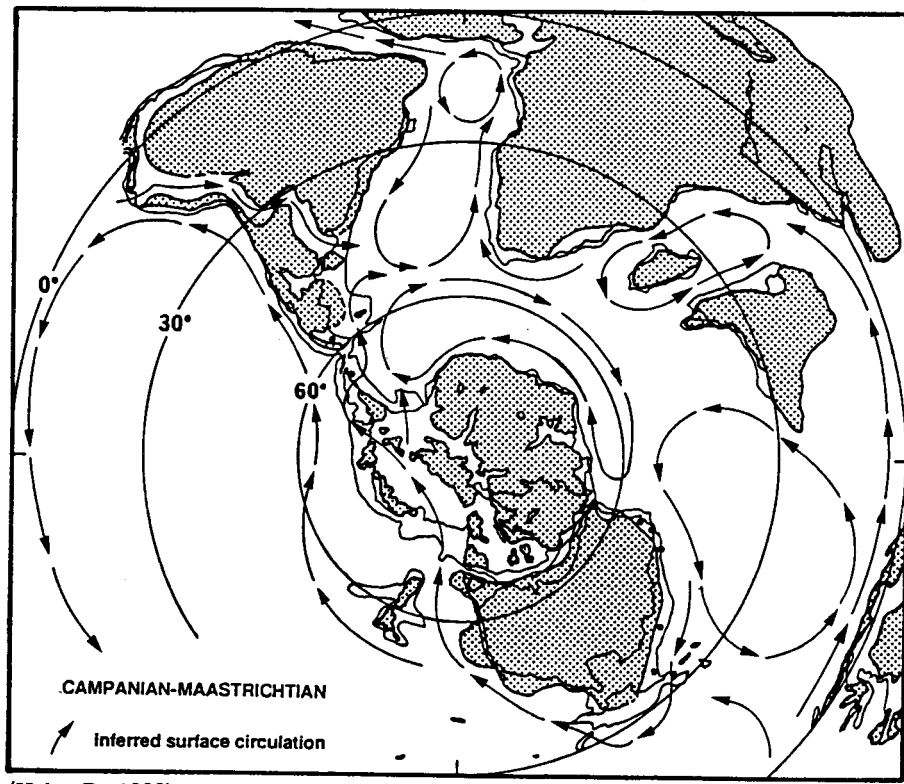

(Huber B. 1988)

Fig. 29 Inferred patterns of surface circulation for the Southern Hemisphere during the Campanian through Maastrichtian.

spreading in Drake Passage began at 29 Ma, but a deep gap could not develop until the ends of submarine ridges along Shackleton Fracture Zone fully cleared, which happened about 23 Ma ago (Barker and Burrell 1977), about at the Oligocene-Miocene boundary.

A clear evidence of a direct erosional response to the onset of the ACC is lacking in the ODP logs off Cape Norvegia, except for the presence of a local hiatus in the Late Oligocene of hole 693, above the horizon of slumped Oligocene deposits at the base of sequence *W4* . There is yet no conclusive causal relationship between this hiatus and the onset of a gyre current, but on the contrary it seems to reflect a possible ice growth pulse, as discussed below.

Barker and Burrell (1977) already remarked that, although the isolation of the Antarctic landmass and its engirdling by the ACC is generally accepted as the onset of a major climatic deterioration, there is no striking coincidence between ACC onset (at 23 Ma) and the renewed cooling, which apparently started at about 16 Ma ago. There is however a close temporal agreement between the inferred onset of the ACC and the emergence in Early Miocene times of that siliceous biofacies which today dominates sedimentation between the Antarctic Convergence and the Antarctic Divergence.

15.3 Paleoclimatic control of Cenozoic Weddell Sea unconformities

It has been noted in the precedent chapter that the opening of Drake Passage apparently has caused little erosional response in the stratigraphic record of the eastern Weddell Sea margin. In fact it appears that erosional unconformities in this area do more directly lock in on climatological signals in Cenozoic times, as illustrated on fig. 30.

This figure represents a composite benthic foraminiferal $\delta^{18}O$ record for Atlantic DSDP sites, corrected to *Cibicidoides* and reported to PDB standard (Miller e.a. 1987). Most of the observed variation of $\delta^{18}O$ in benthic foraminiferal skeletons during the young Cenozoic is due to the enhanced differential incorporation of ^{16}O into the ice of the polar ice caps during glacial periods, leaving the oceans relatively enriched in the heavy isotope ^{18}O. Accordingly, the isotopic ratio of benthic foraminifera can be taken as a measure of the amount of ocean water held in ice-sheets at any given time. The vertical line is drawn through 1.8 per mil ; values greater than this provide evidence for significant continental ice sheets.

If the isotopic ratio of benthic foraminifera can be taken as a measure of the amount of ocean water locked in ice sheets, it is also an indicator of global sea level. Comparisons of the oxygen-isotope composition of foraminiferans at the peak of the last glaciation with the composition of modern ones led to the observation that a difference in $\delta^{18}O$ of 0.1 per mil is equivalent to a 10 m change in sea-level, a relationship valid for changes in the past two million years (Bearman, ed. 1989). If the $\delta^{18}O$ curve reflects sea-level changes and ice sheet dynamics, which along Antarctic margins invariably means variations in cold bottom water flux, in coastal plain and shelf erosion and in sediment flux, it should not be surprising to find some agreement

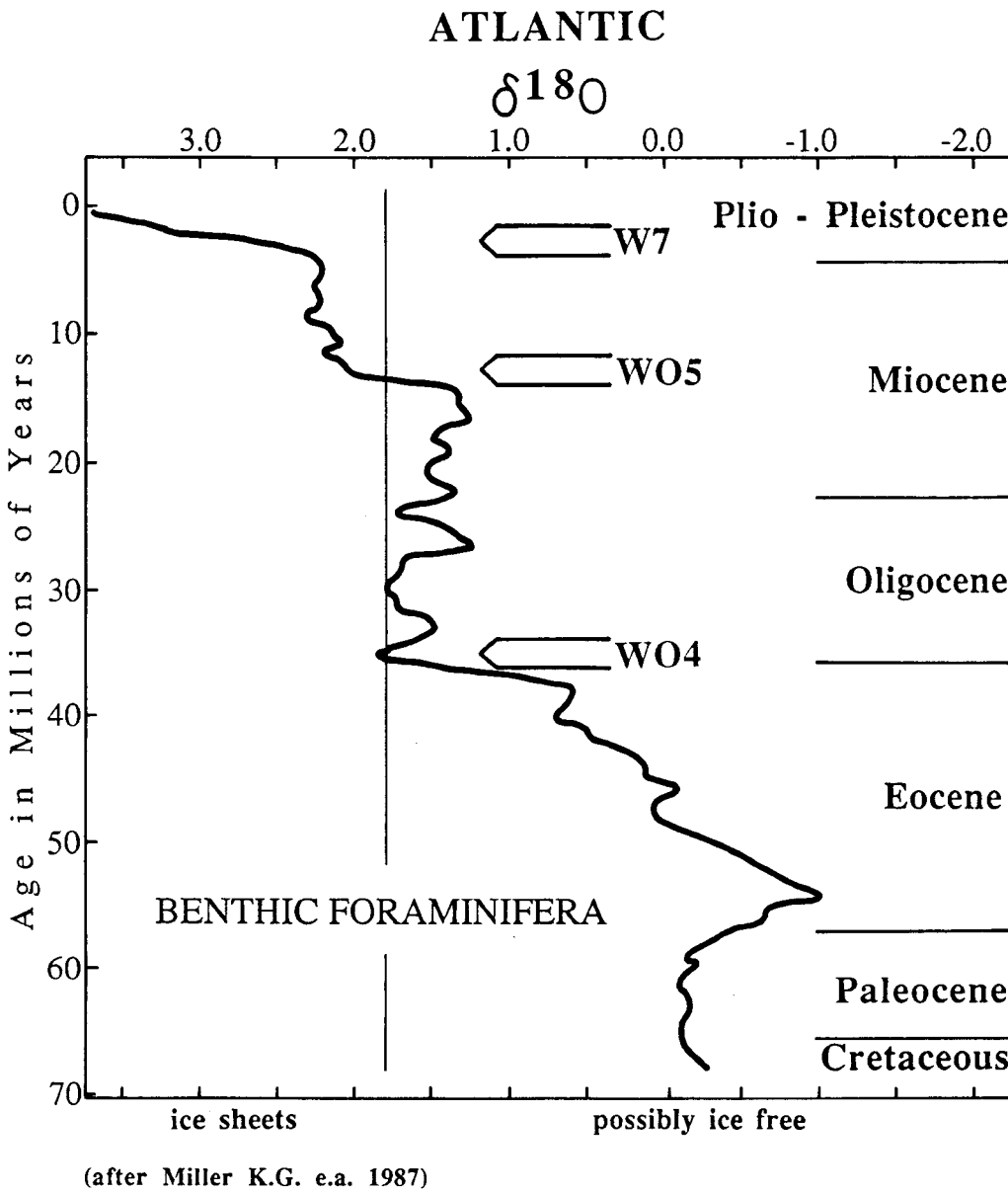

Fig. 30 Coincidence of Weddell Sea unconformities with rises in the composite benthic foraminiferal $\delta^{18}O$ record for Atlantic DSDP sites.

between striking features of this curve and the occurence of major Cenozoic unconformities. As can be seen on fig. 30, this proves to be the case.

The W4 unconformity coincides with the first ice growth event identified on the isotopic ratio curve, at 35 Ma. Also the small hiatus above the slumped Early Oligocene sediments in the base interval of sequence *W4* (cfr. 15.2) seems to coincide with a significant event at 32-28 Ma. The coincidence of W4 with a significant glacial advance suggests that the 60 Ma hiatus on Site 693 has a complex origin, with the possible superposition of at least two erosional processes, one in the Upper Cretaceous to Early Cenozoic (related to the breaching of a Transantarctic seaway) and one in the Early Oligocene, of glacial origin.

The very prominent reflector WO5 marking a Mid-Miocene hiatus (16 to 9 Ma) and heralding a pronounced change in seismic facies also perfectly fits with a major ice growth signal on the $\delta^{18}O$ curve starting at 16 Ma. This unconformity fits the U5 event in Hinz and Kristoffersen (1987), dated 16-13 Ma .

A similar observation also holds for the very conspicuous unconformity W 7 showing on high-resolution seismograms and identified in ODP hole 693 as the base of the Late Pliocene-Pleistocene glacial marine sediment cover. This fully coincides with the recent major ice growth event at about 3-4 Ma, named U2 by Hinz and Kristoffersen (1987).

The excellent fit between these observations turns the isotopic ratio curve into a first order interpretation tool in the seismic-stratigraphic analysis of peri-Antarctic basins.

1.6 Conclusions and perspectives

16.1 The detailed picture of the Weddell Sea sediments and their dynamics

The Antarktis V/4 cruise with its acquisition of more than 2800 km of high quality reflection seismic profiles no doubt takes a special position in the record of the geological reconnaissance of the eastern Weddell Sea. A major reason is the very high resolution achieved both in single channel and in multichannel data over the larger part of the eastern Weddell Sea margin, thus highlighting a hitherto unknown stratigraphic and structural detail. This detail provides among other aspects a valuable information about the role of sediment mass movements in Antarctic deepsea fan deposits, such as those studied in front of Halley Bay. Features like the extensive sediment flow structures observed in sequence *WF 3* and the giant olistolith-like sediment bodies in buried channels along the continental slope had eluded previous investigations, essentially due to a lack of resolution.

16.2 Towards a unified stratigraphic model of the Weddell Sea

The high-resolution multichannel data collected by "Polarstern" helped to bridge the gap between the detailed stratigraphic and lithologic log of the ODP boreholes and the reflection picture of former surveys with deep penetration, such as the BGR profiles. The AWI-RCMG survey and interpretation consequently catalyses a new effort towards a unified approach in the seismic-stratigraphic analysis of the Weddell Sea Basin, a venture jointly undertaken by German, Norwegian and Belgian research teams. This effort involves the exchange of information and the compilation of all data sets pertinent to common research areas, which contributed to an agreement about a common seismic-stratigraphic interpretation and sequence naming procedure. The critical confrontation of interpretations on intersecting lines shot by different partners already yielded stimulating new insights in the geological structure of the eastern Weddell Sea.

16.3 Clues for a precursor of the Antarctic Circumpolar Current

The new joint interpretation effort progressively sheds some new light on the evolution of the sedimentary environment of the South Atlantic and the Weddell Sea Basin through Mesozoic and Cenozoic times. These ongoing efforts directly benefit from the recently released ODP results, which are fully integrated in the emerging model. Some new arguments seem to support the hypothesis of a Late Cretaceous initiation of a precursor of the Antarctic Circumpolar Current through a Transantarctic seaway, a concept which has obvious and stimulating paleoceanographical and paleoclimatological implications. The critical further analysis of this hypothesis will no doubt be a major line of research in the forthcoming programme.

16.4 Underplating as origin of the Explora-Andenes Escarpment

The interpretation of seismic and geological observations around Wegener Canyon and the critical reassessment of former geophysical data leads to a new and relatively straightforward geodynamic model for the origin of the Explora-Andenes Escarpment. This involves underplating and the build-up of an accretionary sediment stack in a local compressional context, bound to a sigmoid bend of the involved transcurrent fault. Forthcoming geophysical programmes could easily check the validity of this hypothesis.

16.5 Extracting the climatic signals from seismic data

The availability of very high-resolution seismic data calibrated on well-documented ODP wells provides a major opportunity to analyse the climatic information locked in the reflection seismograms. A remarkable observation hereby is the excellent match of erosional unconformities

identified on high-resolution reflection seismic profiles collected on the eastern margin of the Weddell Sea with the record of continental ice growth events, reflected in the Atlantic oxygen isotopic ratio log determined for benthic foraminifera. If such a correlation can be confirmed on other Antarctic margins, it can prove a valuable support for the analysis of the paleoclimate records from seismic investigations of the peri-Antarctic sedimentary wedges.

16.6 Forging a European cooperation in the Weddell Sea Basin research

The spirit of international cooperation strongly promoted by the Alfred-Wegener-Institut für Polar- und Meeresforschung in all levels of the geological study of the Weddell Sea Basin, from joint data acquisition to processing and interpretation, certainly has to be acknowledged as a major achievement. It is presently forging a joint European expertise in polar marine geological research, which certainly faces new opportunities and scientific perspectives.

Part 2 : the Antarctic Peninsula

2.1 Research objectives

The second marine geophysical cruise in the framework of the Belgian Research Programme about the Antarctic took again place in cooperation with the Alfred-Wegener-Institut für Polar- und Meeresforschung and this time also in cooperation with the Institut für Geophysik of the Christian-Albrechts Universität zu Kiel. Prof. H. Miller from AWI and Prof. R. Meissner from Kiel were the promotors of a study programme of the structure and evolution of the Antarctic Peninsula, sponsored by the Deutsche Forschungsgemeinschaft (DFG).

During the Antarktis VI/2 cruise of R.V. "Polarstern", some 1400 km of reflection profiles have been recorded, in addition of two refraction profiles (resp. 345 and 65 km long) and magnetic and gravimetric profiles. These profiles primarily addressed the deeper structure of the back-arc spreading basin of Bransfield Strait and the South Shetland Trench with its converging plate boundary environment. The reflection seismic parameters could however be trimmed in such a way that valuable information could also be acquired about the sedimentary cover.

When comparing the Antarctic Peninsula research with the Weddell Sea investigation, one might state that the Antarctic Peninsula Basins involve sedimentation processes not only controlled by paleoceanographic and paleoclimatic factors (as is the case along the passive continental margins of the eastern Weddell Sea) but also by geodynamic processes characteristic of active

margins, such as subduction, back-arc spreading with associated magmatism and, as has been shown by this cruise, by the development of a fore-arc basin. The Antarctic Peninsula is in addition one of the very few geodynamic environments in the world where such well developed converging margin features coexist with nearby mid-oceanic spreading ridge segments, which have been active until a relatively recent geological past.

When such unique geodynamic features are blended with not less exceptional paleoclimatic processes (the proximity of the Antarctic glacial regime) and paleoceanographic events (the opening of Drake Passage in Oligo-Miocene times, initiating the presently known Antarctic Circumpolar Current), it is clear that this area forms an outstanding marine-geological study domain, which in addition is a key element for the understanding of the Cenozoic evolution of the South Atlantic and of the Weddell Sea.

Getting an insight in the structure and evolution of this domain and acquiring some new data in hitherto unexplored parts of this domain was a prime objective of the present research. The processing and interpretation of the results of this recent cruise are still in progress, which means that the results presented below have a preliminary character.

2.2 Previous research

Bransfield Strait and adjacent areas have been a focus of marine geophysical and geological research in the past ten years, with main programmes deployed by the British Antarctic Survey, the Polish Academy of Sciences (1979-1980), the Alfred-Wegener-Institut für Polar- und Meeresforschung and Kiel University (ANT II/3), Brazil (PETROBRAS survey, 1987) and various U.S. cruises. Japanese marine geophysical investigations have been carried out in the Bellingshausen Sea over DSDP drill site 325, linking this important reference borehole to the paleotrench along the continental margin off Adelaide Island (Kimura 1982).

The crustal structure of the marine basins along the northern Antarctic Peninsula has mainly been documented by deep refraction studies carried out by British and Polish investigators (Ashcroft 1972, Guterch e.a. 1985).

The sedimentary cover has mainly been analysed by reflection seismics. Some 1100 km of reflection seismic profiles have been shot by the Polish expedition, essentially in Bransfield Strait and around King George Island. The German ANT II/3 expedition (F.Theilen, Kiel) recorded several high-resolution lines with a single airgun in an area confined to Bransfield Strait. The Brazilian survey, carried out with oil industry standards (8 guns, 72-channels recording), is certainly the most extensive one recorded until now in this region: more than 5000 km of high quality reflection seismic profiles have been shot over Bransfield Strait and the continental shelf as far south as Adelaide Island. This survey is the first to report the presence of a long sedimentary basin on the continental shelf of the Bellingshausen margin, informally named "Câmara Basin".

This basin has also been crossed later in the same year by the Antarktis VI/2 cruise of AWI/Kiel/RCMG and is interpreted in the present report as a typical fore-arc basin. The Brazilian expedition also mentioned the presence of a large submarine fan down-dip of the Câmara Basin, stretching over oceanic crust. The results of this cruise have to our knowledge not yet been published.

2.3 Methods

23.1 Reflection data acquisition

The reflection data set recorded during the Antarktis VI/2 cruise is shown on fig. 31. Profile 1, about 338 km long, ran from Hope Bay across Bransfield Strait, along King George Island and then across the South Shetland Trench. Another two profiles (9 and 2) crossed Bransfield Strait further southwest, while one longitudinal profile has been shot along the southern margin of the South Shetland Islands (profile 8). The oceanic domain with the prominent Hero and Anvers Fracture zones and the ridge-trench collision area off Brabant and Anvers Islands have been investigated with a large seismic loop (lines 3, 4, 5, 6 and 7).

Most reflection profiles have been shot with four BOLT PAR 1500 C airguns from IFREMER, with air chamber volumes of 9 l. Some reflection profiling has also been carried out during refraction shooting with the same guns fitted with 16 l air chambers (refraction line 1), which however did not yield any apparent additional deep crustal information. As the information about the sedimentary cover was poor with these powerful guns, this experiment was not repeated on other lines. A part of profile 3 (fig. 31) has been shot with the same AWI PRAKLA-SEISMOS airguns (2 x 2 l and one of 5 l) which had successfully been used in the Antarktis V/4 cruise in the Weddell Sea the previous year, but they proved too weak in the storm-swept environment of the western Antarctic Peninsula. There was consequently no hope of acquiring in this spring season any meaningful high-resolution data with RCMG's 0.25 l watergun.

The major part of the reflection data has been detected with AWI's 24-channel streamer with an active length of 600 m, built by PRAKLA-SEISMOS. Whenever the deployment of this larger streamer was not possible (e.g. for short lines recorded in between fishery research activities), data could still be recorded with RCMG's manually deployed 100 m streamer with 8 channels.

All digital acquisition took place on RCMG's EG&G ES 2420 seismograph, with data written out on two CIPHER tape drives. Two EPC recorders with different recording scale have been used for analog monitoring.

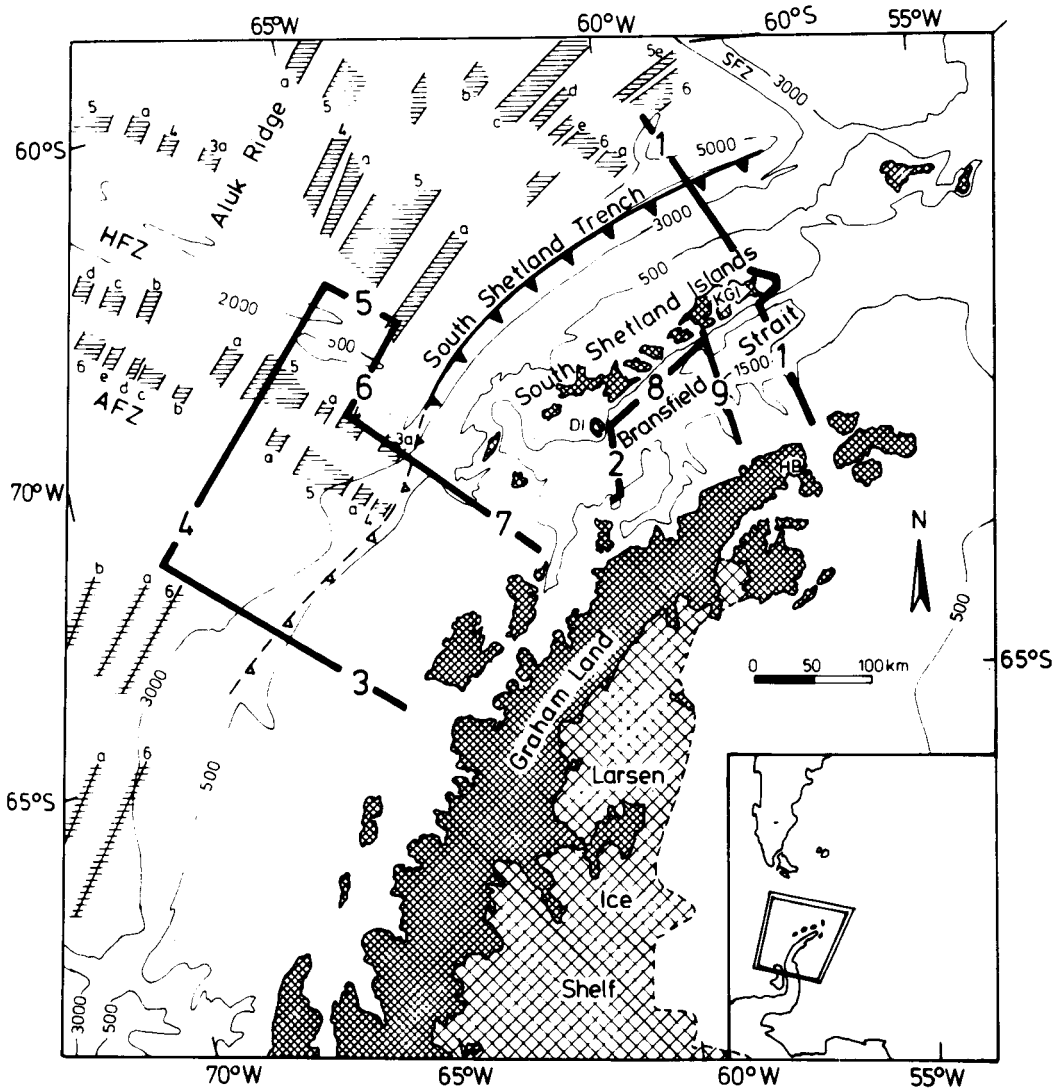

(Meissner R. e.a. 1988)

Fig. 31 Seismic track map of the Antarktis VI/2 cruise.

23.2 Reflection data processing

For the same reasons cited sub 13.2, the bulk of the magnetic tapes recorded during the Antarktis VI/2 cruise are processed at the German partner institutions : at AWI some first processing has taken place on the CONVEX minisupercomputer with DISCO software (COGNISEIS), while Kiel University is processing the data on twinned MicroVAX computers with PHOENIX software (SSL).

23.3 Reflection data interpretation

The present status of all seismic profiles is that a first interpretation has been carried out, with the identification of major depositional sequences but without any formal naming of unconformities or sequences. To our knowledge no sequence naming has been published yet for the Bransfield sequences or the Bellingshausen continental margin. We consequently should start "from scratch". All time to depth conversions on the profiles shown on figs. 35, 38, 39 and 40 have been carried out with a preliminary model assuming a water velocity of 1500 m/s and a sediment velocity of 2000 m/s. Corrections to these depth conversions will be made as more data are available, both by the compilation of published data and by the processing of the multichannel data.

A basic concern before introducing a seismic-stratigraphic nomenclature is to frame the possible geological age of these units, thus trying to establish possible conceptual links with other peri-Antarctic areas such as the Weddell Sea or the Ross Sea sequences and unconformities. In contrast with the eastern Weddell Sea, there is no DSDP or ODP borehole which could be used as calibration well directly in the survey area. The nearest reference well, DSDP hole 325, is more than 500 km further west. The only presently available age information available in this area is locked in the magnetic anomaly pattern of the oceanic crust, which consequently deserves some prior attention.

23.4 Magnetic data interpretation

The pattern of magnetic anomalies of the oceanic plates around the Antarctic Peninsula is well documented by the studies of British Antarctic Survey. The basic document used in our interpretation is BAS Tectonic Map of the Scotia Arc at scale 1:3 000 000 (1985). Another map which has been consulted is the Antarctica Sheet of the Plate-Tectonic Map of the Circum-Pacific Region at scale 1:10 000 000 (Circum-Pacific Council for energy and Mineral Resources 1983). The latter map, probably drafted from the same data base in the considered area, is less convenient for magnetostratigraphic interpretations, but presents some alternative structural interpretations.

A recent aeromagnetic coverage of the Antarctic Peninsula (Parra e.a. 1988) also includes the oceanic plate area northwest of the South Shetland Islands but is - for the oceanic part - taken with some reserve, considering that the lineations offsetting sea-floor anomalies and hence suggesting the presence of fracture zones flagrantly cross the seafloor ridges (e.g. Hero Fracture Zone). It is not excluded that the flight pattern introduced some bias in the contouring of this part of the map. The stuctural interpretation of the Bransfield Strait part of this magnetic survey has been added as background on fig. 32.

The first step in the interpretation of the sea-floor anomalies in terms of geological age was the translation of the magnetic anomaly patterns of the oceanic crust into isochrons, hereby using a standard magnetostratigraphic scale (e.g. Cox and Hart 1986). The result of this analysis is presented on fig. 32.

This isochron map does not only constrain the possible age range of the sedimentary cover on the oceanic plates, but it also offers a full record of the spreading and subduction history of the considered area, thus giving an insight in its geodynamic history.

2.4 Geological interpretation

24.1 Active margin history

A comprehensive analysis of the magnetic anomaly patterns around the Antarctic Peninsula in terms of plate tectonic processes has been published by Barker (1982). We refer to this author for previous literature references dealing with the interpretation of oceanic magnetic anomalies in the southeast Pacific.

The Pacific margin of the Antarctic Peninsula is characterized by a complex subduction history, which lasted from long before the break-up of Pangea up to recent times. The older subduction history left its traces in the ancient accretionary wedge structures and magmatic rocks exposed on the islands and on the mainland, while the more recent , Cenozoic active margin dynamics are well reflected in the magnetic anomalies and the bathymetry of the ocean floor.

Quite striking is the sequence of successive ridge-trench collisions, which probably started in the south of the peninsula some 50 Ma ago. After each collision, which progressively migrated in northward direction, subduction and spreading both stopped in the concerned plate segment ; the trench topography disappeared and the margin became a passive margin. This process proceeded up to about 6 to 4 Ma ago, when the last ridge segment collided just south of Hero Fracture Zone. At this moment, spreading apparently stopped at the northernmost spreading sections, between Hero and Shackleton F.Z., hence before the last ridge segments had reached the trench.The plate segment between Hero and Shackleton F.Z. is hence the last remnant of the subducted Aluk plate.

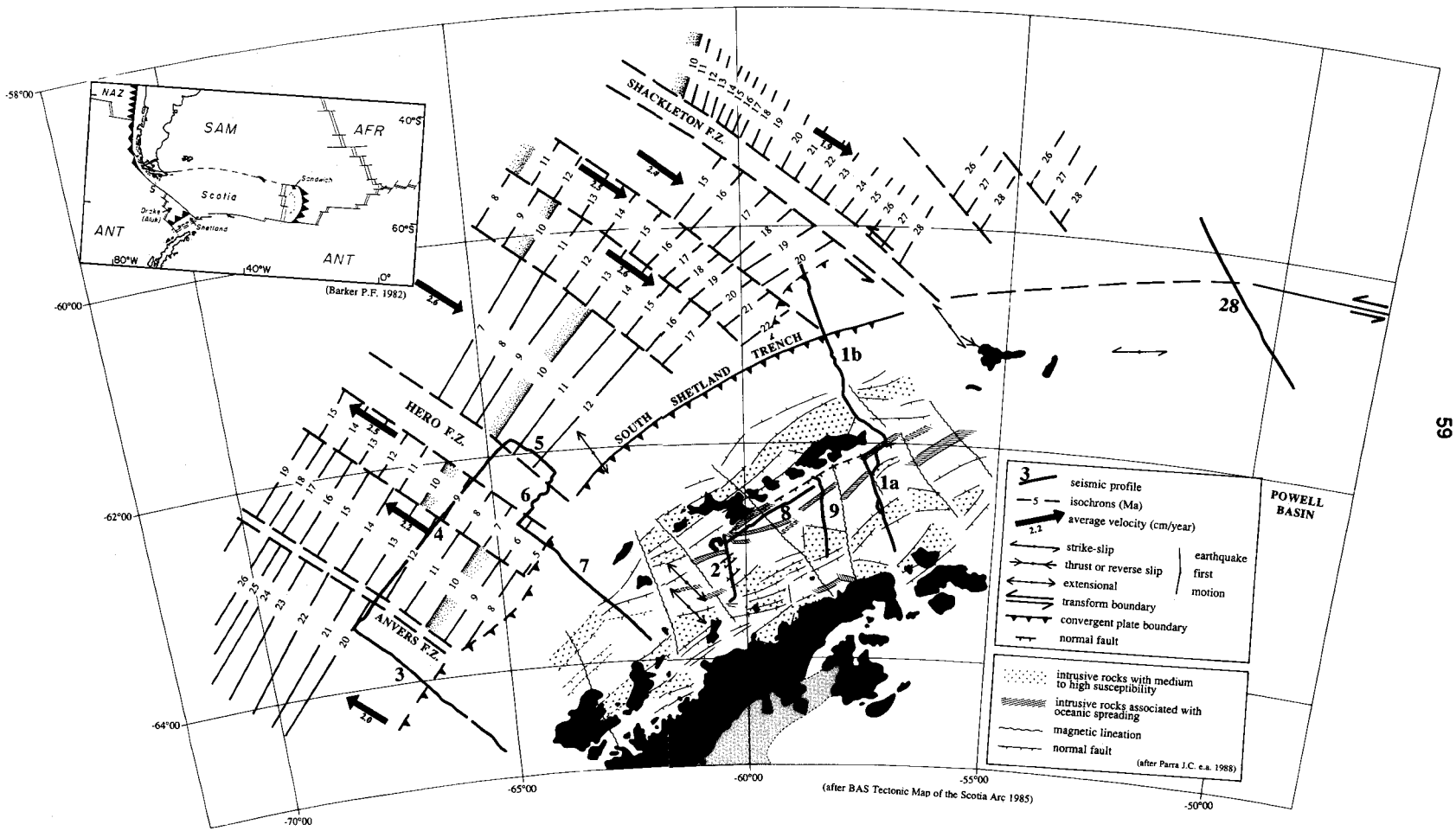

Fig. 32 Structural and aeromagnetical interpretation map around South Shetland Trench.

It has been pointed out by Barker (1982) that the chronology of Bransfield Strait extension seems to be in accord with this process : the back-arc spreading apparently started some 1.3 Ma ago (Roach 1978) but the rifting would have started in part in Late Pliocene times. Also the coinciding length and parallelism of Bransfield Strait, the South Shetland Trench and the desactivated spreading ridges between Hero and Shackleton F.Z. suggest a close relationship. Barker (1982) has proposed that Bransfield Strait opened because of the cessation of spreading, as a result of the continuing sinking of the remnant plate at the trench (the "trench suction" of Forsyth and Uyeda 1975).

24.2 Analysis of the spreading velocities

Half-spreading velocities of the approaching ridge segments south of Shackleton F.Z., averaged over the past 25 Ma, are in the order of magnitude of 20 to 25 mm/a. A closer look at the evolution of these velocities as a function of time however reveals a systematic accelleration, shortly preceding the collision. This observation can be made on fig.33, displaying the half-spreading rate evolution for the plate segments south of Anvers F.Z. (lower left), between Anvers and Hero F.Z. (lower right), between Hero and Shackleton F.Z. (upper right) and northeast of Shackleton F.Z., the Scotia plate (upper left).

The accelleration before the ridge-trench collision south of Hero F.Z. seems to have started about 16 Ma ago, the probable age of the ridge-trench collision southwest of Anvers F.Z.. The gain of momentum acquired by a subducting plate when the ridge approaches the trench might in our opinion reflect an increased net slab pull effect, due among other factors to the decrease in horizontal basal friction force exerted on the (decreasing) basal surface of the subducting slab (fig. 34). The analogy of a sheet of paper slowly pushed over a table's edge, which finally accellerates before falling might be an oversimplified but nevertheless not completely invalid model. This mechanism has possibly been enhanced along this margin by the fact that the ridges migrated in a direction rigorously perpendicular to the trenches, which means that the decoupling of a sinking slab segment from the collided one took place in an abrupt way, hence possibly generating an additional momentum on the adjacent, still partly superficial limb. Such processes possibly might not occur where ridges approach a trench in an oblique way, where the slab pull forces act in a more continuous way, but this hypothesis still has to be controlled (e.g. along the margin of South Chile).

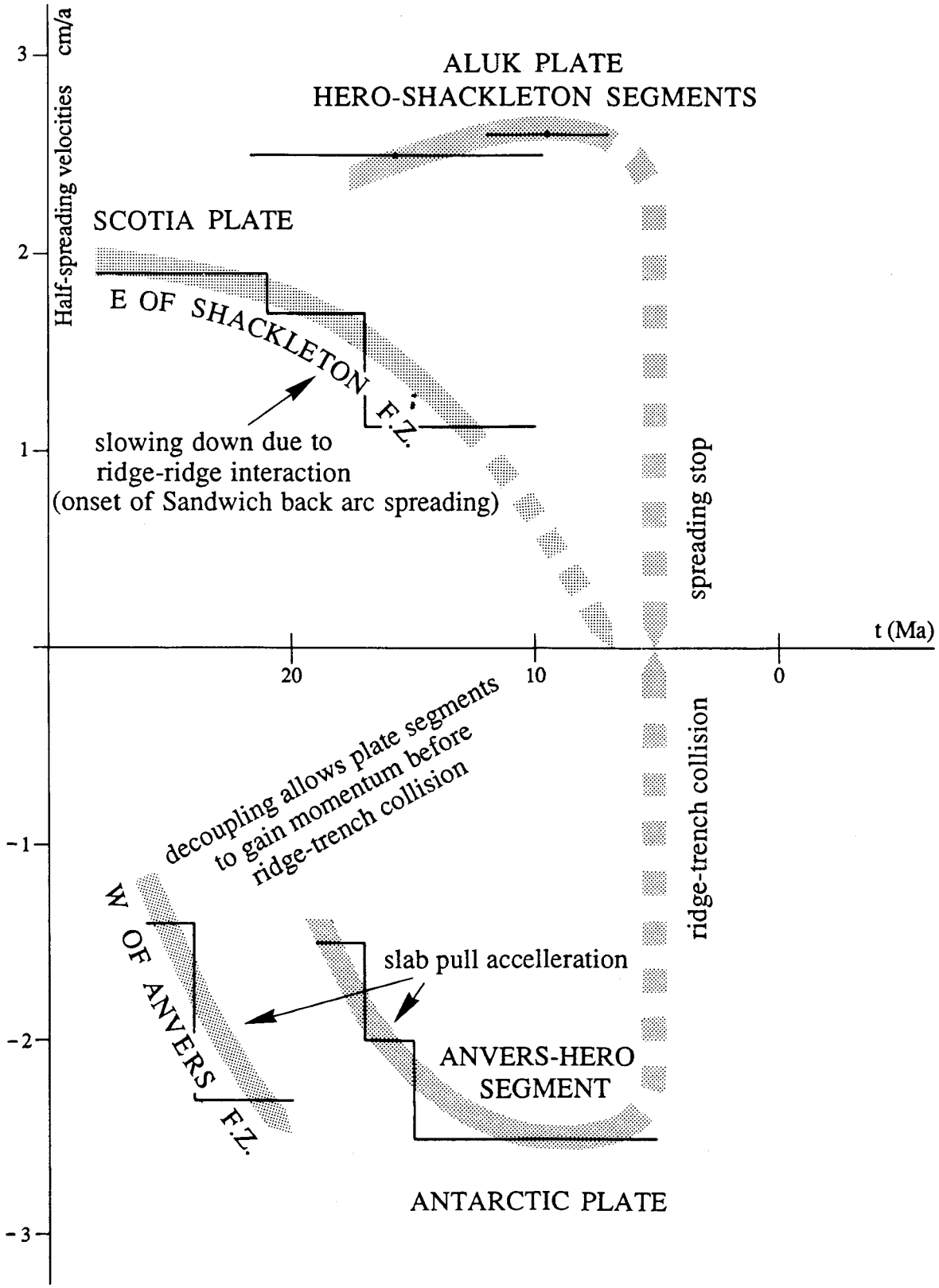

Fig. 33 Evolution of the half-spreading velocities as a function of time.

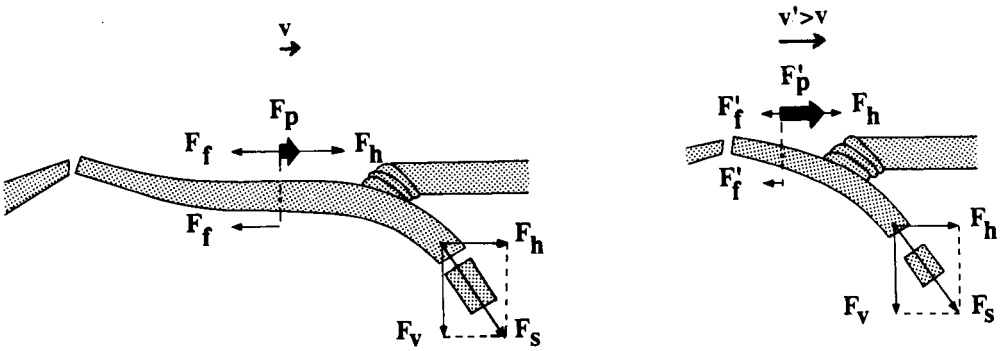

Fig. 34 The gain of momentum acquired by a subducting plate when the ridge approaches the trench might reflect an increased net slab pull effect.

F_S = slab pull force
F_V = vertical component
F_h = horizontal component
F_f, F'_f = basal frictional drag force
F_p, F'_p = net slab pull force
v, v' = slab velocity (half-spreading)

24.3 The oceanic domain and the fracture zones

Profile 4 (fig. 35) is quite informative about the nature and setting of Hero and Anvers Fracture Zones, which have very different geophysical, structural and morphological expressions. It is also the only profile which shows very prominent structures deep in the magmatic oceanic crust, even directly visible on the analog sections.

Anvers F.Z., which is the southernmost one on this profile, is absolutely not reflected in the seafloor topography, except for a faint depression. It separates two segments of oceanic crust of quite different geological age : the southern crust has an age of 19.8 Ma, while the northern one is about 12.2 Ma old (fig.32). The older, cooler oceanic lithosphere has sunk deeper, in accordance with the laws of thermal subsidence (Parsons and Sclater 1977). The vertical offset of the top of the magmatic oceanic lithosphere as a result of the age difference of 7.6 Ma is about 300 m. As a consequence of the age and depth differences across Anvers F.Z., there is also a considerable difference in thickness of the sedimentary cover on both sides : about 900 m south of Anvers F.Z., versus some 500 m north of it (assuming an average sediment velocity of 2000 m/s ; better constrained values should result from the ongoing velocity analyses on the multichannel seismic data). A most conspicuous feature marking the presence of the F.Z. is the alignement of diffraction hyperbolae in the magmatic crust, dipping south. A possible explanation of this feature will be proposed in the following chapter.

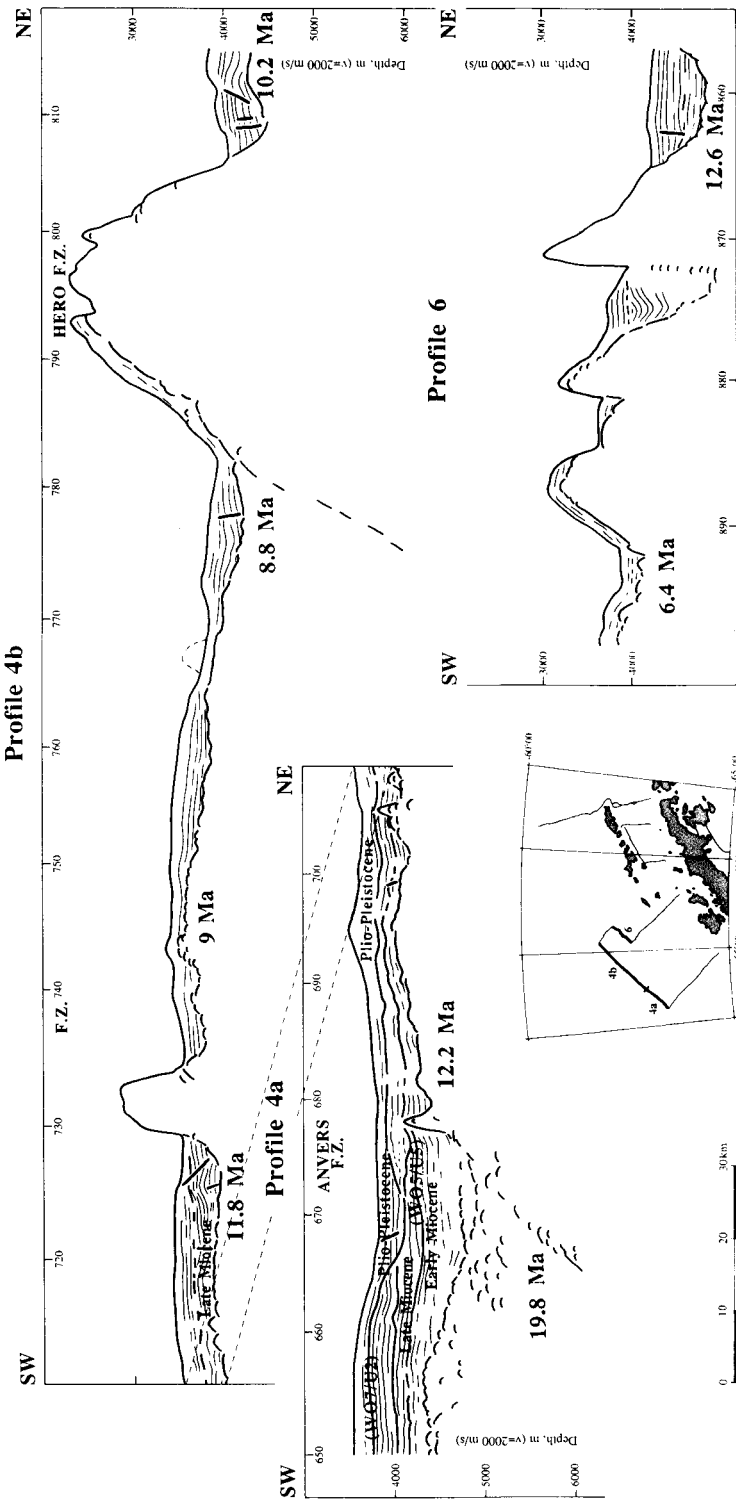

Fig. 35 Interpreted reflection profiles (4 and 6) crossing the Hero and Anvers Fracture Zones.

A second fracture zone, characterized by a much smaller age jump (2.8 Ma), is seen on the central part of profile 4 (4b). The vertical offset of the top of the oceanic lithosphere is consequently smaller, and also the difference in thickness is smaller but nevertheless obvious. A small seamount or ridge is visible, somewhat south of the location of the fracture zone which would be derived from the magnetic anomaly map. One should be careful in interpreting sediment thicknesses across fracture zones characterized by seafloor highs, as increased current velocities at the foot of the ridges might have impeded sedimentation or caused erosion (Davies and Laughton 1972). Such moats have frequently been observed along the continental slope and the Explora-Andenes Escarpment in the Weddell Sea.

The third and most impressive fracture zone on this profile is no doubt the Hero F.Z., characterized by a mighty ridge, towering more than 1500 m above the surrounding seafloor. Its southern flank is covered by a sedimentary layer which is only slightly thinner than that on the southern oceanic plate, suggesting that the ridge emplacement has occurred relatively shortly after the plate segment had spread away from the ridge.

The age contrast across Hero F.Z. is not impressive (1.4 Ma), but one should keep in mind that this contrast is purely fortuitous and changes if we move along the ridge, as the lithospheric segments on both sides did belong to different plates, on either side of a spreading ridge (fig. 32). Strictly speaking, Hero F.Z. should be regarded as a recently extinct transform fault, desactivated when spreading stopped after the last ridge-trench collision, while the preceding two fracture zones were aseismic ridges before subduction stopped. Hero F.Z. was up to the last ridge-trench collision a true plate boundary, separating the Aluk plate from the Antarctic plate to the south just like Shackleton F.Z. separated Aluk plate from Scotia plate to the north.

A most intrigueing feature again is the dipping reflector in the magmatic oceanic crust, plunging in southward direction in continuation of the southern ridge flank. This reflector, also well visible on the analog profile, might yield a clue to the nature of the Hero F.Z. ridge, as discussed in 24.4.

On profile 6 further south, the ridge marking Hero F.Z. is segmented into three ridges. The southwest flank of the southernmost ridge is covered by a thin layer of sediments, which is clearly in continuity with the sedimentary cover of the oceanic plate, as was the case further north. This sedimentary cover is somewhat thinner than in the north, which is not in contradiction with the younger age of the underlying oceanic lithosphere. The sedimentary fill ponded between the two northernmost ridge segments on profile 6 is rather impressive and is composed of a lower, folded sequence truncated by an erosion surface and covered by a younger sedimentary cover. The thickness of the lower sequence is intrigueing, as it looks as if this sequence has been deposited in a relatively early stage of the ridge development, before being deformed, eroded and buried by a sequence which seems to have been deposited in a similar context as the sedimentary cover of the southern ridge segment.

North of the northern ridge on profile 6, another small sedimentary basin shows up. The difference in elevation of the top of the oceanic crust in comparison with that on the other side of Hero F.Z. seems to be at least qualitatively in agreement with the difference in age (6.2 Ma). An analysis of the sediment thickness close to this ridge should however here too be carried out with utmost reserve. As shown on tying profile 5 (fig. 38), parallel to the fracture zone, this little basin forms part of a very peculiar sequence of highs and lows in the magmatic oceanic crust, draped by a sediment cover of quickly changing thickness. Even the magnetic interpreter should be aware of the potential pitfall : the observed sequence of basement highs is likely to generate at the sea surface a rithmically banded anomaly pattern which purely reflects the magmatic bedrock morphology but which possibly could confuse the observation of polarity reversal patterns.

24.4 Fracture zone processes

The two southward dipping reflectors discovered in the oceanic crust where profile 4 intersects the Anvers and Hero Fracture Zones, together with the morphology of the oceanic lithosphere abutting against these surfaces might well be diagnostic for the processes which have shaped the Anvers and Hero F.Z..

As a lithospheric slab moves away from a spreading ridge, it slowly cools. This cooling does not only result in vertical thermal contraction of the lithosphere, but also in horizontal contraction. While vertical thermal contraction is expressed in the subsidence of seafloor with age (Parson and Sclater 1977), horizontal thermal contraction can produce large internal stresses. It is convenient to separate thermal stresses into two parts, the first due to lateral changes in the vertically averaged temperature (thermal contraction stresses s.s.) and the second due to changes in the temperature variation with depth. The latter are referred to as thermal bending stresses (Haxby and Parmentier 1988).

Thermal contracting stresses s.s. may have a variety of important consequences. They may in some way contribute to the formation (Sandwell 1986) and opening of transform faults and fracture zones, where they consequently may contribute in a significant way to magmatic and

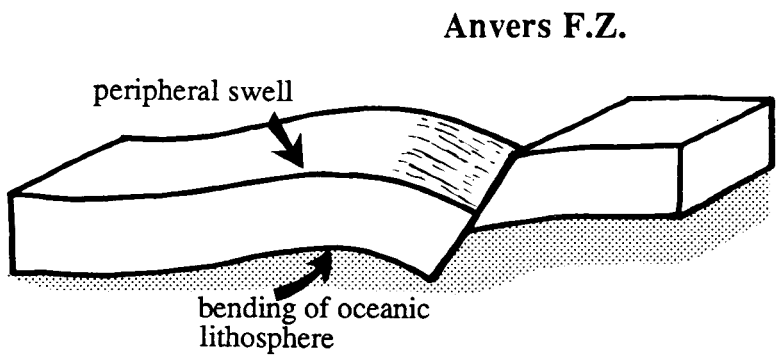

Fig. 36 Model of Anvers F.Z., illustrating the possible thermal bending on the old side of the F.Z., in accordance with the model of Haxby and Parmentier (1988).

hydrothermal processes. Thermal bending stresses are responsible for the flexure of oceanic lithosphere at fracture zones. This process has been described in detail and modelled by Haxby and Parmentier (1988).

At Anvers F.Z., the tensional thermal stresses seem to have been accomodated by a component of downward slip along the dipping fault plane. The bending of the lithosphere against this dipping plane probably occurred in response to the thermal bending stresses described above, in accordance with Haxby and Parmentier's model (fig. 36)

At Hero F.Z., there is clearly more than simple normal faulting and flexural bending against a dipping fault. Here this fault clearly forms the flank of a huge intrusion, which rose high above the seafloor. Two types of intrusion and extrusion at ("leaky") fracture zones are known (Kastens 1987) : the effusive extrusion of basalts or the diapiric extrusion of serpentinite bodies, or a combination of both. Considering the continuity of the crustal reflector with the southern flank of Hero ridge, we are inclined to opt for the hypothesis of a diapiric intrusion of hydrated upper mantle material like serpentinite, at least where our profile crosses the ridge. The presence of basaltic flows associated with such a ridge on other places can certainly not be ruled out.

The diapiric intrusion of a serpentinite body into the fracture zone, opened by the thermal contracting stresses, probably finds its early origin in the hydrothermal circulation of sea water deep in the fracture zones, resulting in serpentinization of upper mantle peridotite. The lowering of the density of these ultramafic rocks by serpentinization generates a buoyancy relative to deep crustal rocks such as gabbros. This buoyancy and the low strength of serpentinite at a temperature of a few hundred degrees Celsius can force the serpentinite body into the fracture zone and create a huge diapiric ridge. A model of such an intrusion in the Vema F.Z. (central Atlantic) is shown on fig. 37 (after Bonatti and Honnorez 1976).

Dredging along the flanks of Hero F.Z. in a future research programme should allow to test this hypothesis.

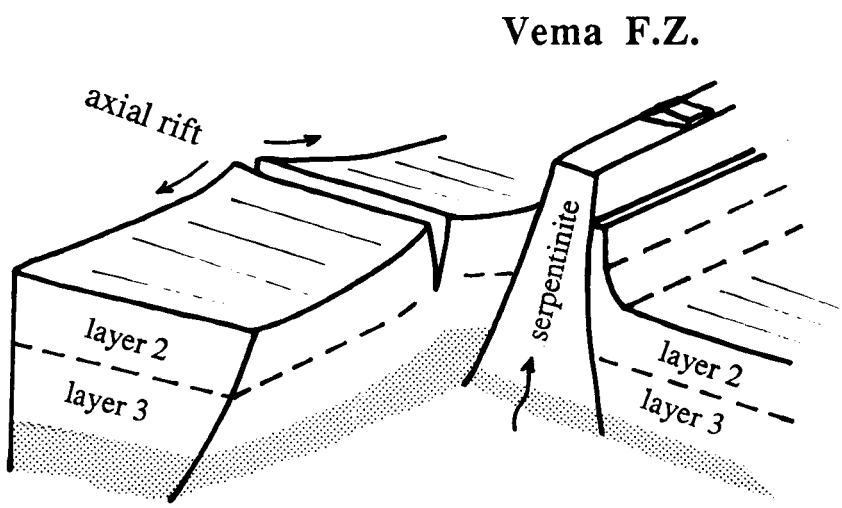

Fig. 37 Model of Vema F.Z. (Central Atlantic, after Bonatti and Honnorez 1976), a possible analog of Hero F.Z. in front of the Antarctic Peninsula.

24.5 Age of the oceanic sedimentary cover

The thickest sedimentary cover shown on profile 4 (4a) south of Anvers F.Z. is situated on oceanic crust with an age of about 20 Ma, which means Early Miocene. There are consequently arguments in favour of assigning an Early Miocene age to the basal depositional sequence, filling the depression south of the fracture zone.

Across Anvers F.Z. on the same profile, the oceanic plate is about 12 Ma old, which locates it in the late Middle Miocene. This means that the lower depositional sequence directly resting on this plate segment might largely be assigned a Late Miocene age. The basal level of this sequence seems to correlate laterally with a prominent unconformity south of Anvers F.Z., which hence suggests a possible hiatus in Middle Miocene times. We are consequently inclined to correlate this event with the U5 event of Hinz and Kristoffersen (1987), dated 16-13 Ma, and thus also with the prominent WO5 unconformity identified on seismograms and on Site 693 along the eastern margin of the Weddell Sea.

The Mid-Miocene hiatus which seems to reflect a major ice advance (cfr. 15.3) is also known from DSDP Site 325, some 500 km further to the southeast (DSDP Leg 35 Shipboard Scientific Party, 1976). On this site it separates a lower unit of coarser clastic rocks of Early Miocene age, drilled over a length of 150 m (down to the bottom of the 720 m deep hole), from a 570 m thick upper unit essentially consisting of Late Miocene and Pliocene claystones, with minor siltstones and sandstones. The whole sedimentary sequence seemed to be of turbiditic origin, except for a few thin beds with mainly biogenic components. The oldest ice-rafted debris occured in Lower Miocene claystone. The thickness of the Late Miocene -Pliocene unit in DSDP Site 325 (570 m) is in perfect agreement with the thickness of the supposed Late Miocene to Plio-Pleistocene sequences in the vicinity of Anvers F.Z. on profile 4 (about 500 m).

On this profile we still see another unconformity, deeply ravinating the underlying (Late Miocene ?) sequence. We are inclined to identify this unconformity with the base of the Plio-Pleistocene deposits. On Site 325, Pliocene deposits are particularly thick (about 400 m out of the 570 m of the upper unit). The high accumulation rates (120-150 m/Ma) of the Early to Middle Pliocene recorded both in well 325 and in other wells in the Bellingshausen Sea (DSDP Sites 322 and 323) suggest vigorous continental erosion and sediment flux during this time. On profile 3 (fig. 38), the sequence of supposed Plio-Pleistocene age at the foot of the continental slope is up to 600 m thick.

24.6 Trench, slope and fore-arc environment

Profiles 3, 7 and 1 (figs. 38 and 39) present three different images of the South Shetland trench and slope environment. Profile 3 shows the sedimentary wedge on top of the collided

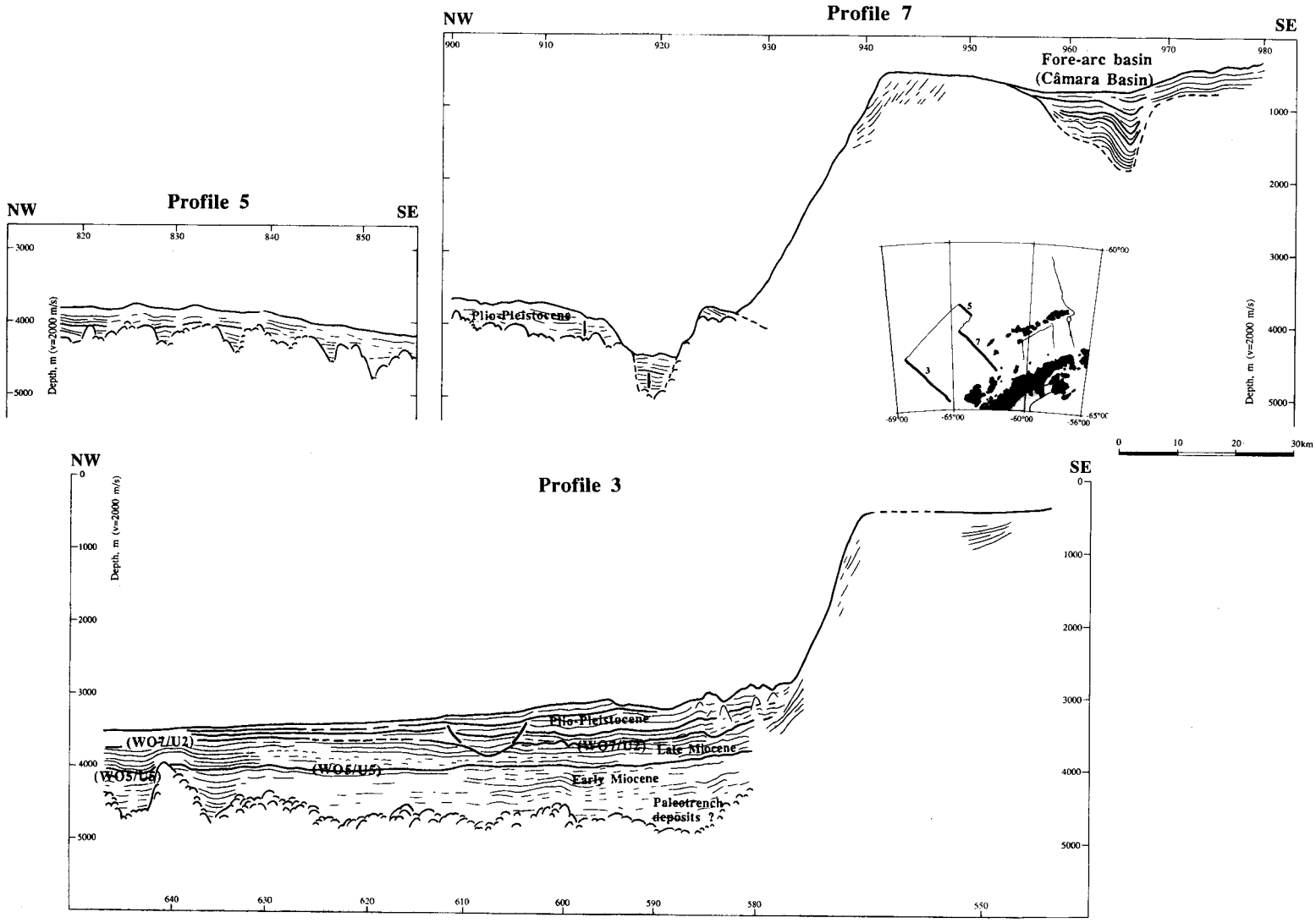

Fig. 38 Interpreted reflection profiles (3, 5 and 7) crossing the South Shetland Trench.

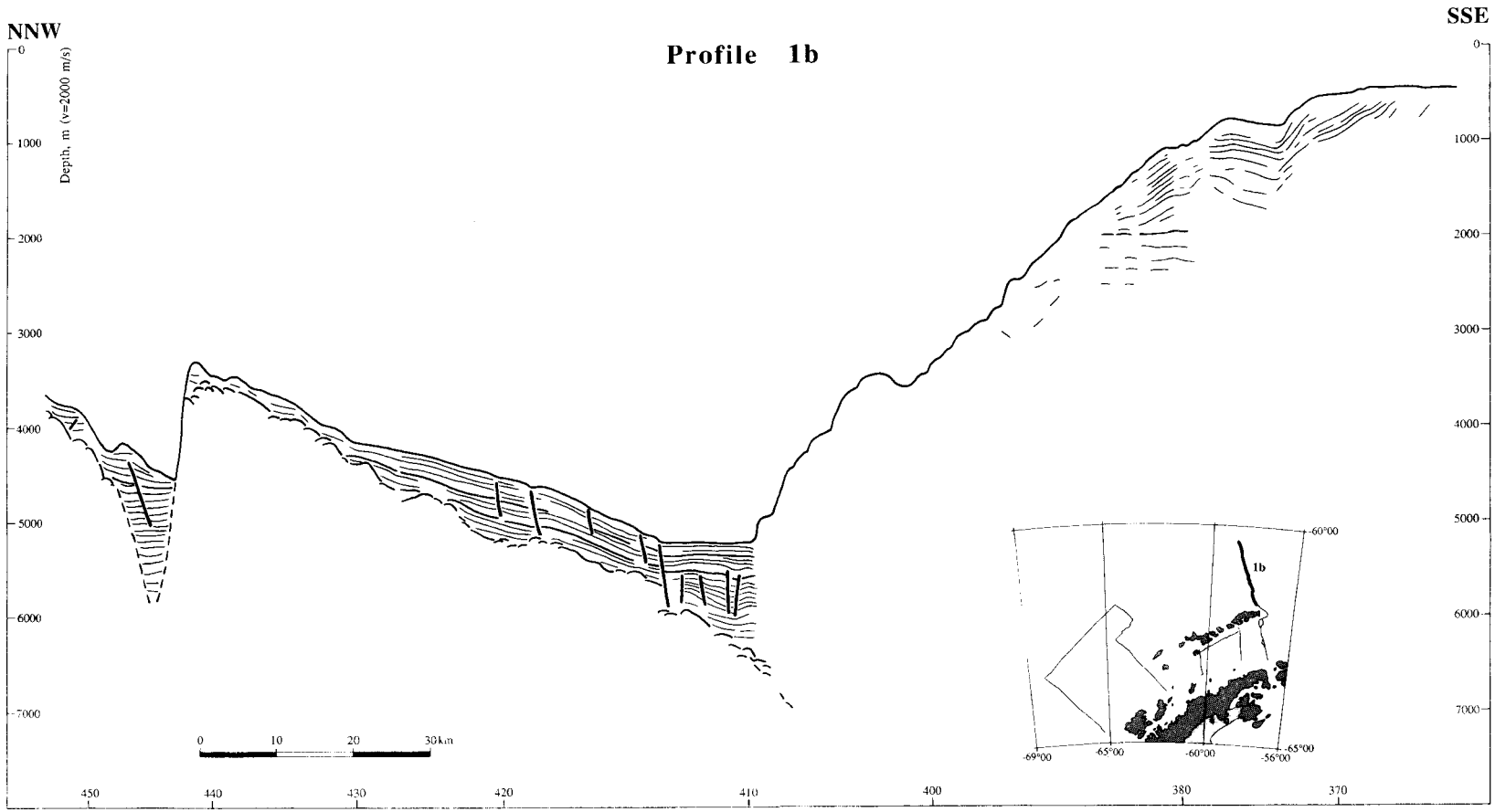

Fig. 39 Interpreted reflection profile (1b) crossing the South Shetland Trench.

Antarctic plate segment, profile 1 shows a classical image of a trench and profile 7 shows a transitional stage between both.

246.1 The paleotrench

The sedimentary wedge at the foot of the continental slope on profile 3 shows the same three depositional sequences as described on the tying profile 4 south of Anvers F.Z. (24.5), however with larger thicknesses. This threefold structure has also been described by Kimura (1982) on his profile 9, linking Site 325 to the continental slope. Kimura's units C, B and A respectively correspond with the Early Miocene, the Late Miocene and the Plio-Pleistocene terrigeneous turbidites, identified in well 325. In accordance with Kimura's observation, we cannot rule out that the lower unit on our profile also includes a basal wedge of paleotrench deposits, characterized by a slightly chaotic reflection configuration.

The large thickness of sediments observed at the foot of this slope (in total about 2000 m, taking into consideration that the lower units will most probably have velocities higher than 2000 m/s), might suggest the proximity of a sediment fan. The initial report of the PETROBRAS cruise (unpublished note presented at the 5th Int. Symp. on Antarctic Earth Sciences, Cambridge 1987) mentions the presence of a large submarine fan on the oceanic basement off Câmara Basin.

An interesting remark is that the age of the unconformity, which we here too would correlate with the WO5 unconformity in the Weddell Sea (the U5 event), is about the same as the age of the local ridge-trench collision (16 Ma). From this time onwards this margin behaved as a normal passive margin. This implies a continuity of deposition over shelf, slope and continental rise, as clearly shown on profile 3 and also on Kimura's profile 9. On our profile, it is possible to identify clear downlap structures on top of the WO5 unconformity. Kimura (1982) already reported that units B and A become strongly prograding east of 80° W.

The lower beds of the Late Miocene turbidites on top of WO5 locally show a wavy to hummocky and chaotic reflection pattern, quite similar to that observed in the slumped horizons of sequence *WF 3* of the Crary Fan off Halley Bay in the Weddell Sea. Both the sedimentary and time context of these sediment deformations could possibly be quite similar.

The erosional nature of unconformity WO7 with local valley incisions, which had already been observed on profile 3, is confirmed on this profile. Normal faults due to differential compaction have developed in the Plio-Pleistocene cover above the buried valley flanks.

246.2 The transitional trench and the Câmara fore-arc basin

Profile 7 (fig. 38), still located south of Hero F.Z. and thus on a site of former ridge-trench collision but at the very edge of the paleotrench extension, shows a structure already quite different from that on profile 3. It should be mentioned that the collision on this segment of the

Antarctic plate occurred in much more recent geological times, about 4 to 5 Ma ago, which might have played a role in the preservation of some trench characteristics.

Considering the young age of the collided plate segment (5-6 Ma), the sedimentary cover of the oceanic plate cannot be much older than Plio-Pleistocene. A most peculiar feature at the foot of the continental slope is a basal step, covered by some sediments. Such inner walls have already been observed in many other trenches, in particular along the Japanese Islands and in the Middle America Trench (DSDP Sites 488 and 494). It might represent a fragment of a subducted crustal slab, bound at its top by a thrust plane. This features might hence represent a late witness of the accretionary processes which no doubt substantially have contributed to the growth of the continental margin on this site.

The top edge of this continental margin shows an important set of obliquely prograding sediments, most of which have probably been deposited and truncated by the advancing grounded ice sheets in the recent Plio-Pleistocene glacial period.

The most interesting feature on this profile however is no doubt the very prominent sedimentary basin met on the continental shelf, characterized on this profile by a sediment thickness of more than thousand metres. The discovery of a long basin on the Bellingshausen shelf had been reported in 1987 by PETROBRAS (cfr. 2.2) and informally named Câmara Basin. Looking at the zig-zag tracks of the PETROBRAS cruise on this part of the shelf, there is little doubt that the basin seen on profile 7 is the Câmara Basin. The only description given in the Brazilian preliminary report however is that the upper sequences of this basin are represented by prograding sediments, which is not obvious on this profile.

Considering both the position and structure of this basin, we believe it is a typical fore-arc basin, previously unknown in literature. This hypothesis is corroborated by the observation of similar basin structures on many other active margins, both recent (e.g. along Western Luzon, Philippines, Lewis and Hayes 1985) and fossil. The genesis of this basin on the back of the accretionary wedge must have been closely related to the growth and rotational uplift of this wedge.

If such an elongated basin has not been reported on the shelf further north, which has been crossed by Brazilian and Polish reflection lines and also by the Antarktis VI/2 profile 1, it may indicate that it is not present north of Hero F.Z., which would yield another clue for the strong segmentation of the continental margin by Hero F.Z. .

246.3 The South Shetland Trench

The northern part of reflection line 1, off King George Island, shows a classical trench profile, however with some puzzling problems.

A first problem is the sedimentary cover of the plunging oceanic plate, which shows a distinct onlap in seaward direction, by which it quickly thins out. A second problem is the steep fault in the northern part of the profile, shaping a kind of secondary, filled trench. This trench-

like feature can easily be followed in the seafloor morphology as a depression, which further south merges with the main trench (fig. 32). A third problem is the fact that the sediments in both trench depressions are barely deformed, which seems in contradiction with a "trench suction" mechanism (24.1) : if Bransfield Strait has been spreading in recent geological times, why is there no apparent compressional deformation in the trench? In other words, where is the space accommodation for the opening created in Bransfield Strait, as it is unlikely that any space accommodation would have been created east of Bransfield Strait, at the side of the peninsular mainland. There is at the present time little conclusive evidence answering these questions.

The problem of the sediment cover is certainly not elucidated by indications of the plate age, as no datable magnetic anomalies have been identified yet. Extrapolating magnetic information from plate segments west of the small secundary trench would suggest an age of 21 to 24 Ma (fig. 32), which means the lowest Lower Miocene. The thickness of the sediments on such a relatively old plate segment is consequently very modest, at least in seaward direction and especially on top of the faulted scarp. There are few arguments for postulating a sedimentary environment starved from sediment supply, considering the proximity of the shelf. We consequently have no explanation for this observation yet, also due to a lack of reference profiles on the Aluk plate further west.

The conspicuous onlap in a way evocates a thermal onlap on a spreading ridge flank, a model certainly difficult to fit into the local tectonic context. Still the relatively large onlap angle clearly does suggest a deposition against a sloping surface, which might argue for a deposition after the generation of the faulted scarp. But why should a relatively old plate segment have remained largely bare of sediments until it got tilted, for whatever reason? Such an argumentation hence also moves the problem of the sediment cover to the problem of the origin and time of origin of the scarp.

The close association of the "secondary trench" with the main one, with which it seems to merge further west in a kind of triple junction, evocates in a first approach an incipient trench backstepping. There is however no evidence of accretionary wedge building along the northern fault scarp. The most plausible explanation seems to be that the small triangular plate fragment, squeezed between the subduction zone of the South Shetland Trench and the still active Shackleton F.Z., chipped off the main Aluk plate and got tilted. One factor which possibly could have contributed to an increase of the stress field in this corner is the fan-shaped opening of Bransfield Strait (24.7). The two-dimensional velocity field analysis presently in development at RCMG, aiming at the reconstruction of relative plate motion velocities and of triple junction migration paths at selected times in the past, will possibly shed some light on this problem. The most straightforward solution will anyhow also be the collection of more field data in this F.Z.-trench triple junction area.

24.7 The back-arc basin of Bransfield Strait

The analysis of the Bransfield data is still in a very initial phase. Literature dealing with gravimetric, magnetic and refraction seismic surveys in this basin is vast and should be carefully evaluated for a sound insight in the structure and geodynamic history of this basin. The Antarktis VI/2 data should also be matched with the former high-resolution data acquired by Kiel University and possibly also other reflection data sets, in a joint effort comparable with the one in action in the Weddell Sea. In the meantime a preliminary interpretation of the seismic profiles has been carried out, presented on fig. 40. The lay-out of the profiles is shown on fig. 32, where the structural interpretation of the aeromagnetic data from Parra e.a. (1988) has been added as background, for illustrative purposes. Elements of this map deemed of lesser relevance for our interpretation will be deleted in a later phase.

The three transverse profiles 2, 9 and 1a (fig. 40) convey an excellent impression of the succession - in space and time - of the rifting and drifting phases which generate an oceanic domain. Spreading propagated from north to south.

Profile 2 which started from the presently active vulcano of Deception Island shows a characteristic graben and horst province, with tilted blocks and rotational fault development in a regime of continental extension. The maximal sediment thickness (600 m) has been found in a central graben, also drawn on fig. 32. The faults do not seem to reach the surface, which rises some doubts about any continuing activity in recent geological times. The focal analysis of earthquakes however still gives evidence of actual normal faulting (fig. 32).

Profile 9, located centrally in Bransfield Strait, probably shows a first phase of development of oceanic crust, possibly constrained to the northern flank of the basin, with a ridge structure which clearly shows on the aeromagnetic interpretation map (fig. 32). The initial rift has developed into an asymmetric basin, with sediment thicknesses of 800 to 1000 m in the axial zone. The prograding sedimentary wedge infilling the basin from the south probably reaches thicknesses larger than 1000 m.

The northernmost profile shows a truely oceanic domain, in the northern part of the profile. Again there is a distinct ridge structure in this domain, marked by an anomaly on the aeromagnetic data. The oceanic crust has been assigned an age of 1.3 Ma by Roach (1978). The sediment thickness of some 300 to 400 m on the oceanic crust reflects high accumulation rates.

The prograding sediment wedge on the southern rim of the basin buries an ancient rift and probably impinges further north on the oceanic crust. The maximal sediment thickness of the prograding sequences amounts to some 800 to 1000 m, while the sediment fill of the buried graben could be rated at another 1000 m.

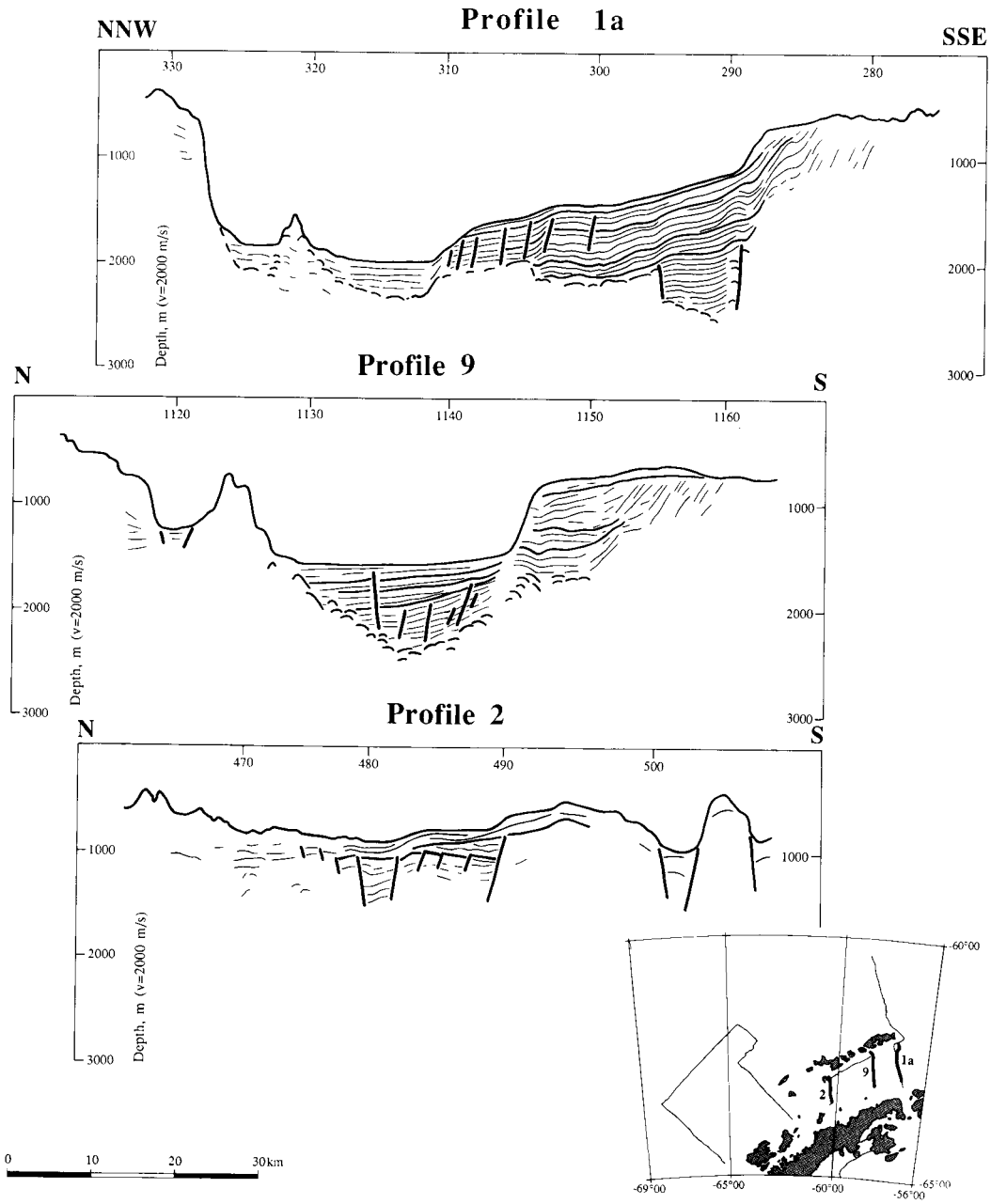

Fig. 40 Interpreted reflection profiles (2, 9 and 1a) crossing Bransfield Strait.

24.8 The transform boundary north of Powell Basin

On the return route of cruise Antarktis V/4 in the Weddell Sea, a profile has been shot over the transform boundary between the Scotia plate in the north and the Antarctic plate with Powell Basin in the south. This profile (ANT V/4-28 shown at far right on fig. 32) crossed a 5300 m deep trench, flanked by huge ridges (fig. 41). A small axial ridge flanked by a very symmetric set of diverging reflectors has been discovered in the deepest part of the trench (B-B'). The main shear zone has apparently been crossed north of the northern ridge on the profile (A-A').

This profile still has to be framed in the regional geodynamic and stratigraphic context, after which a detailed interpretation of the sedimentary sequences and structural features will be carried out. The recently released data from wells 695, 696 and 697 of ODP Leg 113 might provide supporting data.

2.5 Conclusions and perspectives

Although the analysis of the Antarktis VI/2 cruise is still in a preliminary phase, a number of interesting results are already emerging, both in the domain of the geodynamic evolution of the western margin of the Antarctic Peninsula and in the domain of the stratigraphy of the sedimentary basins. The joint analysis of both domains is essential in an active margin area where sedimentation and tectonics are closely linked.

25.1 Dynamics of the converging plate boundary

The acquisition of seismic profiles over some hitherto seismically unexplored oceanic regions off the Antarctic Peninsula motivated a reassessment of the spreading and subduction history from available magnetic data. This analysis has shed some light on the possible role of the slab pull effect on the terminal accelleration of the spreading, recorded shortly before ridge-trench collision. The present reassessment forms the base of a two-dimensional velocity field analysis, which possibly could yield a better insight in the complex Shackleton F.Z.-South Shetland Trench triple junction. It might also help to explain the origin of a secondary trench-like structure, crossed by a reflection profile.

25.2 Thermal contraction effects and magmatic diapirism at fracture zones

The profiles shot over Anvers and Hero F.Z. present to our knowledge the first reflection seismic evidence of thermal bending and magmatic diapirism along these important fracture zones. The fracture planes themselves can be followed deep in the oceanic crust. At Hero F.Z., such a plane

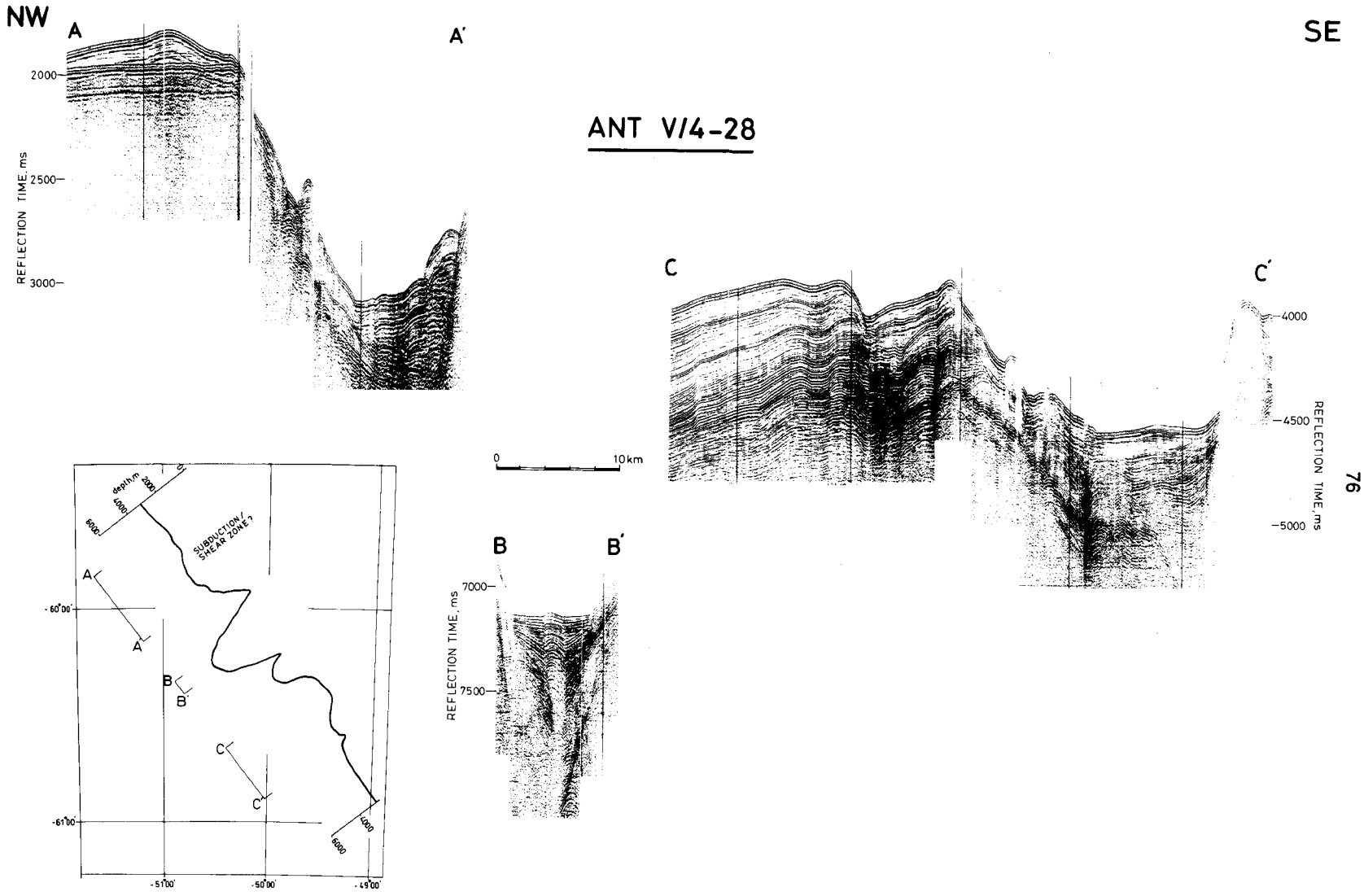

Fig. 41 Reflection profile (ANT V/4-28) recorded across the transform boundary between the Scotia plate and the Antarctic plate

in the oceanic crust can be followed in full continuity with the flank of the ridge, arguing for a diapiric origin of the ridge rather than an effusive one. The most likely nature of the Hero F.Z. ridge on the investigated profile is a serpentinite body, created by deep hydrothermal metamorphism of upper mantle peridotites, in analogy with e.g. Vema F.Z..

25.3 Oceanic seismic stratigraphic analysis

The deficiency of direct borehole control for the analysis of the seismic stratigraphy in the oceanic domain could be mended by a careful constraint of the age of the sedimentary cover through the above mentioned analysis of the magnetic anomaly patterns and their translation into a plate isochron map. The success of this approach was proved by the convergence of the results with those obtained by Japanese investigators further south, by direct shooting over a DSDP reference well: both the structure and the chronostratigraphic interpretation of the margin deposits which are in a similar geodynamic and sedimentary setting yield results in close agreement.

This approach allowed to identify stratigraphic unconformities at geological times which correlate in a very coherent way with some identified in the Weddell Sea. Both domains were in the considered period (Miocene to Plio-Pleistocene times) in open connection through Drake Passage, but the dominant control seems to be again rather climatic than paleoceanographic.

Sediment deformation features in slope foot deposits of Late Miocene age display striking similarities with the sediment flowage and slumping observed in fan deposits in the Weddell Sea, possibly in a similar time context and sedimentary environment.

25.4 Segmentation of the trench, slope and margin

The huge Hero F.Z. seems to have played a major role in the segmentation of the western margin of the Antarctic Peninsula. The hypothesis of the serpentinite nature of this ridge has a profound impact, as the degree of buoyancy of a ridge meeting a trench controls the type and extent of the structural, geochemical and petrological segmentation of that margin. Huge buoyant ridges even can stop subduction, as is known in the Lesser Antilles (Bouysse and Westercamp 1988). Whether such a phenomenon might have played a role in the stop of the subduction after the last ridge-trench collision at the western Peninsula margin deserves due attention.

The segmentation of the margin anyhow is not only expressed in the already well known difference in slope of the continental slope and the areal extent of the South Shetland trench and Bransfield Strait, but also possibly in the areal extent of an elongated basin on the outer shelf south of Hero F.Z., in our study interpreted as a fore-arc basin.

25.5 The rift-drift structure of Bransfield Strait

The sequence of profiles recorded in Bransfield Strait yield additional data about the fan-shaped opening of this back-arc basin and about its sedimentary infill. These data will be as much as possible integrated in the already recorded data set of previous studies in order to contribute to a general seismic-stratigraphic and geodynamic analysis of this remarkable basin. The more general geodynamic analysis of this area will also benefit from the analysis of a reflection profile recorded further west in the axis of Bransfield Strait, across the transform boundary between the Scotia plate and the Antarctic plate.

References

Arthur, M.A. & Natland J.H. (1979) - Carbonaceous sediments in the North and South Atlantic : the role of salinity in stable stratification of Early Cretaceous basins. In : Talwani, M., Hay, W.W. & Ryan, W.B.F. (eds), Deep Drilling Results in the Atlantic Ocean. Continental Margins and Paleoenvironment. Ewing Series 3, Am. Geophys. Union. Washington, D.C., 375-401.

Aschcroft, W.A. (1972) - Crustal structure of the South Shetland Islands and the Bransfield Strait. Brit. Antarct. Surv. Sci. Rep. **66**, 1-43.

Barker, P.F. (1982) - The Cenozoic subduction history of the Pacific margin of the Antarctic Peninsula : ridge crest-trench interactions. J. geol. Soc. London, **139**, 787-801.

Barker, P.F. & Burrell, J. (1977) - The Opening of Drake Passage. Marine Geology, **25**, 15-34.

Bearman (ed) (1989) - The Ocean Basins : there structure and evolution. Open University Course, Milton Keynes.

Bonatti, E. & Honnorez, J. (1976) - Sections of the Earth's Crust in the Equatorial Atlantic. J. Geophys. Res., **23**, 4104-4116.

Bouysse, P. & Westercamp, D. (1988) - Effets de la subduction de rides océaniques sur l'évolution d'un arc insulaire : l'exemple des Petites Antilles. Géologie de la France, **2-3**, 3-38.

Brown, L. F. Jr. & Fisher, W.L. (1977) - Seismic stratigraphic interpretation of depositional surfaces : examples from Brazilian rift and pull-apart basins. Am. Ass. Petr. Geol. Mem., **26**, Tulsa, 213-248.

Cox, A. & Hart, R.B. (1986) - Plate Tectonics - How it Works. Blackwell Scientific Publications, Inc., 392 pp.

Davies, T.A. & Laughton, A.S. (1972) - Sedimentary Processes in the North Atlantic. In : Laughton, A.S., Berggren, W.A. e.a. (eds), Initial Reports DSDP, **12**, Washington (U.S. Govt. Printing Office), 905-934.

de Graciansky, P.C., Deroo, G., Herbin, J.P., Montadert, L., Muller, C., Schaaf, A. & Sigal, J. (1984) - Ocean-wide stagnation episode in the Late Cretaceous. Nature, **308**, 346-349.

Elverhoi, A. & Solheim, A. (1989) - The Barents Sea ; Sediment stratigraphy and Late Quaternary glaciations. In : "Proceedings of the Advanced Research Workshop : Geologic History of the Polar Oceans : Arctic versus Antarctic.", Bremen, October 10-14, 1988 (in press).

Forsyth, D.W. & Uyeda, S. (1975) - On the relative importance of the driving forces of plate motion. Geophys. J. R. astron. Soc., **43**, 163-200.

Guterch, A., Grad, M., Janik, T., Perchuc, E. & Pajchel, J. (1985) - Seismic studies in the crustal structure in West Antarctica 1979-1980 - Preliminary results. Tectonophysics, **114**, 411-429.

Haq, B.U., Hardenbol, J. & Vail, P.R. (1987) - The chronology of fluctuating sea level since the Triassic. Science, Washington, **235**, 1156-1167.

Haugland, K. (1982) - Seismic Reconnaissance Survey in the Weddell Sea. In : Craddock C. (ed), Antarctic Geoscience. Univ. of Wisconsin Press. Madison, 405-413.

Haugland, K., Kristoffersen, Y. & Velde, A. (1985) - Seismic investigations in the southern Weddell Sea Embayment. Tectonophysics, **114**, 293-313.

Haxby, W.F. & Parmentier, E.M. (1988) - Thermal Contraction and the State Stress in the Oceanic Lithosphere. J. Geophys. Res., **93**, 6419-6429.

Henriet, J.P. & Miller, H. (1989) - Some speculations regarding the nature of the Explora-Andenes Escarpment. In : "Proceedings of the Advanced Research Workshop : Geologic History of the Polar Oceans : Arctic versus Antarctic.", Bremen, October 10-14, 1988 (in press).

Hinz, K. & Block, M. (1984) - Results of geophysical investigations in the Weddell Sea and in the Ross Sea, Antarctica. Proc. 11th World Petr. Congr., London, 1983, Wiley, New York, 279-291.

Hinz, K. & Krause, W. (1982) - The continental margin of Queen Maud Land/Antarctica : seismic sequences, structural elements and geological development. Geol. Jb., **E 23**, 17-41.

Hinz, K. & Kristoffersen, Y. (1987) - Antarctica. Recent Advances in the Understanding of the Continental Shelf. Geol. Jb., **E 37**, 1-54.

Huber, B. (1988) - Upper Campanian-Maastrichtian foraminifers of the high southern latitudes : ontogenetic morphometric systematics, biostratigraphy, and paleobiogeography. Ohio State University, Unpublished Ph. D. thesis, 237-313.

Kastens, K.A. (1987) - A Compendium of Causes and Effects of Processes at Transform Faults and Fracture Zones. Reviews of Geoph., **25**, 1554-1562.

Kimura, K. (1982) - Geological and Geophysical Survey in the Bellingshausen Basin, off Antarctica. Antarctic Research, **75**, 12-24.

King, M.S. & Pandit, B.I. (1981) - Some seismic, electrical and thermal properties of subseabottom permafrost samples from the Beaufort Sea. In : Proc. 4th Can. Permafrost Conf., Nat. Research Council of Canada, Calgary.

Ledbetter, M.T. & Ciesielski, P.F. (1982) - Bottom-current erosion along a traverse in the South Atlantic sector of the Southern Ocean. Marine Geology, **46**, 329-343.

Lewis, S.D. & Hayes D.E. (1985) - Forearc basin development along Western Luzon, Philippines. Energy, **10**, 3-4, 281-296.

McCoy, F.W. & Zimmerman, H.B. (1977) - A history of sediment lithofacies in the South Atlantic Ocean. In : Perch-Nielsen, K. & Supko, P. (eds), Initial Reports DSDP, **39**, Washington (U.S. Govt. Printing Office), 459-467.

Meissner, R., Henriet, J.P. & the GRAPE team (1988) - Tectonic features northwest of the Antarctic Peninsula : New evidence from magnetic and seismic studies. Ser. Cient. INACH **38**, 89-105.

Miller, K.G. & Kent D.V. (1987) - Testing Cenozoic eustatic changes : the critical role of stratigraphic resolution. Cushman Foundation for Foraminiferal Research, Special Publication **24**, 51-56.

Miller, H., Henriet. J.P., Jokat, W. & Moons, A. (1988) - High-resolution reflection seismic investigations in the Weddell Sea during the ANTARKTIS V/4 expedition. In : "Proceedings of the Belgian National Colloquium on Antarctic Research", Brussels, October 20, 1987, 65-95.

Miller, H., Henriet, J.P., Kaul, N. & Moons A. (1989) - A fine scale seismic stratigraphy of the eastern margin of the Weddell Sea. In : "Proceedings of the Advanced Research Workshop : Geologic History of the Polar Oceans : Arctic versus Antarctic.", Bremen, October 10-14, 1988 (in press).

Mitchum, R.M., Vail, P.R. & Thompson, S. III (1977) - Seismic Stratigraphy and Global Changes of Sea Level, Part 2: The Depositional Sequence as a Basic Unit for Stratigraphic Analysis. Am. Ass. Petr. Geol. Mem., **26**, Tulsa, 53-62.

Mutter, J.C., Hegarty, K.A., Cande, S.C. & Weissel, J.K. (1985) - Breakup between Australia and Antarctica : a brief review in the light of new data. Tectonophysics, **114**, 255-279.

Natland, J.H. (1978) - Composition, provenance, and diagenesis of Cretaceous clastic sediments drilled on the Atlantic continental rise off southern Africa, DSDP Site 361. In : Bolli, H.M. & Ryan W.B.F. (eds), Initial Reports DSDP, 40, Washington (U.S. Govt. Printing Office), 1025-1061.

Parra, J.C, Yanez G. and USAC-group (1988) - Aeromagnetic Survey on the Antarctic Peninsula and surrounding seas : Integration of the data obtained at different altitudes. Ser. Cient. INACH **38**, 118-131.

Parson , B. & Sclater, J.G. (1977) - An analysis of the variation of ocean floor bathymetry and heat flow with age. J.. Geophys. Res. **82**, 803-827.

Roach, P.J. (1978) - The nature of back-arc extension in Bransfield Strait. Geophys. J. R. astron. Soc., **53**, 165 pp.

Rogers, J.C. & Morack, J.L. (1983) - Geophysical detection of subsea permafrost. In : Geyer, R.A. (ed), CRC Handbook of Geophysical Exploration at Sea, Cleveland, 187-210.

Sandwell, D. (1986) - Thermal stress and the spacing of transform faults. J. Geophys. Res., **91**, 6405-6417.

Shipboard Scientific Party DSDP Leg 35 (1976) - Site 325. Initial Reports, Nat. Sc. Found.

Shipboard Scientific Party ODP Leg 113 (1988) - Sites 691 and 692. Initial Reports, Nat. Sc. Found., 293-328.

Shipboard Scientific Party ODP Leg 113 (1988) - Site 693. Initial Reports, Nat. Sc. Found., 329-447.

Southam, J.R. , Peterson, W.H. & Brass, G.W. (1982) - Dynamics of anoxia. Paleogeogr., Paleoclimatol., Paleoecol. **40**, 183-198.

Vail, P.R., Colin, J.P., Du Chene, R.J., Kuchly, J., Mediavilla, F. & Trifilieff, V. (1987) - La stratigraphie séquentielle et son application aux corrélations chronostratigraphiques dans le Jurassique du Bassin de Paris. Bull. Soc. Géol. France, **8**, III, 1307-1321.

Westbrook, G.K., Lad, J.W., Buhl, P., Bangs, N. & Tiley, G.J. (1988) - Cross section of an accretionary wedge : Barbados Ridge complex. Geology, **16**, 631-635.

Zimmerman, H.B., Boersma, A. & McCoy, F.W. (1987) - Carbonaceous sediments and palaeoenvironment of the Cretaceous South Atlantic Ocean. In : Brooks, J. & Fleet, A.J. (eds), Marine Petroleum Source Rocks. Geol. Soc. Spec. Publ., **26**, 271-286.

Figures